

MODELLING A SOUND RADIATED BY A TURBULENT JET

Tatyana Sergeevna Stanko

M.Sc. Applied Mathematics and Physics

Submitted in accordance with the requirements for the
degree of Doctor of Philosophy

The University of Leeds

School of Process, Environmental and Material Engineering

December 2010



IMAGING SERVICES NORTH

Boston Spa, Wetherby

West Yorkshire, LS23 7BQ

www.bl.uk

BEST COPY AVAILABLE.

VARIABLE PRINT QUALITY

The candidate confirms that the work submitted is her own and that appropriate credit has been given where reference has been made to the work of others.

This copy has been supplied on the understanding that it is copyright material and that no quotation from the thesis may be published without proper acknowledgement.

The right of Tatyana Sergeevna Stanko to be identified as Author of this work has been asserted by her in accordance with the Copyright, Designs and Patents Act 1988.

The University of Leeds

December 2010

Tatyana Sergeevna Stanko

Acknowledgements

The European Commission is gratefully acknowledged for the financial support of the author with an EST Marie Curie Fellowship, contract number MEST-CT-2005-020327.

The author wishes to acknowledge the members of the Engineering Department at the University of Leeds, especially Prof. M.Pourkashanian, Prof. D.B.Ingham, Prof. M.Fairweather and Prof. R.Pollard, who's advice and guidance made this project possible.

I must also thank those persons and organizations external to the department who assisted in my research including Dr. Kevin Hughes and Dr. Ma Lin, and Fluent Europe for the use of their CFD code, especially Dr. Domenico Caridi and Dr. Chris Carey for their advices on using the CFD code in application to acoustical problems.

Finally I would like to express my gratitude to my friends for their kind support.

Abstract

Noise standards around the world for aircrafts have become more stringent. Jet noise is a major source of noise from the aircraft particularly during takeoff and landing. Therefore it is important to investigate the nature of the jet noise and to be able to predict the noise level using numerical approaches. A substantial amount of research work has been performed on numerical investigations of noise. The majority of these may be split into two main approaches: the semi-empirical source models, based on the steady RANS computations, which provides information about turbulent length and time scales which is translated by empirical relations into sound-source spectra, and the 'direct' numerical simulations of the acoustic sources coupled with the analytical transport techniques, namely the Ffowcs Williams – Hawkings (FW-H) equation. The first approach is more specific and case dependent, however it is computationally fast, since it requires only 2D steady RANS simulations. The second approach is basically case independent, however it is very time-consuming since it requires unsteady numerical solutions for the flow field.

The FW-H approach is well developed and widely validated when coupled with the Large Eddy Simulation (LES). However we have found that there are no investigations of the FW-H acoustic model coupled with the unsteady RANS simulations. It is widely accepted that the LES simulation results are usually more detailed than the RANS, but it is still not known to that extent the LES approach is more (or not more) reliable than the URANS for the jet noise prediction purposes. In addition we have discovered that despite the FW-H model being well developed in the commercial CFD software, such as FLUENT, there is no published data on the application of the FW-H model in FLUENT to the jet noise problems.

This research is focused on the validation of the jet acoustic models that exist in FLUENT with the available experimental data. We employ three sets of experimental data, obtained by different research groups, to investigate the turbulence model approach for the source noise modelling and the acoustic model for the simulation of the noise level in the far field. For simplicity, we decided to concentrate our numerical investigations on the jets of relatively low Mach number, up to 0.6, and the flow issuing from the nozzle of a simple geometry, i.e. without chevrons.

It should be noted that so far FLUENT includes two acoustical models which are applicable to jet noise problems, namely the FW-H model and the so-called Goldstein acoustic model, which is effectively one of the numerous variations of the semi empirical source models. The latter model has some difficulties in the current state of realization in FLUENT, and therefore we have reproduced the same approach in a separate software (MatLab) for the post-processing of the acoustics.

In the future the results of this research will be useful for industrial applications to a wide range of jet noise problems.

CONTENTS

Acknowledgements	ii
Abstract	iii
Figures	ix
Tables	xv
Nomenclature	xvii

Chapter 1

Aeroacoustics

1.1 Introduction	1
1.2 Current and future aircraft noise in the UK	1
1.2.1 Measuring sound and noise	1
1.2.2 Current noise levels	3
1.3 Reducing the impact of noise from aviation	5
1.3.1 Reducing aircraft noise at source	5
1.3.2 Aircraft noise components	6
1.4 Jet noise	7
1.5 The purpose of the research	9

Chapter 2

Acoustic methods

2.1 Lighthill's acoustic analogy	12
2.1.1 Theory Description	13
2.1.2 Sound Fields Radiated by Simple Sources	17
2.1.2.a Radiation from a monopole source	17
2.1.2.b Radiation from a dipole source	18
2.1.2.c Radiation from a lateral quadruple source	19
2.1.2.d Radiation from a linear quadruple source	20
2.1.3. Particular cases	22
2.1.4 Lighthill turbulence stress tensor	22
2.1.5 Direct solution of the Lighthill equation	23
2.1.6 Assumptions	24
2.1.7 Eighth power law	25
2.2 Curle's acoustic formulation	27
2.3 Ffowcs Williams – Hawkings acoustic formulation	28
2.3.1 Position of the FW-H surface	30
2.4 Ribner's acoustic formulation	31
2.5 Goldstein's acoustic formulation	36
2.5.1 Determination of the aerodynamic and statistical quantities from the $k - \epsilon$ RANS model	38
2.5.2 Determination of the acoustical intensity spectrum	39
2.5.3 Realisation of the Goldstein's model in the CFD code	40
2.6 Conclusions	41

Chapter 3

CFD methods

3.1 Introduction	43
3.2 Standard $k - \epsilon$ model	44
3.2.1 Transport equations for the Standard $k - \epsilon$ model	44
3.2.2 Modelling the turbulent viscosity	45
3.2.3 Model constants	46
3.3 RNG $k - \epsilon$ model	46
3.3.1 Transport equation for the RNG $k - \epsilon$ model	47
3.3.2 Modelling the turbulent viscosity	47
3.3.3 Calculating the inverse effective Prandtl numbers.....	48
3.3.4 The $R\epsilon$ term in the ϵ equation.....	48
3.3.5 Model constants	49
3.4 Realizable $k - \epsilon$ model.....	49
3.4.1 Transport equation for the Realizable $k - \epsilon$ model.....	50
3.4.2 Modelling the turbulent viscosity	52
3.4.3 Model constants	52
3.5 Reynolds stress model.....	53
3.5.1 Reynolds stress transport equations	53
3.6 Large Eddy Simulation model	58
3.6.1 Filtered Navier-Stokes equations	58
3.6.2 Subgrid-scale models	60
3.6.2.a Smagorinsky-Lilly model	61
3.6.2.b Dynamically Smagorinsky-Lilly model.....	61
3.6.3 Inlet boundary conditions for the LES model	62
3.6.3.a Vortex Method	62
3.6.4 How to run LES in FLUENT 12.0	63
3.7 Conclusions	65

Chapter 4

Cold Propane Jet Simulation

4.1 Introduction	67
4.2 Sandia experiment data	68
4.2.1 Fluid flow	68
4.2.2 Experimental data description.....	70
4.2.3 Data consistency check	70
4.3 2D CFD simulations.....	74
4.3.1. Grid employed to simulate the flow in the pipe.....	74
4.3.2 Grid employed to simulate the free jet flow.....	74
4.4 2D simulation of the flow in the pipe.....	76
4.4.1 Study of the effect of different turbulence models.....	77
4.4.2 Study of the effect of the density law.....	78
4.4.3 Study of the effect of the roughness of the wall.....	80
4.4.4 Study of the effect of the inlet velocity.....	81
4.4.5 Summary of the results of the simulation flow in a pipe	82
4.4.6 Intermediate conclusions.....	84
4.5 2D simulations for a free jet.....	84
4.5.1 Essential parameters for the jet simulation	84

4.5.2 Jet inlet profile specification	85
4.5.3 The choice of the turbulence model	86
4.5.4 Details of the simulation	87
4.5.5 Velocity field simulation results	87
4.5.6 Intermediate conclusions.....	91
4.6 2D acoustics	92
4.6.1 Acoustic results obtained when the initial velocity profile is varied	92
4.6.2 Acoustic results obtained when the co-flow velocity is varied.....	93
4.6.3 Theoretical estimation of the noise level	97
4.6.4 Intermediate conclusions.....	100
4.7 3D CFD simulations.....	101
4.7.1. Pre-processing analysis for 3D LES simulations	101
4.7.2. Mesh for the 3D LES simulation	105
4.7.3. Boundary conditions	106
4.7.4. Flow field simulation results	107
4.8 3D acoustics	113
4.9 Conclusions	115

Chapter 5

Cold Air Jet Simulation

5.1 Introduction	117
5.2 Experimental setup.....	117
5.3 2D simulations	120
5.3.1 Computational grid	120
5.3.2 Boundary conditions and simulation strategy	122
5.3.3 Grid dependency analysis	124
5.3.4 Velocity field simulation results	126
5.3.5. Acoustic field analysis using the Goldstein model	126
5.4 3D simulations	127
5.4.1. Pre-processing analysis for the 3D LES simulation.....	128
5.4.2 Grid for 3D LES simulations	132
5.4.3 Boundary conditions for the 3D simulations	135
5.4.4 Acoustic results	137
5.5 Conclusions	140

Chapter 6

Hot Air Jet Simulation

6.1 Introduction	142
6.2 Experimental setup.....	142
6.2.1 Experimental data: flow field.....	145
6.2.2. Experimental data: acoustic field	146
6.3 Simulations.....	148
6.3.1 Grid employed in the simulations	149
6.3.2 Boundary conditions and simulation strategy	156
6.3.3 Nozzle flow simulations.....	159
6.4 2D test simulation results.....	159
6.4.1 Jet inlet boundary conditions	159
6.4.2 Position of the cylindrical outlet boundary	161

6.4.3 FWH source surface.....	162
6.4.4 Grid dependency	164
6.4.5 2D test results summary	165
6.5 3D simulation results	165
6.5.1. Pre-processing analysis for 3D LES simulations	165
6.5.2 3D mesh and boundary conditions	171
6.5.3 Velocity field.....	172
6.5.4 Acoustic field	176
6.6 Conclusions	181

Chapter 7

Discussion

7.1 General remarks	184
7.2 Numerical scheme	185
7.3 Reflection on the boundaries.....	186
7.4 RANS vs LES	188
7.5 FWH surface	189
7.6 Experimental data for validation.....	190
7.7 On the numerical results.....	191

Chapter 8

Conclusions and Future work

8.1 Conclusions	195
8.1.1 Summary of conclusions	195
8.1.2 General conclusions	198
8.2 Future work	199
References	201

Figures

Figure 1.2.1.1 <i>Sketch of the audible frequencies range.</i>	2
Figure 1.2.1.2 <i>Acoustic weighting curves.</i>	3
Figure 1.2.2.1 <i>The future development of air transport in the UK.</i>	4
Figure 1.3.2.1 <i>The noise distribution components for typical present aircraft.</i>	7
Figure 1.5.1 <i>The concept of thesis</i>	10
Figure 2.1.1.1 <i>Schematic representation of Lighthill's theory of aerodynamic noise.</i>	17
Figure 2.1.2.a.(1) <i>A directivity pattern for a monopole source.</i>	18
Figure 2.1.2.a.(2) <i>A pressure field produced by a monopole source.</i>	18
Figure 2.1.2.b.(1) <i>A directivity pattern for a dipole source.</i>	19
Figure 2.1.2.b.(2) <i>A pressure field produced by a dipole source.</i>	19
Figure 2.1.2.c.(1) <i>A directivity pattern for a lateral quadruple source.</i>	20
Figure 2.1.2.c.(2) <i>A pressure field produced by a lateral quadruple source.</i>	20
Figure 2.1.2.d.(1) <i>A directivity pattern for a linear quadruple source in the near field.</i>	21
Figure 2.1.2.d.(2) <i>A directivity pattern for a linear quadruple source in the far field.</i>	21
Figure 2.1.2.d.(3) <i>A pressure field produced by a linear quadruple source.</i>	21
Figure 2.1.5.1. <i>Acoustic analogy modelling.</i>	24
Figure 2.4.1 <i>Turbulent jet flow configuration (x, θ, ϕ are the spherical coordinates of the point of observation \vec{x} and \vec{y} is the midpoint of the two points \vec{y}' and \vec{y}'').</i>	33
Figure 2.4.2 <i>Noise radiation patterns.</i>	36
Figure 4.2.1.1 <i>A schematic diagram of the Sandia experiment.</i>	71
Figure 4.2.2.1 <i>Experimentally measured by Schefer (1988) inlet profiles of the mean and fluctuating axial velocity. (a) Mean axial velocity; (b) axial velocity rms fluctuations.</i>	73
Figure 4.2.3.1 <i>Analysis of the experimental data: experimentally measured by Schefer (1988): centreline profiles of the mean axial velocity (black symbols) and the mean axial velocity measured at the centreline points of the radial profiles $x/d = 4, 15, 30$ and 50 (red symbols).</i>	75
Figure 4.3.2.1 <i>Jet grid dimensions and structure.</i>	77
Figure 4.4.5.1 <i>Comparison of the turbulent velocity profile in the tube between Prandtl theory and CFD</i>	85

simulations.

Figure 4.5.5.1. Mean and fluctuating axial velocity component profiles at $x/d = 4$; symbols, experimental data; solid line, simulation predictions using the grid N_1 ; dashed line, simulation predictions using the grid N_2 , both with the Prandtl velocity profile as the inlet condition and RSM turbulent model employed.	90
Figure 4.5.5.2 Radial profiles of the mean axial velocity component, \bar{U} , in the jet studied by Schefer (1988), (a), (b), (c) and (d) at $x/d = 4, 15, 30$ and 50 , respectively, and (e) along the axis.	91
Figure 4.5.5.3 Radial profiles of the rms of the axial velocity, $\sqrt{u'^2}$, for the jet studied by Schefer (1988), (a), (b), (c) and (d) at $x/d = 4, 15, 30$ and 50 , respectively, and (e) along the axis.	91
Figure 4.5.5.4 Radial profiles of the rms of the radial velocity component, $\sqrt{v'^2}$, for the jet studied by Schefer (1988), (a), (b), (c) and (d) at $x/d = 4, 15, 30$ and 50 , respectively, and (e) along the axis.	92
Figure 4.5.5.5 Radial profiles of the velocity correlation, $\overline{u'v'}$, for the jet studied by Schefer (1988), (a), (b), (c) and (d) at $x/d = 4, 15, 30$ and 50 , respectively, and (e) along the axis.	92
Figure 4.5.5.6 Radial profiles of mean mixture fraction, \bar{f} , for the jet studied by Schefer (1988) (a), (b), (c) and (d) at $x/d = 4, 15, 30$ and 50 , respectively, and (e) along the axis.	93
Figure 4.6.1.2 The jet acoustic power level (dB) predictions along the axis of the jet. The symbols are experimental data; the solid lines are the simulation results with a flat velocity profile at the inlet; the dashed lines are the simulation results with a Prandtl velocity profile at the inlet; the dotted lines are the simulation results with the profile as obtained from the tube in section 4.4.	94
Figure 4.6.2.1 Jet acoustic power level spectra, P_A [dB], measured by Papamoschou (2007). Notation: U_p primary flow velocity corresponds to U_{jet} , U_s secondary flow velocity corresponds to $U_{co-flow}$, primary flow velocity is fixed	97
Figure 4.6.2.2-4(a,b) Contours of (a) the turbulent kinetic energy, k [m^2s^{-2}], and (b) the acoustic power level, P_A [dB], for a jet with an inlet profile obtained from the pre-simulation in the pipe, and with the co-flow air velocity varied.	98

Figure 4.6.2.5(a) <i>Jet acoustic power level predictions, P_A[dB], at the radial section at a distance $x/d = 4$.</i>	99
Figure 4.6.2.5(b) <i>Jet acoustic power level predictions, P_A[dB], at the radial section at a distance $x/d = 15$.</i>	99
Figure 4.6.2.5(c) <i>Jet acoustic power level predictions, P_A[dB], along the axis.</i>	99
Figure 4.6.3.1 <i>Theoretically predicted directivity compared with the experimentally measured values.</i>	101
Figure 4.7.1.1 <i>Cumulative turbulence kinetic energy spectra (TKE) against the length-scale of the eddies based on the Kolmogorov energy spectrum.</i>	104
Figure 4.7.1.2 <i>Sketch of the elements of the 2D mesh; geometrical dimensions are marked at the key points, the number of nodes thickening of the mesh size is shown by arrows and the stretching ratio is defined in round brackets.</i>	105
Figure 4.7.1.3 <i>Contours of the Kolmogorov length scale (m), obtained in 2D axisymmetrical RANS standard $k - \epsilon$ simulation</i>	106
Figure 4.7.2.1 <i>2D slice of the computational grid used for the LES computations.</i>	108
Figure 4.7.4.1 <i>3D LES results: contours of the instantaneous vorticity of the turbulent jet in the middle section.</i>	110
Figure 4.7.4.2 <i>3D LES results: contours of the instantaneous vorticity of the turbulent jet in the middle section.</i>	111
Figure 4.7.4.3 <i>Radial profiles of the mean axial velocity component (\overline{U}) in the jet, (a, b, c, d) at $x/d = 4, 15, 30$ and 50 and (e) along the axis.</i>	113
Figure 4.7.4.4 <i>Radial profiles of rms of axial velocity ($\sqrt{u'^2}$) the jet, (a, b, c, d) at $x/d = 4, 15, 30$ and 50 and (e) along the axis.</i>	113
Figure 4.7.4.5 <i>Radial profiles of rms of radial velocity component ($\sqrt{v'^2}$) the jet, (a, b, c, d) at $x/d = 4, 15, 30$ and 50 and (e) along the axis.</i>	114
Figure 4.7.4.6 <i>Radial profiles of the velocity correlation ($\overline{u'v'}$) the jet, (a, b, c, d) at $x/d = 4, 15, 30$ and 50 and (e) along the axis.</i>	114
Figure 4.8.1 <i>Theoretically predicted directivity compared with experimentally measured values, LES and unsteady RANS(RSM) simulation results.</i>	116
Figure 5.2.1. <i>NASA Dual PIV setup, from Panda et al. (2004).</i>	120
Figure 5.3.1.1 <i>Sketch of the elements of the 2D grid; geometrical dimensions are marked at the key</i>	124

points, the thickening of the mesh size is shown by arrows and the sketch of the jet mean velocity contours by the grey line.

Figure 5.3.2.1. Sketch of the 2D specified boundary conditions.	125
Figure 5.3.3.1 Grid dependency analysis: RSM simulation results for the mean axial and UU Reynolds stress velocity components measured at the two radial sections located at 5 and 10 nozzle diameters downstream, respectively, and for three grid resolutions.	127
Figure 5.3.5.1 Theoretically predicted directivity compared with the experimentally measured values and the simulation results.	129
Figure 5.4.1.1 Cumulative turbulence kinetic energy spectra (TKE) against the length-scale of the eddies based on the Kolmogorov energy spectrum.	131
Figure 5.4.1.2 Sketch of the elements of the 2D grid; geometrical dimensions are marked at key points, the number of nodes thickening of the mesh size is shown by arrows and the stretching ratio is defined in round brackets.	131
Figure 5.4.1.3 Contours of Kolmogorov length scale (m), obtained in 2D axisymmetrical RANS standard $k-\epsilon$ simulation, bulk velocity is 195ms^{-1} .	133
Figure 5.4.1.4 Contours of Kolmogorov length scale (m) in the jet core region obtained in 2D axisymmetrical RANS standard $k-\epsilon$ simulation, bulk velocity is 195ms^{-1}	133
Figure 5.4.2.1 Sketch of the elements of the 2D axisymmetric slice of the 3D grid; geometrical dimensions are marked at the key points, the number of nodes in the thickening of the mesh size is shown by arrows and the stretching ratio is defined in round brackets	135
Figure 5.4.2.2 Grid for the LES computations: (a) front view, (b) side view of the 3D grid.	136
Figure 5.4.4.1 Directivity of the $1/3$ – octave intensity for a jet velocity 195ms^{-1} and for four values of the Strouhal number. Legend: red symbols – simulation results, white symbols – experimental data obtained by Lush (1971).	140
Figure 5.4.4.2 Theoretically predicted directivity compared with the experimentally measured values and the simulation results.	142
Figure 6.2.1 Theoretically predicted directivity compared with the experimentally measured values and the simulation results.	145
Figure 6.2.2 The NASA Acoustic reference nozzle system, with an ARN2 (2in) nozzle, see Bridges and Wernet (2003).	146

Figure 6.2.1.1. <i>Radial profiles of the mean axial velocity component from a fixed axial position of $x/d=3$. The axial velocity data were from the PIV measurements of Bridges and Wernet (2003).</i>	148
Figure 6.2.2.1 <i>The effect of the heating of the narrowband spectra of the jet, Panda et al. (2004).</i>	149
Figure 6.2.2.2 <i>Far field noise spectra measured for different microphone position angles, Tanna et al.(1976). Legend: black symbols – at $[30]^\circ$; green symbols – at $[90]^\circ$ and red symbols – at $[130]^\circ$ from the jet axis.</i>	150
Figure 6.3.1. <i>Sketch of the elements of the 2D grid; geometrical dimensions are marked at the key points, the number of nodes thickening of the mesh size is shown by arrows and the stretching ratio is defined in round brackets.</i>	155
Figure 6.3.2 <i>Sketch of the of the 2D slice of the nozzle; geometrical dimensions are marked at the key points, the number of nodes of the mesh size is shown and stretching ratio is defined in round brackets.</i>	157
Figure 6.3.2.1 <i>Sketch of the 2D specified boundary conditions</i>	159
Figure 6.4.1.1 <i>Plots of the U_{rms} velocity profiles at the radial section at an axial distance $x/d=3$ obtained from the jet flow 2D simulation; the initial and mass flux profile is flat, the turbulence profile is varied.</i>	162
Figure 6.4.1.2 <i>Plots of the noise simulation results for the 2D jet, using FW-H approach, where the initial and mass flux profile is flat, the turbulence profile is varied.</i>	162
Figure 6.4.2.1 <i>Plots of the noise simulation results for the 2D jet, using the FW-H approach, where the initial jet profile is flat, at the position of the radial pressure outlet varied. Legend: black symbols – experimental data by Tanna (1976); red line – Case 1, green line – Case 2, blue line - Case 3.</i>	164
Figure 6.4.3.1 <i>Plots of the noise simulation results for the 2D jet, using the FWH approach, where the position of the cylindrical open FWH source surface is varied. Legend: black symbols – experimental data by Tanna (1976); red line – FWH(int1), green line – FWH(15in), blue line – FWH(30in).</i>	165
Figure 6.4.4.1 <i>Plots of the noise simulation results for the 2D jet, using the FW-H approach, where the position of the cylindrical open FW-H source surface is varied.</i>	167
Figure 6.5.1.1 <i>Contours of the Kolmogorov length scale (m), obtained in 2D axisymmetrical RANS standard $k - \epsilon$ simulation.</i>	169

Figure 6.5.1.2 <i>Contours of the cell size over TKE 90%, obtained in 2D axisymmetrical RANS standard $k - \epsilon$ simulation on mesh.</i>171
Figure 6.5.1.3 <i>Fragment of contours of the cell size over TKE 50%, obtained in 2D axisymmetrical RANS standard $k - \epsilon$ simulation on mesh.</i>172
Figure 6.5.1.4 <i>Fragment of contours of the cell size over TKE 30%, obtained in 2D axisymmetrical RANS standard $k - \epsilon$ simulation on mesh.</i>172
Figure 6.5.3.1 <i>3D LES results: contours of the instantaneous vorticity of the turbulent jet in the middle section.</i>175
Figure 6.5.3.2 <i>3D LES results: contours of the instantaneous velocity derivatives of the turbulent jet in the middle section.</i>175
Figure 6.5.3.3 <i>Radial profiles of the mean axial and rms velocity components from a fixed axial position of $x/d = 3$ and centreline mean axial velocity</i>176
Figure 6.5.4.1 <i>Plots of the noise simulation results, obtained using the FW-H approach, at two angular microphone positions and the radius of 72 nozzle diameters.</i>179
Figure 6.5.4.2 <i>Theoretically predicted directivity compared with experimentally measured values and different simulation results.</i>181
Figure 6.5.4.2 <i>Theoretically predicted directivity compared with experimentally measured values and different simulation results.</i>183

Tables

Table 3.2.3.1 <i>Standard $k - \epsilon$ model constants.</i>	47
Table 3.3.5.1 <i>RNG model constants.</i>	50
Table 3.4.3.1 <i>Realizable model constants.</i>	54
Table 4.2.1.1 <i>Test section dimensions and inlet conditions.</i>	71
Table 4.2.3.1 <i>Velocity flux over radial sections along the jet axis at four locations using two interpolation methods.</i>	74
Table 4.2.3.2 <i>Comparison of the experimentally measured values of UV flow field component taken in radial sections and axial positions.</i>	75
Table 4.3.2.1 <i>Details of the Grid N_1.</i>	77
Table 4.3.2.2 <i>Details of the Grid N_2.</i>	78
Table 4.4.1.1 <i>Simulation details for the case C_1.</i>	80
Table 4.4.1.2 <i>The maximum axial velocity at the outlet of the pipe obtained in the CFD simulations using different modifications of RANS.</i>	80
Table 4.4.2.1 <i>Simulation details for the case C_2.</i>	81
Table 4.4.2.2 <i>The maximum axial velocity at the outlet of the pipe obtained in the CFD simulations using different modifications of RANS.</i>	82
Table 4.4.3.1 <i>Simulation details for case C_3.</i>	82
Table 4.4.3.2 <i>The maximum axial velocity at the outlet of the pipe obtained in the CFD simulations using different modifications of RANS.</i>	83
Table 4.4.4.1 <i>Simulation details for case C_4.</i>	84
Table 4.4.4.2 <i>The maximum axial velocity at the outlet of the pipe obtained in the CFD simulations using different modifications of RANS.</i>	84
Table 4.4.5.1 <i>The maximum axial velocity value at the outlet from the tube 1m long. Results are presented for four different turbulence models and cases C_1, C_2, C_3, C_4.</i>	85
Table 4.5.4.1 <i>Model details for the simulation of the jet flow.</i>	89
Table 4.6.2.1 <i>The effect of the jet/ co-flow velocity ratio on the maximum jet noise generation and on the total noise power per unit length.</i>	96
Table 4.7.1.1 <i>Key values of the cumulative turbulence kinetic energy spectra against length-scale of eddies based on the Kolmogorov energy spectrum.</i>	104
Table 4.7.1.2 <i>Key values of the turbulence length scale along the jet axis required for LES when TKE is resolved by 90%, 80% and 50%.</i>	106

Table 4.7.3.1 <i>Model details for the simulation of the jet flow.</i>	109
Table 5.2.1 <i>Coordinates of the microphone locations (where the angle is measured from the jet direction) in inches and metres in the Lush (1971) experiment.</i>	122
Table 5.2.2.1 <i>Summary of the boundary conditions employed.</i>	126
Table 5.3.1.1 <i>Key values of the cumulative turbulence kinetic energy spectra against the length-scale of eddies based on the Kolmogorov energy spectrum.</i>	131
Table 5.3.1.2 <i>Summary of the boundary conditions employed.</i>	133
Table 5.3.1.3 <i>Number of nodes required for the LES (195ms⁻¹) when TKE is resolved by 90%, 80% and 70%.</i>	135
Table 5.3.3.1 <i>Summary of the boundary conditions for LES simulations.</i>	139
	147
Table 6.2.1 <i>Operating conditions of the NASA experiment.</i>	
Table 6.2.2 <i>Coordinates of the microphone locations (where the angle is measured from the jet direction) in inches and meters in the NASA experiment, Panda et al. (2004).</i>	148
Table 6.2.3 <i>Coordinates of the microphone locations (where the angle is measured from the jet direction) in inches and meters in the Tanna et al. (1976) experiment.</i>	148
Table 6.3.1 <i>Structural elements of the mesh.</i>	158
Table 6.3.2.1 <i>Details of the simulation cases.</i>	159
Table 6.3.2.2 <i>Summary of the boundary conditions employed.</i>	160
Table 6.4.2.1 <i>Details of the simulation cases.</i>	164
Table 6.5.1.1 <i>Key values of the cumulative turbulence kinetic energy spectra against length-scale of eddies based on the Kolmogorov's energy spectrum.</i>	169
Table 6.5.1.2 <i>Key values of the turbulence length scale along the jet axis required for LES when TKE is resolved by 90%, 80% and 50%.</i>	170
Table 6.5.2.1: <i>Summary of the boundary conditions employed.</i>	174

Nomenclature

Roman letters

A_c	<i>Correlation area.</i>
$C_{\rho\rho}$	<i>Density autocorrelation function.</i>
c_0	<i>Speed of sound in the fluid in its equilibrium.</i>
d	<i>Nozzle diameter.</i>
dt	<i>Numerical time step.</i>
d/dt	<i>Total derivative with respect to time.</i>
G	<i>Filter function.</i>
\vec{g}	<i>Gravitation vector.</i>
H	<i>Heaviside operator.</i>
I	<i>Acoustic intensity, $\frac{W}{m^2}$.</i>
I_ω	<i>Acoustic intensity spectrum.</i>
K_a	<i>The von Karman constant.</i>
L	<i>Characteristic length scale.</i>
L_p	<i>Sound pressure level, dB.</i>
l_0	<i>Kolmogorov turbulent length scale.</i>
M	<i>Mach number.</i>
M_c	<i>Convection Mach number, based on ambient speed of sound.</i>
M_a	<i>Acoustic Mach number, based on local speed of sound.</i>
N	<i>Label of the numerical setup.</i>
\vec{n}	<i>Normal vector.</i>
p	<i>Thermodynamic pressure.</i>
p_0	<i>Ambient pressure.</i>
p'	<i>Pressure fluctuations.</i>
P_a	<i>Acoustic power, $\frac{W}{m^3}$.</i>
P_{ref}	<i>Reference acoustic power, $\frac{W}{m^3}$.</i>
Pr	<i>Prandtl number.</i>
R	<i>The molar gas constant.</i>
\vec{r}	<i>Distance in polar and spherical coordinates, m.</i>
Re	<i>Reynolds number.</i>
\mathfrak{R}_{ijkl}	<i>The two-point fourth-order correlation tensor.</i>

S	<i>Integration surface.</i>
Sc	<i>Schmidt number.</i>
\bar{S}_{ij}	<i>The rate-of-strain tensor.</i>
T	<i>Temperature, K.</i>
t	<i>Time, s.</i>
T_{ij}	<i>Lighthill turbulence stress tensor.</i>
U	<i>Mean flow velocity component, $\frac{m}{s}$.</i>
U_c	<i>Axial eddy convection velocity component, $\frac{m}{s}$.</i>
$\vec{u}, \vec{v}, \vec{w}$	<i>Fluid velocity components, $\frac{m}{s}$.</i>
V	<i>Chapter 2: Space volume, m^3; Chapters 4-6: velocity component, $\frac{m}{s}$</i>
W	<i>Acoustic power, $\frac{W}{m^3}$.</i>
W_ω	<i>Acoustic power spectrum.</i>
\vec{x}	<i>Space vector.</i>

Greek letters

α, β	<i>Coefficients.</i>
Γ	<i>Circulation.</i>
γ	<i>The isentropic expansion factor.</i>
δ_{ij}	<i>Kronecker delta.</i>
ϵ	<i>Turbulent dissipation rate.</i>
$\vec{\eta}$	<i>Space vector.</i>
θ, ϕ	<i>Angle.</i>
k	<i>Turbulent kinetic energy.</i>
μ	<i>Viscosity, $\frac{kg}{s \cdot m}$</i>
$\vec{\xi}$	<i>Space vector.</i>
ρ	<i>Fluid density, $\frac{kg}{m^3}$.</i>
$\bar{\rho}$	<i>Mean density, $\frac{kg}{m^3}$.</i>
ρ_0	<i>Ambient density, $\frac{kg}{m^3}$.</i>
ρ'	<i>Density density, $\frac{kg}{m^3}$.</i>
Σ	<i>Viscous (or traceless) part of the stress tensor.</i>
τ	<i>Retarded time, s.</i>

ω_f *Characteristic frequency, Hz.*

Abbreviations

<i>DNS</i>	<i>Direct Numerical Simulation</i>
<i>LES</i>	<i>Large Eddy Simulation.</i>
<i>RANS</i>	<i>Reynolds Average Navier-Stokes.</i>
<i>TR</i>	<i>Temperature ratio.</i>
<i>TKE</i>	<i>Turbulent kinetic energy.</i>
<i>URANS</i>	<i>Unsteady Reynolds Average Navier-Stokes.</i>

Chapter 1

Aeroacoustics

1.1 Introduction

Since the 1950s when jet aircraft entered civil aviation, the problem of their noise became crucial. Despite over the last few decades much research work has been performed to reduce the noise level of aircraft the problem still exists.

1.2 Current and future aircraft noise in the UK

For many people living around airports, noise is the most evident environmental impact of aviation. Community action groups have been established at many of the UK's airports, particularly where noise is an issue of considerable concern. The quality of life of many people living under the approach or departure flight path can be affected by aircraft noise. These effects arise from the effect of noise on concentration or sleep and from feelings of anger, frustration and powerlessness to control the noise. However, while many people have expressed concerns over aircraft noise, there remain considerable uncertainties over the precise nature of its effects.

Noise is usually defined as unwanted sound. However, people's reactions to particular sounds are highly individual and depend on many factors, such as its loudness and pitch; how often the sound occurs; its similarity to background sound; and a range of social factors.

1.2.1 Measuring sound and noise

Sound is a periodic disturbance of the atmosphere that human beings can hear. Periodical disturbances, so-called frequencies, are expressed in *Hz* (hertz), with unit *cycle/s* or s^{-1} . Frequency is inversely proportional to the wave length. Not all frequencies are audible by humans, but only frequencies in the range $20\text{Hz} - 20\,000\text{Hz}$. Figure 1.2.1.1 shows a sketch of the audible range of frequencies:

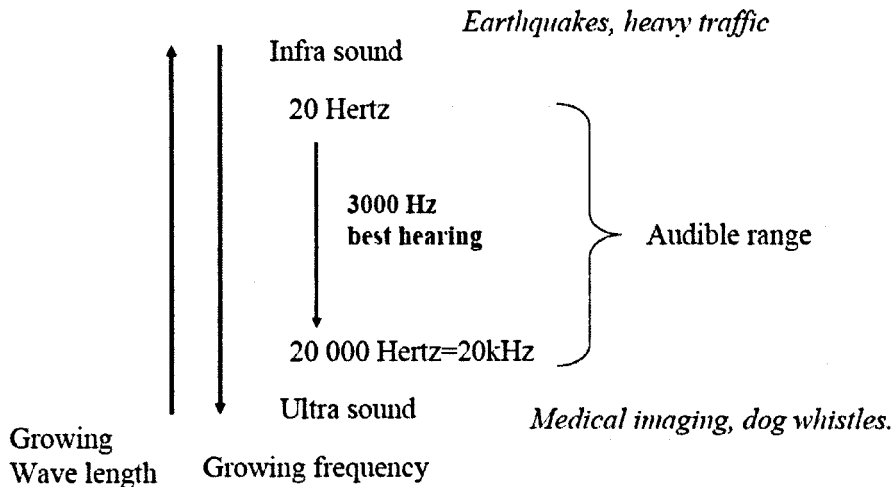


Figure 1.2.1.1 *Sketch of the audible frequencies range.*

In addition to frequency, volume (or loudness) is another main sound characteristic. The volume is the level of energy in the sound wave: the higher the energy, the louder the sound. This is measured on the scale of decibels (dB). The decibel is a logarithmic unit which indicates the relative acoustic power of sound to a specified or implied reference level, $L_p = 10 \cdot \log \left(\frac{P_a}{P_{ref}} \right)$. The reference acoustic power is set to be $P_{ref} = 10^{-12} \frac{W}{m^3}$, a threshold of human perception.

A reason for using the decibel is that the ear is capable of detecting a very large range of sound pressures. The ratio of the sound pressure that causes permanent damage from short exposure to the limit that (undamaged) ears can hear is above a million. Because the power of a sound wave is proportional to the square of the pressure, the ratio of the maximum power to the minimum power is above one (short scale) trillion. To deal with such a range, logarithmic units are useful: the \log of a trillion is 12, so this ratio represents a difference of $120dB$.

Since the human ear is not equally sensitive to all the frequencies of sound within the entire spectrum, noise levels at maximum human sensitivity — middle A and its higher harmonics (between 2 and 4kHz) — are factored more heavily into sound descriptions using a process called frequency weighting, see Figure 1.2.1.2.

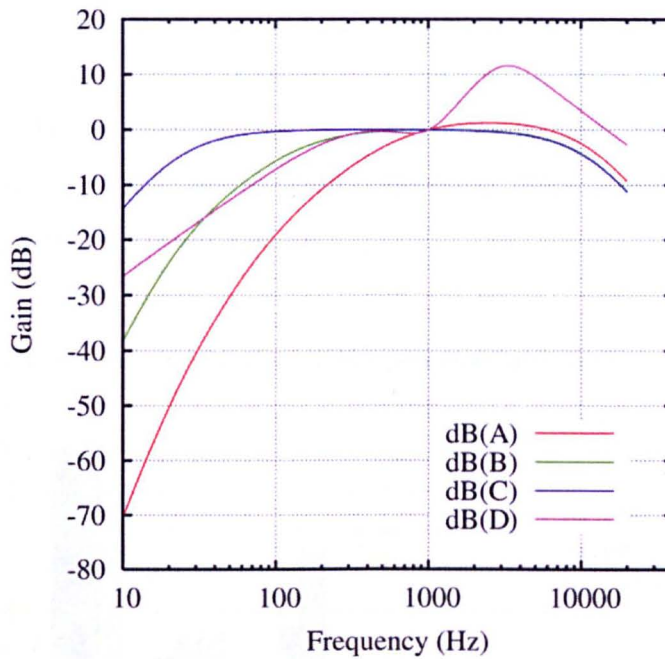


Figure 1.2.1.2 *Acoustic weighting curves.*

In this figure, A-weighting is only really valid for relatively quiet sounds and for pure tones. The B and C curves were intended for louder sounds (though they are less used) while the D curve is used in assessing loud aircraft noise.

According to Tipler (1991) a volume of normal breathing is about 10dB , soft whisper – 30dB , normal conversation 60dB , busy traffic – 70dB , average factory – 80dB , Niagara Falls – 90dB .

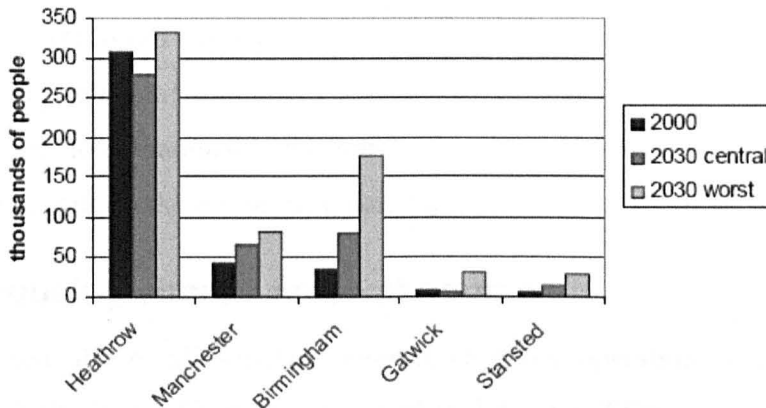
Present aircraft noise is not beyond 60dB , but it is annoying as being out of control for people living near an airport. Vacuum cleaners are noisier than an aircraft overhead, but can be switched off at will.

1.2.2 Current noise levels

Noise from aviation largely comes from aircraft approaching or taking off from airports. Individual aircrafts have become quieter but flight frequencies have increased, and so noise from aircraft gives rise to increasing community concern. In particular, landing noise is of increasing importance, and has become the dominant reason for complaints at some airports.

The largest airports are already operating close to their operating capacity limits. Thus, with no expansion of the infrastructure, the noise climate would be expected to improve over the next few decades as quieter aircraft come into service. This is illustrated in figure 1.2.2.1, which shows the noise climate around various UK airports under different growth scenarios.

Forecast noise exposure from expansion at UK airports under three scenarios



Source: based on figures quoted in Department for Transport, *The future development of air transport in the United Kingdom: a national consultation*, July 2002 (and second edition, February 2003).

Figure 1.2.2.1 *The future development of air transport in the UK.*

However, providing new infrastructure, such as additional runways, would mean that the effects of increase in aircraft movements could outstrip improvements in technology and thus increase noise exposure. Indeed, the Government's consultation documents estimate that an additional runway at Heathrow would double passenger numbers by 2030, leading to a further 25 000 people being exposed to noise levels above 57dB, even with quieter aircraft.

In contrast, European noise policy aims to ensure that, on average, there should be no short term increase in the number of people exposed to high levels of noise and that these numbers should be reduced in the long term. Thus, if the number of people exposed to aircraft noise increases in line with the forecasts, compliance with EU policy would require equivalent reductions in the number exposed to noise elsewhere (and perhaps from other sources).

1.3 Reducing the impact of noise from aviation

There are three main tiers of regulation governing aircraft noise in the UK: international, EU and national. At the international level, the International Civil Aviation Organization (ICAO) sets progressively tighter certification standards (known as chapters) for noise emission from civil aircraft. In addition to these specific requirements, the ICAO requires members to adopt a “balanced approach” to noise management which looks beyond individual aircraft to:

- reducing aircraft noise at source
- land-use planning
- changes to operational procedure
- restrictions on the use of the noisiest aircraft.

1.3.1 Reducing aircraft noise at source

As mentioned above, all subsonic aircraft currently operating in the EU must comply with the ICAO Chapter 4 standard (valid since 2006), which represents a reduction of 10dB on measurements for Chapter 3 aircraft. The Chapter 3 noise standard was agreed in 1977. These standards are regulated with reference to the sum of measurements taken at three separate locations. Thus, in terms of perceived loudness at any one measurement location, Chapter 4 compliance could correspond to a reduction in noise energy of around 3dB, i.e. a halving of the sound energy. Aircraft are replaced roughly every 20-35 years (although in Europe the average is around 8 years), and hence further reductions in noise at source will require restrictions in the use of the noise Chapter 3 aircraft or incentives to use quieter, Chapter 4 compliant aircraft. However, there is no agreed date for phasing out Chapter 3 aircraft.

Over the past 30 years or so, improvements in aircraft technology have resulted in a reduction in noise of about 20dB. These improvements are continuing, with modern aircraft being successively quieter than their predecessors. Indeed, Rolls-Royce reports that modern aircraft can achieve 18 – 24dB below the Chapter 3 standard. However, further improvements beyond the Chapter 4 standards are increasingly difficult to achieve, although there is much pressure to develop aircraft with significantly lower noise levels than is currently possible.

Aircraft noise arises from both engines and the movement of turbulent air over the physical structure (airframe) of an aircraft. To date, noise reduction has focused mainly on reducing engine noise. The Advisory Council for Aeronautics Research in Europe (ACARE) is a group which brings together the key players in Europe's aerospace industry. ACARE has set a target for the industry to halve the perceived aircraft noise by 2020. However, there is no guarantee that this target will be met. Current technology points to the target being achievable, but translating laboratory-tested concepts into a fully functioning aircraft raises challenges – not least that the noise performance of a new aircraft is difficult to characterise fully before it is built and flown.

1.3.2 Aircraft noise components

For the sake of obtaining a better understanding of the nature of noise it is advantageous to divide the total noise into a set of components which have different contributions to the total level. It is also of use to consider the approach and takeoff noise of aircraft separately. Figure 1.3.2.1 is representative of the noise distribution components for typical present aircraft.

On the vertical axis of figure 1.3.2.1 a maximum perceived noise level in *dB* is shown, while a set of noise components divided into groups for approach and takeoff aircraft noise, respectively, is shown on the horizontal axis.

First of all let us interpret the total noise levels from figure 1.3.2.1. We observe that the total perceived noise level is about 5dB higher on landing than on takeoff. At first this may appear to be strange, since the airplane is heavier on takeoff because of full fuel reservoirs and we know that the heavier the airplane the noisier it is, but the measured trend is the opposite. However, the reason for this becomes clear when we recall that the data are presented in the perceived noise level, where not only the amplitude but also the duration of noise is important. Since the angle of the flight during takeoff (up to 20°) is steeper than that during landing ($2.7^\circ - 4^\circ$), Pierson (1985), the period of detecting the noise during approach is longer than for a takeoff and the resulting perceived noise is higher. However the noise amplitude is lower for lighter planes with empty fuel reservoirs.

Now let us have a look at the noise components separately. According to figure 1.3.2.1, the fan inlet noise and airframe noise are the main contributions to the total noise level when an aircraft approaches. Jet exhaust noise is high, 85dB , but this is the least important level of noise compared to other components. While considering total takeoff noise the situation changes significantly: fan exhaust noise and jet noise become the strongest components, about 100dB each, while airframe noise falls by up to 80dB . This research is focused of a jet noise investigation.

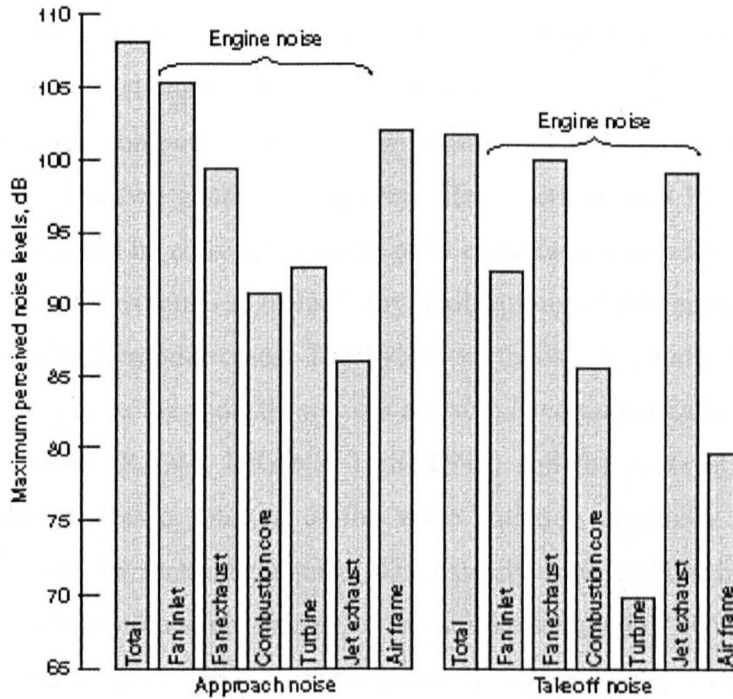


Figure 1.3.2.1 The noise distribution components for typical present aircraft. Picture from Ilan Kroo (2005).

1.4 Jet noise

A substantial amount of research work has been performed for investigating jet noise problems. The aeroacoustics as a discipline was established by Sir James Lighthill in 1952 when he published his famous acoustic analogy, Lighthill (1952). The elegance and generality of the acoustic analogy was awesome in its impact. The direct consequence of the theory was a so-called *eighth power law* stating that the noise produced by an airflow, in the absence of resonators and boundaries, would scale on the eighth power of the jet velocity. This was easy to check, and experimental confirmation of that velocity index was soon forthcoming. In 1955, Curl published his extension of Lighthill's analogy to include the effect of flow boundaries. This approach relates sound exactly to integrals of surface and volume

source terms and specifies precisely what are these source terms. Once they are known, so is the sound field. The development of the Lighthill approach was continued by Ribner (1964), Goldstein and Rosenbaum (1973) and Lilley (1974). The most general version of the acoustic analogy was proposed by Ffowcs Williams and Hawkings (1969). In this version they took into account all possible acoustic sources, such as quadrupoles, dipoles and monopoles.

The rapid development of computers in recent decades has inspired scientists to develop numerical methods for noise investigation. The Lighthill analogy allows the decoupling of the acoustic generation from the acoustic propagation appeared to be a perfect match for computational analysis. Computational aeroacoustics (CAA) could be classified in two general categories: direct methods and hybrid methods. The direct methods can be considered as the most exact technology for CAA and the most computationally expensive. In fact, any applications of this approach are still limited to very simple model cases. The hybrid methods are usually based on the acoustic analogy, where the acoustic sources are simulated numerically using any of the CFD approaches (RANS, URANS, LES, DNS) and the noise at the receiver position is calculated as a solution of the wave equation originally proposed by Lighthill. Some of the methods require 3D unsteady flow field solutions in the source region, while others are based on a simple steady 2D RANS solutions followed by a set of assumptions of the physical nature of the acoustic sources (length and time scales).

In recent years both approaches have been extensively developed in the application to the jet noise problems. For example, the MGBK method, originally proposed by Batchelor (1960), was recently developed by Self and Azarpyvand (2008) where they considered the time and length scales of the acoustic sources to be frequency dependent. Khavaran and Kenzakowski (2007) modified a physics-based jet noise prediction methodology based on the RANS input to improve the noise prediction for heated jets. However the semi-empirical approach recommended itself to be a fast tool for jet noise predictions, it is not uniform and requires careful tuning for each new application.

In contrast, the Ffowcs Williams and Hawkings (FW-H) analogy is the most universal and applicable for not only jet noise problems, but also for fan noise, boundary layer noise and any other aerodynamically generated noise problems. This approach is highly sensitive to the exact resolution of the acoustic sources. Therefore it involves relatively time-consuming calculations of the flow field in the source region. For example, Freud (2001) applied FW-H approach coupled with DNS for noise predictions from the low Reynolds number turbulent jet, Borodny and Lele (2002) employed LES for higher Reynolds number jets. It is interesting to note that we did not find any published papers on jet noise predictions using the FW-H approach coupled with unsteady RANS calculations.

1.5 The purpose of the research

In this thesis we have focused our attention on jet noise problems. The two main approaches for predicting jet noise are employed, namely: the semi-empirical acoustic model based on Goldstein and Rosenbaum (1973) and the Ffowcs Williams and Hawkings (1969) acoustic analogy. Both approaches are realised in the commercial CFD software FLUENT 12.0, however some modifications are required. There were no published studies on jet noise using FLUENT before this research work. In addition, we did not find any papers on the comparison of these two approaches for jet noise problems.

The FW-H acoustic analogy is based on unsteady flow field simulations, which are usually done using DNS or LES. There are no papers so far on the application of the FW-H analogy coupled with the unsteady RANS for jet noise problems. Therefore we have performed LES, as well as unsteady RANS, simulations for each of the cases investigated and compared the obtained results.

Since the acoustic analogy is based on the resolved acoustic sources, we are interested in validating both the flow field and the acoustic field characteristics of the jet. For these purposes we require a set of experimentally measured data for the flow field and the noise field at the same time. In addition, we are interested in low Mach number jets with relatively simple nozzle geometry, in order to simplify the initial problem. We have found it challenging to discover a suitable set of

experimentally measured data. In fact, it appears to be very rare for the noise level and the flow field measurements to be performed at the same time.

The only set of data satisfying both requirements is the Panda (2004) experimental study of the hot air round jet, where the flow field measurements are limited by single radial section profiles and the noise level was measured at two microphone positions. In addition to this rather limited information, we have found very detailed flow field measurements of the cold propane jet performed by Schefer and Dibble (2001) with no noise measurements and very detailed acoustic measurements of a cold air jet, Lush (1971) with no flow field data. We believe that the superposition of all three sets of data is sufficient for the validation of the simulation approach.

Figure 1.5.1 illustrates the concept of this research: we have three experimental cases for validation including SANDIA, Schefer (1988), with detailed measurements of the velocity field, Lush (1971) with detailed measurements of acoustic field and NASA, Panda (2004), with some measurements of the acoustic and velocity field. For the simulation of the acoustic sources, i.e. the flow field, we employ RANS, URANS and LES turbulent models implemented in FLUENT. For the acoustic modeling we employ FW-H analogy, implemented in FLUENT and coupled with URANS or LES solution, and broad band noise (BNS) semi-empirical acoustic model, partly implemented in FLUENT and fully realized in MATLAB. The BNS acoustic model is based on steady RANS solution of the flow field.

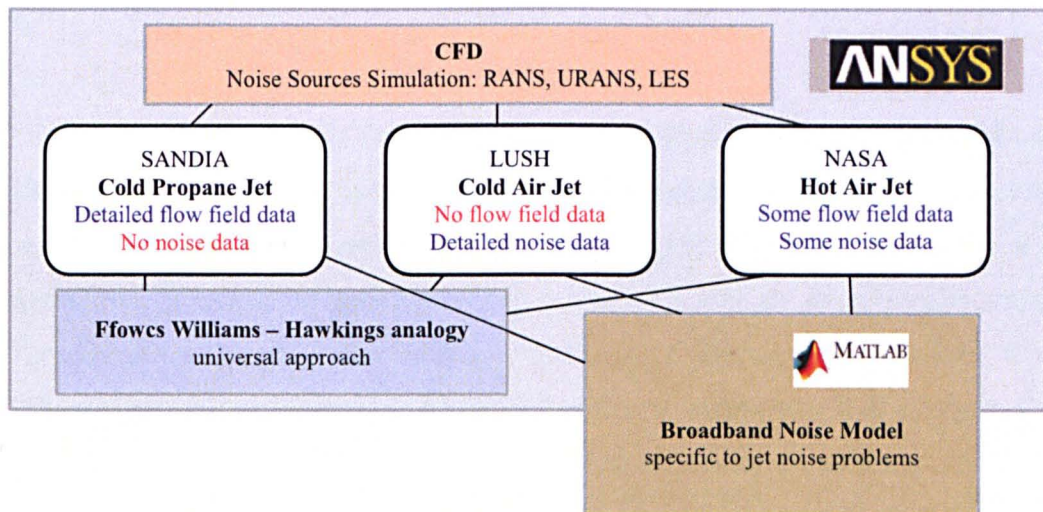


Figure 1.5.1 *The concept of thesis.*

Chapter 7 is fully devoted to the discussion of the advantages and disadvantages of the turbulent and acoustic models employed in this study. We discuss the limitations of the models and the assumptions adopted in this research connected to the technical issues of the CFD simulations, i.e. boundary conditions, numerical discretization schemes, introduction of the initial turbulent fluctuations for LES, etc.

In Chapter 8, namely the conclusion chapter, we give recommendations for the optimal application of the CFD approach to jet noise problems.

Chapter 2

Aeroacoustic methods

2.1 Lighthill's acoustic analogy

Aeroacoustics in the early 1950s was not an established discipline. Scientists studied noise by measuring the radiated acoustic power under different experimental conditions. Large jets were noisier than small jets and fast jets noisier than slow jets. By that time it was clear that the expansion ratio across the propulsive nozzle is important, as well as the temperature, density and the speed of sound variations in the exhaust streams of jets with different propulsive gases. However whether the pressure ratio or the jet Mach number was more important than the jet power or propulsive thrust, or how important the jet density was compared with the speed of sound or the mean jet temperature, was not clear.

It was Lighthill (1952) who set a general theory of sound generated aerodynamically that abruptly changed the situation. Lighthill rearranged the Navier-Stokes equations, which govern the flow of a compressible, viscous fluid into an inhomogeneous wave equation. Thereby he made an analogy between fluid mechanics and acoustics. The following Citation Classic (1991) by Lighthill is about it:

“One day in 1946, Britain’s assistant director of scientific research convinced me – then a 25-year-old senior lecturer in applied mathematics at Manchester University – that the problem of understanding noise emitted by jets from aero-engines was at the same time a matter of great practical importance and an exceptionally exiting theoretical challenge. A jet, after all, was one of the classical turbulent flows, hitherto viewed as a complex pattern of vorticity completely free of those fluid dilatations that, on the other hand, must mediate observed sound emissions. Sitting the next day in the London train, I could not stop wondering how to characterize jets in a new way that would permit estimation of their noise fields.

Like most mathematicians, I normally write down too many equations! But on that railway journey, I fortunately had only the proverbial back of an envelope with me; so I really was forced to think. The theory's essential idea emerged before my journey's end.

It depended first of all on a choice of the right dependant variable: not the pressure, whose relationship with turbulent velocity fluctuations had been shown to be so complicated, but density. This was needed for a theory concentrating not so much on the turbulence itself, where density variations hardly matter, as on the sound emissions where they must necessarily be significant.

On the envelope's modest back, a first equation could then be written down, specifying local rate of change of density as the inward component (minus the divergence) of mass flux. What could be said, however, about the rate of change of mass flux? Careful thought was needed to recognize that an answer (the next writing on the envelope) might be given by the momentum equation not in the standard Euler form but in a much less standard form due to Reynolds. Later, I appreciated how fortunate for my theory was the fact that flux of mass is identical with density of momentum. I was content on that train to contemplate adiabatic process only! For these, the momentum flux had just two components.

Delightedly, I recognized that a linear equation connected acoustic density fluctuations to the quadratic turbulent quantity described as its momentum transport or instantaneous Reynolds stress. The classical Kirchoff solution to this linear equation could be applied in its simplified far-field form to give the radiated sound.

This idea, after much refinement, finally "saw the light" in my 1952 paper."

2.1.1 Theory Description

Following Lighthill (1952, 1954) we need to start from the fundamental equations.

The first equation of interest is the conservation of mass equation:

$$\frac{\partial \rho}{\partial t} + \nabla \cdot (\rho \vec{v}) = \frac{\partial \rho}{\partial t} + \frac{\partial \rho v_i}{\partial x_i} = 0 \quad (2.1.1.1)$$

where ρ and \vec{v} represent the fluid density and velocity, respectively. Here we use the Einstein notation, i.e. when an index variable appears twice in a single term, it implies that we are summing over all of its possible values.

The second equation of interest is the conservation of momentum equation:

$$\rho \frac{\partial \vec{v}}{\partial t} + \rho(\vec{v} \cdot \nabla)\vec{v} = \left(\frac{\partial \rho v_i}{\partial t} + \frac{\partial \rho v_i v_j}{\partial x_j} \right) = - \frac{\partial P_{ij}}{\partial x_j} \quad (2.1.1.2)$$

where P_{ij} is the stress tensor.

We take the time derivative of the mass conservation law (2.1.1.1):

$$\frac{\partial^2 \rho}{\partial t^2} + \frac{\partial^2 \rho v_i}{\partial t \partial x_i} = 0 \quad (2.1.1.3)$$

and subtract from it the divergence of the momentum equation (2.1.1.2):

$$\frac{\partial^2 \rho v_i}{\partial x_i \partial t} + \frac{\partial^2 \rho v_i v_j}{\partial x_i \partial x_j} = - \frac{\partial^2 P_{ij}}{\partial x_i \partial x_j} \quad (2.1.1.4)$$

To obtain the exact equation:

$$\frac{\partial^2 \rho}{\partial t^2} = \frac{\partial^2 (\rho v_i v_j - \sigma_{ij})}{\partial x_i \partial x_j} + \frac{\partial^2 p}{\partial x_i^2} \quad (2.1.1.5)$$

where p and σ are the pressure and viscous parts of the stress tensor.

Equation (2.1.1.5) has no simple physical meaning. When however we add to both sides the term $-c_0^2 \frac{\partial^2 \rho}{\partial x_i^2}$, then we obtain a non-homogeneous wave equation which is called the analogy of Lighthill:

$$\frac{\partial^2 \rho}{\partial t^2} - c_0^2 \frac{\partial^2 \rho}{\partial x_i^2} = \frac{\partial^2 (\rho v_i v_j - \sigma_{ij})}{\partial x_i \partial x_j} + \frac{\partial^2 (p - c_0^2 \rho)}{\partial x_i^2} \quad (2.1.1.6)$$

This equation is valid for any value of the velocity c_0 . One could introduce here the velocity of propagation of light in a vacuum, for example. With such a choice for c_0 , the equation is rather meaningless. The equation becomes interesting when we use here the speed of sound c_0 in the reference quiescent state (ρ_0, p_0) of the fluid surrounding a listener. From here we introduce deviations from this reference state:

$$\begin{aligned} \rho' &= \rho - \rho_0 \\ p' &= p - p_0 \end{aligned} \quad (2.1.1.7)$$

to obtain:

$$\frac{\partial^2 \rho'}{\partial t^2} - c_0^2 \frac{\partial^2 \rho'}{\partial x_i^2} = \frac{\partial^2 (\rho v_i v_j - \sigma_{ij})}{\partial x_i \partial x_j} + \frac{\partial^2 (p' - c_0^2 \rho')}{\partial x_i^2} \quad (2.1.1.8)$$

which is still exact because ρ_0 , p_0 and c_0 are constants. While the analogy of Lighthill is exact, its power is that it forms a suitable starting point to obtain approximate solutions. Furthermore the analogy provides a definition of the acoustical field in the presence of a flow. When the right-hand side terms in the analogy are negligible, we have a homogeneous wave equation. The solution of this equation is determined by the initial of boundary conditions (vibrating walls). In such cases we call the flow acoustical. Aeroacoustics is the study of flow conditions in which the right hand side of the analogy is the most important source of sound.

On the right-hand side of the equation (2.1.1.8) are the quadrupole sources. We describe in details the different type of sources in the next section 2.1.2.

Now let us have another look at the equation (2.1.1.5). As discussed by Hirschberg (2001), we rearrange the terms in this equation to obtain:

$$-\frac{\partial^2 p}{\partial x_i^2} = \frac{\partial^2 (\rho v_i v_j - \sigma_{ij})}{\partial x_i \partial x_j} - \frac{\partial^2 p}{\partial t^2} \quad (2.1.1.9)$$

Now we add to both sides of the equation the term $\frac{1}{c_0^2} \frac{\partial^2 p}{\partial t^2}$ and introduce deviations from reference state:

$$\frac{1}{c_0^2} \frac{\partial^2 p'}{\partial t^2} - \frac{\partial^2 p}{\partial x_i^2} = \frac{\partial^2 (\rho v_i v_j - \sigma_{ij})}{\partial x_i \partial x_j} + \frac{\partial^2}{\partial t^2} \left(\frac{p'}{c_0^2} - \rho' \right) \quad (2.1.1.10)$$

This is still an exact solution and it is also called the Lighthill analogy. However one may notice that the pressure-density source term is of a dipole nature, i.e. a much stronger source than the quadrupole!

This is how we reach the roots to the aeroacoustics. As long as we consider analogies as exact equations, any variable can be used to describe the acoustical field. They are all equivalent. However then the analogy is simply a reformulation of the exact conservation law equations which does not provide new information by itself. We use the analogies to introduce approximations. In that case we see that depending on the type of application considered a certain variable will provide a better basis for an intuitive approach than another. Clearly, when considering sound production by unsteady combustion, we should use p' rather than ρ' , as it is done by

Ihme et al. (2009) or Bailly et al. (2010). When considering sound produced by bubbly liquids then the density fluctuations ρ' will provide more insight than the pressure fluctuations p' , as shown by, for example, Crighton and Ffowcs Williams (1969). For the noise generated by turbulence, the best choice is density fluctuations, and therefore equation (2.1.1.8) is chosen in this thesis.

Remark

However it is widely accepted that the equation (2.1.1.8) is exact since obtained from Navier-Stokes equations directly, there is a tricky moment when we add and subtract an artificial term, $c_0^2 \nabla^2 \rho$. It is impossible to argue that this is incorrect mathematically, however we need to emphasise that by adding on “artificial” term $c_0^2 \nabla^2 \rho$ to the right hand side of the equation (2.1.1.5) we obtain a new source term in the wave equation. In other words, originally artificially generated term “mysteriously” receives real physical properties. A detailed discussion is beyond the scope of this thesis, see Fedorchenko (2000).

Using the conventional form the Lighthill's equation can be written as

$$\frac{\partial^2 \rho}{\partial t^2} - c_0^2 \nabla^2 \rho = \frac{\partial^2 T_{ij}}{\partial x_i \partial x_j} \quad (2.1.1.11)$$

where

$$T_{ij} = \rho v_i v_j - \sigma_{ij} + (p - c_0^2 \rho) \delta_{ij} \quad (2.1.1.12)$$

δ_{ij} is the Kronecker delta, which is 1 if $i = j$ and 0 otherwise, and T_{ij} is the so-called Lighthill turbulence stress tensor for the acoustic field.

Figure 2.1.1.1 schematically describes Lighthill's theory of aerodynamic noise generated by a turbulent jet.

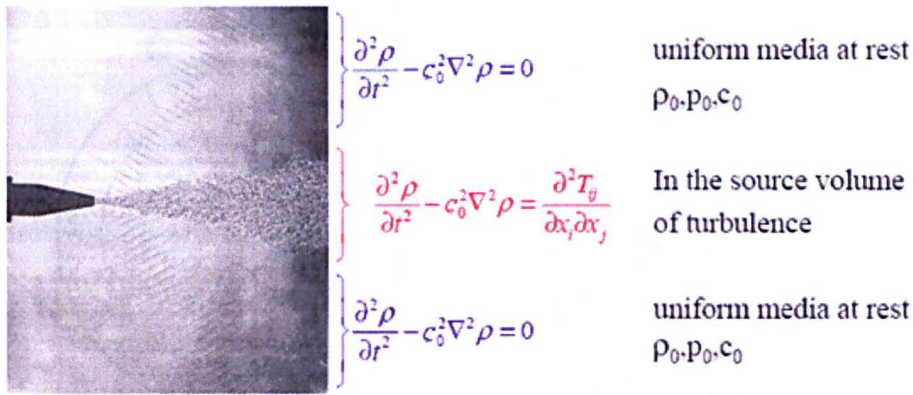


Figure 2.1.1.1 Schematic representation of Lighthill's theory of aerodynamic noise, picture from Westley and Woolley (1968).

The inhomogeneous wave equation (2.1.1.11) is the governing equation in the region where the sources of turbulence are concentrated, while in the regions without turbulent sources the noise is considered as propagating in a uniform media at rest and is described by a homogenous wave equation.

2.1.2 Sound Fields Radiated by Simple Sources

On the right hand side of equation (2.1.1.11), Lighthill (1952, 1954) evolved noise sources to distinguish them from the wave operator on the left hand side of the equation (2.1.1.11). Lighthill's approach enables us to divide one acoustic problem into two parts: the noise radiation and the noise propagation, and to solve them separately. The right hand side of the equation (2.1.1.11) represents the so-called quadruple sources. It is appropriate to outline briefly the simple acoustic sources in the following subsections. I would like to acknowledge Dr. Daniel A. Russell from Kettering University, USA for providing one with free access to the following figures (2.1.2.a -2.1.2.d) for demonstrating acoustic sources.

2.1.2.a Radiation from a monopole source

A monopole is a source which radiates sound equally well in all directions. The simplest example of a monopole source would be a sphere whose radius alternately expands and contracts sinusoidally in time. The monopole source creates a sound wave by alternately introducing and removing fluid into the surrounding region. A boxed loudspeaker at low frequencies acts as a monopole. The directivity pattern for a monopole source is schematically shown in Figure 2.1.2.a.(1).

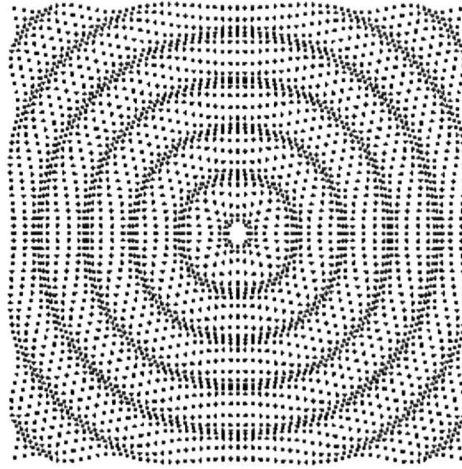
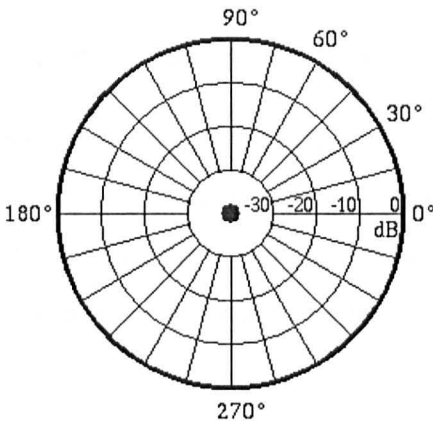


Figure 2.1.2.a.(1) *A directivity pattern for a monopole source.* **Figure 2.1.2.a.(2)** *A pressure field produced by a monopole source.*

Figure 2.1.2.a.(2) shows the pressure field produced by a monopole source. Individual points on the grid simply move back and forth about some equilibrium position while the spherical wave expands outwards. Monopole based noise usually appears when unsteady mass injection takes place. The acoustic power of a monopole source is proportional to the cubic power of the speed and linearly with the Mach number ($\sim U^3 M$).

2.1.2.b Radiation from a dipole source

A dipole source consists of two monopole sources of equal strength but opposite phase and separated by a small distance compared with the wavelength of sound. While one source expands the other source contracts. The result is that the fluid (air) near the two sources sloshes back and forth to produce the sound. A sphere which oscillates back and forth acts like a dipole source, as does an unboxed loudspeaker (while the front is pushing outwards the back is sucking in). A dipole source does not radiate sound in all directions equally. The directivity pattern shown in Figure 2.1.2.b.(1) looks like a figure “8”; there are two regions where sound radiates very well, and two regions where the sound cancels out.

Figure 2.1.2.b.(2) shows the pressure field produced by a dipole source. At the centre of the pressure field you can see sloshing back and forth caused by the dipole motion. The regions where the sound is cancelled shows up along the vertical axes

(the grid motion is almost zero). Furthermore, the wave fronts expanding to the right and left are 180° out of phase with each other.

Monopole based noise usually appears when unsteady external forces exist, for example flow over a cavity. The acoustic power of a dipole source is proportional to the cube of the speed and Mach number ($\sim U^3 M^3$). Monopole and dipole sources dominate at low Mach numbers.

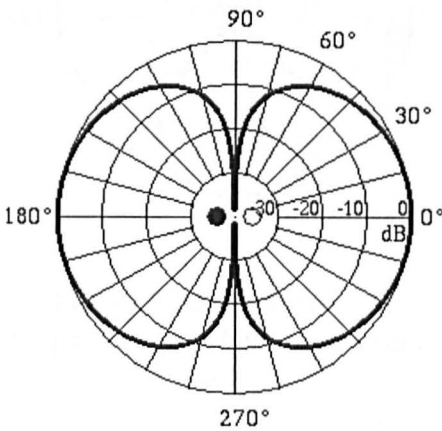


Figure 2.1.2.b.(1) A directivity pattern for a dipole source.

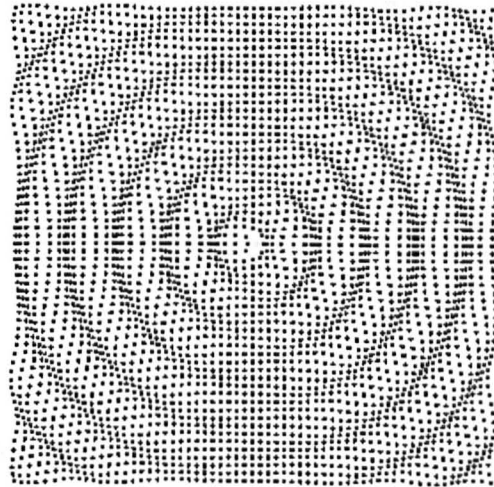


Figure 2.1.2.b.(2) A pressure field produced by a dipole source.

2.1.2.c Radiation from a lateral quadruple source

If two opposite phase monopoles make up a dipole, then two opposite dipoles make up a quadruple source. In a *Lateral Quadruple* arrangement the two dipoles do not lie along the same line (four monopoles with alternating phase at the corners of a square). The directivity pattern for a lateral quadruple, see figure 2.1.2.c.(1), looks like a clover-leaf pattern; sound is radiated well in front of each monopole source, but sound is cancelled at points equidistant from adjacent opposite monopoles.

Figure 2.1.2.c.(2) shows the pressure field produced by a lateral quadruple source. At the centre of the pressure field one can see the quadruple motion as the particles alternate motion in the horizontal and vertical directions, while the back and forth

motion is caused by the dipole motion. The regions where sound is cancelled shows up along the diagonals (where the grid motion is almost zero). Furthermore, there is 180° phase difference between the horizontal and vertical wave fronts.

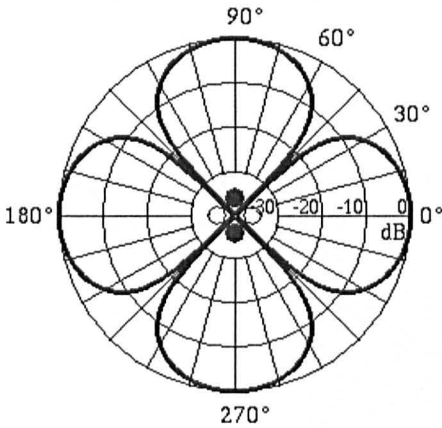


Figure 2.1.2.c.(1) A directivity pattern for a lateral quadrupole source.

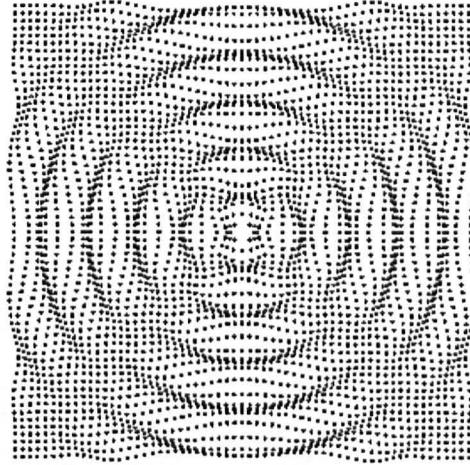


Figure 2.1.2.c.(2) A pressure field produced by a lateral quadrupole source.

2.1.2.d Radiation from a linear quadrupole source

If two opposite phase dipoles lie along the same line then they make up a *Linear Quadrupole* source. A tuning-fork is a good example of a linear quadrupole source (each time acts as a dipole as it vibrates back and forth, and the two tones oscillate in opposite directions). What makes the linear quadrupole interesting is that there is a very obvious transition from the *near field* (see figure 2.1.2.d(1)) to the *far field* (see figure 2.1.2.d(2)). In the near field there are four maxima and four minima, with the maxima along the quadrupole axis being about 5dB louder than the maxima perpendicular to the quadrupole axis. The near field directivity pattern is shown in figure 2.1.2.d.(1).

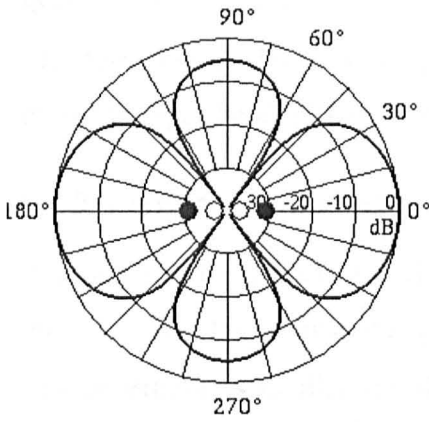


Figure 2.1.2.d.(1) A directivity pattern for a linear quadruple source in the near field.

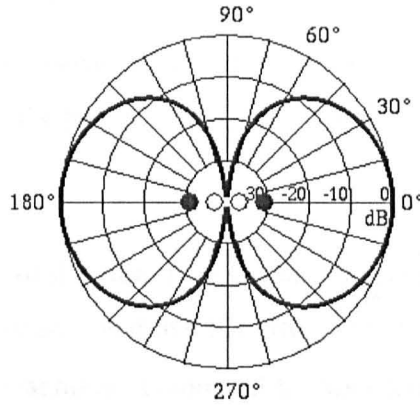


Figure 2.1.2.d.(2) A directivity pattern for a linear quadruple source in the far field.

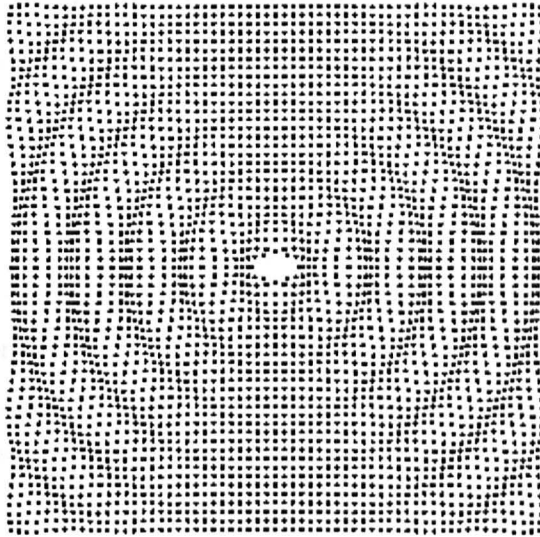


Figure 2.1.2.d.(3) A pressure field produced by a linear quadruple source.

In the far field there are only two maxima (along the quadruple axis) and two minima (perpendicular to the quadruple axis) as shown in figure 2.1.2.d.(2).

Figure 2.1.2.d.(3) shows the pressure field radiated by a linear quadruple. At the centre of the figure one can see the quadruple near field pattern. As the wave expands outwards it becomes almost a spherical wave (notice that the left and right moving wave fronts are in phase as opposed to the case in the dipole source) except that the amplitude is severely reduced in the vertical direction.

Quadruple based noise dominates when unsteady shear stress exists, for example in a free turbulent jet. The acoustic power of a quadruple source is proportional to the cube of the speed and a Mach number to the power of five ($\sim U^3 M^5$).

2.1.3. Particular cases

(I) In practice the effect of the viscosity of the fluid is customary neglected, i.e. one takes $\sigma_{ij} = 0$. This because it is generally accepted that the effect of the latter on the noise generation is smaller in order of magnitude compared to other terms, such as the velocity term $\rho v_i v_j$ and the pressure-density term $(p - c_0^2 \rho) \delta_{ij}$. Assuming that $\sigma_{ij} = 0$, one can rewrite expression (2.1.1.12) as follows:

$$T_{ij} = \rho v_i v_j + (p - c_0^2 \rho) \delta_{ij} \quad (2.1.3.1)$$

Moreover, in the absence of viscous stresses the momentum flux term $\frac{\partial^2 \rho v_i v_j}{\partial x_i \partial x_j}$ in the equation (2.1.1.11) is usually considered as the primary source of sound in an isothermal jet.

(II) Once the viscosity of the fluid cannot be neglected, the viscous tensor σ is estimated assuming that the fluid is Newtonian. A Newtonian fluid is a fluid that flows like water, i.e. its stress curve is linear and passes through the origin. The viscous tensor is proportional to velocity gradient perpendicular to the direction of shear, where the constant of proportionality is known as the viscosity, μ :

$$\sigma = \mu \frac{dv}{dx} \quad (2.1.3.2)$$

Using this assumption, one then can rewrite expression (2.1.1.12) as follows:

$$T_{ij} = \rho v_i v_j + -\mu \left[\frac{\partial v_i}{\partial x_j} + \frac{\partial v_j}{\partial x_i} - \frac{2}{3} \frac{\partial v_k}{\partial x_k} \delta_{ij} \right] + (p - c_0^2 \rho) \delta_{ij} \quad (2.1.3.3)$$

2.1.4 Lighthill turbulence stress tensor

Following Freund (2003), we can split the Lighthill stress tensor T_{ij} into a mean component, T_{ij}^m , a component that is linear in the velocity fluctuations T_{ij}^l , a component that is quadratic in the velocity fluctuations and the so-called entropy component T_{ij}^s :

$$T_{ij} = \underbrace{T_{ij}^m}_{\text{no noise}} + \underbrace{T_{ij}^l}_{\text{shear noise}} + \underbrace{T_{ij}^n}_{\text{self noise}} + \underbrace{T_{ij}^s}_{\text{enthalpy noise}} \quad (2.1.4.1)$$

where

$$T_{ij}^m = \rho \overline{v_i v_j} + (\overline{p} - c_0^2 \overline{\rho}) \delta_{ij} \quad (2.1.4.2)$$

$$T_{ij}^l = \rho \overline{v_i v_j'} + \rho \overline{v_j v_i'} \quad (2.1.4.3)$$

$$T_{ij}^n = \rho v_i' v_j' \quad (2.1.4.4)$$

$$T_{ij}^s = (p' - c_0^2 \rho') \delta_{ij} \quad (2.1.4.5)$$

By definition, the mean component T_{ij}^m does not produce the noise. In expressions (2.1.4.2), (2.1.4.3) and (2.1.4.4) the density, ρ , in the $\rho v_i v_j$ term has not been decomposed into a mean and a fluctuating part. Freund shows that the noise from T_{ij} is almost the same as that from

$$T_{ij}^{\overline{p}} = \overline{\rho} v_i v_j + (p' - c_0^2 \rho') \delta_{ij} \quad (2.1.4.6)$$

where $\overline{\rho}$ is a mean density, p' and ρ' are pressure and density fluctuations respectively.

The noise from the term T_{ij}^l is called the shear noise since this component consists of turbulent fluctuations interacting with the sheared mean flow. The noise from the term T_{ij}^n is called the self noise since this component consists of turbulent fluctuations interacting with themselves. The last term in (2.1.4.1), T_{ij}^s , is the so-called entropy noise.

Lilley (1974) showed that the T_{ij}^s term in the expression (2.1.4.1) contains both isentropic and non-isentropic components. Futher, Uzun et al. (2005) showed that the components in the expression (2.1.4.1) are highly correlated and hence such source decomposition may not be that useful for careful noise prediction.

2.1.5 Direct solution of the Lighthill equation

From the theory of differential equations, it is known that a solution of an inhomogeneous differential equation is the sum of the solution for the corresponding homogeneous equation and one particular solution to the inhomogeneous equation. This means that once the right hand side of equation (2.1.1.11) is known one can solve the full equation.

For example, Lighthill has shown that the density fluctuations detected at a point \vec{x} in the far field are originated from the localized turbulent region (V), see Figure 2.1.5.1, is given by

$$\rho(\vec{x}, t) - \rho_0 = \frac{x_i x_j}{4\pi c_0^4 x^3} \int_V \frac{\partial^2}{\partial t^2} T_{ij} \left(\vec{y}, t - \frac{|\vec{x} - \vec{y}|}{c_0} \right) d\vec{y} \quad (2.1.5.1)$$

$$T_{ij} = \rho v_i v_j + [(p - p_0) - c_0^2(\rho - \rho_0)]\delta_{ij} + \sigma_{ij} \quad (2.1.5.2)$$

where p and ρ are the local pressure and density and p_0 , ρ_0 and c_0 are the ambient pressure, density and speed of sound.

It should be noted that the equation (2.1.5.1) could be rearranged in terms of pressure, using the relationship between the pressure and density in the fluid. For example, for an ideal gas $p \cong c_0^2 \rho$. Therefore the form of the equation is the same for pressure, except for constants.

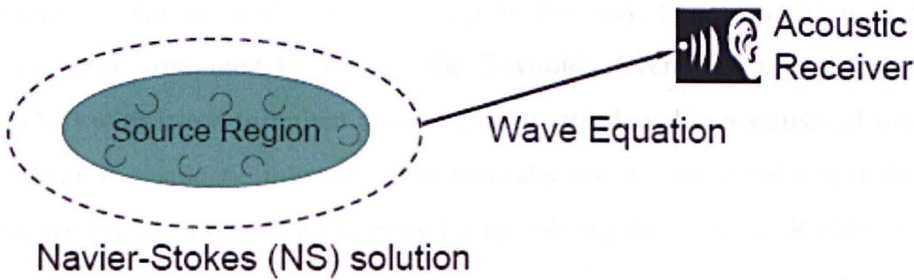


Figure 2.1.5.1. Acoustic analogy modelling.

2.1.6 Assumptions

From one aspect it is important to realize that Lighthill's equation is exact in the sense that no approximations of any kind have been made in its derivation. From another aspect, there is a set of implicit assumptions that have been used to derive the Lighthill equation. Firstly, the analogy rests on the assumption that noise generation and propagation are decoupled, that is the flow generated noise does not impact on the internal dynamics of the flow. Secondly, the fluid is assumed to be homogenous where the viscosity is negligible. Thirdly, the turbulence is considered to be acoustically slow (velocity fluctuations are small compared to the speed of sound).

Lighthill considered an appropriate model for turbulence in which the fractional variation of density is small and T_{ij} is effectively equal to $\rho_0 v_i v_j$, where ρ_0 is the mean density. Turbulence of characteristic length and velocity scales, L and U respectively, define a time scale $\frac{L}{U}$, and sound of this period will have a wavelength $\frac{c_0 L}{U}$, which is much larger than the source scale when the Mach number $\frac{U}{c_0}$ is sufficiently small.

In practice, using an acoustic analogy is a two-step procedure. In the first step, an unsteady computational fluid dynamics (CFD) analysis is used to compute aerodynamic sources. The second step consists in computing the propagation and radiation of these aerodynamic sources.

The main advantage of this approach is that most of the convectional flow simulations can be used in the first step. In this way, the mean turbulent parameters of the flow computed by solving the Reynolds Average Navier-Stokes equations (RANS) with $k - \epsilon$ turbulent closure can be introduced in a statistical source model to obtain the acoustic intensity. It is naturally more convenient to use the unsteady flow parameters to evaluate directly T_{ij} by solving the unsteady RANS (URANS) or using Large Eddy Simulation (LES) or using Direct Numerical Simulation (DNS).

2.1.7 Eighth power law

The elegance and generality of Lighthill's theory is the awesomeness in its impact. In fact, it is the so-called *eighth power law* that is still wildly used as an accuracy check on experimental measurements. The integral solution (2.1.5.1-2) first allows us to establish, by dimensional analysis, the scaling law of the acoustic power for a subsonic jet as the eight power of the jet velocity (U^8).

Indeed, let us consider only the velocity term, $\rho v_i v_j$, in the stress tensor T_{ij} in the integral solution (2.1.5.1). Take for scaling a characteristic length L , characteristic velocity U and a mean density ρ_0 , then

$$T \approx \rho_0 U U \quad \text{and} \quad \frac{\partial}{\partial t} \approx \frac{U}{L} \quad \Rightarrow \quad p \approx \frac{1}{x} \left(\frac{U}{L} \right)^2 \rho_0 U^2 L^3 \quad (2.1.7.1)$$

Therefore pressure scales as

$$p \approx \rho_0 U^4 \frac{L}{x} \quad (2.1.7.2)$$

By definition, the acoustic intensity is proportional to the pressure squared, and the total acoustic power W is the intensity integrated over a spherical surface of radius x and

$$W \approx U^8 \quad (2.1.7.3)$$

The total acoustic power thus scales on the eighth power of jet velocity. This is Lighthill's *eighth power law* and was derived before data were available to confirm it. It is strictly only true for low speed flows, because we have implicitly assumed the source to be compact. At higher speeds, the characteristic frequency of the source increases and interference effects between different regions of the jet become important.

The airflow, in the absence of resonators and boundaries, was proven to be equivalent in its sound-generating ability to a distribution of quadruples and, provided that these quadruples scaled with the variables defining the hydrodynamic mean flow, the power of the noise that it produced would scale on the eighth power of the jet velocity. However the power of the propulsive jet itself only increases with the cube of the jet velocity (U^3), as shown by Ffowcs Williams (1995). This means that there is a sort of efficiency in the noise production which goes as the fifth power of the velocity which is the ratio of the acoustic energy to the jet power. The acoustic efficiency, or the ratio of the noise energy emitted to the jet power delivered, therefore varies as the fifth power of the jet Mach number. So this efficiency increases if one can reduce the jet Mach number (ratio of the jet velocity to the atmospheric speed of sound). It is strictly true only for low speed flows, because we have an implicit assumption that sources are compact. At higher speeds the characteristic frequency of the source increases and interference effects between different regions of the jet become important.

A recent noise data analysis, performed by Tam (2005), examines a more general power law AU^n , where the amplitude A and power n are parameters that depend on the angle (an angle to the jet axis that we measure the noise) and the jet temperature.

2.2 Curle's acoustic formulation

It was in 1955 that Curle published his extension of Lighthill's acoustic analogy to include the effect of flow boundaries. He showed that boundary terms could provide effective mass and momentum injection into the flow. This is acoustically equivalent to monopole and dipole sources of fundamentally greater acoustic efficiency than Lighthill's volume quadruples. The Lighthill/Curle approach relates sound exactly to integrals of surface and volume source terms and specifies precisely what these source terms are. Once they are known, so is the sound field.

Far-field sound generated by a boundary layer flow over a solid body at low Mach numbers is a question of interest in Curle's theory. The Curle's integral based on an acoustic analogy can be used to approximate the local contribution from the body surface to the total acoustic power, namely

$$p'(\vec{x}, t) = \frac{1}{4\pi c_0} \int_S \frac{(x_i - y_i)n_i}{r^2} \frac{\partial p}{\partial t}(\vec{y}, \tau) dS(\vec{y}) \quad (2.2.1)$$

where $\tau = t - \frac{r}{c_0}$ is the emission time and S is the integration surface.

The sound intensity in the far field thereby can be approximated by

$$\overline{p'^2} \approx \frac{1}{16\pi^2 c_0^2} \int_S \frac{\cos^2 \theta}{r^2} \overline{\left[\frac{\partial p}{\partial t}(\vec{y}, \tau) \right]^2} A_c(\vec{y}) dS(\vec{y}) \quad (2.2.2)$$

where A_c is the correlation area, $r \equiv |\vec{x} - \vec{y}|$ and θ is the angle between $|\vec{x} - \vec{y}|$ and the wall-normal direction \vec{n} .

The mean-square time derivative of the surface pressure and the correlation area are approximated in terms of turbulent quantities, such as turbulent kinetic energy, dissipation rate, and wall shear. The advantage of this approach, from a computational point of view, is that the model does not require the transient solution to any governing fluid dynamics equations. All the models need is what typical RANS model would provide, such as the mean velocity field, turbulent kinetic

energy and dissipation rate. Therefore the use of the Curl model requires less computational resources than the following models.

2.3 Ffowcs Williams – Hawkings acoustic formulation

The evolution of the technique generated by Lighthill in response to a pressing aeronautical noise issue, the jet noise problem, is described in the following sections.

Large engines make most of their noise by the motion of aerofoils at very high speed. Helicopter blades travel with tip velocities close to sonic speeds and there are immediate prospects of large aircraft being propelled with supersonically moving propellers. The adaptation of Lighthill's theory to that problem was made by Ffowcs Williams and Hawkings (1969). The basic theory for that case goes as follows:

Lighthill's equation in terms of pressure,

$$\frac{\partial^2 p}{\partial t^2} - c_0^2 \nabla^2 p = \frac{\partial^2 T_{ij}}{\partial x_i \partial x_j} \quad (2.3.1)$$

is a statement of the exact laws of momentum and mass balance in the fluid exterior to moving surfaces, a region which can be defined by the volume in which the Heaviside operator H is unity. Elsewhere, in the interior of the surfaces $H = 0$. Of course, H is a function of both space and time and is constant on surfaces attached to the body boundaries that move with speed \vec{u} , thus H is defined by

$$\frac{\partial H}{\partial t} + u_i \frac{\partial H}{\partial x_i} = 0 \quad (2.3.2)$$

When equation (2.3.1) is multiplied by the Heaviside function and the function absorbed inside the differential operators then a new equation results and this is an equation for the sound field exterior to the body, namely:

$$\begin{aligned} \frac{\partial^2 p'}{\partial t^2} - c_0^2 \nabla^2 p' &= \frac{\partial^2 (T_{ij} H(f))}{\partial x_i \partial x_j} - \frac{\partial}{\partial x_i} \left\{ (P_{ij} n_j + \rho u_i (u_n - v_n)) \delta(f) \right\} \\ &+ \frac{\partial}{\partial t} \left\{ (\rho_0 v_n + \rho (u_n - v_n)) \delta(f) \right\} \end{aligned} \quad (2.3.3)$$

where

u_i is a fluid velocity component in the x_i direction

u_n is a fluid velocity component normal to the surface $f = 0$

v_i is the surface velocity component in the x_i direction

v_n is the surface velocity component normal to the surface

$\delta(f)$ is the Dirac delta function

$H(f)$ is the Heaviside function

p' is the sound pressure at the far field $p' = p - p_0$

$f = 0$ denotes a mathematical surface introduced to “embed” the exterior flow problem $f > 0$ in an unbounded space, which facilitates the use of generalized function theory and the free-space Green function to obtain the solution. The surface $f = 0$ corresponds to the source (emission) surface, and can be made coincident with a body (impermeable) surface or a permeable surface off the body surface.

n_i is the unit normal vector pointing toward the exterior region $f > 0$

c_0 is the far-field sound speed

T_{ij} is the Lighthill stress tensor.

The solution of the equation (2.3.3) is obtained using the free-space Green function ($\delta(f)/4\pi r$). The complete solution consists of surface and volume integrals. The surface integrals represent the contributions from monopole and dipole acoustic sources, and partially from quadrupole sources, whereas the volume integrals represent quadrupole (volume) sources in the region outside the source surface. The contribution of the integrals becomes small when the flow is low subsonic and the source surface encloses the source region. Omitting volume integrals, we have:

$$p'(\vec{x}, t) = p'_T(\vec{x}, t) + p'_L(\vec{x}, t) \quad (2.3.4)$$

where

$$4\pi p'_T(\vec{x}, t) = \int_{f=0} \left(\frac{\rho_0(\dot{U}_n + U_n)}{r(1 - M_r)^2} \right) dS \quad (2.3.5)$$

$$+ \int_{f=0} \left(\frac{\rho_0 U_n (r\dot{M}_r + c_0(M_r - M^2))}{r^2(1 - M_r)^3} \right) dS$$

$$4\pi p'_L(\vec{x}, t) = \frac{1}{c_0} \int_{f=0} \left(\frac{\dot{L}_r}{r(1 - M_r)^2} \right) dS + \int_{f=0} \left(\frac{L_r - L_M}{r^2(1 - M_r)^2} \right) dS \quad (2.3.6)$$

$$+ \frac{1}{c_0} \int_{f=0} \left(\frac{L_r (r\dot{M}_r + c_0(M_r - M^2))}{r^2(1 - M_r)^3} \right) dS$$

where

$$U_i = v_i + \frac{\rho}{\rho_0} (u_i - v_i) \quad (2.3.7)$$

$$L_i = \sigma_{ij} \hat{n}_j + \rho u_i (u_n - v_n) \quad (2.3.8)$$

When the integration surface coincides with an impenetrable wall, the two terms on the right hand side of the equation (2.3.4), $p'_T(\vec{x}, t)$ and $p'_L(\vec{x}, t)$, are often referred to as the thickness and loading terms, respectively, in light of their physical meaning. The square brackets in the equations (2.3.5) and (2.3.6) denote that the kernels of the integrals are computed at the corresponding retarded times, τ , defined as follows, given the observed time, t , and the distance to the observer, r

$$\tau = t - \frac{r}{c_0} \quad (2.3.9)$$

The various subscripted quantities appearing in equations (2.3.5) and (2.3.6) are the inner products of a vector and a unit vector implied by the subscript. For instance, $L_r = \vec{L} \cdot \vec{r} = L_i r_i$ and $U_n = \vec{U} \cdot \vec{n} = U_i n_i$, where \vec{r} and \vec{n} denote the unit vectors in the radiation and wall-normal directions, respectively. The dot over a variable denotes source-time differentiation of that variable.

It is important to note that the surface $f = 0$ is not required to coincide with the body surface or walls. The formulation permits source surfaces to be permeable, and therefore can be placed in the interior of the flow. When a permeable source surface is placed at a certain distance from the body surface, the integral solutions given by equations (2.3.5) and (2.3.6) include the contributions from the quadrupole sources within the region enclosed by the source surface. In practise this means that, when using a permeable source surface, the mesh resolution needs to be sufficient to resolve the transient flow structures inside the volume enclosed by the permeable surface.

2.3.1 Position of the FW-H surface

One of the main parameters in FW-H is a source surface, namely the shape and position in space. On the one hand, the source surface must enclose most of the acoustic sources, but it must not be too far from the acoustic sources to avoid the damping effect due to numerical viscosity. Whilst searching the literature, it was found that the problem of the shape and the position of the FW-H surface is still an open question. However a closed FW-H surface is necessary to be consistent with

the fundamentals of the FW-H approach, but the predictions of the FW-H surface left open were much closer to experiments in many situations. Shur et al. (2003) used funnel-shaped surfaces for the DNS simulations of a cold low Reynolds number jet in order to fit the turbulence region. They have found that a surface with a radius 25 nozzle diameters at the end is the largest that avoids the sound deterioration caused by the special near-boundary approximation. However Trucker (2008) emphasise that, in general, when a portion of the downstream disk is left open, the question is how much should be left open? Later he shows that a wide range of answers can be gained depending on the sound intensity curve (different disk-opening levels are presented: 0L, 0.25L, 0.5L, 0.75L, and 1L, where the label “0L” corresponds to no disk and “1L” to fully closed). In particular, comparison with the noise measurements of a cold jet obtained by Tanna (1970) shows that the LES simulations with a 0.25L closed FW-H surface produces the best agreement with the experimental data. Trucker (2008) suggests that “a simple cylindrical surface is probably the most appropriate choice since it reduces the potential for solution tuning”, and we will follow his recommendations in this research.

2.4 Ribner’s acoustic formulation

Current formulations of the generation of aerodynamic noise by turbulence all require statistical information with regard to the turbulent flow field. One of these, based on the general theory for flow noise of Lighthill, is the specialized formulation for jet noise of Ribner (1964a, 1964b). Ribner’s formulation is important to mention as it is followed by Goldstein formulation, that is used in this thesis.

Lighthill’s solution for the wave equation (2.1.1.11) is given in Chapter 2.1.5. He has shown that the density fluctuations detected at a point \vec{x} in the far field are originated from the localized turbulent region (V), is given by equations (2.1.5.1-2). We repeat these equations in this Chapter for the sake of completeness:

$$\rho(\vec{x}, t) - \rho_0 = \frac{x_i x_j}{4\pi c_0^4 x^3} \int_V \frac{\partial^2}{\partial t^2} T_{ij} \left(\vec{y}, t - \frac{|\vec{x} - \vec{y}|}{c_0} \right) d\vec{y} \quad (2.4.1)$$

$$T_{ij} = \rho v_i v_j + [(p - p_0) - c_0^2(\rho - \rho_0)]\delta_{ij} + \sigma_{ij} \quad (2.4.2)$$

In isothermal turbulent flows at high Reynolds number, the source term T_{ij} is dominated by the intensity of turbulence $\rho v_i v_j$. In such flows where it is reasonable to suppose that T_{ij} is a stationary random function of time, one can define the density autocorrelation function by

$$C_{pp}(\vec{x}, \tau) = \frac{(\rho(\vec{x}, t + \tau) - \rho_0)(\rho(\vec{x}, t) - \rho_0)}{\rho_0 c_0^{-3}} \quad (2.4.3)$$

It follows from equations (2.5.1-2) that this function is related to the source term by

$$C_{pp}(\vec{x}, \tau) = \frac{\rho_0 x_i x_j x_k x_l}{16\pi^2 c_0^5 x^6} \iint_V \frac{\partial^2}{\partial t^2} u'_i u'_j(\vec{y}', t') \frac{\partial^2}{\partial t^2} u''_k u''_l(\vec{y}'', t'') d\vec{y}' d\vec{y}'' \quad (2.4.4)$$

where $t' = t - \frac{|\vec{x} - \vec{y}'|}{c_0}$, $t'' = t + \tau - \frac{|\vec{x} - \vec{y}''|}{c_0}$, \vec{y}' and \vec{y}'' are two running points in the source domain (V). This domain (V) is identified as the one occupied by the jet flow. Ffowcs Williams (1963) shows that equation (2.4.4) can be cast in the following form:

$$C_{pp}(\vec{x}, \tau) = \frac{\rho_0 x_i x_j x_k x_l}{16\pi^2 c_0^5 x^6} \iint_V \frac{\partial^4}{\partial \tau^4} \mathfrak{R}_{ijkl} \left(\vec{y}', \vec{\eta}, \tau + \frac{\vec{\eta} \cdot \vec{x}}{c_0 x} \right) d\vec{y}' d\vec{\eta} \quad (2.4.5)$$

$$\mathfrak{R}_{ijkl}(\vec{y}', \vec{\eta}, \tau) = \overline{u'_i u'_j(\vec{y}', t) u''_k u''_l(\vec{y}'', t + \tau)} - \mathfrak{R}_{ijkl}^0(\vec{y}', \vec{\eta}) \quad (2.4.6)$$

where \mathfrak{R}_{ijkl} represents the two-point time-delayed fourth-order correlation tensor. It is found convenient to introduce an arbitrary time-independent tensor \mathfrak{R}_{ijkl}^0 and this is eventually chosen to further simplify the algebraic calculations of the integrand. Equations (2.4.5-6) use the vector separation $\vec{\eta} = \vec{y}'' - \vec{y}'$ and the retarded time $\frac{\vec{\eta} \cdot \vec{x}}{c_0 x}$ observed at the points \vec{y}' and \vec{y}'' .

In the Lighthill (1952, 1954) and Ffowcs Williams (1963) papers it was explained that one can introduce the moving-axis transformation

$$\vec{\xi} = \vec{\eta} - i U_{ic} \tau \quad (2.4.7)$$

where U_{ic} is in the axial eddy convection velocity in the direction of the unit vector \hat{i} which is the mean flow direction. Then one can substitute expression (2.4.7) into equations (2.4.5-6) in order to neglect the retarded time effects. It should be noted that this moving axis transformation is an optional choice to account for source convection. Alternatively, the nozzle-fixed axes may be retained and the source motion allowed for in the form of the term \mathfrak{R}_{ijkl} . Ribner (1964a) employs the latter

and demonstrates the equivalence of both approaches. Thus upon introducing the moving frame correlation tensor, $\mathfrak{R}_{ijkl}(\vec{y}', \vec{\xi}, \tau) = \mathfrak{R}_{ijkl}(\vec{y}', \vec{\eta}, \tau)$, equations (2.4.5-6) become, after eliminating the retarded time effects:

$$C_{pp}(\vec{x}, \tau) = \frac{\rho_0 x_i x_j x_k x_l}{16\pi^2 c_0^5 x^6} \iint_V \frac{1}{C^5} \left(\frac{\partial^4}{\partial \tau^4} \mathfrak{R}_{ijkl}(\vec{y}', \vec{\xi}, \tau) \right)_{\tau = \frac{r'}{C}} d\vec{\xi} d\vec{y}' \quad (2.4.8)$$

where C is the convection factor $C = 1 - M_c \cos \theta$, $\cos \theta = \frac{x_1}{x}$, θ is the angle between the direction between the mean flow and the direction of observation \vec{x} (see Figure 2.4.1), and M_c designates the convection Mach number. Following Ribner (1964a, b) one can let $C_{pp}(\vec{x}/\vec{y}', \tau)$ denote the autocorrelation function at the point \vec{x} due to the sound emitted from a unit volume at \vec{y}' . Then we obtain the following:

$$C_{pp}(\vec{x}, \tau) = \int_{jet} C_{pp}(\vec{x}/\vec{y}', \tau) d\vec{y}' \quad (2.4.9)$$

and

$$C_{pp}(\vec{x}, \tau) = \frac{\rho_0 x_i x_j x_k x_l}{16\pi^2 c_0^5 x^6} \int_V \frac{1}{C^5} \left(\frac{\partial^4}{\partial \tau^4} \mathfrak{R}_{ijkl}(\vec{y}', \vec{\xi}, \tau) \right)_{\tau = \frac{r'}{C}} d\vec{\xi} \quad (2.4.10)$$

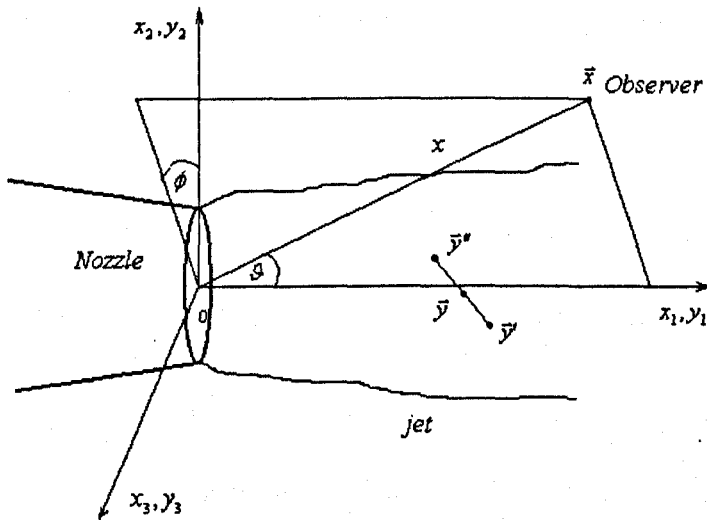


Figure 2.4.1 Turbulent jet flow configuration (x, θ, ϕ are the spherical coordinates of the point of observation \vec{x} and \vec{y} is the midpoint of the two points \vec{y}' and \vec{y}'').

Ribner rewrote equation (2.4.10) in a form where $\overline{u_x'^2 u_x''^2}$ governs the acoustic emission in the x direction (the x index indicates that the velocity is projected in the direction of the observation). This form is by far simpler than original equation (2.4.10): the single correlation $\overline{u_x'^2 u_x''^2}$ replaces some 36 correlations $\overline{u_i' u_j' u_k'' u_l''}$. In a later model, Ribner (1964b) reformulates the model so as to calculate the relative contribution of all the different correlations. The assumptions made by Ribner are the following:

- (a) The noise pattern of the round jet is axisymmetric.
- (b) The mean flow is nearly parallel to the axis that allows us to decompose the instantaneous local velocity to be a sum of the parallel mean flow and the turbulent fluctuations with zero mean, namely:

$$u_i(\vec{y}, t) = U_i(\vec{y})\delta_{1i} + u_{ti}(\vec{y}, t) \quad (2.4.11)$$

Introducing this decomposition into \mathfrak{R}_{ijkl} , and assuming that the turbulence is locally homogeneous, \mathfrak{R}_{ijkl} may be written in the form (for $\mathfrak{R}_{ijkl}^0(\vec{y}, \vec{\xi}) = 0$):

$$\begin{aligned} & \mathfrak{R}_{ijkl}(\vec{y}, \vec{\xi}, \tau) \\ &= \underbrace{\overline{u_{ti}' u_{tj}' u_{tk}'' u_{tl}''}}_{\text{self noise}} \\ &+ \underbrace{U_1' U_1'' \left(\delta_{1i} \delta_{1k} \overline{u_{tj}' u_{tl}''} + \delta_{1j} \delta_{1l} \overline{u_{ti}' u_{tk}''} + \delta_{1j} \delta_{1k} \overline{u_{ti}' u_{tl}''} + \delta_{1i} \delta_{1l} \overline{u_{tj}' u_{tk}''} \right)}_{\text{shear noise}} \end{aligned} \quad (2.4.12)$$

- (c) The joint probability of u_{ti}' and u_{ti}'' is assumed to be normal.
- (d) The two-point correlation $\mathfrak{R}_{ij}(\vec{y}, \vec{\xi}, \tau)$ is factorable into a space factor and a time factor:

$$\mathfrak{R}_{ij}(\vec{y}, \vec{\xi}, \tau) = \mathfrak{R}_{ij}(\vec{y}, \vec{\xi}) \exp(-\omega_f^2 \tau^2) \quad (2.4.13)$$

$$\mathfrak{R}_{ij}(\vec{y}, \vec{\xi},) = \overline{u_{tm}^2} \left[\left(f + \frac{1}{2} \xi f \frac{\partial f}{\partial \xi} \right) \delta_{ij} - \frac{1}{2} \frac{\partial f}{\partial \xi} \frac{\xi_i \xi_j}{\xi} \right] \quad (2.4.14)$$

$$f(\xi) = \exp\left(-\frac{\pi \xi^2}{L_1^2}\right) \quad (2.4.15)$$

where ω_f is a typical angular frequency of the turbulence. We define L_1 as the longitudinal integral scale of the turbulence and $\overline{u_{tm}^2}$ as $\frac{2}{3}$ of the kinetic turbulent energy k .

- (e) To evaluate the two point function $U_1'(\vec{y}') U_1''(\vec{y}'')$ in terms of $U_1^2(\vec{y})$, where \vec{y} is the midpoint of \vec{y}' and \vec{y}'' , Ribner (1964b) proposed a Gaussian expression. However this model is not well adapted to real situations.

Inserting all the above assumptions into equation (2.4.10), the expression for the acoustical directional intensity for the shear and self-noise per unit volume of the jet can be obtained from the corresponding autocorrelation function for $\tau = 0$:

$$I^{Se.N.}((x, \theta), \vec{y}) = C_{pp}^{Se.N.}((x, \theta), \vec{y}, \tau = 0) = \frac{3\sqrt{2}\rho_0 L_1^3 u_{tm}^2}{4\pi^2 c_0^5 x^2} \omega_f^4 \frac{D_i^{Se.N.}}{C^5} \quad (2.4.16)$$

$$I^{Sh.N.}((x, \theta), \vec{y}) = C_{pp}^{Sh.N.}((x, \theta), \vec{y}, \tau = 0) = \frac{3\rho_0 L_1^5 u_{tm}^2}{8\pi^3 c_0^5 x^2} \left(\frac{\partial U_1}{\partial y_2}\right)^2 \omega_f^4 \frac{D_i^{Sh.N.}}{C^5} \quad (2.4.17)$$

where

$$D_i^{Sh.N.} = \frac{1}{2}(\cos^2 \theta + \cos^4 \theta) \quad (2.4.18)$$

$$D_i^{Se.N.} = 1 \quad (2.4.19)$$

Clearly the isotropic directivity of the self-noise is a necessary consequence of the isotropy of the turbulence. The expression of the acoustical directional intensity for the total noise per unit volume of the jet appears as the sum of the shear and self-noise contributions:

$$I((x, \theta), \vec{y}) = I^{Se.N.}((x, \theta), \vec{y}) + I^{Sh.N.}((x, \theta), \vec{y}) \quad (2.4.20)$$

This total intensity can be put in the form:

$$\left[\underbrace{A}_{self\ noise} + \underbrace{\frac{B}{2}(\cos^2 \theta + \cos^4 \theta)}_{shear\ noise} \right] \times \underbrace{\frac{1}{C^5}}_{convection\ effect} \quad (2.4.21)$$

The self noise contribution is radiated isotropically, while the shear noise has a dipole-like pattern. The combined pattern for $A = B = 1$ is a quasi-ellipsoid with the long axis in the direction of the jet axis, see on figure 2.4.2.

As a consequence of the convection effect, the factor $\frac{1}{C^5}$ enhances the intensity of the sound in the downstream direction and largely attenuates the sound generation in the upstream region, see the last picture in figure 2.4.2. This effect becomes more apparent at high Mach numbers. To avoid this oversimplification, Ribner (1964b) and Ffowcs-Williams (1963) found it necessary to allow for variations in the retarded time with source position. This led to a modification factor

$$C_m = \sqrt{(1 - M_c \cos \theta)^2 + \alpha^2 M_c^2} \quad (2.4.22)$$

where $\alpha M_c = \frac{\omega_f L_1}{c_0 \sqrt{\pi}}$ and Ribner (1964b) assumed that $\alpha = 0.55$, however experiments indicate that α is closer to 0.3.

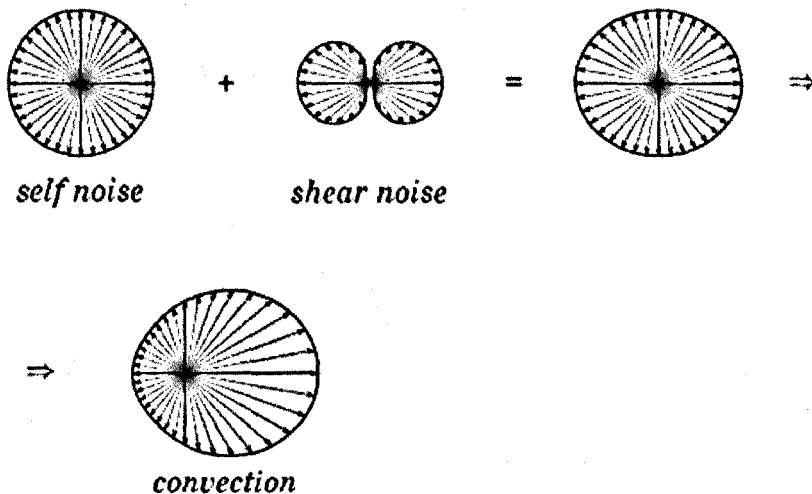


Figure 2.4.2 Noise radiation patterns.

2.5 Goldstein's acoustic formulation

The model devised by Goldstein and Rosenbaum (1973) generalized the Ribner model as described in the previous section 2.4. It is argued by Goldstein and Rosenbaum (1973) that it is more appropriate to assume that the turbulence in the jet is axisymmetric. In fact the mean flow introduces a preferred direction so that the isotropic turbulence description is not as adequate because it neglects important anisotropies, such as the marked reduction in the transverse integral scale.

For the sake of brevity, only the assumptions which differ from those introduced in the Ribner model are reviewed:

(a) The arbitrary time-independent tensor $\mathfrak{R}_{ijkl}^0(\vec{y}', \vec{\eta})$ is chosen as:

$$\mathfrak{R}_{ijkl}^0(\vec{y}', \vec{\eta}) = U_1'^2 \delta_{1j} \delta_{1l} \overline{u_{tk}'' u_{tl}''} + U_1''^2 \delta_{1j} \delta_{1l} \overline{u_{ti}' u_{tj}'} + U_1'^2 U_1''^2 \delta_{1l} \delta_{1j} \overline{u_{tk}'' u_{tl}''} + \overline{u_{ti}' u_{tj}' u_{tk}'' u_{tl}''} \quad (2.5.1)$$

(b) To treat the axisymmetric turbulence situation, it is necessary to introduce the point \vec{y} defined by

$$\vec{y} = \left(\vec{y}_1', \frac{\vec{y}_2' + \vec{y}_2''}{2}, \frac{\vec{y}_3' + \vec{y}_3''}{2} \right) \quad (2.5.2)$$

According to this definition, \vec{y} is not the midpoint of \vec{y}' and \vec{y}'' as in the isotropic case.

(c) For axisymmetric turbulence, the two-point correlation $\mathfrak{R}_{ij}(\vec{y}, \vec{\xi}, \tau)$ may be expressed in terms of two independent scalar functions:

$$\mathfrak{R}_{ij} = \epsilon_{jlm} \frac{\partial q_{im}}{\partial \xi_l} \quad (2.5.3)$$

where

$$q_{im} = \xi_k (\epsilon_{imk} Q_1 + \epsilon_{ilk} (\delta_{1m} Q_2 + \xi_m Q_3)) \quad (2.5.4)$$

$$Q_3 = \left(\frac{\partial}{\partial \xi_1} - \frac{\xi_1}{\xi_2} \frac{\partial}{\partial \xi_3} \right) Q_1 \quad (2.5.5)$$

where ϵ_{imk} is the antisymmetric symbol $\epsilon_{imk} = 0.5(j-l)(l-m)(m-i)$.

Acceptable models for Q_1 and Q_2 , from a kinematical point of view, are given by:

$$Q_1(\vec{y}, \vec{\xi}, \tau) = -\frac{1}{2} \overline{u_{t1}^2} f(\vec{y}, \tau) \exp \left(-\sqrt{\left(\frac{\xi_{23}^2}{L_2^2} + \frac{\xi_1^2}{L_1^2} \right)} \right) \quad (2.5.6)$$

$$Q_2(\vec{y}, \vec{\xi}, \tau) = -(\overline{u_{t2}^2} - \overline{u_{t1}^2}) f(\vec{y}, \tau) \exp \left(-\sqrt{\left(\frac{\xi_{23}^2}{L_2^2} + \frac{\xi_1^2}{L_1^2} \right)} \right) \quad (2.5.7)$$

where

$$\xi_{23}^2 = \xi_2^2 + \xi_3^2 \quad (2.5.8)$$

Here L_1 and $\overline{u_{t1}^2}$ (L_2 and $\overline{u_{t2}^2}$) are the longitudinal (transversal, respectively) integral scales and kinetic energy of the turbulence. The function f was not specified in the Goldstein model. It is consistent to adopt a temporal Gaussian function for $f(\vec{y}, \tau)$ as was done in Ribner's model in the isotropic case:

$$f(\vec{y}, \tau) = \exp(-\omega_f^2 \tau^2) \quad (2.5.9)$$

Where the \vec{y} dependence is implicit in ω_f .

Assuming that the axis of symmetry coincides with the axis of the jet then, after some tedious calculations, the following expressions are obtained for the acoustical directional intensities per unit volume of the jet relative to the shear and self-noise:

$$I^{Se.N.}((x, \theta), \vec{y}) = C_{pp}^{Se.N.}((x, \theta), \vec{y}, \tau = 0) = \frac{12\rho_0 L_1 L_2^2 \overline{u_{t1}^2}^2}{5\pi c_0^5 x^2} \omega_f^4 \frac{D_i^{Se.N.}}{C^5} \quad (2.5.10)$$

$$\begin{aligned} I^{Sh.N.}((x, \theta), \vec{y}) &= C_{pp}^{Sh.N.}((x, \theta), \vec{y}, \tau = 0) \\ &= \frac{24\rho_0 L_1^4 \overline{u_{t1}^2}}{\pi c_0^5 x^2} \left(\frac{\partial U_1}{\partial y_2} \right)^2 \omega_f^4 \frac{D_i^{Sh.N.}}{C^5} \end{aligned} \quad (2.5.11)$$

where

$$D_i^{Se.N.} = 1 + 2 \left(\frac{M}{9} - N \right) \cos^2 \theta \sin^2 \theta + \frac{1}{3} \left(\frac{M^2}{7} + M - \frac{3}{2} N \left(3 - 3N + \frac{\Delta^2}{2} \right) \sin^4 \theta \right) \quad (2.5.12)$$

$$D_i^{Sh.N.} = \cos^2 \theta \left(\cos^2 \theta + \frac{1}{2} \left(\frac{1}{\Delta^2} - 2N \right) \sin^2 \theta \right) \quad (2.5.13)$$

In these expressions the effects of the anisotropic structure of the turbulence appears through the following parameters:

$$\Delta = \frac{L_2}{L_1}, \quad N = 1 - \frac{\overline{u_{t2}^2}}{\overline{u_{t1}^2}} \quad \text{and} \quad M = \left(\frac{2}{3} \left(\Delta - \frac{1}{\Delta} \right) \right)^2 \quad (2.5.14)$$

If we rewrite the expression for the total acoustical intensity in a form similar to relation (2.4.13), we find that the self-noise contribution is now directional. The radiation pattern (for $\Delta = \frac{1}{3}$ and $N = \frac{1}{3}$) has a dipolar shape where the dipole axis is in the transverse direction ($\theta = 90^\circ$). The present shear noise radiation pattern resembles that of the Ribner model (see figure 2.4.2). It should be noted that in the limiting case of isotropic turbulence ($\Delta = 1$ and $M = N = 0$) the directivity expressions (2.5.12) and (2.5.13) become identical to those of Ribner (1964b).

2.5.1 Determination of the aerodynamic and statistical quantities from the $k - \epsilon$ RANS model

All the necessary aerodynamic and statistical quantities we need in order to estimate the noise generation using Goldstein's model could be obtained from the steady RANS standard $k - \epsilon$ solution:

$$\overline{u_{t1}^2} = \frac{8}{9} k \quad (2.5.1.1)$$

$$\overline{u_{t2}^2} = \frac{4}{9} k \quad (2.5.1.2)$$

$$L_1 = \frac{\left(\overline{u_{t1}^2} \right)^{\frac{3}{2}}}{\epsilon} \quad (2.5.1.3)$$

$$L_2 = \frac{\left(\overline{u_{t2}^2} \right)^{\frac{3}{2}}}{\epsilon} \quad (2.5.1.4)$$

$$\omega_f = 2\pi \frac{\epsilon}{k} \quad (2.5.1.5)$$

The convection effects of the jet noise are represented by the factor $\frac{1}{c^5}$ in the equations for the self and the shear noise components (2.5.10-11). This factor is calculated using the expression (2.4.22), where it is necessary to know the turbulent convection Mach number, M_c , which requires information about the eddy convection velocity U_{1c} . Unfortunately, the $k - \epsilon$ model cannot provide the eddy convection velocity U_{1c} . In general, this velocity is considered constant throughout the jet and is equal to 0.6 – 0.7 of the value of the mean jet exit velocity U_1 .

2.5.2 Determination of the acoustical intensity spectrum

The equations for the self noise and shear noise intensity (2.5.10-11) are derived with the assumption that the time delay for the autocorrelation function is $\tau = 0$. Using this assumption we lose the information about the noise spectra which is included by the temporal Gaussian function for $f(\vec{y}, \tau)$ as shown in equation (2.5.9). If we assume that $\tau \neq 0$, then the acoustic intensity spectrum $I_\omega(\vec{x})$ is obtained by applying the temporal Fourier transform of the density autocorrelation $C_{pp}(\vec{x}, \tau)$ defined in the relation (2.4.5):

$$I_\omega(\vec{x}) = \frac{1}{2\pi} \int_{-\infty}^{+\infty} C_{pp}(\vec{x}, \tau) e^{j\omega\tau} d\tau \quad (2.5.2.1)$$

where $j^2 = -1$ and ω designates the angular frequency. Let us denote W , $W_\omega(\vec{y})$, $I_\omega((x, \theta), \vec{y})$, respectively, the total acoustic power, the acoustical power spectrum (emitted from a unit volume located at \vec{y}), and the directional acoustical intensity spectrum:

$$W = \int_V \int_{-\infty}^{+\infty} W_\omega(\vec{y}) d\vec{y} d\omega \quad (2.5.2.2)$$

$$W_\omega(\vec{y}) = 2\pi x^2 \int_0^\pi I_\omega((x, \theta), \vec{y}) \sin \theta d\theta \quad (2.5.2.3)$$

$$I_\omega((x, \theta), \vec{y}) = \frac{1}{2\pi} \int_{-\infty}^{+\infty} C_{pp}((x, \theta), \vec{y}) e^{j\omega\tau} d\tau \quad (2.5.2.4)$$

where the autocorrelation function $C_{pp}((x, \theta), \vec{y})$ of the noise field radiated by a unit volume located at \vec{y} is the axisymmetric version of the general expression given by (2.4.9-10). Using the assumptions in the Goldstein model, $I_\omega((x, \theta), \vec{y})$ may be expressed in terms of the statistical turbulent flow properties for the self noise and the shear noise as follows:

$$I_{\omega}^{Se.N.}((x, \theta), \vec{y}) = \frac{\rho_0 L_1 L_2^2}{40\sqrt{2}\pi^{1.5} c_0^5 x^2} \frac{\omega^4}{u_{t1}^2} \exp\left(-\frac{\omega^2 C^2}{8\omega_f^2}\right) D_i^{Se.N.} \quad (2.5.2.5)$$

$$I_{\omega}^{Sh.N.}((x, \theta), \vec{y}) = \frac{\rho_0 L_1 L_2^4}{\pi^{1.5} c_0^5 x^2} \frac{\omega^4}{u_{t1}^2} \left(\frac{\partial U_1}{\partial y_2}\right)^2 \exp\left(-\frac{\omega^2 C^2}{4\omega_f^2}\right) D_i^{Sh.N.} \quad (2.5.2.6)$$

where the directivity of the self noise and the shear noise are given by expressions (2.5.12) and (2.5.13), respectively.

2.5.3 Realisation of the Goldstein's model in the CFD code

At this stage we should mention that the Goldstein acoustical model in the form of self and the shear noise intensities as defined by expressions (2.5.10-13), where the time dependency of the acoustic spectrum is not taken into account, is realized in FLUENT 12.0. It presents the acoustics in terms of the total acoustic power emitted by the unit volume of a turbulent jet defined as:

$$\begin{aligned} P_A(\vec{y}) &= \int_0^{2\pi} \int_0^{\pi} I((x, \theta), \vec{y}) x^2 \sin \theta \, d\theta \, d\phi \\ &= 2\pi x^2 \int_0^{\pi} I((x, \theta), \vec{y}) \sin \theta \, d\theta \end{aligned} \quad (2.5.3.1)$$

where $I((x, \theta), \vec{y})$ is the directional acoustic intensity per unit volume of a jet defined by:

$$I((x, \theta), \vec{y}) = I^{Se.N.}((x, \theta), \vec{y}) + I^{Sh.N.}((x, \theta), \vec{y}) \quad (2.5.3.2)$$

where the self and shear noise components expressed by (2.5.10-13). The total acoustic power could be reported both in the dimensional units $\left(\frac{W}{m^3}\right)$ and in dB computed from

$$L_p = 10 \text{Log} \left(\frac{P_A}{P_{ref}} \right) \quad (2.5.3.3)$$

where P_{ref} is the reference acoustic power which is equal to $10^{-12} \frac{W}{m^3}$ by default.

The form in which the acoustic data are presented is not ideal since it is difficult to validate the noise simulation results. In FLUENT we obtain the information about the total acoustic power emitted by a single jet volume (computational cell in terms of the CFD calculations). In other words we have collected the noise level data detected by an infinite number of microphones spread around the whole space. This information cannot be compared with the experimental measurements obtained by a single microphone because of the extra integrations over the microphone angular

position θ in the expression (2.5.3.1) and because FLUENT's interpretation of the Goldstein model does not consider the noise intensity as a spectra, but rather as an integrated value. These are the two main shortcomings of the realization of the Goldstein acoustic model realised in the commercial solver.

In order to avoid these difficulties, we have to realize the acoustic simulation subroutine using external tools, in particular MatLab. Therefore the noise simulations is realized in two steps: (i) the flow in 2D axisymmetric $k - \epsilon$ RANS simulation of the jet in FLUENT 12.0, and (ii) the noise calculation subroutine based on the aerodynamic and statistical quantities from the $k - \epsilon$ RANS solutions in MatLab.

It should be noted that the Goldstein acoustic model is essentially axisymmetrical and therefore we need to use an axisymmetric CFD solver in order to produce the aerodynamic and statistical quantities. The description of the CFD modelling is presented in Chapter 3.

2.6 Conclusions

In Chapter 2 we have described the fundamental equations originally proposed by Lighthill (1952) and the direct consequence from his acoustic model – the *eight power law*, which states that the acoustic power emitted by the turbulent jet is proportional to the eight power of its velocity. We have shown the evolution of the Lighthill approach to the most general acoustic formulation made by Ffowcs Williams and Hawkings (1969), FW-H. This model is valid for all kinds of aerodynamically generated noise, including the rotor noise, boundary layer noise and, of course, the jet noise. The FW-H acoustic model is realised in FLUENT 12.0.

In addition we have discussed the evolution of the original Lighthill (1952, 1954) formulation to the specific jet noise models developed by Ribner (1964a ,b) and Goldstein (1973). These models include many simplifications of the jet structure. For example the axisymmetry of the jet flow is one of the basic assumptions. Therefore the application of these acoustic formulations is limited to axisymmetric round jets. However the numerical simulations of the noise, using Ribner's and Goldstein's model, are essentially easier and faster than for the FW-H model, since

it requires aerodynamic and statistical quantities which can be obtained from the steady 2D $k - \epsilon$ RANS solutions.

Finally we have discussed the realization of the Goldstein acoustic formulation in FLUENT 12.0 and made suggestions for the improvement of this model.

Chapter 3

CFD Methods

3.1 Introduction

An acoustic analogy proposed by Lighthill (1952, 1954) is a two-step procedure. In the first step, a computational fluid dynamics (CFD) analysis is used to compute the aerodynamic sources. The second step consists of computing the propagation and radiation of these aerodynamic sources. The accuracy of acoustic predictions depends on the accuracy of modelling the aerodynamic sources in the first step of the procedure, i.e. the model of turbulence used on the first step is an important issue.

Some of the acoustical formulations have been adopted to use typical steady Reynolds Averaged Navier-Stokes Solution (RANS), for example the Curl (1955), Ribner (1964) and Goldstein (1973) formulations. In these theories the mean turbulent parameters of the flow computed by solving the RANS with a $k - \epsilon$ turbulent closure which can be introduced in a statistical source model to obtain the acoustic intensity.

It is naturally more convenient to use the unsteady flow parameters to evaluate directly Lighthill's stress tensor, T_{ij} , by solving the unsteady RANS (URANS) or by the Large Eddy Simulation (LES) or by Direct Numerical Simulation (DNS). Unsteady solutions are the basis for the Ffowcs Williams – Hawkings (1969) acoustical formulation.

However, in this chapter we give only a brief review of the RANS turbulent models, particularly those that are used in the current research work and the LES model.

3.2 Standard $k - \epsilon$ model

The simplest “complete models” of turbulence are two-equation models in which the solution of two separate transport equations allows the turbulent velocity and length scales to be independently determined. The standard $k - \epsilon$ turbulent model was proposed by Launder and Spalding (1974).

It is a semi-empirical model based on the transport equations for the turbulence kinetic energy (k) and its dissipation rate (ϵ). The model transport equation for k is derived from the exact equation, while the model transport equation for ϵ was obtained using physical reasoning and bears little resemblance to its mathematically exact counterpart, Launder and Spalding (1974).

In the derivation of the $k - \epsilon$ model, the assumption is that the flow is fully turbulent, and the effects of molecular viscosity are negligible. The standard $k - \epsilon$ model is therefore valid only for fully turbulent flows.

3.2.1 Transport equations for the Standard $k - \epsilon$ model

The turbulent kinetic energy, k , and its rate of dissipation, ϵ , are obtained from the following transport equations:

$$\frac{\partial}{\partial t}(\rho k) + \frac{\partial}{\partial x_i}(\rho k u_i) = \frac{\partial}{\partial x_j} \left(\left(\mu + \frac{\mu_t}{\sigma_k} \right) \frac{\partial k}{\partial x_j} \right) + G_k + G_b - \rho \epsilon - Y_M + S_k \quad (3.2.1.1)$$

and

$$\begin{aligned} \frac{\partial}{\partial t}(\rho \epsilon) + \frac{\partial}{\partial x_i}(\rho \epsilon u_i) \\ = \frac{\partial}{\partial x_j} \left(\left(\mu + \frac{\mu_t}{\sigma_\epsilon} \right) \frac{\partial \epsilon}{\partial x_j} \right) + C_{1\epsilon} \frac{\epsilon}{k} (G_k + C_{3\epsilon} G_b) - C_{2\epsilon} \rho \frac{\epsilon^2}{k} \\ + S_\epsilon \end{aligned} \quad (3.2.1.2)$$

where G_k represents the generation of turbulence kinetic energy due to the mean velocity gradient, calculated as:

$$G_k = -\overline{\rho u'_i u'_j} \frac{\partial U_j}{\partial x_i} \quad (3.2.1.3)$$

G_b is the generation of turbulence kinetic energy due to buoyancy:

$$G_b = \beta g_i \frac{\mu_t}{Pr_t} \frac{\partial T}{\partial x_i} \quad (3.2.1.4)$$

where Pr_t is the turbulent Prandtl number and g_i is the component of the gravitation vector in the i direction. For the Standard $k - \epsilon$ model, the default value for $Pr_t = 0.85$ is taken. The coefficient of thermal expansion, β , is defined as :

$$\beta = -\frac{1}{\rho} \left(\frac{\partial \rho}{\partial T} \right)_p \quad (3.2.1.5)$$

For ideal gases, equation (3.2.1.4) reduces to:

$$G_b = -g_i \frac{\mu_t}{\rho Pr_t} \frac{\partial \rho}{\partial x_i} \quad (3.2.1.6)$$

The coefficient Y_M in the k transport equation (3.2.1.1) represents the contribution of the fluctuating dilatation in compressible turbulence (compressibility effects are normally neglected in low-Mach-number flows) to the overall dissipation rate, calculated as:

$$Y_M = 2\rho\epsilon M_t^2 \quad (3.2.1.7)$$

where M_t is the turbulent Mach number, defined as:

$$M_t = \sqrt{\frac{k}{c_0^2}} \quad (3.2.1.8)$$

The coefficients $C_{1\epsilon}$, $C_{2\epsilon}$ and $C_{3\epsilon}$ are assumed to be constant. The degree to which ϵ is affected by the buoyancy is determined by the constant $C_{3\epsilon}$. Usually in commercial CFD software packages $C_{3\epsilon}$ is not specified, but instead calculated according to the following relation:

$$C_{3\epsilon} = \tanh \left| \frac{v}{u} \right| \quad (3.2.1.9)$$

where v is the component of the fluid flow velocity parallel to the gravitation vector and u is the component of the fluid flow velocity perpendicular to the gravitation vector. Thus, $C_{3\epsilon} = 1$ for buoyant shear layers for which the main flow direction is aligned with the direction of gravity, and $C_{3\epsilon} = 0$ for buoyant shear layers that are perpendicular to the gravitational vector.

The coefficients σ_k and σ_ϵ in equations (3.2.1.1) and (3.2.1.2) are the turbulent Prandtl numbers for k and ϵ , respectively, and S_k and S_ϵ are source terms.

3.2.2 Modelling the turbulent viscosity

The turbulent viscosity (eddy viscosity), μ_t , is modelled by combining k and ϵ as follows:

$$\mu_t = \rho C_\mu \frac{k^2}{\epsilon} \quad (3.2.2.1)$$

where C_μ is a constant.

3.2.3 Model constants

The model constants have been determined from experimental data with air and water and for fundamental turbulent shear flows, including homogeneous shear flows and decaying isotropic grid turbulence. They have been found to work fairly well over a wide range of wall-bounded and free shear flows. The default values for the model constants are represented in table 3.2.3.1. However in the current research the default values have been adjusted for a free mixture shear flow.

Table 3.2.3.1 Standard $k - \epsilon$ model constants.

$C_{1\epsilon}$	$C_{2\epsilon}$	C_μ	σ_k	σ_ϵ
1.44	1.92	0.09	1.0	1.3

3.3 RNG $k - \epsilon$ model

The RNG $k - \epsilon$ model was derived using a rigorous statistical technique (called the renormalization group theory) by Choudhury (1993). It is similar to the Standard $k - \epsilon$ model, but includes the following refinements:

- (a) An additional term in the ϵ equation that significantly improves the accuracy for rapidly strained flows.
- (b) The effect of swirl on the turbulence is included, and this enhances the accuracy for swirling flows.
- (c) An analytical formula for the turbulent Prandtl numbers, whereas the Standard $k - \epsilon$ model uses constant values.
- (d) An analytically-derived differential formula for the effective viscosity that accounts for low-Reynolds-number effects, while the Standard $k - \epsilon$ model is only a high-Reynolds-number model. However the effective use of this feature does depend on an appropriate treatment of the near-wall region.

These features make the RNG $k - \epsilon$ model more accurate and reliable than the Standard $k - \epsilon$ model over a wide range of fluid flows.

3.3.1 Transport equation for the RNG $k - \epsilon$ model

The RNG $k - \epsilon$ model has a similar form to the Standard $k - \epsilon$ model. We have the turbulent kinetic energy, k , and its rate of dissipation, ϵ , obtained from the transport equations :

$$\frac{\partial}{\partial t}(\rho k) + \frac{\partial}{\partial x_i}(\rho k u_i) = \frac{\partial}{\partial x_j} \left(\alpha_k \mu_{eff} \frac{\partial k}{\partial x_j} \right) + G_k + G_b - \rho \epsilon - Y_M + S_k \quad (3.3.1.1)$$

and

$$\begin{aligned} \frac{\partial}{\partial t}(\rho \epsilon) + \frac{\partial}{\partial x_i}(\rho \epsilon u_i) \\ = \frac{\partial}{\partial x_j} \left(\alpha_\epsilon \mu_{eff} \frac{\partial \epsilon}{\partial x_j} \right) + C_{1\epsilon} \frac{\epsilon}{k} (G_k + C_{3\epsilon} G_b) - C_{2\epsilon} \rho \frac{\epsilon^2}{k} \\ - R_\epsilon + S_\epsilon \end{aligned} \quad (3.3.1.2)$$

In these equations, G_k represents the generation of turbulence kinetic energy due to the mean velocity gradient, calculated as in equation (3.2.1.3), G_b is a generation of the turbulence kinetic energy due to buoyancy, calculated as described in equation (3.2.1.4), and Y_M represents the contribution of the fluctuating dilatation in compressible turbulence to the overall dissipation rate, calculated as described in equation (3.2.1.7). The quantities α_k and α_ϵ are the inverse effective Prandtl numbers for k and ϵ , respectively, S_k and S_ϵ are source terms.

3.3.2 Modelling the turbulent viscosity

The scale elimination procedure in RNG theory results in a differential equation for the turbulent viscosity:

$$d \left(\frac{\rho^2 k}{\sqrt{\epsilon \mu}} \right) = 1.72 \frac{\hat{\nu}}{\sqrt{\hat{\nu}^3 - 1 + C_\nu}} d\hat{\nu} \quad (3.3.2.1)$$

where $\hat{\nu} = \frac{\mu_{eff}}{\mu}$ and $C_\nu \approx 100$. This equation may be integrated to obtain an accurate description of how the effective turbulent transport varies with the effective Reynolds number, allowing the RNG model to better handle low-Reynolds-number and near-wall fluid flows. In the high-Reynolds-number limit, equation (3.3.2.1) gives the same form of the equation as for a Standard $k - \epsilon$ model (see equation (3.2.2.1)), namely

$$\mu_t = \rho C_\mu \frac{k^2}{\epsilon} \quad (3.3.2.2)$$

with $C_\mu = 0.0845$, derived using RNG theory. It is interesting to note that this value of C_μ is very close to the empirically-determined value of 0.09, see table 3.2.3.1, as used in the Standard $k - \epsilon$ model.

3.3.3 Calculating the inverse effective Prandtl numbers

The inverse effective Prandtl numbers, α_k and α_ϵ , are computed using the following formula derived analytically by the RNG theory, Choundhury (1993):

$$\left| \frac{\alpha - 1.3929}{\alpha_0 - 1.3929} \right|^{0.6321} \left| \frac{\alpha + 2.3929}{\alpha_0 + 2.3929} \right|^{0.3679} = \frac{\mu_{mol}}{\mu_{eff}} \quad (3.3.3.1)$$

where $\alpha_0 = 1.0$. In the high-Reynolds-number limit $\left(\frac{\mu_{mol}}{\mu_{eff}} \ll 1 \right)$, $\alpha_k = \alpha_\epsilon \approx 1.393$.

3.3.4 The R_ϵ term in the ϵ equation

The main difference between the Standard $k - \epsilon$ and RNG models lies in an additional term in the dissipation rate transport equation (3.3.1.2) given by

$$R_\epsilon = \frac{C_\mu \rho \eta^3 \left(1 - \frac{\eta}{\eta_0}\right) \epsilon^2}{1 + \beta \eta^3} k \quad (3.3.4.1)$$

where $\eta \equiv \frac{sk}{\epsilon}$, $\eta_0 = 4.38$, $\beta = 0.012$. The effects of this term in the RNG ϵ equation can be seen more clearly by rearranging the transport equation (3.3.1.2). On using expression (3.3.4.1), the third and fourth terms on the right hand side of equation (3.3.1.2) can be merged, and the resulting ϵ equation can be written as:

$$\begin{aligned} & \frac{\partial}{\partial t} (\rho \epsilon) + \frac{\partial}{\partial x_i} (\rho \epsilon u_i) \\ & = \frac{\partial}{\partial x_j} \left(\alpha_\epsilon \mu_{eff} \frac{\partial \epsilon}{\partial x_j} \right) + C_{1\epsilon} \frac{\epsilon}{k} (G_k + C_{3\epsilon} G_b) - \tilde{C}_{2\epsilon} \rho \frac{\epsilon^2}{k} \end{aligned} \quad (3.3.4.2)$$

where $\tilde{C}_{2\epsilon}$ is given by

$$\tilde{C}_{2\epsilon} \equiv C_{2\epsilon} + \frac{C_\mu \eta^3 \left(1 - \frac{\eta}{\eta_0}\right)}{1 + \beta \eta^3} \quad (3.3.4.3)$$

In regions where $\eta < \eta_0$, the R_ϵ term makes a positive contribution to the dissipation rate, and $\tilde{C}_{2\epsilon}$ becomes larger than $C_{2\epsilon}$. For instance, in the logarithmic layer it can be shown that $\eta \approx 3.0$, giving $\tilde{C}_{2\epsilon} \approx 2.0$, which is close in magnitude to the value $C_{2\epsilon} = 1.92$ in the Standard $k - \epsilon$ model, see table 3.2.3.1. As a result, for

weakly to moderately strained flows, the RNG model tends to give results largely comparable to the Standard $k - \epsilon$ model.

However, in regions of large strain rate ($\eta > \eta_0$) the R_ϵ term makes a negative contribution to the dissipation rate, making the value of $\tilde{C}_{2\epsilon}$ less than $C_{2\epsilon}$. In comparison with the Standard $k - \epsilon$ model, the smaller destruction of ϵ augments the dissipation rate, reducing k and, eventually, the effective viscosity.

As a result, in rapidly strained flows, the RNG model yields a lower turbulent viscosity than the Standard $k - \epsilon$ model. Thus, the RNG models is more responsible for the effects of rapid strain and streamline curvature than the Standard $k - \epsilon$ model, and this explains the superior performance of the RNG model for certain classes of flows.

3.3.5 Model constants

The model constants $C_{1\epsilon}$ and $C_{2\epsilon}$, given in table 3.3.5.1, in the equation (3.3.1.2) have values, derived analytically by the RNG theory.

Table 3.3.5.1 RNG model constants.

$C_{1\epsilon}$	$C_{2\epsilon}$	C_μ
1.42	1.68	0.0845

3.4 Realizable $k - \epsilon$ model

The Realizable $k - \epsilon$ model is a relatively recent development, Shih et al. (1995) and it differs from the Standard $k - \epsilon$ model in two important ways:

- (a) It contains a new formulation for the turbulent viscosity.
- (b) A new transport equation for the dissipation rate, ϵ , has been derived from an exact equation for the transport of the mean-square vorticity fluctuation.

The term “realizable” means that the model satisfies certain mathematical constraints on the Reynolds stress which are consistent with the physics of turbulent flows. Neither the Standard $k - \epsilon$ model nor the RNG $k - \epsilon$ model is realizable.

A benefit of the realizable $k - \epsilon$ model is that it should more accurately predict the spreading rate of both planar and round jets. Also it is likely to provide a superior performance for flows involving rotation, boundary layers under strong adverse pressure gradients, separation, and recirculations.

In the Realizable $k - \epsilon$ model the expression for the normal Reynolds stress in an incompressible strained mean flow is obtained by combining the Boussinesq relationship and the eddy viscosity definition, as follows:

$$\overline{u^2} = \frac{2}{3}k - 2\nu_t \frac{\partial U}{\partial x} \quad (3.4.1)$$

Using equation (3.2.2.1) for the turbulent viscosity $\nu_t \equiv \frac{\mu_t}{\rho}$, we obtain the result that the normal stress, $\overline{u^2}$, which by definition is a positive quantity, becomes negative, i.e. “non-realizable”, when the strain is large enough to satisfy

$$\frac{k}{\epsilon} \frac{\partial U}{\partial x} > \frac{1}{3C_\mu} \approx 3.7 \quad (3.4.2)$$

The most promising way to ensure the realizability is to make C_μ variable by sensitizing it to the mean flow (mean deformation) and the turbulence (k, ϵ). The notion of variable C_μ has been suggested by many experimentalists, for example Reynolds (1987) found C_μ to be about 0.09 in the inertial sublayer of equilibrium boundary layers, and 0.05 in a strong homogeneous shear flow.

3.4.1 Transport equation for the Realizable $k - \epsilon$ model

The modelled transport equation for k and ϵ in the Realizable model are as follows:

$$\frac{\partial}{\partial t}(\rho k) + \frac{\partial}{\partial x_i}(\rho k u_i) = \frac{\partial}{\partial x_j} \left(\left(\mu + \frac{\mu_t}{\sigma_k} \right) \frac{\partial k}{\partial x_j} \right) + G_k + G_b - \rho \epsilon - Y_M + S_k \quad (3.4.1.1)$$

and

$$\begin{aligned} & \frac{\partial}{\partial t}(\rho \epsilon) + \frac{\partial}{\partial x_i}(\rho \epsilon u_i) \\ &= \frac{\partial}{\partial x_j} \left(\left(\mu + \frac{\mu_t}{\sigma_k} \right) \frac{\partial \epsilon}{\partial x_j} \right) + \rho C_1 S \epsilon - \rho C_2 \frac{\epsilon^2}{k + \sqrt{\nu \epsilon}_k} \\ &+ C_{1\epsilon} \frac{\epsilon}{k} C_{3\epsilon} G_b + S_\epsilon \end{aligned} \quad (3.4.1.2)$$

where $C_1 = \max \left[0.43, \frac{\eta}{\eta+5} \right]$, $\eta = S \frac{k}{\epsilon}$, $S = \sqrt{2S_{ij}S_{ij}}$.

In these equations, G_k represents the generation of turbulence kinetic energy due to the mean velocity gradient, calculated as in equation (3.2.1.3), G_b is the generation of turbulence kinetic energy due to buoyancy, calculated as described in equation (3.2.1.4), and Y_M represents the contribution of the fluctuating dilatation in compressible turbulence to the overall dissipation rate, calculated as described in equation (3.2.1.7). C_1 and C_2 are constants, σ_k and σ_ϵ are the turbulent Prandtl numbers for k and ϵ respectively, and S_k and S_ϵ are source terms.

It should be noted that the k equation (3.4.1.1) is the same as that used in the Standard $k - \epsilon$ model (3.2.1.1) and the RNG $k - \epsilon$ model (3.3.1.1) except for the model constants. However, the form of the ϵ equation is quite different from those in the Standard and RNG-based $k - \epsilon$ models, see equations (3.2.1.2) and (3.3.1.2). One of the features of this approach is that the production term in the ϵ equation (the second term on the right-hand side of the equation (3.4.1.1)) does not involve the production of k , i.e. it does not contain the same G_k term as in the other $k - \epsilon$ models. It is postulated that the present form better represents the spectral energy transfer.

Another desirable feature is that the destruction term (the next to last term on the right-hand side of equation (3.4.1.1)) does not have any singularities, i.e. its denominator never vanishes, even if k vanishes or becomes less than zero. This feature is in contrast to that found in traditional $k - \epsilon$ models, which have a singularity due to k being present in the denominator.

This model has been extensively validated for a wide range of fluid flows by Kim et al. (1997) and Shih et al. (1995), including rotating homogeneous shear flows, free flows including jets and mixing layers, channel and boundary layer flows, and separated flows. For all these cases, the performance of the model has been found to be substantially better than that of the Standard $k - \epsilon$ model (with default coefficients).

3.4.2 Modelling the turbulent viscosity

The eddy viscosity is computed in the same way as in other $k - \epsilon$ models (equations 3.2.2.1 and 3.3.2.2), namely

$$\mu_t = \rho C_\mu \frac{k^2}{\epsilon} \quad (3.4.2.1)$$

The difference between the Realizable $k - \epsilon$ model and the Standard and RNG $k - \epsilon$ models is that C_μ is no longer a constant, but it is computed using the following equation:

$$C_\mu = \frac{1}{A_0 + A_S \frac{k\bar{U}}{\epsilon}} \quad (3.4.2.2)$$

where

$$\bar{U} \equiv \sqrt{S_{ij}S_{ij} + \hat{\Omega}_{ij}\hat{\Omega}_{ij}} \quad (3.4.2.3)$$

and

$$\hat{\Omega}_{ij} = \Omega_{ij} - 2\varepsilon_{ijk}\omega_k \quad (3.4.2.4)$$

$$\Omega_{ij} = \bar{\Omega}_{ij} - \varepsilon_{ijk}\omega_k \quad (3.4.2.5)$$

and $\bar{\Omega}_{ij}$ is the mean rate-of-rotation tensor viewed in a rotating reference frame with angular velocity ω_k . The model constants A_0 and A_S are given by $A_0 = 4.04$, $A_S = \sqrt{6} \cos \phi$ where

$$\phi = \frac{1}{3} \cos^{-1}(\sqrt{6}W), \quad W = \frac{S_{ij}S_{jk}S_{ki}}{\bar{S}^3}, \quad \bar{S} = \sqrt{S_{ij}S_{ij}}, \quad S_{ij} = \frac{1}{2} \left(\frac{\partial u_j}{\partial x_i} + \frac{\partial u_i}{\partial x_j} \right) \quad (3.4.2.6)$$

It can be seen that C_μ is a function of the mean strain and rotation rates, the angular velocity of the system of rotation, and the turbulence fields (k and ϵ). C_μ in the equation (2.4.2.1) can be shown to recover the standard value of 0.09 for an inertial sublayer in an equilibrium boundary layer.

3.4.3 Model constants

The model constants C_2 , σ_k and σ_ϵ have been established to ensure that the model performs well for certain canonical flows and these are given in table 3.4.3.1.

Table 3.4.3.1 *Realizable model constants.*

$C_{1\epsilon}$	C_2	σ_k	σ_ϵ
1.44	1.9	1.0	1.2

3.5 Reynolds stress model

The Reynolds stress model (RSM), originally proposed by Laufer et al. (1975) is based on abandoning the isotropic eddy-viscosity hypothesis. The RSM closes the Reynolds-averaged Navier-Stokes equations by solving transport equations for the Reynolds stresses, together with an equation for the dissipation rate. This means that five additional transport equations are required in 2D flows, in comparison to seven additional transport equations solved in 3D.

Since the RSM accounts for the effects of streamline curvature and rapid changes in strain rate in a more rigorous manner than two-equation models, it has greater potential to give accurate predictions for complex flows. However, the fidelity of the RSM predictions is still limited by closure assumptions employed to model various terms in the exact equations for the Reynolds stresses. The modelling of the pressure-strain and dissipation-rate terms is particularly challenging, and often considered to be responsible for compromising the accuracy of RSM predictions.

The RSM might not always yield results that are clearly superior to the simpler models in all cases of the flows to warrant the additional computational expense. However, use of the RSM is a must when the flow features of interest are the result of anisotropy in the Reynolds stresses.

The exact form of the Reynolds stress transport equations may be derived by taking moments of the exact momentum equation. This is a process wherein the exact momentum equations are multiplied by a fluctuating property, the product then being Reynolds-averaged. Unfortunately, several of the terms in the exact equation are unknown and modelling assumptions are required in order to close the equations.

3.5.1 Reynolds stress transport equations

The exact equations for the transport of the Reynolds stresses, $\overline{\rho u'_i u'_j}$, may be written as follows:

$$\begin{aligned}
& \underbrace{\frac{\partial}{\partial t} (\overline{\rho u'_i u'_j})}_{\text{local time derivative}} + \underbrace{\frac{\partial}{\partial x_k} (\rho u_k \overline{u'_i u'_j})}_{C_{ij} \equiv \text{convection}} \\
&= - \underbrace{\frac{\partial}{\partial x_k} (\overline{\rho u'_i u'_j u'_k} + p (\delta_{kj} u'_i + \delta_{ik} u'_j))}_{D_{T,ij} \equiv \text{turbulent diffusion}} \\
&+ \underbrace{\frac{\partial}{\partial x_k} \left(\mu \frac{\partial}{\partial x_k} (\overline{u'_i u'_j}) \right)}_{D_{L,ij} \equiv \text{molecular diffusion}} - \underbrace{\rho \left(\overline{u'_i u'_k} \frac{\partial u_j}{\partial x_k} + \overline{u'_j u'_k} \frac{\partial u_i}{\partial x_k} \right)}_{P_{ij} \equiv \text{stress production}} \\
&- \underbrace{\rho \beta (\overline{g_i u'_j \theta} + \overline{g_j u'_i \theta})}_{G_{ij} \equiv \text{buoyancy production}} + \underbrace{p \left(\frac{\partial u'_i}{\partial x_j} + \frac{\partial u'_j}{\partial x_i} \right)}_{\phi_{ij} \equiv \text{pressure strain}} \\
&- \underbrace{2\mu \frac{\partial u'_i}{\partial x_k} \frac{\partial u'_j}{\partial x_k}}_{\epsilon_{ij} \equiv \text{dissipation}} \\
&- \underbrace{2\rho \Omega_k (\overline{u'_i u'_m} \epsilon_{ikm} + \overline{u'_j u'_m} \epsilon_{ikm})}_{F_{ij} \equiv \text{production by system rotation}} + \underbrace{S_{user}}_{\text{user-defined source term}}
\end{aligned} \tag{3.5.1.1}$$

where the various terms in these exact equations, C_{ij} , $D_{L,ij}$, P_{ij} and F_{ij} do not require modelling. However, $D_{T,ij}$, G_{ij} , ϕ_{ij} and ϵ_{ij} need to be modelled in order to close the system of equations. The following section describes the modelling assumptions required for the closure of the set of equations.

3.5.2 Modelling turbulent diffusive transport

The $D_{T,ij}$ term can be modelled by the generalized gradient-diffusion model of Daly and Harlow (1970):

$$D_{T,ij} = C_s \frac{\partial}{\partial x_k} \left(\rho \frac{k \overline{u'_k u'_l}}{\epsilon} \frac{\partial \overline{u'_i u'_j}}{\partial x_l} \right) \tag{3.5.2.1}$$

However this equation can result in numerical instabilities, so it has been simplified in FLUENT 12.0 in order to use a scalar turbulent diffusivity as follows:

$$D_{T,ij} = \frac{\partial}{\partial x_k} \left(\frac{\mu_t}{\sigma_k} \frac{\partial \overline{u'_i u'_j}}{\partial x_k} \right) \tag{3.5.2.2}$$

The turbulent viscosity, μ_t , is computed using equation (3.2.2.1). The value of σ_k is different from that in the standard and realizable $k - \epsilon$ models and equals 0.82.

3.5.3 Modelling the pressure-strain term

The pressure-strain term in equation (3.5.1.1) is modelled according to the proposals by Gibson and Launder (1978). The classical approach to modelling ϕ_{ij} uses the following decomposition:

$$\phi_{ij} = \phi_{ij,1} + \phi_{ij,2} + \phi_{ij,\omega} \quad (3.5.3.1)$$

where $\phi_{ij,1}$ is the slow pressure-strain term, also known as the return-to-isotropy term, $\phi_{ij,2}$ is called the rapid pressure-strain term and $\phi_{ij,\omega}$ is the wall-reflection term. The slow pressure-strain term, $\phi_{ij,1}$, is modelled as

$$\phi_{ij,1} \equiv -C_1 \rho \frac{\epsilon}{k} \left(\overline{u'_i u'_j} - \frac{2}{3} \delta_{ij} k \right) \quad (3.5.3.2)$$

with $C_1 = 1.8$. The rapid pressure-strain term, $\phi_{ij,2}$, is modelled as

$$\phi_{ij,2} \equiv -C_2 \left(\left(P_{ij} + F_{ij} + \frac{5}{6} G_{ij} - C_{ij} \right) - \frac{2}{3} \delta_{ij} \left(P + \frac{5}{6} G + C \right) \right) \quad (3.5.3.3)$$

where $C_2 = 0.60$, P_{ij} , F_{ij} , G_{ij} and C_{ij} are defined in equation (3.5.1.1), $G = \frac{1}{2} G_{kk}$, $P = \frac{1}{2} P_{kk}$ and $C = \frac{1}{2} C_{kk}$. The wall-reflection term, $\phi_{ij,\omega}$, is responsible for the redistribution of the normal stress near the wall. It tends to damp out the normal stress perpendicular to the wall, while enhancing the stresses parallel to the wall. This term is modelled as:

$$\begin{aligned} \phi_{ij,\omega} \equiv & -\hat{C}_1 \frac{\epsilon}{k} \left(\overline{u'_k u'_m n_k n_m} \delta_{ij} - \frac{3}{2} \overline{u'_i u'_k n_j n_k} - \frac{3}{2} \overline{u'_j u'_k n_i n_k} \right) \frac{C_l k^{\frac{3}{2}}}{\epsilon d} \\ & + \hat{C}_2 \left(\phi_{km,2} n_k n_m \delta_{ij} - \frac{3}{2} \phi_{ik,2} n_j n_k - \frac{3}{2} \phi_{jk,2} n_i n_k \right) \frac{C_l k^{\frac{3}{2}}}{\epsilon d} \end{aligned} \quad (3.5.3.4)$$

where $\hat{C}_1 = 0.5$, $\hat{C}_2 = 0.3$, n_k is the x_k component of the unit normal to the wall, d is the normal distance to the wall, and $C_l = \frac{C_\mu^{3/4}}{K_a}$, where $C_\mu = 0.09$ and K_a is von Karman constant equal to 0.4187.

3.5.4 Effects of buoyancy on turbulence

The production terms in due to buoyancy in the equation (3.5.1.1) are modelled as

$$G_{ij} = (\overline{J_i U_j} + \overline{J_j U_i}) = -\beta (g_i \overline{u_j \theta} + g_j \overline{U_i \theta}) \quad (3.5.4.1)$$

$$\overline{U_i \theta} = \frac{\mu_t}{Pr_t} \left(\frac{\partial T}{\partial x_i} \right) \quad (3.5.4.2)$$

where Pr_t is the turbulent Prandtl number for the energy, with a default value of 0.85, and the coefficient of thermal expansion, β , given by the expression:

$$\beta = -\frac{1}{\rho} \left(\frac{\partial \rho}{\partial T} \right)_p \quad (3.5.4.3)$$

From the expression (3.5.4.3) we obtain G_{ij} for ideal gas:

$$G_{ij} = -\frac{\mu_t}{\rho Pr_t} \left(g_i \frac{\partial \rho}{\partial x_j} + g_j \frac{\partial \rho}{\partial x_i} \right) \quad (3.5.4.4)$$

3.5.5 Modelling the turbulence kinetic energy

In general, when the turbulence kinetic energy is needed for modelling a specific term, and it is obtained by taking the trace of the Reynolds stress tensor:

$$k = \frac{1}{2} \overline{u'_i u'_i} \quad (3.5.5.1)$$

In order to solve a transport equation for the turbulence kinetic energy we use the following model equation:

$$\begin{aligned} \frac{\partial}{\partial t} (\rho k) + \frac{\partial}{\partial x_i} (\rho k u_i) \\ = \frac{\partial}{\partial x_j} \left(\left(\mu + \frac{\mu_t}{\sigma_k} \right) \frac{\partial k}{\partial x_j} \right) + \frac{1}{2} (P_{ii} + G_{ii}) - \rho \epsilon (1 + 2M_t^2) \\ + S_k \end{aligned} \quad (3.5.5.2)$$

where $\sigma_k = 0.82$ and S_k is a user-defined source term. This equation is obtained by contracting the modelled equation for the Reynolds stresses (3.5.1.1). As one might expect, it is essentially identical to equation (3.2.1.1) used in the standard $k - \epsilon$ model. Although equation (3.4.5.2) is solved globally throughout the flow domain, the values of k obtained are used only for boundary conditions. In every other case, k is obtained from equation (3.5.5.1). However, this is a minor point, since the values of k obtained with either method should be very similar.

3.5.6 Modelling the dissipation rate

The dissipation tensor, ϵ_{ij} , is modelled as

$$\epsilon_{ij} = \frac{2}{3} \delta_{ij} (\rho \epsilon + Y_M) \quad (3.5.6.1)$$

where $Y_M = 2\rho\epsilon M_t^2$ is an additional ‘‘dilatation dissipation’’ term according to the model by Sarkar and Balakrishnan (1990). The turbulent Mach number in this term is defined as

$$M_t = \sqrt{\frac{k}{c_0^2}} \quad (3.5.6.2)$$

where $c_0 \equiv \sqrt{\gamma RT}$ is the speed of sound. This compressibility modification always takes effect when the compressible form of the ideal gas law is used.

The scalar dissipation rate, ϵ , is computed with a model transport equation similar to that used in the standard $k - \epsilon$ model (3.2.1.2):

$$\begin{aligned} \frac{\partial}{\partial t}(\rho\epsilon) + \frac{\partial}{\partial x_i}(\rho\epsilon u_i) \\ = \frac{\partial}{\partial x_j} \left(\left(\mu + \frac{\mu_t}{\sigma_\epsilon} \right) \frac{\partial \epsilon}{\partial x_j} \right) + C_{\epsilon 1} \frac{1}{2} (P_{ii} + C_{\epsilon 3} G_{ii}) \frac{\epsilon}{k} - C_{\epsilon 2} \rho \frac{\epsilon^2}{k} \\ + S_\epsilon \end{aligned} \quad (3.5.6.3)$$

where $\sigma_\epsilon = 1.0$, $C_{\epsilon 1} = 1.44$, $C_{\epsilon 2} = 1.92$, $C_{\epsilon 3}$ is evaluated as a function of the local flow direction relative to the gravitational vector, see expression (3.2.1.9), and S_ϵ is a user-defined source term.

The turbulent viscosity is computed similarly to the $k - \epsilon$:

$$\mu_t = \rho C_\mu \frac{k^2}{\epsilon} \quad (3.5.6.4)$$

where $C_\mu = 0.09$.

3.5.7 Convective heat and mass transfer modelling

With the RSM in FLUENT 12.0, the turbulent heat transport is modelled using the concept of Reynolds' analogy to turbulent momentum transfer. The *modelled* energy equation is thus given by the following:

$$\frac{\partial}{\partial t}(\rho E) + \frac{\partial}{\partial x_i}(u_i(\rho E + p)) = \frac{\partial}{\partial x_j} \left(\left(k + \frac{c_p \mu_t}{Pr_t} \right) \frac{\partial T}{\partial x_j} + u_i (\tau_{ij})_{eff} \right) + S_h \quad (3.5.7.1)$$

where E is the total energy and $(\tau_{ij})_{eff}$ is the deviatoric stress tensor, defined as:

$$(\tau_{ij})_{eff} = \mu_{eff} \left(\frac{\partial u_j}{\partial x_i} + \frac{\partial u_i}{\partial x_j} \right) - \frac{2}{3} \mu_{eff} \frac{\partial u_k}{\partial x_k} \delta_{ij} \quad (3.5.7.2)$$

The term involving $(\tau_{ij})_{eff}$ represents the viscous heating, and is always computed in the density-based solvers in FLUENT 12.0. It is not computed by default in the pressure-based solver, but it can be enabled. The default value of the Prandtl number is 0.85, however it is possible to change this value in FLUENT 12.0.

The turbulent mass transfer is treated similarly, with a default turbulent Schmidt number ($Sc = \frac{\mu}{\rho D}$, D is mass diffusivity) of 0.7. This value could be changed in FLUENT 12.0.

3.6 Large Eddy Simulation model

The Large Eddy Simulation model (LES) is a turbulence model where large eddies are resolved directly, while small eddies are modelled. The model was formulated by Smagorinsky in the late 1960s and became popular in later years. The LES is much a more accurate model for the numerical simulations of turbulent flows because it involves fewer assumptions about the nature of the turbulence. However it is a much more time consuming methodology, as LES requires finer mesh than any of the RANS methods. The rationale behind LES can be summarized as follows:

- Momentum, mass, energy and other passive scalars are transported mostly by large eddies.
- Large eddies are more problem-dependent. They are dictated by the geometries and boundary conditions of the fluid flow involved.
- Small eddies are less dependent on the geometry, tend to be more isotropic, and are consequently more universal.
- The chance of finding a universal turbulence model is much higher for small eddies.

Resolving only the large eddies allows one to use a much coarser mesh and larger time-step sizes in LES than in direct solutions of the Navier-Stokes equations, where the mesh scale should be able to resolve the smallest turbulence structures, defined by the Kolmogorov scale. However, LES still requires a substantially finer mesh than those typically used for RANS calculations. In addition, LES has to be run for a sufficiently long flow-time to obtain the stable statistics of the flow being modelled. As a result, the computational cost involved with LES is normally orders of magnitudes higher than for steady RANS calculations in terms of memory (RAM) and CPU time. Therefore, high-performance computing (e.g. parallel computing) is a necessity for LES, especially for industrial applications.

3.6.1 Filtered Navier-Stokes equations

The governing equations employed for LES are obtained by filtering the time-dependent Navier-Stokes equations in either Fourier (wave-number) space or configuration (physical) space. The filtering process effectively filters out the eddies whose scales are smaller than the filter width or grid spacing used in the computations. The resulting equations thus govern the dynamics of large eddies.

A filtered variable (denoted by an overbar) is defined by

$$\bar{\phi}(x) = \int_D \phi(x') G(x, x') dx' \quad (3.6.1.1)$$

where D is the fluid domain, and G is the filter function that determines the scale of the resolved eddies.

In this thesis we use the approach where the finite-volume discretization implicitly provides the filtering operation:

$$\bar{\phi} = \frac{1}{V} \int_v \phi(x') dx', \quad x' \in v \quad (3.6.1.2)$$

where V is the volume of a computational cell. The filter function, $G(x, x')$, implied is given by

$$G(x, x') = \begin{cases} 1/V, & x' \in v \\ 0, & \text{otherwise} \end{cases} \quad (3.6.1.3)$$

It should be noted that the LES capability is applicable to compressible flows. However for the sake of a concise notation the theory presented here is for incompressible flows.

Filtering the Navier-Stokes equations we obtain

$$\frac{\partial \rho}{\partial t} + \frac{\partial}{\partial x_i} (\rho \bar{u}_i) = 0 \quad (3.6.1.4)$$

and

$$\frac{\partial}{\partial t} (\rho \bar{u}_i) + \frac{\partial}{\partial x_j} (\rho \bar{u}_i \bar{u}_j) = \frac{\partial}{\partial x_j} \left(\mu \frac{\partial \sigma_{ij}}{\partial x_j} \right) - \frac{\partial \bar{p}}{\partial x_i} - \frac{\partial \tau_{ij}}{\partial x_j} \quad (3.6.1.5)$$

where σ_{ij} is the stress tensor due to the molecular viscosity which is defined by

$$\sigma_{ij} \equiv \left(\mu \left(\frac{\partial \bar{u}_i}{\partial x_j} + \frac{\partial \bar{u}_j}{\partial x_i} \right) \right) - \frac{2}{3} \mu \frac{\partial \bar{u}_i}{\partial x_i} \delta_{ij} \quad (3.6.1.6)$$

and τ_{ij} is the subgrid-scale stress defined by

$$\tau_{ij} \equiv \rho \bar{u}_i \bar{u}_j - \rho \bar{u}_i \bar{u}_j \quad (3.6.1.7)$$

3.6.2 Subgrid-scale models

The subgrid-scale stress resulting from the filtering operation are unknown, and requires modelling. The subgrid-scale turbulence models applied in this thesis employ the Boussinesq hypothesis as in the RANS models, and computing subgrid-scale turbulent stress from

$$\tau_{ij} - \frac{1}{3}\tau_{kk}\delta_{ij} = -2\mu_t\bar{S}_{ij} \quad (3.6.2.1)$$

where μ_t is the subgrid-scale turbulent viscosity. The isotropic part of the subgrid-scale stresses τ_{kk} is not modelled, but added to the filtered static pressure term. \bar{S}_{ij} is the rate-of-strain tensor for the resolved scale defined by

$$\bar{S}_{ij} \equiv \frac{1}{2}\left(\frac{\partial\bar{u}_i}{\partial x_j} + \frac{\partial\bar{u}_j}{\partial x_i}\right) \quad (3.6.2.2)$$

For compressible flows, it is convenient to introduce the density-weighted (or Favre) filtering operator:

$$\phi = \frac{\overline{\rho\phi}}{\bar{\rho}} \quad (3.6.2.3)$$

The Favre Filtered Navier-Stokes equation takes the same form as equation (3.6.1.5). The compressible form of the subgrid stress tensor is defined as:

$$T_{ij} = -\rho u_i u_j - \bar{\rho} u_i u_j \quad (3.6.2.4)$$

This term is split into its isotropic and deviatoric parts

$$T_{ij} = \underbrace{T_{ij} - \frac{1}{3}T_{ll}\delta_{ij}}_{\text{deviatoric}} + \underbrace{\frac{1}{3}T_{ll}\delta_{ij}}_{\text{isotropic}} \quad (3.6.2.5)$$

The deviatoric part of the subgrid-scale stress tensor is modelled using the compressible form of the Smagorinsky model:

$$T_{ij} - \frac{1}{3}T_{ll}\delta_{ij} = 2\mu_t\left(\delta_{ij} - \frac{1}{3}\delta_{ll}\delta_{ij}\right) \quad (3.6.2.6)$$

As for incompressible flows, the term involving T_{ll} can be added to the filtered pressure or simply neglected. Indeed, this term can be rewritten as $T_{ll} = \gamma M_{sgs}^2 \bar{p}$ where M_{sgs} is the subgrid Mach number. This subgrid Mach number can be expected to be small when the turbulent Mach number of the flow is small.

However there exist numerous models for μ_t but in this thesis only two of them will be used, namely the Smagorinsky-Lilly and the dynamic Smagorinsky-Lilly models.

The subgrid-scale turbulent flux of a scalar, ϕ , is modelled using a subgrid-scale turbulent Prandtl number given by

$$q_j = -\frac{\mu_t}{\sigma_t} \frac{\partial \phi}{\partial x_j} \quad (3.6.2.7)$$

where q_j is the subgrid-scale flux.

In the dynamic models, the subgrid-scale turbulent Prandtl number or Schmidt number is obtained by applying the dynamic procedure originally proposed by Germano et al. (1996) to the subgrid-scale flux.

3.6.2.a Smagorinsky-Lilly model

This simple model was first proposed by Smagorinsky (1963). In the Smagorinsky-Lilly model, the eddy-viscosity is modelled by

$$\mu_t = \rho L_S^2 |\bar{S}| \quad (3.6.2.a.1)$$

where L_S is the mixing length for subgrid scales and $|\bar{S}| \equiv \sqrt{2\bar{S}_{ij}\bar{S}_{ij}}$. Here L_S is computed using

$$L_S = \min(K_a d, C_S \sqrt{V}) \quad (3.6.2.a.2)$$

where K_a is the von Karman constant, d is the distance to the closest wall, C_S is the Smagorinsky constant, and V is the volume of the computational cell.

Lilly derived $C_S = 0.17$ for homogenous isotropic turbulence in the inertial subrange. However, this value was found to cause excessive damping of large-scale fluctuations in the presence of mean shear and in transitional flows at near solid boundaries, and has to be reduced in such regions. In short, C_S is not an universal constant, which is the most serious shortcoming of this simple model. Nonetheless, a value of C_S around 0.1 has been found to yield good results for a wide range of flows.

3.6.2.b Dynamic Smagorinsky-Lilly model

Germano et al. (1996), and subsequently Lilly (1992), conceived a procedure in which the Smagorinsky model constant C_S is dynamically computed based on the information provided by the resolved scales of motion. Thus the dynamic procedure

prevents users to specify the model constant C_S in advance. The details of the model implementation can be found in Kim et al. (1997).

The value C_S obtained using the dynamic Smagorinsky-Lilly model varies in time and space over a fairly wide range of values. In order to avoid numerical instability, C_S is clipped at zero and is specified to be 0.23 by default.

3.6.3 Inlet boundary conditions for the LES model

The LES is applied for unsteady simulations, and there is a need to specify not only the mean flow parameters but also the unsteady components at the inlet boundaries. There exist many different methodologies to do this but only one of them is considered in this thesis, namely the Vortex Method.

3.6.3.a Vortex Method

In order to generate a time-dependent inlet condition, a random 2D vortex method is considered. With this approach, a perturbation is added to the mean velocity profile via a fluctuating vorticity field (i.e. two-dimensional in the plane normal to the streamwise direction). The vortex method is based on the Lagrangian form of the 2D evolution equation of the vorticity and the Biot-Savart law. A particle discretization is used to solve this equation. These particles, or “vortex points”, are convected randomly and they carry information about the vorticity field. If N is the number of vortex points and A is the area of the inlet section, the amount of vorticity carried by a given particle I is represented by the circulation Γ_i and an assumed spatial distribution η :

$$\Gamma_i(x, y) = \left(\frac{\pi A k(x, y)}{3N(2\ln(3) - 3\ln(2))} \right)^{\frac{1}{4}} \quad (3.6.3.a.1)$$

$$\eta(\vec{x}) = \frac{1}{2\pi\sigma^2} \left(2\exp\left(-\frac{|\vec{x}|^2}{2\sigma^2}\right) - 1 \right) \times 2\exp\left(-\frac{|\vec{x}|^2}{2\sigma^2}\right) \quad (3.6.3.a.2)$$

where k is the turbulence kinetic energy. The parameter σ provides control over the size of a vortex particle. The resulting discretization for the velocity field is given by

$$\vec{u}(\vec{x}) = \frac{1}{2\pi} \sum_{i=1}^N \Gamma_i \frac{((\vec{x}_i - \vec{x}) \times \vec{z}) \left(1 - \exp\left(-\frac{|\vec{x} - \vec{x}_i|^2}{2\sigma^2}\right) \right)}{|\vec{x} - \vec{x}_i|^2} \quad (3.6.3.a.3)$$

where \vec{z} is the unit vector in the streamwise direction. Originally, see Sergent (2002), the size of the vortex was fixed by an ad hoc of σ . To make the vortex method generally applicable, a local vortex size is specified through a turbulent mixing length hypothesis. Further σ is calculated from a known profile of the mean turbulence kinetic energy and mean dissipation rate at the inlet according to the following:

$$\sigma = \frac{ck^{1.5}}{2\epsilon} \quad (3.6.3.a.4)$$

where $c = 0.16$. To ensure that the vortex will always belong to resolved scales, the minimum value σ in equation (3.6.3.a.4) is bounded by the local grid size. The sign of the circulation of each vortex is changed randomly at each characteristic time scale τ . In the general implementation of the vortex method, this time scale represents the time necessary for a 2D vortex to be convected by the bulk velocity in the boundary normal direction to travel along n times its mean characteristic 2D size (σ_m), where m is fixed to be 100 for the numerical testing. The vortex method considers only velocity fluctuations in the plane normal to the streamwise direction.

In this thesis, a simplified linear kinematic model (LKM) for the streamwise velocity fluctuations is used, see Mathey et al. (2003). It is derived from a linear model that mimics the influence of the two-dimensional vortex in the streamwise mean velocity field. If the mean streamwise velocity U is considered as a passive scalar, the fluctuation u' resulting from the transport of U by the planar fluctuating velocity field v' is modelled by

$$u' = -v' \cdot \vec{g} \quad (3.6.3.a.5)$$

where \vec{g} is the unit vector aligned with the mean velocity gradient ∇U . When this mean velocity gradient is equal to zero, a random perturbation can be considered instead.

It should be noted that the nature of the vortex method that requires the inlet boundary to be normal to the streamwise direction.

3.6.4 How to run LES in FLUENT 12.0

There are some recommendations on how to run Large Eddy Simulations in Fluent:

- Run a steady state RANS until convergence. Save the case and data files.

- Use the `solve/initialize/init-instantaneous-vel` text command to generate the instantaneous velocity field out of the steady state RANS. This command should be executed before the LES viscosity option is switched on. This option is available for all RANS-based models and it creates a much more realistic initial field for the LES run. In addition it assists in the reduction of the time needed for the LES simulation to reach a statistically stable mode.
- Enable LES. FLUENT will automatically turn on the unsteady solver option and choose the second-order implicit formulation. The bounded central-differencing spatial discretization scheme is enabled automatically for the momentum equations.
- Run LES until the flow becomes statistically steady (for example, monitor the instantaneous pressure at the jet core). Save the case and data files.
- Initialize the statistics of the flow parameters using the `solve/initialize/init-flow-statistics` text command. Before restarting the solution, enable the Data Sampling for the Time Statistics in the Iterate panel. While this option is enabled, FLUENT will gather data for the time statistics while performing LES. The statistics collected at each sampling interval can be post-processed and we can view both the mean and the root-mean-square values of the velocity components.
- Continue until we obtain statistically stable data. The duration of the simulation can be determined beforehand by estimating the mean flow residence time in the solution domain (L/U , where L is the characteristic length of the solution domain and U is the characteristic mean flow velocity). The simulation should be run at least a few mean flow residence times.
- In order to set the appropriate number of iterations per time step (pressure-based solver) it is useful to set up a monitor reporting of the averaged property of the flow field at some surface, for example the mass flux through the radial surface at 10 nozzle diameters downstream. This parameter should reach a stable value within a number of iterations inside one time-step. The default number of iterations per time-step in FLUENT 12.0 is 20. If the stable value is not achieved within 20 iterations we should increase this number to 25, 30, etc. when necessary. Otherwise we may reduce the number to 10 or even 5 or less. The number of iterations per time-step required for a

stable solution should reduce as the calculation proceeds. However we should emphasise that it is recommended not to change the number of iterations per time-step when calculating the noise signal using FW-H model.

3.7 Conclusions

In Chapter 3 we have shown that in addition to the acoustic modelling, an essential part in the numerical simulation of aerodynamically generated noise is the flow field modelling. In general, for the flow field modelling, different numerical approaches could be applied. These approaches include the solution of the Naviers-Stokes equations for the fluid motion. In this chapter we have considered in detail two different approaches to the numerical solution of the Navier-Stokes equations, namely: the Reynolds averaged approach (RANS) and the Large Eddy Simulation approach (LES).

The nature of the RANS approach is based on the assumption that the turbulence flow field can be expressed in the form of the main mean and the smaller fluctuating components. Then, after substituting this expression into the Navier-Stokes equations, and performing the averaging procedure, we obtain the transport equations for the new turbulent parameters: the turbulent kinetic energy, k , and the turbulent dissipation rate, ϵ . First, we introduced the Standard $k - \epsilon$ turbulence model and the values of the semi-empirical constants. Then we showed the evolution of the standard model to the more sophisticated RNG $k - \epsilon$ model, and finally to the Reynolds-Stress model. The latter model is widely used in the present research for the flow field simulation of the turbulent jets as giving more information about the flow field fluctuations in the jet shear layer – major source of noise. In general, the RANS approaches are well recommended for the flow modelling in a wide variety of applications because they are reasonably fast and accurate.

Finally we have introduced the LES approach which fundamentally differs from the RANS in its nature. Instead of splitting the flow characteristics into the mean and fluctuating components in the LES we apply a filtering procedure. This procedure enables us to resolve 'directly' (i.e. by solving the exact Navier-Stokes equations) the turbulence vorticies, which are larger than the size of the filter and use the

modelling only for smaller turbulence sub-scaled structures. We have described two different approaches for the sub-grid modelling in LES. In addition, the LES approach is essentially unsteady and therefore requires careful specification of the inlet boundary conditions. We have described one of the possible solutions for the specification of the random fluctuations at the inlet boundary which is realized in FLUENT.

Chapter 4

Cold Propane Jet Simulation

4.1 Introduction

As mentioned in Chapter 1, using an acoustic analogy is a two-step procedure. In the first step, a computational fluid dynamics (CFD) analysis is used to compute the aerodynamic sources of noise. Different approaches could be used on this aspect: Direct Numerical Simulation (DNS), which gives the “real” fluid field quantities without any assumptions about the nature of turbulence, Freund (2001); Large Eddy Simulation (LES), which provides us with “real” fluid field quantities for large scale flow structures and approximated values for small scale flow structures, which, in their turn, are calculated with an assumption about the nature of turbulence in a small computational cell, Borodny and Lele (2002), Bogey et al. (2003); Reynolds Average Navier-Stokes Simulation (RANS) with a $k - \epsilon$ turbulent closure (described in detail in Chapter 3) which provides us with the mean turbulent parameters and is based on an assumption of the nature of turbulence, Ribner (1964a), Goldstein and Rosenbaum (1973), Azarpyvand and Self (2008); and some other less popular methods.

The DNS and LES approaches are the most expensive in terms of computational resources and time. Furthermore, these methods are extremely sensitive to the grid resolution. In practice, it is usually convenient to start with the less time-consuming RANS method to obtain the aerodynamic sources of noise. In addition, there is a set of acoustic formulations, which were adapted especially to RANS to predict aeroacoustic noise, such as the Ribner (1964a, b) (see Chapter 2.4) and Goldstein (1973) acoustic formulations (see Chapter 2.5).

For the present research work, the experimental data, obtained by the Sandia National Laboratory, Schefer et al. (1985, 1986, and 1987), Dibble et al. (1984, 1985, and 1987) and Gouldin et al. 1986, on a nonreacting round jet of propane into a co-flowing air has been used. The detailed measured data are summarized by

Schefer on the Sandia National Laboratory web page (<http://www.sandia.gov/TNF/DataArch/ProJet.html>) with free access. For the sake of simplicity from here we will refer to this summarized data as Schefer (1988), however the exact date of the publication of the material is unknown. It should be mentioned that the experiment has been repeated by Schefer and Dibble in 2001, Schefer and Dibble (2001), but with slightly different jet conditions (2001), for example the maximum centreline jet velocity in 1987 is $u_{max} = 69ms^{-1}$, while in 2001 it is $u_{max} = 70ms^{-1}$. Here we use the data from Schefer (1988) in order to validate the mean turbulence parameters computed using the RANS and LES simulations.

4.2 Sandia experiment data

4.2.1 Fluid flow

The fluid flow equipment is a forced-draft vertical wind tunnel with an axisymmetric fuel jet located at the upstream end of the test section. The fully-windowed test section has a 20cm square cross section and is 200cm long. The fuel nozzle has an inside diameter of 0.526cm and an outer diameter of 0.9cm. The fuel jet (bulk) velocity was $53ms^{-1}$ ($\pm 0.1ms^{-1}$) and the coflow air velocity was $9.2ms^{-1}$ ($\pm 0.1ms^{-1}$), see Figure 4.2.1.1 The test section dimensions and the inlet conditions are summarized in table 4.2.1.1. Velocity measurements at the test section inlet showed that the maximum velocity at the centreline of the jet exit of $u_{max} = 69ms^{-1}$ and this is consistent with fully-developed, turbulent pipe flow ($u_{j,max} = 1.28u_{j,bulk}$). A thin boundary layer was also measured along the outer edge of the jet pipe with a thickness of approximately 0.3 jet diameters at the exit plane of the jet, where jet diameter is 0.526cm.

The data set includes the mean axial and radial velocity components, the rms fluctuations of each velocity component, and the correlation between the axial and radial velocity. The measurements were made using a two-colour laser Doppler velocimetry (LDV) system. In the data analysis, it is assumed that the seed particles (0.85 μm diameter) follow the motion of the fluid and that the difference between the diffusivity of the particle and the fluid is negligible. Seeds were added

alternately into the jet or into the co-flowing air stream, giving different values for the velocity components of the flow.

Table 4.2.1.1 Test section dimensions and inlet conditions.

Orientation	Vertical
Test section	30cm × 30cm
Jet tube exit	0.526cm (inside nozzle diameter) and 0.9cm (outside nozzle diameter)
Length of fuel jet tube straight section	2m
Propane jet velocity	53ms ⁻¹ (±0.1ms ⁻¹)
Propane jet temperature	294K (±2K)
Coflow air velocity	9.2ms ⁻¹ (±0.1ms ⁻¹)
Coflow air temperature	294K (±2K)
Reynolds number (based on jet exit diameter)	68 000
Coflow air turbulence	0.4%
Axial pressure gradient	6Pa m ⁻¹

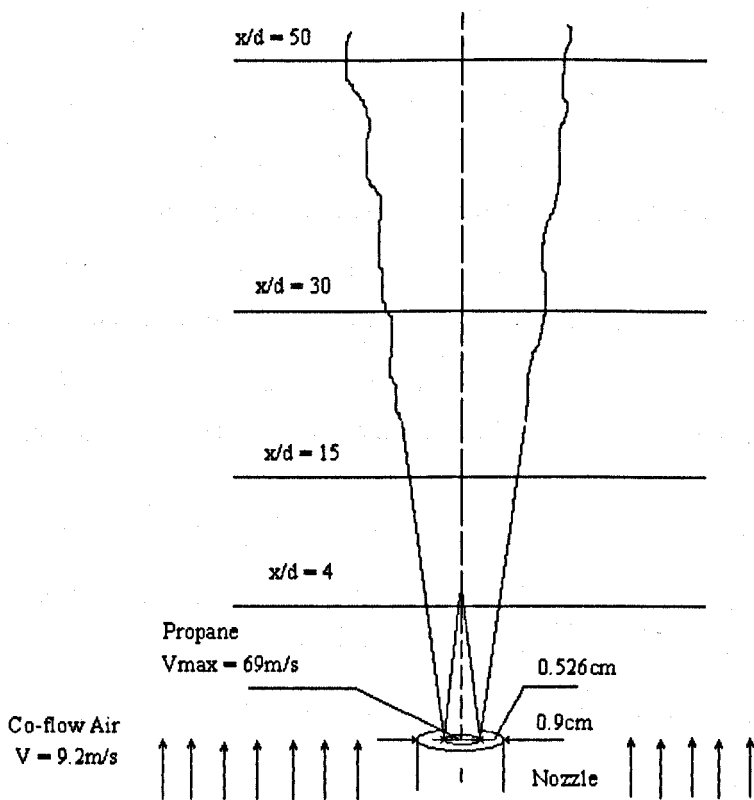


Figure 4.2.1.1 A schematic diagram of the Sandia experiment.

Velocity measurements were taken: in the radial sections at positions: $x/d = 4, 15, 30$ and 50 ; and in the axial direction along the jet axis ($y/d = 0$), as shown in figure 4.2.1.1.

4.2.2 Experimental data description

The experimental data reported by Schefer (1988) are presented in file format, and this is very useful for validation purposes since it allows us to avoid interpretation errors when converting the plots of the experimentally measured values into numbers. Figure 4.2.2.1 represents an example of the experimental measurements of the inlet radial velocity profile ($x/d = 0$), where the radial distance is normalized by the jet exit diameter, D . The growth of a thin boundary layer with a thickness of approximately 0.3 jet diameters is apparent along the outer surface of the jet tube. At increasing radial distances, the mean and fluctuating velocity rapidly approach free stream values of 9.2ms^{-1} and 0.4%, respectively. We should note that the velocity profiles at the fuel tube exit are consistent with the fully-developed turbulent pipe flow. Therefore for the numerical simulation we may employ the analytical function obtained by Prandtl (1934) for the inlet velocity profile of the jet.

4.2.3 Data consistency check

Several checks on the data were performed by Schefer (1988) to assess the accuracy of the measurements. Conservation of propane (on a mass basis) was verified by integrating the velocity and the propane mass fraction measurements across the flow field. The integrations were carried out at three axial locations $x/d = 15, 30$ and 50 and the total propane mass flux compared with the calibrated value based on the mass flow meter reading. The total propane mass flux at the jet exit was 2.3gms^{-1} , and the mass flux calculated at each axial location agreed with this value to within 5%.

In addition to the conservation of propane, momentum must also be conserved across the flow field. Integration of the total momentum at the above three axial locations was found by Sandia experimentalists to agree within 3% of the inlet value.

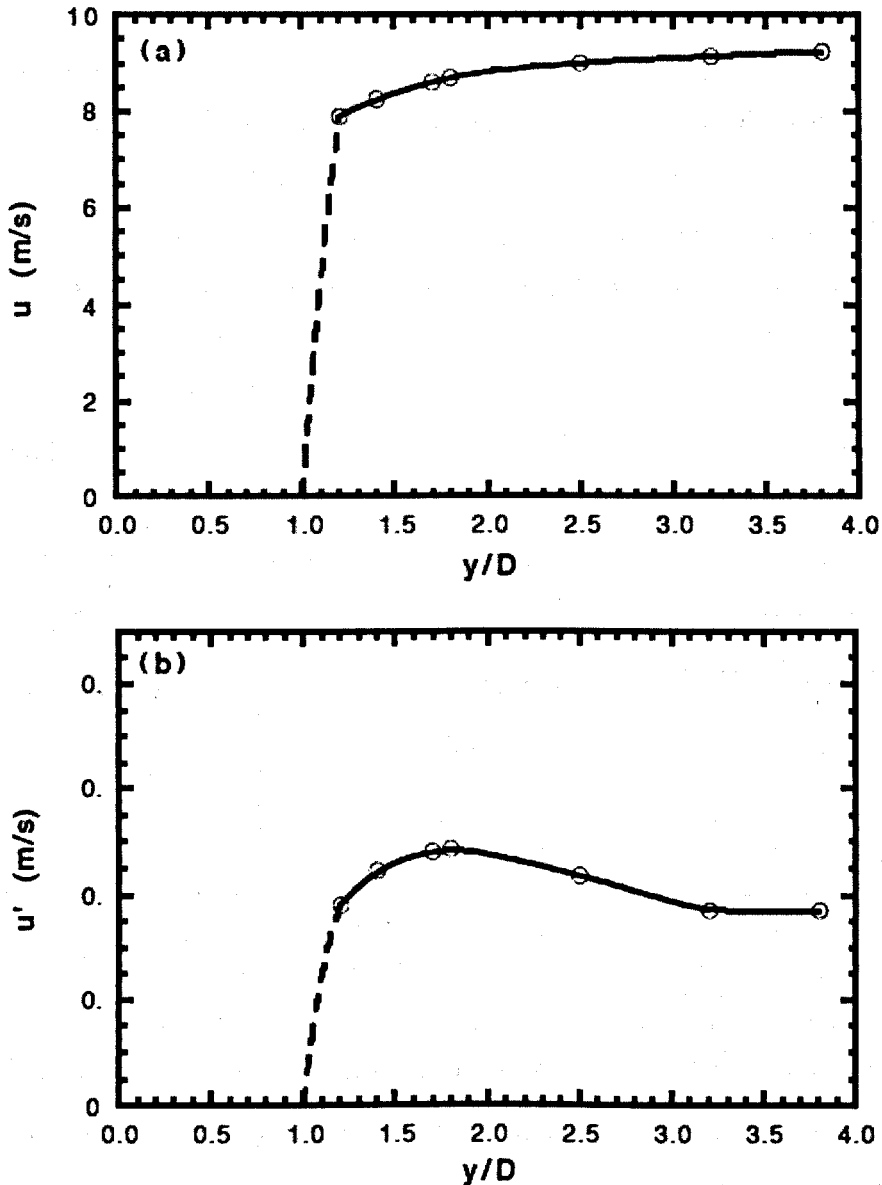


Figure 4.2.2.1 Experimentally measured by Schefer (1988) inlet profiles of the mean and fluctuating axial velocity. (a) Mean axial velocity; (b) axial velocity rms fluctuations.

As a part of the current research, a velocity flux check has been performed based on the published mean velocity data at four axial locations $x/d = 15, 30$ and 50 . Integration of the total velocity flux calculated at each axial location, where measured data are distributed between -4cm and 4cm along the y -direction, is presented in table 4.2.3.1.

Here we have two different interpolation models to estimate the velocity flux over the radial sections: the first one (IM1) is based on the assumption that the velocity profile is linear between the two close experimental points and it is a constant

beyond the available experimental data range, i.e. the velocity does not change from the last point of the available experimental data to the last point of the interval, $[-4cm$ and $4cm]$; in the second model (IM2), we assume that the velocity varies linearly between the two closest experimental points, as was assumed in the model IM1, but the velocity beyond the available experimental data range is no longer a constant. In this model the velocity changes linearly up to a certain point in the radial section, where it becomes equal to the co-flow air velocity ($9.2ms^{-1}$) and it remains constant at this value $9.2ms^{-1}$ up to the last point of the region of interest $[-4cm$ and $4cm]$.

Table 4.2.3.1 *Velocity flux over radial sections along the jet axis at four locations using two interpolation methods.*

<i>Axial Locations</i>	<i>Velocity flux using IM1</i>	<i>Velocity flux using IM2</i>
$x/d = 4$	$146.44m^{-1}s^{-1}$	$113.78m^{-1}s^{-1}$
$x/d = 15$	$132.01m^{-1}s^{-1}$	$114.757m^{-1}s^{-1}$
$x/d = 30$	$123.71m^{-1}s^{-1}$	$116.09m^{-1}s^{-1}$
$x/d = 50$	$109.65m^{-1}s^{-1}$	$105.27m^{-1}s^{-1}$

For the first interpolation model, the integration of the total velocity flux at the first three axial locations was found to agree with each other within about 15%. For the second interpolation model the agreement is much better and the accuracy is about 2%. Both interpolation models for the velocity flux over the last radial section $x/d = 50$ fails to accurately estimate the velocity flux in the interval $[-4cm$ and $4cm]$. This is due to the flatness of the velocity profile, which cannot be easily correctly estimated by using a linear function.

Since the measurements were performed in both radial sections and along the jet axis, we may compare the experimentally measured data from the intersection points of the radial sections and the axial direction. Figure 4.2.3.1 illustrates the experimental measurements of the mean axial velocity component obtained along the jet axis (black symbols) and at the axial positions of four radial sections $x/d = 4, 15, 30$ and 50 . On the left figure the seeds were added to the co-flowing air, on the right – to the jet fuel. The discrepancy in the experimentally measured values at the first radial profile is clearly seen, in case with seeds added to the jet flow in

particular. However the discrepancy in the experimentally measured values along the axis and at the radial sections further downstream is negligible.

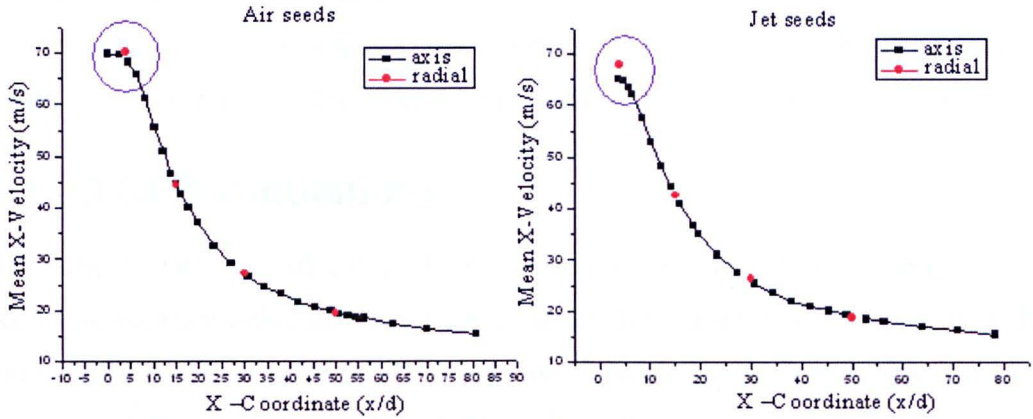


Figure 4.2.3.1 Analysis of the experimental data: experimentally measured by Schefer (1988): centreline profiles of the mean axial velocity (black symbols) and the mean axial velocity measured at the centreline points of the radial profiles $x/d = 4, 15, 30$ and 50 (red symbols).

We now compare the experimentally measured values for the velocity correlation UV . At the centre of the radial section $x/d = 4$, UV is $-0.0380m^2s^{-2}$. However when measuring the same value along the jet axis at the position $x/d = 4.7$ and $y/d = 0$ we obtain $UV = 4.9724m^2s^{-2}$. Table 4.2.3.2 summarizes the experimental data inconsistency for the velocity correlation UV .

Table 4.2.3.2 Comparison of the experimentally measured values of UV flow field component taken in radial sections and axial positions.

Experimental data UV measured at the radial sections	Experimental data UV measured along the axis
$x/d = 4, \quad y/d = 0$ $UV = -0.0380m^2s^{-2}$	$x/d = 4.7, \quad y/d = 0$ $UV = 4.9724m^2s^{-2}$
$x/d = 15, \quad y/d = 0.015$ $UV = 1.4699m^2s^{-2}$	$x/d = 15.1, \quad y/d = 0$ $UV = 6.7669m^2s^{-2}$
$x/d = 30, \quad y/d = 0$ $UV = 0.00230m^2s^{-2}$	$x/d = 30.8, \quad y/d = 0$ $UV = 1.8360m^2s^{-2}$
$x/d = 50, \quad y/d = 0$ $UV = 0.03160m^2s^{-2}$	$x/d = 50.6, \quad y/d = 0$ $UV = 0.2474m^2s^{-2}$

We should keep in mind the inconsistency of the experimentally measured values at the $x/d = 4$ radial profile when analyzing the CFD simulation results. Moreover, it is possible that we may not rely on the experimental measurements obtain from the first radial section. Therefore we concentrate our comparisons on the experimental values obtained at $x/d = 15, 30$ and 50 for validation of our simulation results.

4.3 2D CFD simulations

The natural symmetry of the problem allows us to consider a two-dimensional axisymmetric flow rather than having to consider the full three-dimensional flow. In addition we can divide the problem into two separate parts: flow in the tube and flow in the free jet. These simplifications assist us in saving computational resources and time. In general, to start the computational modelling we need to first create a grid. In the following section we describe the grids employed in the current research.

Three different grids have been employed for the computational simulation of a propane jet: one grid to simulate the flow in the pipe and two grids to simulate the flow in the jet with different inlet conditions.

4.3.1. Grid employed to simulate the flow in the pipe

According to the Sandia experimental description, the tube was $2m$ long. However it is not necessary to make a computational model for such a long pipe because the flow becomes fully developed after $25d-40d$ downstream, Nikuradse (1937). Therefore in the current work a $1m$ tube ($0.263cm \times 100cm$) – much longer than required $40d$ – has been used rather than of a $2m$ long tube. However further resolution of the grid is not important for this simulation we have used rather fine grid with a total number of nodes in the 2D of 73500, where 49 nodes are equally distributed over the inlet edge of the tube and 1500 nodes are equally distributed along the wall of the tube. The estimated value of y^+ for this mesh is less than 1 – this means that the boundary layer is well resolver by the mesh.

4.3.2 Grid employed to simulate the free jet flow

The test section dimensions are known from the Sandia experiment, see table 4.2.1.1. As we are modelling an axisymmetric flow then only half of the domain is required, i.e. the maximum grid size in the y -direction (x -direction is chosen along

the axis of the jet and the y direction is perpendicular to the axis) should be 15cm from the axis. The maximum grid size in the x -direction is determined by the experimental data available at the radial section at a distance $x/d = 50$, consequently the x_{max} is 43cm . In addition, the grid was extended in the x -direction by 2.7cm along the nozzle in order to allow the air injection into the stream. It should be noted that the number of nodes along the nozzle radius must be equal to the number determined for the flow in the pipe. This is important since we use the velocity profile obtained from the tube as the inlet condition for the jet. The full grid dimensions are illustrated in figure 4.3.2.1.

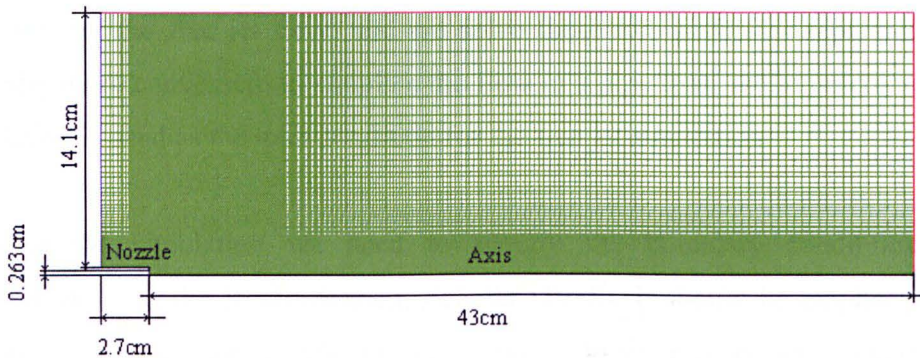


Figure 4.3.2.1 Jet grid dimensions and structure.

In order to study the effect of the mesh resolution on the numerical solution, two grids were created with a different total number of nodes: N_1 and N_2 (where $N_2 \approx 1.5N_1$). For the second grid we increase the number of nodes along the axis of the domain and accordingly change the successive ratio in order to connect smoothly the partitions of the grid. The details of both grids are listed in tables 4.3.2.1 and 4.3.2.2.

Table 4.3.2.1 Details of the Grid N_1 .

N_1 , 64800 nodes	Dimensions	Number of nodes	Node distribution (Successive ratio)
Nozzle radius	0.263cm	49	1
Nozzle length	2.7cm	40	0.9
Nozzle edge	0.187cm	25	1
Air inlet	14.1cm	80	0.945
Free flow domain	43cm	400	0.988

Table 4.3.2.1 Details of the Grid N_2 .

N_2 , 95600 nodes	Dimensions	Number of nodes	Node distribution (Successive ratio)
Nozzle radius	0.263cm	49	1
Nozzle length	2.7cm	40	0.9
Nozzle edge	0.187cm	25	1
Air inlet	14.1cm	80	0.945
Free flow domain	43cm	600	0.992

4.4 2D simulation of the flow in the pipe

As we have discussed in Section 4.2, the problem is divided into two parts: flow in the pipe and the free jet flow, and we solve these two problems separately. It is naturally more convenient to simulate the flow in a pipe first, as the outcome of this simulation is used as the inlet condition for the free jet simulation.

To start the simulation we need to specify the boundary conditions using information from the Sandia Report, Schefer (1988). It should be emphasised that information concerning the inlet propane velocity to the pipe is not an exact value, but rather an approximate value, since no direct measurement of the inlet velocity was performed during the experimental investigation. However, there is no extra information available, and we need to make an assumption on the inlet boundary condition. Therefore the inlet condition is assumed to be a flat velocity profile with a value of 53ms^{-1} , as specified in the Sandia Report, Schefer (1988).

We are interested in obtaining the maximum velocity value, 69ms^{-1} , according to the data from the experiment by Schefer (1988). Moreover we can validate the simulation results with a theoretical prediction for the velocity profile of fully turbulent flow in a pipe, obtained by Prandtl (1934):

$$\frac{U}{U_{max}} = \left(1 - \frac{y}{0.5d}\right)^{\frac{1}{7}} \quad (4.4.1)$$

where d is the diameter of the pipe, U_{max} is the maximum velocity at the outlet of the pipe, U is the current velocity and y is the current location.

It is important to specify the key parameters which make the main influence on the CFD simulation results:

- (a) the inlet velocity,
- (b) the model of the turbulence,
- (c) the roughness of the wall,
- (d) the density law.

In order to evaluate the influence of each of these parameters we need to consider different combinations of those parameters for situations.

4.4.1 Study of the effect of different turbulence models

The case C_1 is created to study the effect of different turbulence models (parameter) for the incompressible flow in the pipe with a flat velocity profile as the inlet boundary condition. The details of the case C_1 are listed in table 4.4.1.1. Four simulations have been performed using four different turbulence models:

- The Standard $k - \epsilon$ model
- The RNG $k - \epsilon$ model
- The Realizable $k - \epsilon$ model
- The Reynolds Stress model

The resulting maximum axial velocity detected at the outlet of the pipe is reported in table 4.4.1.2 for the grid N_1 and four RANS turbulent modifications employed for the simulation. The aim of these simulations is to obtain a reasonable velocity profile at the outlet from the pipe. We have a validation parameter, namely the maximum velocity $69ms^{-1}$, as measured experimentally. Varying the main parameters (turbulence model, density law, roughness of the wall, velocity inlet) we have attempted to obtain the numerical result to be as close as possible to the experimental data. The effect of varying the turbulence model is presented in table 4.4.1.2 and in the first column of table 4.4.5.1 We may observe the maximum velocity value being more than 10% underpredicted for all the turbulence models investigated (compared to the desirable maximum jet core outlet velocity of $69ms^{-1}$). The accuracy of the experimental study of Schefer (1988) is stated to be $\pm 0.1ms^{-1}$, therefore we present our simulation results with the same level of accuracy.

Table 4.4.1.1 *Simulation details for the case C₁*

Material	Propane with constant density
Turbulence model	Parameter
Velocity inlet	Flat velocity profile 53ms^{-1} $T = 294\text{K}$ Turbulence intensity: 4% Hydraulic diameter: 0.263cm
Tube walls	Adiabatic, no roughness effects
Outlet	Pressure outlet = P_{atm} , $T = 294\text{K}$ Back flow: Turbulence intensity: 10% Hydraulic diameter: 0.263cm
Solver	Axisymmetric, Pressure Based, Implicit, Steady

Table 4.4.1.2 *The maximum axial velocity at the outlet of the pipe obtained in the CFD simulations using different modifications of RANS.*

Turbulence model	Case C ₁ ($\rho = \text{const}$)
Standard $k - \epsilon$	61.9
RNG $k - \epsilon$	62.6
Realizable $k - \epsilon$	62.6
Reynolds stress	61.9

4.4.2 Study of the effect of the density law

The next important parameter of interest is the gas density law. Once the material characteristics of the propane are changed from being of constant density to the ideal gas-law, the inlet conditions should be changed as well. The formulation of the ideal gas law:

$$pV = nRT \quad (4.4.2.1)$$

where p is the absolute pressure of the gas, V is the volume of the gas, n is the number of moles of the gas, R is the gas constant and is equal to $8.314 \frac{\text{J}}{\text{Kmol}}$, and finally, T is the absolute temperature.

Due to the solver requirements of FLUENT 12.0, the velocity inlet should be replaced by the mass flux as the inlet boundary condition when using the ideal gas

law for the density. The mass flux is calculated as the product of the velocity of the flow times the density of the flow, $mass\ flux = U \times \rho$. For a given velocity, $53ms^{-1}$, and density of the propane, $\rho_{(C_3H_8)} = 1.91kgm^{-3}$, we have a mass flux of $101.23kgm^{-2}s^{-1}$. The case C_2 was created to study the effect of the density law on the results obtained from the numerical simulations for the different turbulence models. The full details of this case C_2 are listed in table 4.4.2.1:

Table 4.4.2.1 Simulation details for the case C_2

Material	Propane, ideal gas law
Turbulence model	Parameter
Mass flux inlet	Flat profile $1.91 \frac{kg}{m^3} \times 53 \frac{m}{s} = 101.23 \frac{kg}{sm^2}$ $T = 294K$ Turbulence intensity: 4% Hydraulic diameter: 0.263cm
Tube walls	Adiabatic, no roughness effects
Outlet	Pressure outlet = P_{atm} , $T = 294K$ Back flow: Turbulence intensity: 10% Hydraulic diameter: 0.263cm
Solver	Axisymmetric, Pressure Based, Implicit, Steady

We employ the same list of turbulence models as was specified for the case C_1 . The resulting maximum axial velocity detected at the outlet of the pipe is reported in table 4.4.2.2 (and in the second column of table 4.4.5.1) for the grid N_1 and four RANS turbulent modifications employed for the simulation. We observe that the maximum velocity value is again underpredicted, but the values are closer to the experimentally measured data. The Reynolds Stress model gives the best agreement with the experimental data, but it still underpredicts the maximum velocity value by about 4%.

Table 4.4.2.2 The maximum axial velocity at the outlet of the pipe obtained in the CFD simulations using different modifications of RANS.

Turbulence model	Case $C_2(\rho = \text{ideal gas})$
Standard $k - \epsilon$	65.2
RNG $k - \epsilon$	65.5
Realizable $k - \epsilon$	65.2
Reynolds stress	66.0

4.4.3 Study of the effect of the roughness of the wall

The effect of the roughness of the wall could have an influence on the resulting velocity profile. A general recommendation for the roughness height parameter is that it should be, at least, half the height of the cell closest to the wall surface. For the current grid this value should be less than 0.00263cm . Thus for the current research the roughness height is chosen to be $h_1 = 0.0025\text{cm}$ and $h_2 = 0.001\text{cm}$. The details of this case C_3 are listed in table 4.4.3.1.

Table 4.4.3.1 Simulation details for case C_3

Material	Propane, ideal gas law
Turbulence model	Parameter
Mass flux inlet	Flat profile $1.91 \frac{\text{kg}}{\text{m}^3} \times 53 \frac{\text{m}}{\text{s}} = 101.23 \frac{\text{kg}}{\text{sm}^2}$ $T = 294\text{K}$ Turbulence intensity: 4% Hydraulic diameter: 0.263cm
Tube walls	Adiabatic, Roughness height: $h_1 = 0.0025\text{cm}$ and $h_2 = 0.001\text{cm}$
Outlet	Pressure outlet = P_{atm} , $T = 294\text{K}$ Back flow: Turbulence intensity: 10% Hydraulic diameter: 0.263cm
Solver	Axisymmetric, Pressure Based, Implicit, Steady

We employ the same list of turbulence models as was specified for the case C_1 . The effects of varying the roughness of the wall ($h_1 = 0.0025\text{cm}$, $h_2 = 0.001\text{cm}$) are

presented in table 4.4.3.2 and in the third and fourth columns of table 4.4.5.1, respectively. It is observed that the maximum velocity value is in better agreement with the experimental data than in the previous situations investigated for all the turbulence models. Hence the Reynolds Stress turbulence model overpredicts the maximum velocity value by about 3% when $h_1 = 0.0025\text{cm}$ and by about 0.3% when $h_2 = 0.001\text{cm}$. The last simulation result, obtained from the case C_3 using the Reynolds Stress model, will be considered as the base result for the simulation of the free stream jet, as it gives the best agreement with the experimental data compared to the other situations.

Table 4.4.3.2 *The maximum axial velocity at the outlet of the pipe obtained in the CFD simulations using different modifications of RANS.*

Turbulence model	Case $C_3(h_1 = 0.0025\text{cm})$	Case $C_3(h_2 = 0.001\text{cm})$
Standard $k - \epsilon$	66.0	64.9
RNG $k - \epsilon$	66.5	65.8
Realizable $k - \epsilon$	66.5	65.7
Reynolds stress	71.3	69.1

4.4.4 Study of the effect of the inlet velocity

In order to improve the previous results, we may increase the inlet velocity value up to 53.1ms^{-1} , as it is determined experimentally within $\pm 0.1\text{ms}^{-1}$. Since the ideal gas law is considered, the velocity inlet should be recalculated in terms of the mass flux rate. For a given inlet velocity, 53.1ms^{-1} , and the density of the propane gas, $\rho_{(C_3H_8)} = 1.91\text{kgm}^{-3}$, we have a mass flux of $101.421\text{kgm}^{-2}\text{s}^{-1}$. For the current simulation we choose the roughness of the wall height to be $h_2 = 0.001\text{cm}$ as we determined in section 4.4.3. The details of this case C_4 are listed in table 4.4.4.1.

We employ the same list of turbulence models as was specified for the case C_1 . The effect of varying the inlet velocity is presented in table 4.4.4.2 and in the fifth column of table 4.4.5.1. It is observed that the simulated maximum velocity value is increased by about 0.2% and this agrees with the increase in the inlet velocity by 0.2% at the inlet boundary condition. The Standard, RNG and Realizable $k - \epsilon$ turbulence models underpredict the maximum velocity value, while the Reynolds Stress model overpredicts the maximum velocity value by about 3.5%.

Table 3.4.4.1 *Simulation details for case C₄*

Material	Propane, ideal gas law
Turbulence model	Varied
Mass flux inlet	Flat profile $1.91 \frac{kg}{m^3} \times 53.1 \frac{m}{s} = 101.421 \frac{kg}{sm^2}$ $T = 294K$ Turbulence intensity: 4% Hydraulic diameter: 0.263cm
Tube walls	Adiabatic, Roughness height: $h_2 = 0.001cm$
Outlet	Pressure outlet = P_{atm} , $T = 294K$ Back flow: Turbulence intensity: 10% Hydraulic diameter: 0.263cm
Solver	Axisymmetric, Pressure Based, Implicit, Steady

Table 4.4.4.2 *The maximum axial velocity at the outlet of the pipe obtained in the CFD simulations using different modifications of RANS.*

Turbulence model	Case C ₄ ($U = 53.1ms^{-1}$)
Standard $k - \epsilon$	66.1
RNG $k - \epsilon$	66.6
Realizable $k - \epsilon$	66.6
Reynolds stress	71.5

4.4.5 Summary of the results of the simulation flow in a pipe

From the summary table 4.4.5.1 of the simulation results we observe that in the Case C₃, where the density is considered as being not constant but obeys the ideal gas law (3.4.2.1), the effect of the roughness of the wall is included with a roughness height parameter, $h = 0.001cm$, and the turbulence model is the Reynolds stress model, then the validation parameter (maximum velocity value) is in the best agreement with the experimental data ($69ms^{-1}$) compared to all the other cases investigated.

Finally, we can compare the shape of the velocity profile obtained from the CFD simulations with the theoretical prediction from the Prandtl theory, Tietjens (1934), on the flow in a tube. Let us determine the maximum velocity value, $U_{max} = 69\text{ms}^{-1}$, as was obtained in the experimental investigation, in the formula for the Prandtl velocity profile described by equation (4.4.2.1) and compare with the results obtained in case C_3 ($h = 0.001\text{cm}$).

Table 4.4.5.1 The maximum axial velocity value at the outlet from the tube 1m long. Results are presented for four different turbulence models and cases C_1, C_2, C_3, C_4 .

Turbulence model	Case C_1 ($\rho = \text{const}$)	Case C_2 ($\rho =$ <i>ideal gas</i>)	Case C_3 ($h_1 =$ 0.0025cm)	Case C_3 ($h_2 =$ 0.001cm)	Case C_4 ($U =$ 53.1ms^{-1})
Standard $k - \epsilon$	61.9	65.2	66	64.9	66.1
RNG $k - \epsilon$	62.6	65.5	66.5	65.8	66.6
Realizable $k - \epsilon$	62.6	65.1	66.5	65.7	66.6
Reynolds stress	61.9	66.0	71.3	69.1	71.4

The Prandtl velocity profile is plotted in figure 4.4.5.1 by the dashed line and the results of the simulations by the solid line, where the velocity values are plotted at every tenth point of the computational grid. It is observed that, in general, there is a good agreement between the shapes of the velocity profile obtained from the numerical simulation and that predicted theoretically by Prandtl (1934). A small discrepancy between the two curves appears only near to the nozzle wall, where the exact roughness of the wall parameter is unknown. Therefore both profiles will be used in Section 4.5 as the inlet condition for the jet simulations.

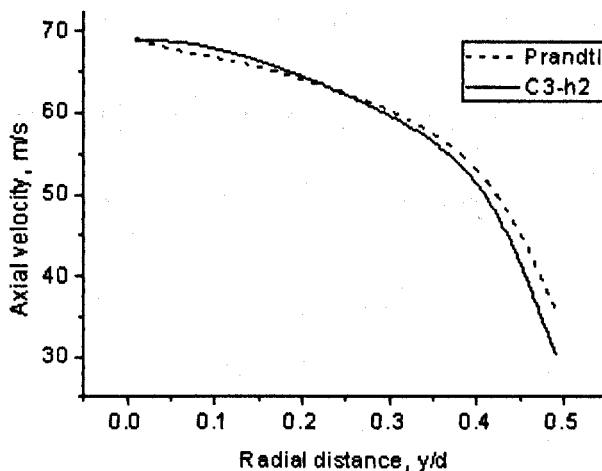


Figure 4.4.5.1 *Comparison of the turbulent velocity profile in the tube between Prandtl theory and CFD simulations.*

4.4.6 Intermediate conclusions

It has been shown in this section that it is possible to simulate the velocity profile for the flow in a pipe using a simple 2D axisymmetrical grid and the RSM turbulence model. The results of the simulation are in good agreement with the available experimental data and also with the theoretical predictions. The velocity profile, obtained from the simulation can be used as an inlet boundary condition for the simulation flows in the propane jet.

4.5 2D simulations for a free jet

In Section 4.3 we described two grids which are used for the jet flow simulations: the grid N_1 , consisting of 64 800 nodes, and the grid N_2 , of 95 600 nodes. Full details of the two grids are summarized in tables 4.3.2.1 and 4.3.2.2, respectively. These grids have similar geometrical dimensions, but different mesh resolutions in order to study the effect of grid dependency on the results obtained from the CFD simulations.

In this case there is more experimental data available for validation than there was in the pipe flow case. In particular the averaged velocity components, rms fluctuations of each velocity component and the mixture mass fractions at radial sections at four different locations $x/d = 4, 15, 30$ and 50 , and along the axis of the jet $y/d = 0$. The aim of this part of the research is to obtain the velocity field for a free jet flow using CFD simulations. The influence of the different parameters in the CFD model are studied to obtain the best agreement with the experimental data.

4.5.1 Essential parameters for the jet simulation

The following lists the CFD model parameters that are assumed to have the most influence on the computational predictions:

- The inlet velocity profile
- The density law
- The turbulence model
- The turbulence specification method

- The grid resolution

In order to validate the jet flow simulation results, the Schefer (1988) measurements of the mean velocity and propane mass fraction were employed. The initial velocity profile for a jet flow is unknown from the experiment and therefore it has to be modelled. The details of the simulations performed are summarised in table 4.5.4.1.

4.5.2 Jet inlet profile specification

Three different initial velocity profiles for the jet have been applied to the simulations, namely: the flat velocity profile, the fully developed turbulent velocity profile, obtained from the simulation of the flow in the tube and the theoretical prediction for the velocity profile of a turbulent flow in a tube, derived by Prandtl, see equation (4.4.1). Here the Prandtl (1934) velocity profile is defined as:

$$\frac{U}{U_{max}} = \left(1 - \frac{y}{0.5 \cdot d}\right)^{\frac{1}{7}} \quad (4.5.1)$$

where $d = 0.526\text{cm} = 0.00526\text{m}$ is the diameter of the pipe, $U_{max} = 69\text{ms}^{-1}$, is the maximum velocity at the outlet of the pipe, and U is the current velocity and y is the current radial location. The following is a code illustrating the realisation in FLUENT using a simple UDF function:

```
#include "udf.h"
DEFINE_PROFILE(inlet_x_MasFlux, thread, index)
{
    real coord[ND_ND];          /* this will hold the
                                position vector */
    real y;
    face_t f;

    begin_f_loop(f, thread) /* loops over all faces in the thread
                              passed in the macro argument */
    {
        F_CENTROID(coord, f, thread);
        y = coord[1];

        F_PROFILE(f, thread, index) =
            131.79*pow(1-y/(0.00263), 1/7);
    }
    end_f_loop(f, thread)
}
```

Fluent always operates in Cartesian coordinates and we use the same approach, since a two-dimensional problem is being considered. It should be noted that the jet axis is directed along the x -axis, and therefore the inlet is in the y -direction, perpendicular to the jet axis. The Prandtl equation (4.5.1) is valid for the inlet velocity, however we employ the mass flux of the flow at the inlet. Therefore in order to translate the expression (4.5.1) in terms of mass flux we simply multiply both U and U_{max} by the propane density, $\rho_{(C_3H_8)} = 1.91 \text{ kg m}^{-3}$. From this we obtain the maximum inlet mass flux to be $131.79 \text{ kg s}^{-1} \text{ m}^{-2}$.

The calculation process loops across each node of the given surface f . The exact surface is linked later in FLUENT manually. In fact this UDF function could be applied to any surface. However we are interested in profiling the jet inlet mass flux. Therefore after the code is interpreted in FLUENT we need to choose the UDF option only on the jet inlet boundary condition panel. When the executed program reads the coordinates of each node from the array `coord [0,1,2]`, specified as the real number array "real coord[ND_ND]" at the beginning, where ND_ND means that the dimensions of the massive is defined automatically, depending on the FLUENT solver dimensions (2D or 3D). Therefore the x coordinate corresponds to first element of the array, labelled as "0", $x = \text{coord}[0]$, the y coordinate corresponds to the second element, labelled as "1", $y = \text{coord}[1]$, and the z coordinates corresponds to the third element, labelled as "2", $z = \text{coord}[2]$. The current code uses only two variables, x and y , and calculates the value of the mass flux at the centre the node, using the Prandtl expression (4.5.1). The same procedure is refitted for each node of the surface f .

4.5.3 The choice of the turbulence model

It should be mentioned that different RANS turbulence models have been studied during this research, but it appears not to be appropriate to include all the results of simulations in this thesis. This is because it was found that the RANS models give rather poor predictions for the jet velocity distribution at the radial sections, not presented here, for the results obtained at the radial section at $x/d = 4$. However, the Reynolds Stress turbulent model (RSM) was found to be the most appropriate model for the propane jet simulations, because it simulates jet diffusion (a product of the shear stress effects) better than do the RANS models. Therefore, only the

results obtained using the Reynolds Stress turbulent model are presented in this Chapter.

4.5.4 Details of the simulation

Table 4.5.4.1 Model details for the simulation of the jet flow.

Material	Mixture: propane-air, ideal gas law
Turbulence model	Reynolds Stress
Propane inlet, Mass flux ($U_j\rho$)	Flat profile $1.91 \frac{kg}{m^3} \times 69 \frac{m}{s} = 131.79 \frac{kg}{sm^2}$ or Prandtl profile or the profile, obtained from the tube $T = 294K$ Turbulence intensity: 4% Hydraulic diameter: 0.263cm
Air inlet, Mass flux ($U_j\rho$)	Flat profile $1.225 \frac{kg}{m^3} \times 9.2 \frac{m}{s} = 11.27 \frac{kg}{sm^2}$ $T = 294K$ Turbulence intensity: 0.4% Hydraulic diameter: 14.55cm
Outlet	Pressure outlet = P_{atm} , $T = 294K$ Back flow: Turbulence intensity: 10% Hydraulic diameter: 15cm
Solver	Axisymmetric, Pressure Based, Implicit, Steady

4.5.5 Velocity field simulation results

The simulation results, compared against the Schefer (1988) measurements for the mean axial velocity component (\overline{U}), rms fluctuating velocity components ($\sqrt{u'^2}, \sqrt{v'^2}$) and their correlations ($\overline{u'v'}$) are presented in figures 4.5.5.2-5, respectively. The agreement between the velocity measurements and the numerical predictions is good for all the inlet velocity profiles investigated. A significant underproduction for the velocity correlation is observed along the axis, see figure

4.5.5.5(e). This discrepancy could be explained by the experimental data inconsistency, as discussed in Section 4.2.3.

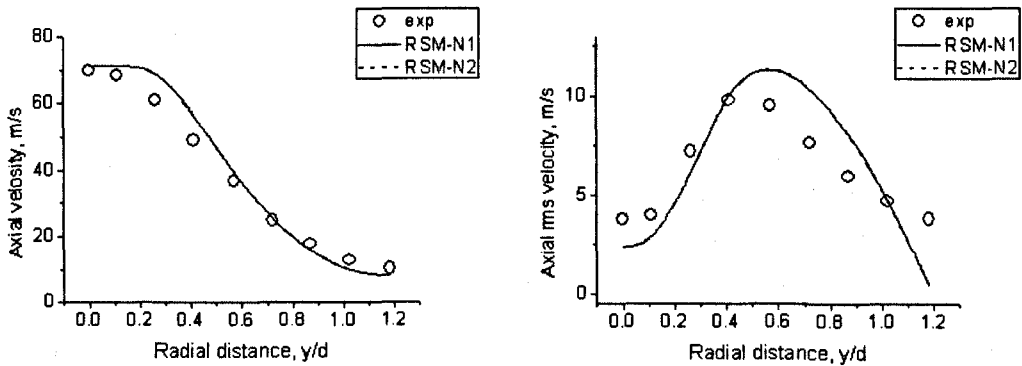
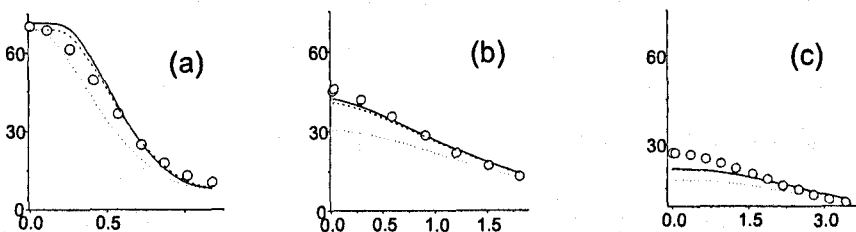


Figure 4.5.5.1. Mean and fluctuating axial velocity component profiles at $x/d = 4$; symbols, experimental data; solid line, simulation predictions using the grid N_1 ; dashed line, simulation predictions using the grid N_2 , both with the Prandtl velocity profile as the inlet condition and RSM turbulent model employed.

The simulation results for the mean mass fraction of propane, compared against the experimental data, are given in figure 4.5.5.6. It is observed that in general there is good agreement between the CFD predictions and the experimental data. In particular, the jet flow simulations with the inlet velocity profile, obtained from the tube, reproduce better results in the initial region of the jet (see plots (a) and (e) in figures 4.5.5.2-6), than the cases with the flat or the Prandtl velocity profile. However a further development of the jet flow is better predicted with the flat or the Prandtl velocity profile, than with a velocity profile obtained from the tube, see plots (b, c, d, e) in figures 4.5.5.2-6.



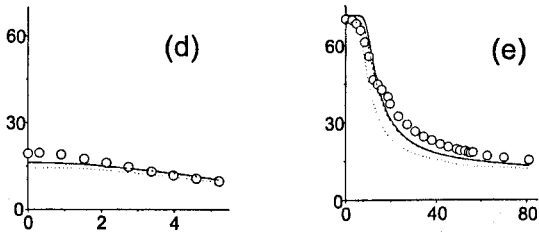


Figure 4.5.5.2 Radial profiles of the mean axial velocity component, \bar{U} , in the jet studied by Schefer (1988), (a), (b), (c) and (d) at $x/d = 4, 15, 30$ and 50 , respectively, and (e) along the axis.*

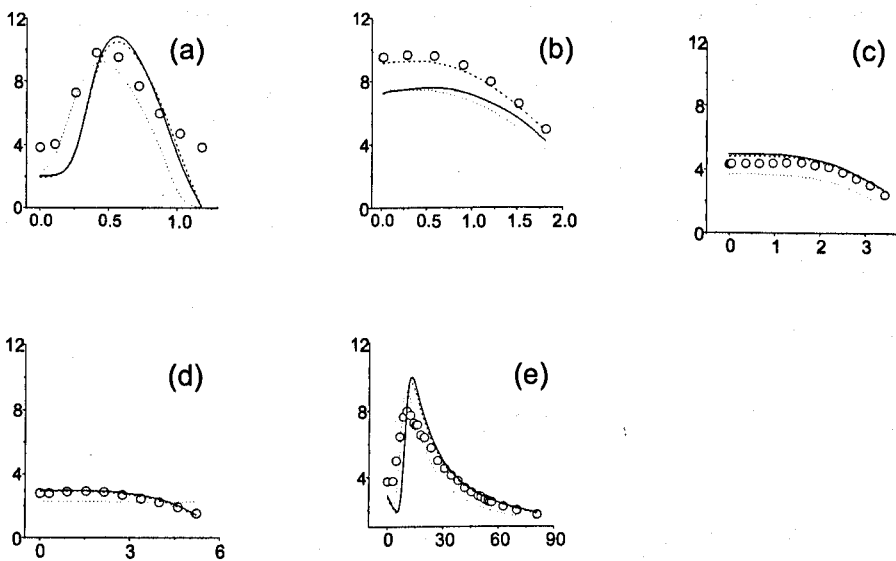
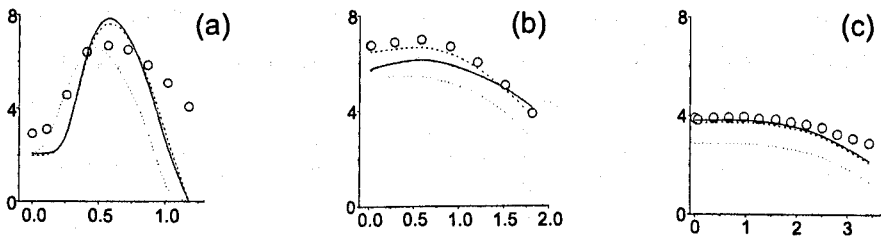


Figure 4.5.5.3 Radial profiles of the rms of the axial velocity, $\sqrt{u'^2}$, for the jet studied by Schefer (1988), (a), (b), (c) and (d) at $x/d = 4, 15, 30$ and 50 , respectively, and (e) along the axis.*



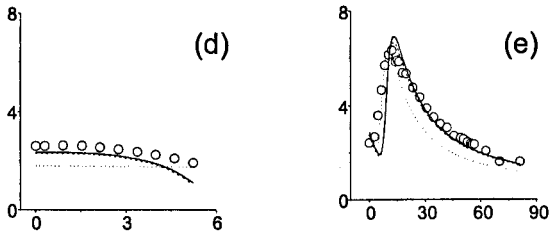


Figure 4.5.5.4 Radial profiles of the rms of the radial velocity component, $\sqrt{v'^2}$, for the jet studied by Schefer (1988), (a), (b), (c) and (d) at $x/d = 4, 15, 30$ and 50 , respectively, and (e) along the axis.*

*Legend: the symbols are experimental data; the solid lines are the simulation results with a flat velocity profile at the inlet; the dashed lines are the simulation results with a Prandtl velocity profile at the inlet; the dotted lines are the simulation results with the profile as obtained from the tube in Section 4.4

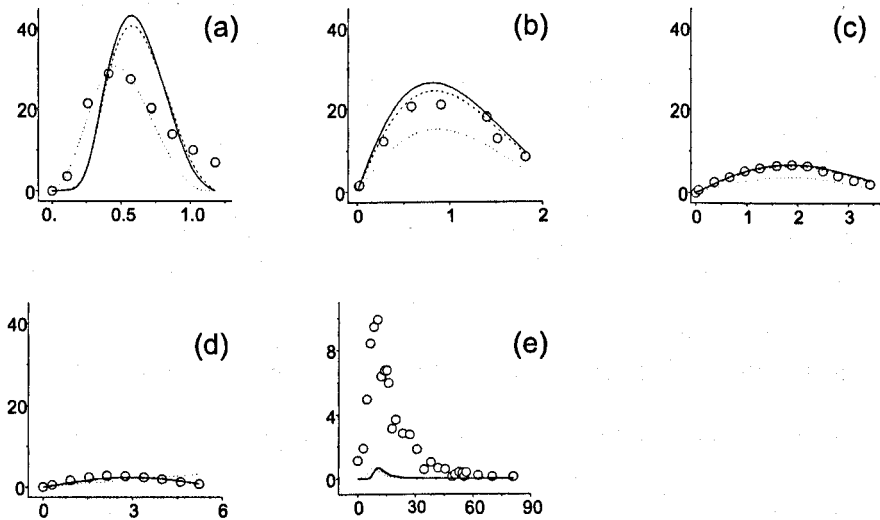
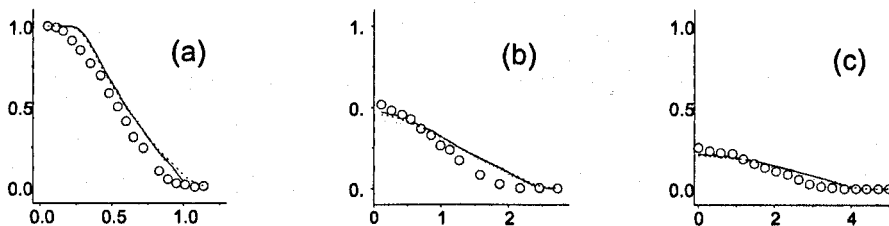


Figure 4.5.5.5 Radial profiles of the velocity correlation, $\overline{u'v'}$, for the jet studied by Schefer (1988), (a), (b), (c) and (d) at $x/d = 4, 15, 30$ and 50 , respectively, and (e) along the axis.*



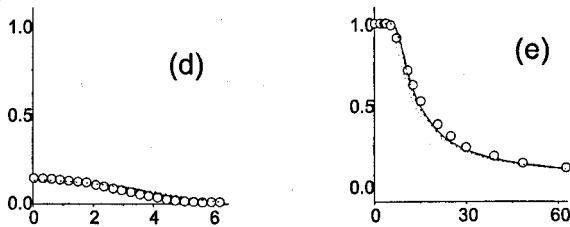


Figure 4.5.5.6 Radial profiles of mean mixture fraction, \bar{f} , for the jet studied by Schefer (1988) (a), (b), (c) and (d) at $x/d = 4, 15, 30$ and 50 , respectively, and (e) along the axis.*

*Legend: the symbols are experimental data; the solid lines are the simulation results with a flat velocity profile at the inlet; the dashed lines are the simulation results with a Prandtl velocity profile at the inlet; the dotted lines are the simulation results with the profile as obtained from the tube in Section 4.4

Possibly, this is because the jet flow in the experimental investigation was not a fully developed turbulent flow. The shear layer develops not as fast as expected for a fully developed turbulent flow. However, the agreement with the experimental data is good and this indicates that the CFD code is capable of modelling the main physical characteristics of the fluid flow correctly. Therefore the simulation results may be considered to be reliable and used as a basis for the noise predictions.

In addition we should mention that the effect of the grid resolution was found to be negligible, figure 4.5.5.1. This could be explained by very good resolution of the first grid, N_1 , consisting of 64 800 nodes, so that the finer grid N_2 , 95 600 nodes, does not produce the improved solution. The results reported in this section are for the grid N_1 .

4.5.6 Intermediate conclusions

It has been shown in this section that it is possible to simulate the jet flow using a simple 2D axisymmetrical grid and the RSM turbulence model. The results of the simulation are in good agreement with the available experimental data. The influence of the velocity inlet profile of the predicted results is found to be insignificant. The simulation results are found to be sufficiently reliable to be used as a basis for the noise predictions.

4.6 2D acoustics

The broadband noise model, namely the Goldstein jet noise model, Goldstein and Rosenbaum (1973), based on the mean turbulence characteristics of the flow, is employed to calculate an approximate measure of the radiated noise at the source location, see Chapter 2.5 for a description of the model.

4.6.1 Acoustic results obtained when the initial velocity profile is varied

The jet acoustic power level, in dB, measured along the jet axis compared for three different inlet velocity profiles are presented in figure 4.6.1.1.

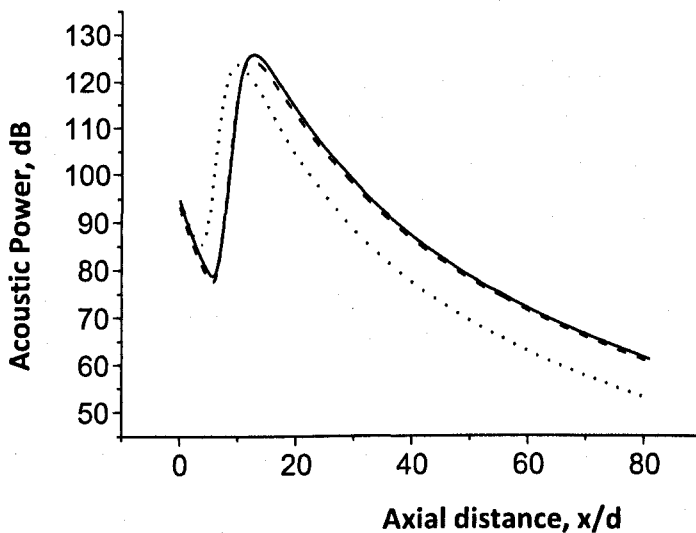


Figure 4.6.1.1 The jet acoustic power level (dB) predictions along the axis of the jet. The symbols are experimental data; the solid lines are the simulation results with a flat velocity profile at the inlet; the dashed lines are the simulation results with a Prandtl velocity profile at the inlet; the dotted lines are the simulation results with the profile as obtained from the tube in section 4.4.

The influence of the initial velocity profile on the maximum noise level generated by the jet is found to be very small, but there is a shift in the noise power peak between the results obtained using the inlet velocity profile obtained from the tube simulation and the results obtained using the Prandtl inlet velocity profile and the flat inlet velocity profile. The shift in the maximum noise level indicates that the mixing layer, which makes the most contribution to the total jet noise generation, develops faster in the case with the inlet velocity profile obtained from the tube,

rather than in the case where the inlet velocity profile is defined as flat or the Prandtl function.

4.6.2 Acoustic results obtained when the co-flow velocity is varied

In Chapter 2.5 we have described the acoustical model, namely Goldstein model, which is incorporated in the FLUENT 12.0 solver. We have described the theoretical basis of the Goldstein approach and the limitations of the realization of this model in FLUENT. Here we rewrite the basic equations of the Goldstein's acoustic model, Goldstein and Rosenbaum (1973). The total noise generated by a jet is defined as the sum of the two components:

$$I((x, \theta), \vec{y}) = I^{Se.N.}((x, \theta), \vec{y}) + I^{Sh.N.}((x, \theta), \vec{y}) \quad (4.6.2.1)$$

$$I^{Se.N.}((x, \theta), \vec{y}) = \frac{12\rho_0 L_1 L_2^2}{5\pi c_0^5 x^2} \overline{u_{t1}^2} \omega_f^4 \frac{D_i^{Se.N.}}{C^5} \quad (4.6.2.2)$$

$$I^{Sh.N.}((x, \theta), \vec{y}) = \frac{24\rho_0 L_1^4 \overline{u_{t1}^2}}{\pi c_0^5 x^2} \left(\frac{\partial U_1}{\partial y_2}\right)^2 \omega_f^4 \frac{D_i^{Sh.N.}}{C^5} \quad (4.6.2.3)$$

Here $\overline{u_{t1}^2}$ is proportional to the kinetic energy of turbulence and U_1 is the axial jet velocity. The self-noise component, $I^{Se.N.}((x, \theta), \vec{y})$, depends mainly on the turbulent kinetic energy of the jet, while the shear noise component depends on both the kinetic energy of the jet as well as on the mean axial velocity of the jet flow. Therefore in order to study the influence of the shear-noise component, $I^{Sh.N.}((x, \theta), \vec{y})$, we may change the relative jet velocity, namely $U_{jet}/U_{co-flow}$, where U_{jet} is the maximum velocity of the propane jet, $U_{co-flow}$ is the initial velocity of the co-flow air, and keep the U_{jet} constant.

In the experimental study of the cold propane jet performed by Schefer (1988), the parameter $U_{jet}/U_{co-flow} = 7.5$. Basically, we may vary this ratio in any way, however for the purpose of this thesis we change it in the range 3.75 and 15, i.e. the velocity of the jet is fixed and the co-flow air velocity, $U_{co-flow}$, is doubled or halved. Figures 4.6.2.2-4 show the contours of the turbulent kinetic energy of the jet ($k[m^2s^{-2}]$) and the jet acoustic power ($P_A[dB]$) for $U_{jet}/U_{co-flow} = 7.5, 3.75$ and 15, respectively. Figures 4.6.2.2-4 show that the increase in the co-flow velocity results in a decrease in the jet angle of expansion

and vice versa, i.e. when the co-flow velocity is reduced then the expansion jet angle increases.

Figures 4.6.2.5 represent the jet noise power (dB) predictions for the basic jet with $U_{jet}/U_{co-flow} = 7.5$, the jet with a doubled co-flow velocity, $U_{jet}/U_{co-flow} = 3.75$, and a halved co-flow velocity, $U_{jet}/U_{co-flow} = 15$, measured at the radial sections at distances $x/d = 4$ and 15, and along the jet axis, respectively. It is observed that, in general, the noise level generated by the jet reduces when the co-flow velocity increases. The maximum noise power level (dB) goes down when we reduce the co-flow velocity, as does the total noise power per unit length (dB), see table 4.6.2.1.

This behaviour is in qualitative agreement with the experimental investigations performed, for example by Papamoschou (2007). Papamoschou showed that the noise level is suppressed when the velocity ratio, $U_{co-flow}/U_{jet}$, varies from 0 to 0.53, where the jet velocity, U_{jet} , is fixed., see figure 4.6.2.1. In this research the velocity ratio, $U_{co-flow}/U_{jet}$, changes from approximately 0.06 to approximately 0.27. Therefore it is captured in the velocity range from 0 to 0.53 in the Papamoschou experimental work and this illustrates that the noise level is suppressed when the co-flow velocity is increased.

Table 4.6.2.1 *The effect of the jet/ co-flow velocity ratio on the maximum jet noise generation and on the total noise power per unit length.*

$U_{jet}/U_{co-flow}$	Max Noise Power, dB	Total Noise Power, dB
3.75	134.52	81.82
7.5	133.16	81.59
15	132.15	80.73

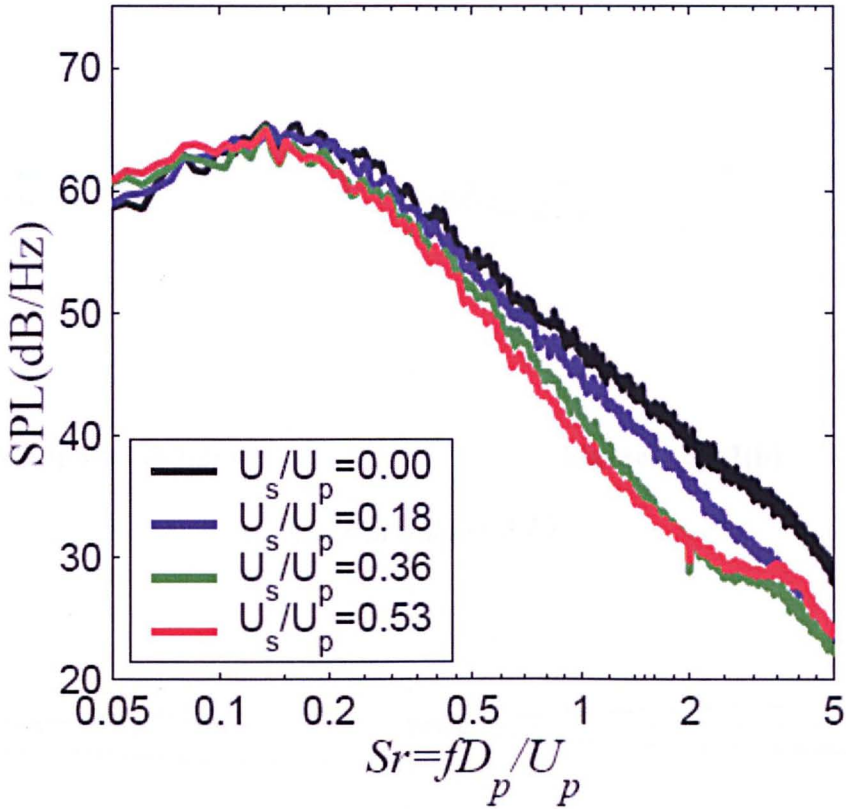


Figure 4.6.2.1 Jet acoustic power level spectra, P_A [dB], measured by Papamoschou (2007). Notation: U_p primary flow velocity corresponding to U_{jet} , U_s secondary flow velocity corresponding to $U_{co-flow}$, primary flow velocity is fixed.

From figure 4.6.2.1 we observe that the acoustic power of the jet flow reduces when the secondary/primary flow velocity is increased, i.e. $U_{co-flow}/U_{jet}$. However in this thesis we adopt the opposite relation: primary/secondary velocity flow, i.e. $U_{jet}/U_{co-flow}$, in order to work with >1 values. Therefore the range of values from 15 to 3.75 in our notation correspond to the range from 0.06 to 0.27 in the Papamoschou notation. In this range the acoustic power decreases when the secondary/primary velocity ratio is increased or in our notation when the primary/secondary ratio is decreased. That is exactly as we observe in our numerical experimental study, see figures 4.6.2.5. This is an important observation, which illustrates that the Goldstein model produces at least qualitatively correct acoustic results.

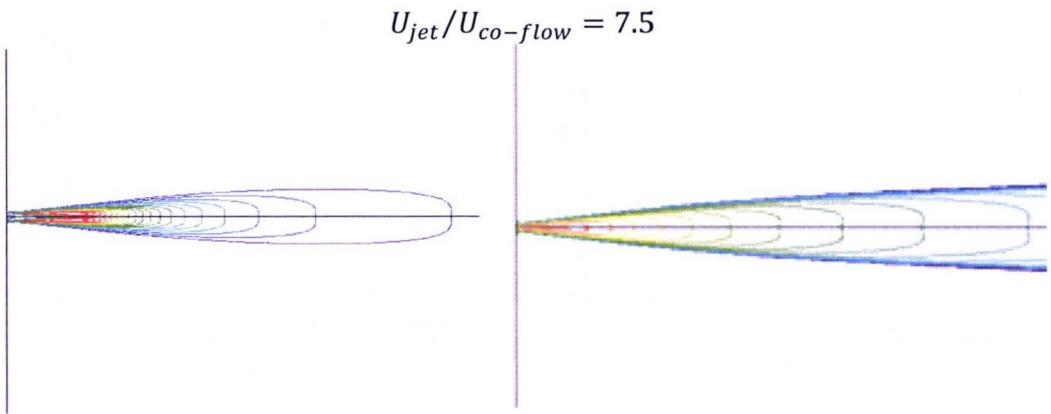


Figure 4.6.2.2(a)

Figure 4.6.2.2(b)

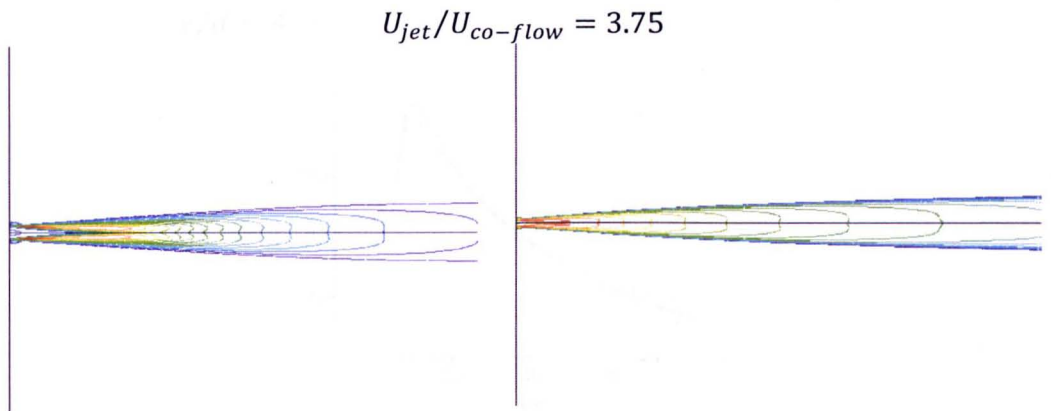


Figure 4.6.2.3(a)

Figure 4.6.2.3(b)

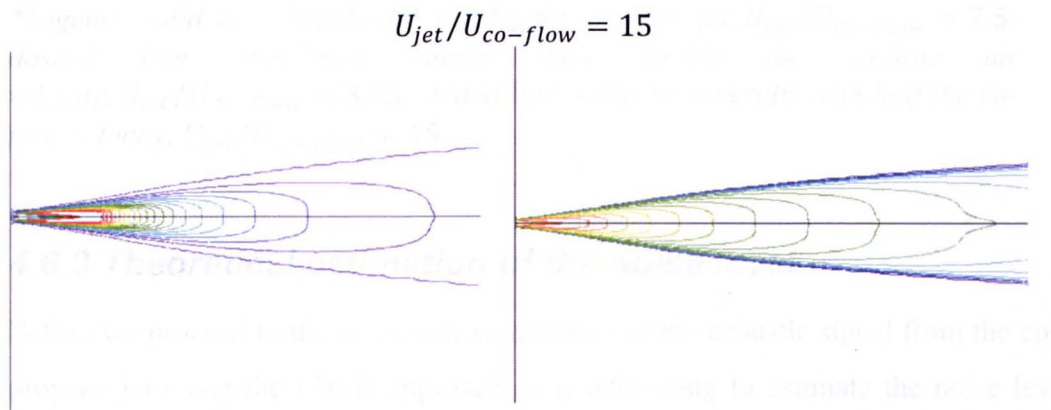


Figure 4.6.2.4(a)

Figure 4.6.2.4(b)



Contours of (a) the turbulent kinetic energy, $k[m^2s^{-2}]$, and (b) the acoustic power level, $P_A[dB]$, for a jet with an inlet profile obtained from the pre-simulation in the pipe, and with the co-flow air velocity varied.

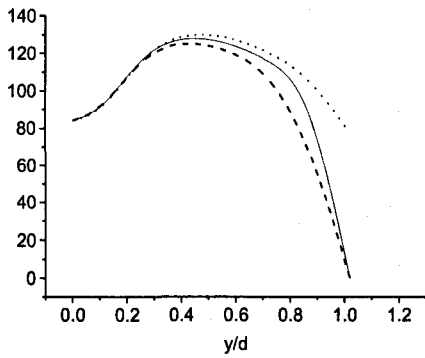


Figure 4.6.2.5(a) Jet acoustic power level predictions, P_A [dB], at the radial section at a distance $x/d = 4$.*

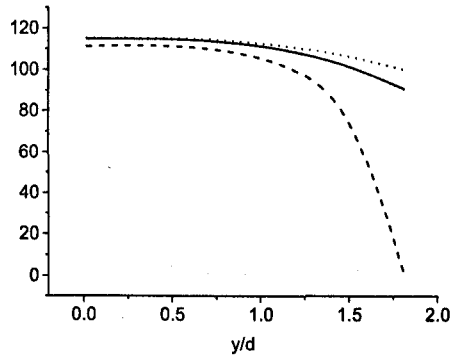


Figure 4.6.2.5(b) Jet acoustic power level predictions, P_A [dB], at the radial section at a distance $x/d = 15$.*

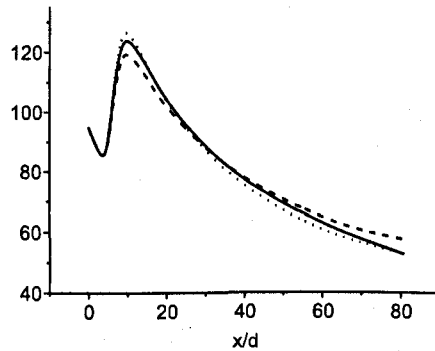


Figure 4.6.2.5(c) Jet acoustic power level predictions, P_A [dB], along the axis.*

*Legend: solid line, simulation results for a basic jet, $U_{jet}/U_{co-flow} = 7.5$; dashed line, simulation results with double the co-flow air velocity, $U_{jet}/U_{co-flow} = 3.75$; dotted line, simulation results with half the co-flow velocity, $U_{jet}/U_{co-flow} = 15$.

4.6.3 Theoretical estimation of the noise level

Before we proceed to the numerical simulations of the acoustic signal from the cold propane jet using the FW-H approach, it is interesting to estimate the noise level using a simple dimensional approach.

Lighthill's (1952) result for the far-field intensity of the noise generated by a turbulent flow forms the starting-point for this analysis. This result was modified slightly in order to apply the noise radiation from a jet by Ffowcs Williams (1963).

The result for the far-field intensity, I , may be written in dimensional form as follows:

$$I(\theta, R) \sim \frac{\rho_m^2 U_j^8 D^2}{\rho_0 c_0^5 R^2 (1 - M_c \cos \theta)^5} D(\theta) \quad (4.6.3.1)$$

where ρ_m is the density in the mixing region, U_j the jet velocity, D the nozzle diameter, $\rho_0 = 1.204 \text{kgm}^{-3}$ and $c_0 = 343 \text{ms}^{-1}$ the density and speed of sound in the external fluid at a distance R from the jet to the observer and θ the angle between the direction of the emission of the sound and the downstream jet axis. The function $D(\theta)$ is the directivity of the unconnected quadrupole distribution, and we assume that all the quadrupoles are randomly oriented, so that $D(\theta) = 1$, and M_c is the speed of convection defined as:

$$M_c = 0.67 \frac{U_j}{c_0} \quad (4.6.3.2)$$

Since no experimental investigations of the noise have been performed for this jet, we should make some hypothetical assumptions on how the noise could be detected. Let us imagine that there is a set of microphones for noise measurements. The microphones are located on a circle of radius 0.6312m ($120d$) and are positioned along the stand at intervals of $7\frac{1}{2}^\circ$ from $7\frac{1}{2}^\circ$ to 105° to the jet axis. We choose these microphones since they have been employed by Lush (1971) in his experimental investigation of the jet noise, however in his work the nozzle diameter was equal to 0.025m and therefore the actual radial distance of the microphones corresponding to $120d$ was 3m .

It should be noted that the acoustic intensity in dB is as follows:

$$\text{Intensity} = 10 \text{Log}_{10} \left(\frac{I}{I_{\text{ref}}} \right) \quad (4.6.3.3)$$

where $I_{\text{ref}} = 10^{-12} \frac{\text{W}}{\text{m}^2}$ is the reference intensity.

From the expression (4.6.3.1) we may obtain that acoustic intensity is proportional to the expression on the r.h.s, but not equal. In order to obtaining the exact values, we need to adjust the theoretical predictions with the experimental measurements obtained at some angle position, for example $\theta = 90^\circ$.

For adjustment purposes, we need some experimental measurements of the noise level, and these are not available for the cold propane jet under investigation. However we have found some experimentally measured data, obtained by Lush (1971), for a cold air jet with similar operating conditions, namely: $M = 0.2$, $TR = 1$, $T = 300K$. Therefore it is reasonable to employ the acoustic intensity measured by Lush (1971) at $\theta = 90^\circ$ for this jet as a reference value for global adjustment. However we need to take into account the difference in densities of these two jets. From equation (4.6.3.1) for the Lush conditions, we obtain 99dB and 101dB after employing the density correction (the density of the cold propane in the mixing layer of the jet is obtained from the CFD simulations is $\rho_m \cong 1.5kgm^{-3}$). Therefore the correction for the experimental data is +2dB. The experimentally measured, Lush (1971), acoustic intensity at $\theta = 90^\circ$ for air is 57dB, and therefore for propane it would be 59dB. From this data we may find that the global adjustment factor to be -42dB.

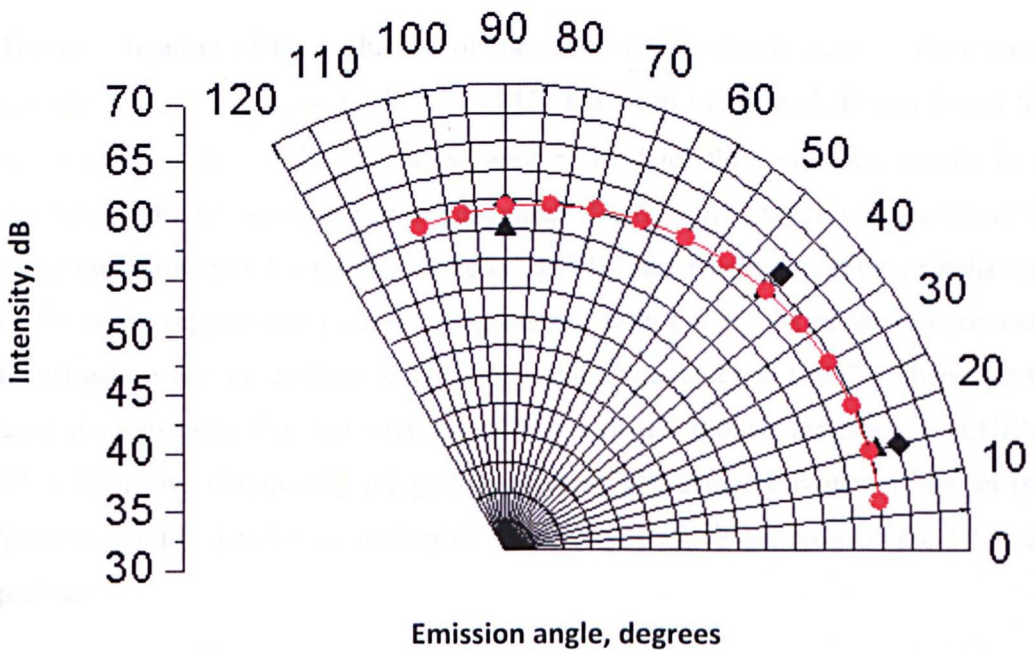


Figure 4.6.3.1 Theoretically predicted directivity compared with the experimentally measured values.

Legend: red line – theory, equation (4.6.3.1), triangles – experimentally measured values for air jet $M = 0.2$, $TR = 1$, $T = 300K$, Lush (1971); diamonds – adjusted experimental values for propane.

Figure 4.6.3.1 illustrates the theoretically predicted directivity for a cold propane jet with $M = 0.2$ and the experimentally measured values, Lush (1971), for a cold air

jet with $M = 0.2$, in addition to the adjusted values for a propane jet with similar conditions. We may observe that after global adjustment is applied for the theoretically predicted values, the theory, see equation (4.8.1.1), underestimates the noise intensity at low angular positions of the receiver by about 4dB. This discrepancy is due to our simplifications in the theory by assuming the randomly oriented quadrupoles, which is not exactly the situation in real jets.

4.6.4 Intermediate conclusions

The Reynolds Stress 2D axisymmetric simulation results, obtained in section 4.5, have been employed to numerically evaluate the jet acoustic power using the Goldstein acoustic model, Goldstein and Rosenbaum (1973), in the FLUENT 12.0 realisation. It has been shown in this section that the modifications of the shape of the initial velocity profile does not significantly change the maximum jet noise power generated, but it changes only the position of the noise peak.

The investigation of the influence of the jet/co-flow velocity ratio in three cases, namely: $U_{jet}/U_{co-flow} = 3.75, 7.5$ and 15 , has been performed. It was found that an increase in the co-flow velocity, with a fixed jet flow velocity, results in an increase in the jet acoustic power generated. We have no experimental data on the noise measurements for this jet, Schefer (1988), however the qualitative behaviour of the noise suppression is in good agreement with the results of the experimental investigation for the co-flow jets, for example Papamoschou (2007). Therefore we have demonstrated that the very simplified acoustic model, realized in FLUENT 12.0, where we obtain only integrated values of the acoustic power of the jet (see Section 2.5 for details) is applicable for the qualitative analysis of the jet noise problems.

Finally, the theoretical estimation of the possible directivity of the noise intensity, generated by a cold propane jet has been performed using the Lighthill dimensional analysis. For calibration of the theoretical perditions, we employed the experimentally measured noise intensities obtained for a cold air jet operating under similar experimental conditions by Lush (1971). Based on the dimensional analysis,

we have found that the noise intensity of the propane is +2dB higher than the noise intensity of the air jet under the simulated conditions.

4.7 3D CFD simulations

The aim of the 3D simulations is to obtain the flow field that will be used in the Ffowcs Williams-Hawkings (FW-H) noise model, see Chapter 2 Section 2.3 for the model description. The accuracy of the FW-H acoustic model depends strongly on the accuracy of the flow field simulation results. Therefore it is interesting to investigate the use of unsteady LES turbulence models as a tool for the flow simulations in cold jet co-flows with high density differences. In this section we focus mainly on the LES simulations, therefore the mesh for the simulation is designed with respect to LES. Finally we note that the nature of LES turbulence modelling does not allow us to perform grid dependency analysis, since the grid itself is a filter in the LES approach.

4.7.1. Pre-processing analysis for 3D LES simulations

For LES calculations it is essential to build a mesh with respect to the turbulent kinetic energy resolution. Since the kinetic energy is practically independent of the mesh resolution, when RANS is used, we may build a simple 2D axisymmetrical mesh for 2D simulations of the jet and then employ the simulation results as estimations of the mesh resolution for the full 3D LES calculations.

First of all we need to decide to what extent we will resolve the turbulence kinetic energy spectra. Of course this strongly depends on our computational resources available, in other words we are limited to build a mesh having no more than $4 - 5 \times 10^6$ nodes in total.

Let us consider the turbulence kinetic energy spectra as a function of the turbulent integral length scale, see figure 4.7.1.1. Here the turbulence eddies length scale is defined after Kolmogorov as:

$$l_0 \cong \frac{k^{\frac{3}{2}}}{\epsilon} \quad (4.7.1.1)$$

This means that the size of the smallest turbulence eddy in the Kolmogorov theory may not be smaller than l_0 , and all eddies having the size less than l_0 will be

damped by the turbulence viscosity. The key values of the spectra are listed in table 4.7.1.1.

From there we may find that if, for example, we are interested in resolving $0.9k$, i.e. 90% of the total turbulence kinetic spectra (TKE), we have to resolve the eddies of size $0.16l_0$, where l_0 is a Kolmogorov scale. Therefore the grid cell dimension is smaller than the size of the smallest Kolmogorov eddy. However if we decide to resolve 50% of the total turbulence kinetic energy spectra, then the size of the cell should be $1.6l_0$, which is an order of magnitude larger than for the 90% resolution.

Table 4.7.1.1 Key values of the cumulative turbulence kinetic energy spectra against length-scale of eddies based on the Kolmogorov's energy spectrum.

	l/l_0
$k(l) = 0.1k$	6.1
$k(l) = 0.5k$	1.6
$k(l) = 0.8k$	0.42
$k(l) = 0.9k$	0.16

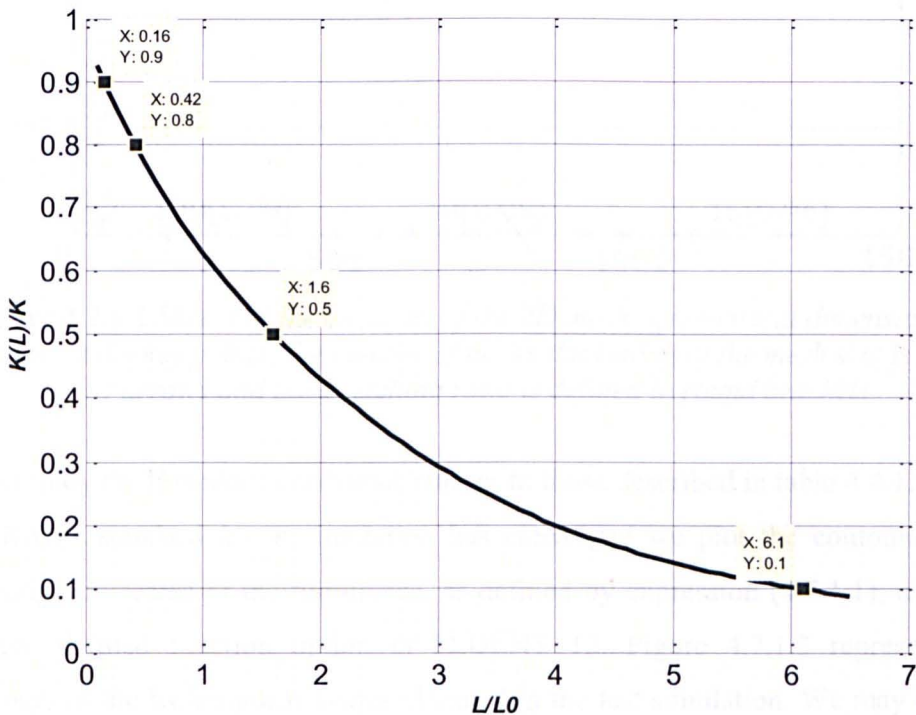


Figure 4.7.1.1 Cumulative turbulence kinetic energy spectra (TKE) against the length-scale of the eddies based on the Kolmogorov energy spectrum.

For our analysis we employ the fact that the kinetic energy of the flow field is almost independent of the mesh resolution. Therefore we may build a test 2D mesh for the flow field simulation and obtain the contours of the turbulent kinetic energy from simple RANS standard $k - \epsilon$ simulations. We are interested in building a mesh having the dimensions large enough to incorporate all radial sections used for the experimental studies. Therefore the mesh should be at least $0.26m$ ($50d$ nozzle diameters) long in the axial direction and $5d - 8d$ nozzle diameters in the radial direction. In addition we should create a buffer zone in order to reduce to a minimum the influence of the pressure fixed boundary conditions at the outlets. Therefore the computational domain should be at least three times longer than the jet region, namely $150d$ nozzle diameters. A sketch of the mesh is presented in figure 4.7.1.2. The fine jet region is diverging with a computationally comfortable 3% angle. The total number of nodes of this mesh is 6045.

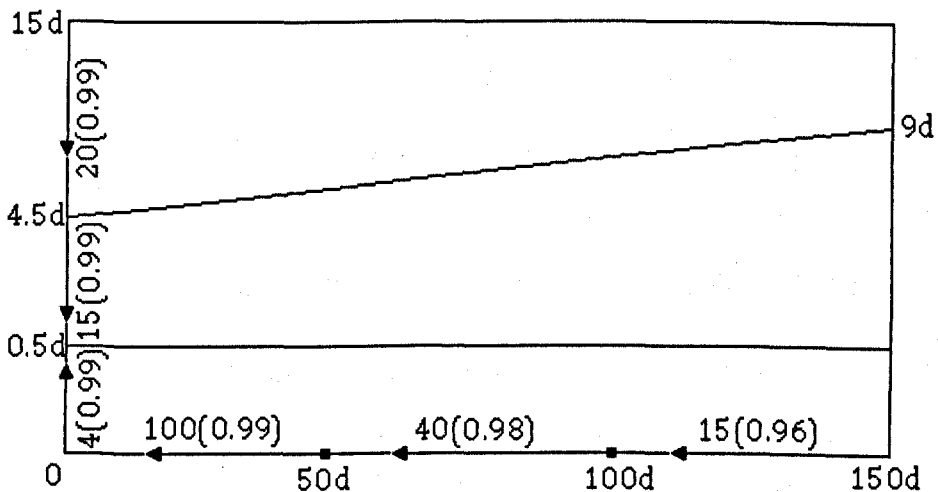


Figure 4.7.1.2 Sketch of the elements of the 2D mesh; geometrical dimensions are marked at the key points, the number of nodes thickening of the mesh size is shown by arrows and the stretching ratio is defined in round brackets.

We employ the boundary conditions similar to those described in table 4.4.1.1. After the RANS standard $k - \epsilon$ simulation has converged we plot the contours of the Kolmogorov scales of the turbulence, as defined by expression (4.7.1.1), using the custom defined function option in FLUENT 12. Figure 4.7.1.3 represents the contours of the Kolmogorov scales obtained in the test simulation. We may observe the increase in the turbulent scales in the downstream direction. The most important information for us is the distribution of the length-scales along the jet axis because

we will use these values as cell dimensions when building the full 3D mesh for the LES simulations. The distribution of the Kolmogorov length scales near the radial outlet boundary is not important since we do not expect to observe a strong turbulent flow there, because this is a region of co-flowing air.

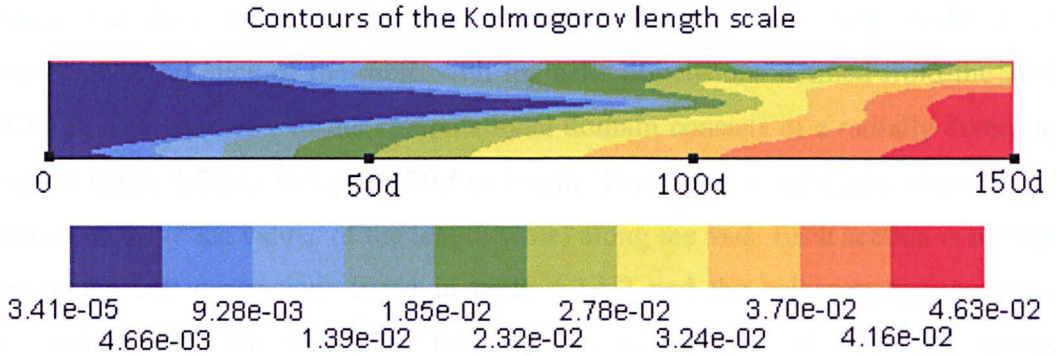


Figure 4.7.1.3 Contours of the Kolmogorov length scale (m), obtained in 2D axisymmetrical RANS standard $k - \epsilon$ simulation.

Table 4.7.1.2 Key values of the turbulence length scale along the jet axis required for LES when TKE is resolved by 90%, 80% and 50%.

l_0	90% TKE	80% TKE	50% TKE
$3.41 \cdot 10^{-5}$	$5.46 \cdot 10^{-6}$	$1.43 \cdot 10^{-5}$	$5.46 \cdot 10^{-5}$
$4.66 \cdot 10^{-3}$	$7.46 \cdot 10^{-4}$	$1.96 \cdot 10^{-3}$	$7.46 \cdot 10^{-3}$
$9.28 \cdot 10^{-3}$	$1.48 \cdot 10^{-3}$	$3.90 \cdot 10^{-3}$	$1.48 \cdot 10^{-2}$
$1.39 \cdot 10^{-2}$	$2.22 \cdot 10^{-3}$	$5.84 \cdot 10^{-3}$	$2.22 \cdot 10^{-2}$
$1.85 \cdot 10^{-2}$	$2.96 \cdot 10^{-3}$	$7.77 \cdot 10^{-3}$	$2.96 \cdot 10^{-2}$
$2.32 \cdot 10^{-2}$	$3.71 \cdot 10^{-3}$	$9.74 \cdot 10^{-3}$	$3.71 \cdot 10^{-2}$
$2.78 \cdot 10^{-2}$	$4.45 \cdot 10^{-3}$	$1.17 \cdot 10^{-2}$	$4.45 \cdot 10^{-2}$
$3.24 \cdot 10^{-2}$	$5.18 \cdot 10^{-3}$	$1.36 \cdot 10^{-2}$	$5.18 \cdot 10^{-2}$
$3.70 \cdot 10^{-2}$	$5.92 \cdot 10^{-3}$	$1.55 \cdot 10^{-2}$	$5.92 \cdot 10^{-2}$
$4.16 \cdot 10^{-2}$	$6.66 \cdot 10^{-3}$	$1.75 \cdot 10^{-2}$	$6.66 \cdot 10^{-2}$
$4.63 \cdot 10^{-2}$	$7.41 \cdot 10^{-3}$	$1.94 \cdot 10^{-2}$	$7.41 \cdot 10^{-2}$

However it is interesting to plot the contours of the exact Kolmogorov length scales, we are more interested in finding the turbulence scales distribution for the LES simulations, when the turbulence kinetic energy spectra is resolved by 90%, 80% and 50%, respectively. Therefore we need to plot values of $0.16l_0$, $0.42l_0$ and $1.6l_0$

respectively, where l_0 is a Kolmogorov turbulence length scale. Clearly the shape of the contours will not change, but the absolute values are scaled. Table 4.7.1.2 presents the absolute values of the Kolmogorov scale contours.

4.7.2. Mesh for the 3D LES simulation

Once the distribution of the length scales is known, we may build a 2D axisymmetrical slice of the mesh with the cells dimensions defined from the table 4.7.1.2. The geometry of the computational domain consists of a radially diverging region (form $4.5d$ to $9d$) and $150d$ in length. The region is split into nine sections (since we have ten values of the length scale) along the axis. Each section is meshed using the cell dimensions listed in table 4.7.1.2 and the cell size distribution is smoothed using the successive ratio option. In the case of 90% TKE spectra resolution we obtain a 2D slice of 35 800 nodes in total, however the region near the nozzle outlet is resolved using the dimensions of 50% TKE, therefore, strictly speaking, our mesh should be considered as the one to resolve about 75% TKE. We have done so, since the estimation of the true size of the full 3D 80% TKE gives us the value of $\sim 7.88 \cdot 10^6$ for the total number of nodes without buffers, which is above the computational capacity available for this research.

In addition we have built the coarser mesh extensions in the radial direction in order to create a buffer zone, and put the radial outlet boundary conditions further from the jet axis. Each extension has about a three times coarser mesh resolution than the previous one. The full mesh therefore consists of four elements: (1) jet flow region of 35 800 nodes, (2) an extension up to $15d$ in the radial direction with 3 625 nodes in total, (3) a second extension up to $45d$ in the radial direction with 1 300 nodes, and (4) a third extension which goes up to $75d$ in the radial direction with 168 nodes, see figure 3.7.2.1. In total we obtain for 2D slice consisting of 40 893 nodes. This corresponds to $\sim 3.6 \cdot 10^6$ nodes in the full 3D cylindrical case, where we repeat the 2D slice 88 times around the jet axis. This is slightly below our limitation of $4 \cdot 10^6$ nodes.

Here we built a mesh with buffer zoned in axial direction downstream and in radial direction. This buffer zone protects the flow field solution of the jet from the artificially reflected from outlet boundaries acoustic waves. However one can notice

that the inlet boundary is not protected by buffer zone. The buffer zone is technically impossible to apply in the present setup, since the inlet flow must be carefully resolved by the fine mesh. This is of course implies that there may occur the reflection from the inlet, but we can accept it because the acoustic directivity pattern of the turbulent jet is strongly stretched in the axial direction downstream, therefore only minor portion of noise propagates in the upstream direction. This is proved by our 2D simulations, see figures 4.6.2.2-4. Find more about boundary conditions in the discussion Chapter 7.

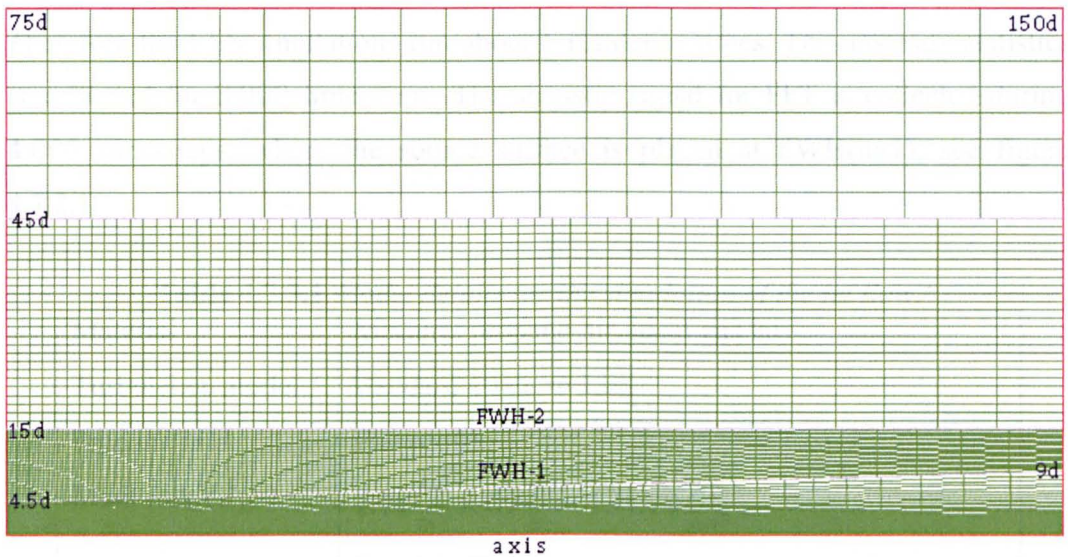


Figure 4.7.2.1 2D slice of the computational grid used for the LES computations.

The two joining surfaces of the final mesh are used as FWH surfaces for the acoustic simulations: joint (1)-(2) diverging open cylinder surface, FWH-1, and joint (2)-(3) open cylinder surface, FWH-2.

4.7.3. Boundary conditions

Initially, the simulations were performed to obtain a steady RANS standard $k - \epsilon$ solution in order to obtain an initial distribution of the averaged flow field parameters. Then these results are used as an initial flow field for the unsteady RANS and LES. A summary of the boundary conditions applied in FLUENT 12.0 in order to obtain a steady solution is listed in table 4.7.3.1.

4.7.4. Flow field simulation results

During the preliminary simulations it was found that the employment of the random vortex generator at the inlet profile of the jet introduces too much turbulence into the flow during the LES simulations. Therefore all the results presented are obtained in the case where no random fluctuations are involved. The ‘natural’ numerical viscosity of the mesh is found to be sufficient for the development of the turbulence. The LES computations were run for about 10^4 iterations, where the time-step is $5 \cdot 10^{-6} s$, and consequently the physical time is $5 \cdot 10^{-2} s$. The mean flow resistance time is estimated as $t = L/U = 0.789m/69ms^{-1} \cong 1 \cdot 10^{-2} s$. Therefore the LES simulations run about 5 residence times. The unsteady statistics is collected for 8 000 time-steps. The acoustic signal for FFT is collected during 4 000 time-steps, where the source surface is placed at FWH(int1), see figure 4.7.2.1.

Table 4.7.3.1 Model details for the simulation of the jet flow.

Material	Mixture: propane-air, ideal gas law
Turbulence model	standard $k - \epsilon \Rightarrow$ LES
Propane inlet, Mass flux ($U_j \rho$)	Flat profile $1.91 \frac{kg}{m^3} \times 69 \frac{m}{s} = 131.79 \frac{kg}{sm^2}$ $T = 294K$ Turbulence intensity: 4% Hydraulic diameter: 0.526cm
Air inlet, Mass flux ($U_j \rho$)	Flat profile $1.225 \frac{kg}{m^3} \times 9.2 \frac{m}{s} = 11.27 \frac{kg}{sm^2}$ $T = 294K$ Turbulence intensity: 0.4% Viscosity ratio: 2
Outlet	Pressure outlet = P_{atm} , $T = 294K$ Back flow: Turbulence intensity: 10% Viscosity ratio: 2
Solver	3D, Pressure Based, Implicit, Unsteady

Figure 4.7.4.1 illustrates the LES results for the contours of the instantaneous vorticity of the turbulent jet in the middle section.

Figure 4.7.4.2 illustrate the combination of the velocity derivatives, q , defined as:

$$q_1 = -\left(\frac{\partial V}{\partial x} \cdot \frac{\partial U}{\partial y} + \frac{\partial W}{\partial x} \cdot \frac{\partial U}{\partial z} + \frac{\partial W}{\partial y} \cdot \frac{\partial V}{\partial z}\right) \quad (4.7.4.1)$$

$$q_2 = -0.5 \left(\left(\frac{\partial U}{\partial x}\right)^2 + \left(\frac{\partial V}{\partial y}\right)^2 + \left(\frac{\partial W}{\partial z}\right)^2 \right) \quad (4.7.4.2)$$

$$q = q_1 + q_2 \quad (4.7.4.3)$$

where U, V, W are the velocity components. This combination illustrates well the development of the turbulence in the jet flow.

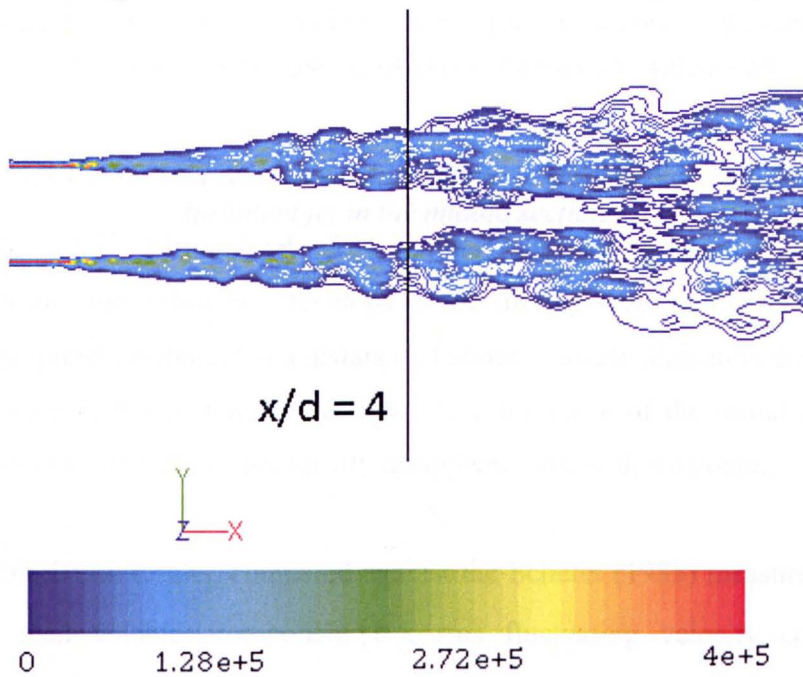


Figure 4.7.4.1 3D LES results: contours of the instantaneous vorticity of the turbulent jet in the middle section.

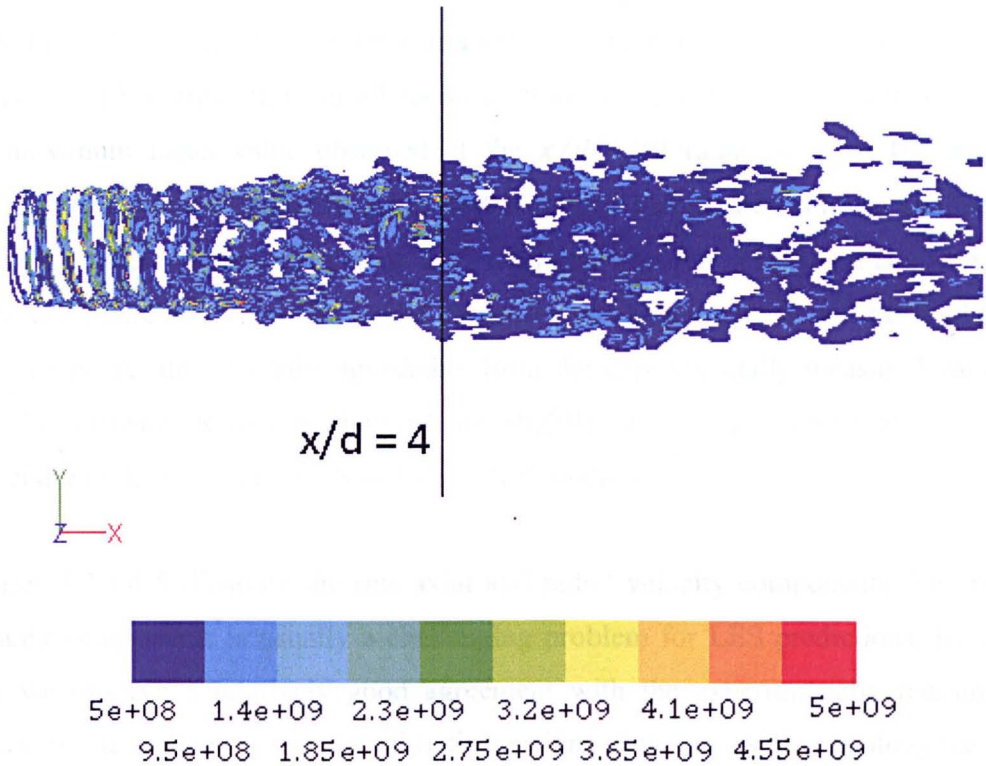


Figure 4.7.4.2 3D LES results: contours of the instantaneous vorticity of the turbulent jet in the middle section.

From figures 4.7.4.1-2 it is clearly observed that there are no initial fluctuations at the jet inlet and the turbulence develops in the mixing layer of the jet. The flow becomes completely turbulent at a distance of about 5 nozzle diameters downstream. At the distance of the first radial section, some influence of the initial conditions could be detected, however it practically disappears further downstream.

The LES simulation results, compared against the Schefer (1988) measurements for the mean axial velocity component (\overline{U}), rms fluctuating velocity components ($\sqrt{u'^2}, \sqrt{v'^2}$) and their correlations ($\overline{u'v'}$) are presented in figures 4.7.4.3-6, respectively. In general, the agreement between the velocity measurements and the numerical predictions is remarkably good.

Figure 4.7.4.3 illustrate the LES and unsteady RANS predictions for the mean velocity component. The shape of the profile obtained at the closest to the nozzle edge radial section is slightly different from the experimentally measured profile and this demonstrates that the numerically predicted jet profile is more flatter at the

beginning of the jet, however the maximum value is predicted correctly. The agreement of the experimental measurements and numerical simulations is almost perfect for LES simulations at all radial sections, except small underestimation of the maximum mean value observed at the $x/d = 30$ radial section. The mean velocity component obtained from the unsteady RANS simulation is lower and more flattened than the experimental values at all the radial sections. This trend is observed in the last figure (d), where the results are presented along the jet centreline: the LES predictions are almost undistinguishable from the experimentally measured values and the unsteady RANS predictions are slightly above the experimental curve, especially in the region from 18 to 40 nozzle diameters.

Figures 4.7.4.4-5 illustrate the rms axial and radial velocity components. The rms velocity components is usually a challenging problem for LES predictions. In this case we observe a relatively good agreement with the experimentally measured values for the rms components at all radial sections of the jet, as well as along the jet axis. It is interesting to note that at the $x/d = 4$ radial section we observe that there is an excess in the velocity fluctuations, which emphasis the lack of the initial turbulence in the jet. This is due to the absence of the random fluctuations at the inlet in the LES simulations. However the better agreement of the rms components downstream of the jet shows that the turbulence is developed well and even becomes 'too strong' in the radial direction, since we observe an underprediction for the $\sqrt{v'^2}$ velocity component at $x/d = 30$ and 50. The unsteady RANS predictions show a different trend: both the rms components are overestimated at $x/d = 15$, then, further downstream at $x/d = 30$, the rms components are captured better than in the LES computations. Finally at $x/d = 50$ the unsteady RANS predictions of $\sqrt{v'^2}$ are much closer, however still below, the experimental curve, while the $\sqrt{u'^2}$ from LES are found to be in better agreement with the experimentally measured values than the predictions obtained from the unsteady RANS. These trends are clearly observed in figures 4.7.4.4-5(d), where we have presented the data along the jet centreline. First of all we observe the difference in the initial boundary conditions for the unsteady RANS and LES calculations: no initial turbulent fluctuations in the case of LES and 10% turbulence intensity in the case of RANS. The latter is closer to the conditions of the experiment.

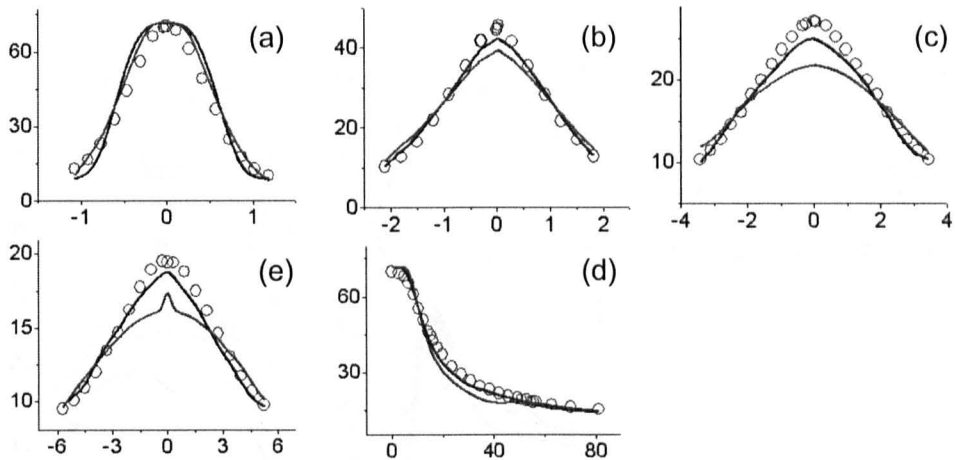


Figure 4.7.4.3 Radial profiles of the mean axial velocity component (\bar{U}) in the jet, (a, b, c, d) at $x/d = 4, 15, 30$ and 50 and (e) along the axis.*

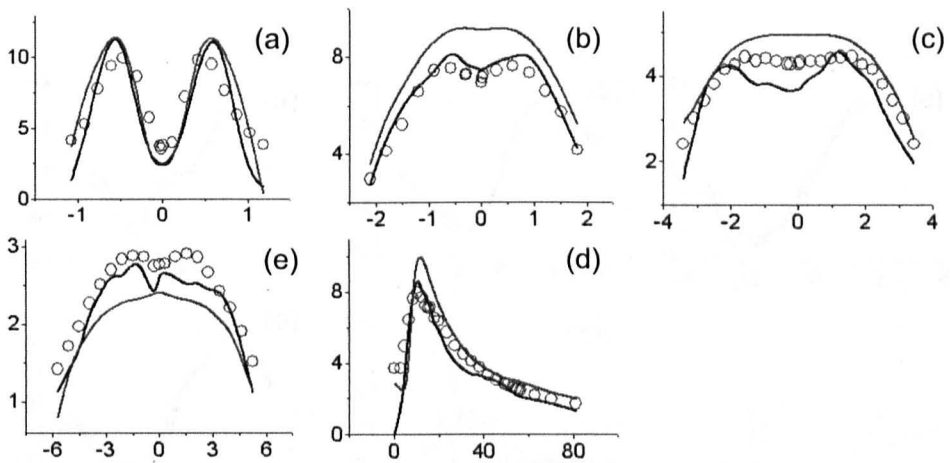


Figure 4.7.4.4 Radial profiles of rms of axial velocity ($\sqrt{u'^2}$) in the jet, (a, b, c, d) at $x/d = 4, 15, 30$ and 50 and (e) along the axis.*

*Legend: the symbols are experimental data by Schefer (1988); the black lines are the LES simulation results; the blue line are the unsteady RANS (RSM) simulation result, both with a flat velocity profile at the inlet.

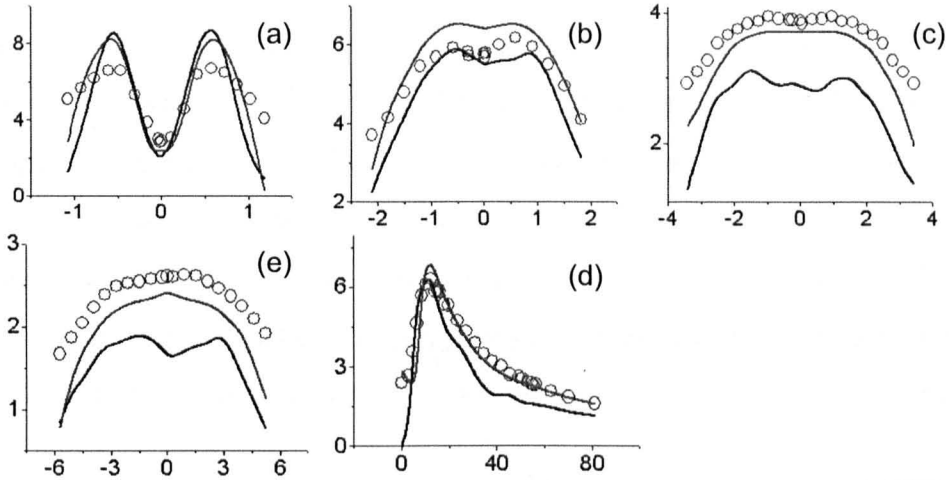


Figure 4.7.4.5 Radial profiles of rms of radial velocity component ($\sqrt{v'^2}$) the jet, (a, b, c, d) at $x/d = 4, 15, 30$ and 50 and (e) along the axis. *

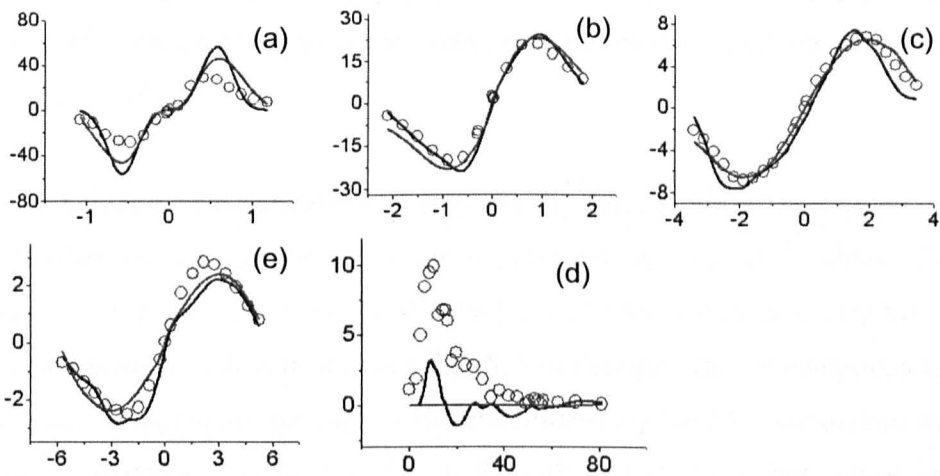


Figure 4.7.4.6 Radial profiles of the velocity correlation ($\overline{u'v'}$) the jet, (a, b, c, d) at $x/d = 4, 15, 30$ and 50 and (e) along the axis. *

*Legend: the symbols are experimental data by Schefer (1988); the black lines are the LES simulation results; the blue line are the unsteady RANS (RSM) simulation result, both with a flat velocity profile at the inlet..

Then the rms values increases rapidly to a maximum (which is captured well by the LES and it is overestimated by the RANS), then reduces along the axis and repeats the experimentally observed behaviour of the jet. It is interesting to note that $\sqrt{v'^2}$ is captured slightly better by the RANS computations than by LES

Finally, we have reported the predictions of the $(\overline{u'v'})$ velocity component, see figure 4.7.4.6. The agreement with the experimentally measured values is very good at all radial sections for both the LES and RANS approaches. The significant underpredictions of the $(\overline{u'v'})$ component observed along the axis is surprising and makes us examine the experimentally measured data more carefully. Indeed, based on the axial positions from the radial profiles we always have values for $(\overline{u'v'})$ close to zero, however on the axial profile it jumps rapidly to 10 at about $x/d = 15$, the value which is not observed at the radial profile placed at the same position.

In conclusion, we may state that the LES calculations generally better predict well the velocity field components compared to the unsteady RANS. Therefore we may expect that the pressure field (the pressure is essential for noise predictions in the FWH model) is also reasonably predicted based on the LES unsteady solution. However we will employ the noise simulation procedure based on the unsteady RANS computations.

From the velocity field validation we may predict that the noise level based on the LES simulations are slightly below the experimentally measured values. This is because the jet noise in the case of the cold gas is mainly dominated by the shear noise component, which in its turn is a function of the rms velocity components. The rms velocity components are slightly underestimated by the LES computations and are over-estimated by the RANS. This will result in a stronger shear noise for the RANS predicted velocity field and a weaker shear noise for the LES predictions. Consequently the RANS jet will be noisier than that predicted using LES.

4.8 3D acoustics

After a statistically stable LES and unsteady RANS solutions are obtained we employ a FW-H acoustic model in order to predict the noise level from the jet. The acoustic signal for FFT is collected during 4 000 time-steps, where the source surface is placed at FWH(int1), see figure 4.7.2.1.

The microphones are located on a circle of radius $0.6312m$ ($120d$) and are positioned along the stand at intervals of $7\frac{10}{2}$ from $7\frac{10}{2}$ to 105^0 to the jet axis. We

choose these microphone positions as they have been employed by Lush (1971) in his experimental investigation of the jet noise. However in the work of Lush the nozzle diameter $0.025m$ and therefore the actual radial distance of the microphones corresponding to $120d$ was $3m$.

Figure 4.8.1 illustrates the directivity of the numerically predicted noise level, theoretically predicted directivity (see equation 4.6.3.1) for a cold propane jet with $M = 0.2$ and the experimentally measured values, Lush (1971), for a cold air jet with $M = 0.2$, in addition to the adjusted values for a propane jet with similar conditions.

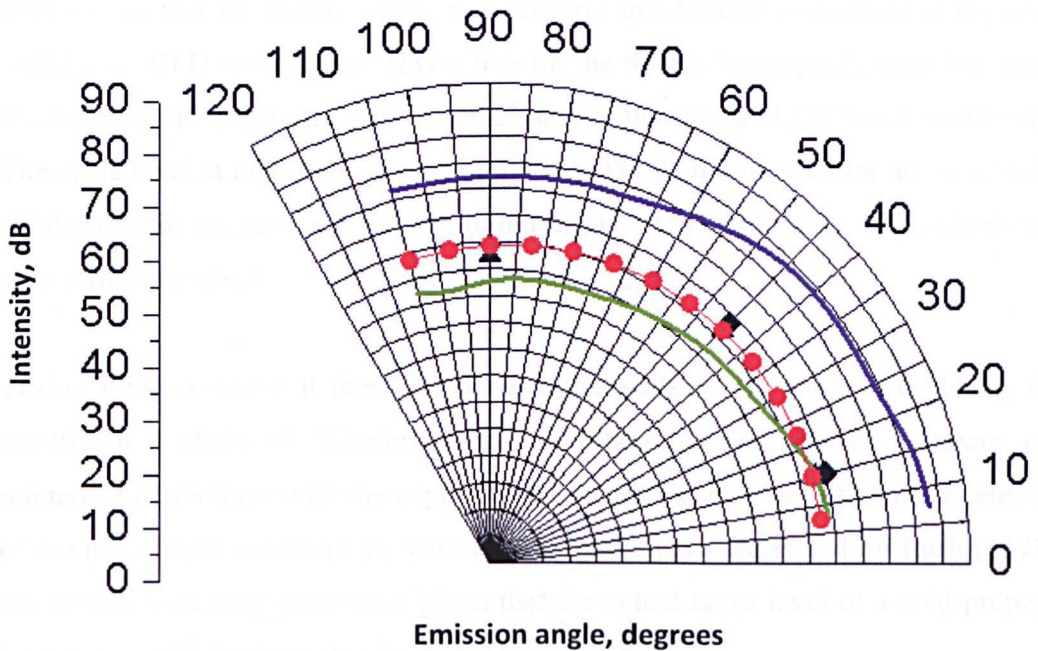


Figure 4.8.1 Theoretically predicted directivity compared with the experimentally measured values, LES and unsteady RANS(RSM) simulation results.

Legend: green line – LES simulation results, blue line – unsteady RANS (RSM) simulation results, red line – theory adjusted to Lush (1971), triangles – experimentally measured values for air jet $M = 0.2$, $TR = 1$, $T = 300K$, Lush (1971); diamonds – adjusted experimental values for propane.

We observe that the noise level obtained from the unsteady RANS computations is higher than the LES-based predictions at all angular positions. The discrepancy is about 20 dB. However the shape of the noise directivity curves are similar. As we

anticipated earlier in Section 4.7, the RANS-based jet is noisier than the LES-based jet.

Hence since there is no valid experimental data then it is difficult to conclude which approach (LES- or RANS-based) is most accurate. Nevertheless, we choose to rely on the experimental measurements by Lush (1971) for the noise from a similar jet. Based on this assumption, the LES-based predictions are closer to that observed by Lush during his experimental studies. In particular, we observe that the slope of the experimentally measured noise values is larger than that predicted by the simplified Lighthill theory, equation (4.6.3.1), while the LES predictions, coupled with the FWH noise model approach, shows a similar trend as that measured experimentally. This means that the nature of the non-uniform quadrupole orientation is captured well by the CFD simulations. This is true for the RANS-based predictions too, since the shape of the directivity pattern is the same as that for the LES-based predictions. The noise level at high microphone angles is lower than measured for an air jet with similar conditions, however the maximum discrepancy is less than 10%, which is a very promising result.

Taking into account that there are no measurements of the noise level during the experimental study of Schefer (1988), and therefore we cannot compare our numerical predictions with the experimental values but only with the measurements of the noise from a cold air jet with the similar velocity measured by Lush (1971), our results look very optimistic, given that the actual noise level of a cold propane jet would not be far from that predicted by our values.

4.9 Conclusions

In this Chapter the cold propane jet has been examined numerically. We have employed the experimentally measured values of the velocity field (no noise data) obtained by Schefer (1988) for the validation of the simulation results. The experimental data has been reviewed critically, and we have found that the data are not consistent at $x/d = 4$ radial section.

We started numerical simulations from the 2D axisymmetric RANS simulation. The flow field simulation results are found to be in good agreement with the

experimentally measured values. Based on the steady RANS solution, we have evaluated numerically the jet acoustic power using the Goldstein acoustic model, Goldstein and Rosenbaum (1973), using the FLUENT 12.0 realisation. Then we investigated the influence of the jet/co-flow velocity ratio in three cases: $U_{jet}/U_{co-flow} = 3.75, 7.5$ and 15. It was observed that the increase in the co-flow velocity, with a fixed jet flow velocity, results in an increase in the jet acoustic power generated. This qualitative behaviour is in agreement with the results of the experimental investigation for the co-flow jets obtained, for example, by Papamoschou (2007).

In addition the alternative acoustic model, based on the Lighthill dimensional analysis, was performed, where for calibration of the theoretical predictions we employed the experimentally measured noise intensities obtained for a cold air jet operating under similar experimental conditions, Lush (1971). Based on the dimensional analysis, we found that the noise intensity of the propane is +2dB higher than the noise intensity of the air jet under the simulated conditions.

We continued investigations of the propane jet with the 3D LES and unsteady RANS calculations. The simulation flow field results are found to be in good agreement with the experimentally measured values for the LES computations. We have also anticipated that the RANS-based noise predictions will be higher than the LES-based predictions. This was confirmed by the FWH simulations. We employed the FWH acoustic model realised in FLUENT 12.0 based on the LES and RANS unsteady solutions for noise predictions. The simulation results were compared with the theoretically predicted values, based on the Lighthill dimensional analysis and the experimentally measured values for a cold air jet under similar conditions, Lush (1971). We found that the LES-based predicted noise level could be close to reality.

Chapter 5

Cold Air Jet Simulations

5.1 Introduction

In Chapter 4 we have employed the very detailed velocity field data of the cold propane jet, measured by Schefer (1988) from the Sandia National Laboratory for validation of the numerical simulation results. However there were no noise measurements for this experiment, and therefore we may only perform the noise simulations without the option of validating our results with experimental measurements on other quantities. In order to evaluate the noise prediction we referred to the Lush (1971) measurement data. In this Chapter 5, we focus on the cold air jet experiment study performed by Lush. This experimental data has become popular as an example data set for the validation of noise simulation numerical models. Only noise measurements are presented in this study, and therefore we have no opportunity to compare the flow field simulation results with the experimental measurements. We postulate that a detailed numerical study of all these three cases is sufficient to validate our numerical approach.

5.2 Experimental setup

The jet noise rig consists essentially of a nozzle exhausting into a large anechoic chamber which measures $9m \times 9m \times 7.2m$. The chamber is lined on all walls inside with acoustic foam wedges, $1m$ long, which render it anechoic down to about $100Hz$. Compressed air at approximately room temperature is supplied to the nozzle via a control valve and a silencer setting chamber. This chamber is cylindrical with a diameter of $300mm$ and a length of $1.5m$ and is designed to reduce the valve noise so that it is negligible compared with the jet mixing noise. This is achieved by lining the chamber at intervals of $300mm$. The baffles overlap so that there is no direct sound path. The valve noise can just be detected with the nozzle removed and it consists of tones at about $5, 8$ and $12kHz$ of intensity $30 - 45dB$. This level is always below the jet mixing noise.

The resulting settling chamber has a diameter of 150mm, which gives an area contraction ratio of 36:1 used with a 25mm diameter convergent nozzle. The large contraction ratio ensures that the flow velocity in the settling chamber is very low, rising to a maximum of about 5ms^{-1} at choking. This, in turn, ensures that the noise generated by the flow in the duct is very small.

The nozzle is made of fibreglass and designed to give a uniform velocity profile at the exit. It has an exit diameter of 25mm.

The microphone may be mounted at various angles to the jet axis using a permanent stand constructed of a light steel framework. The stand resembles the quadrant of a circle of radius 3m and, since the jet issues vertically downwards from the roof of the chamber, it is mounted vertically with the centre of the quadrant at the nozzle exit. Microphone holders are positioned along the stand at intervals of $7\frac{1}{2}^{\circ}$ from $7\frac{1}{2}^{\circ}$ to 105° to the jet axis, see figure 5.2.1

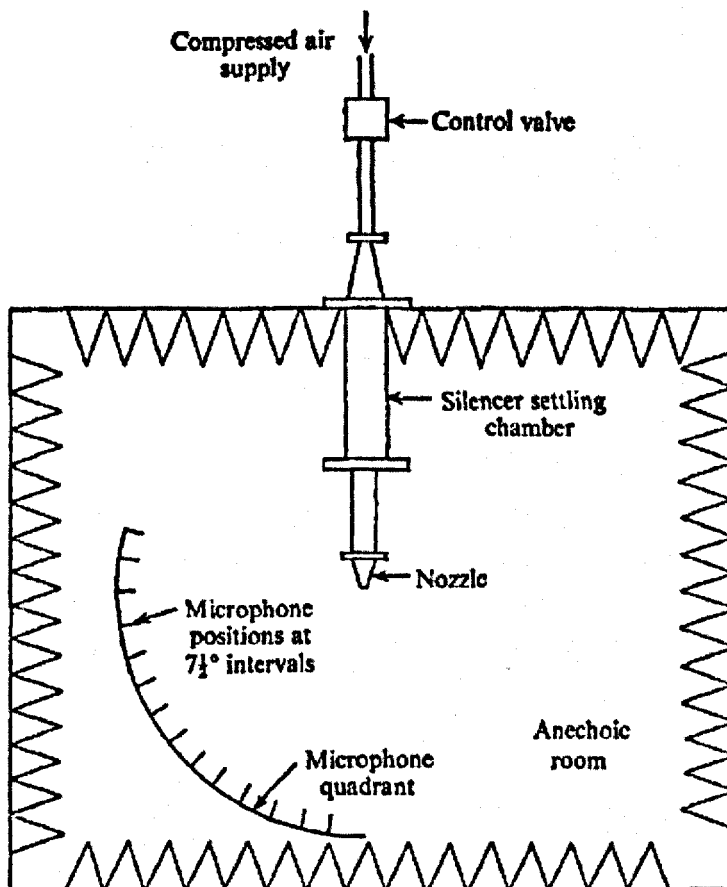


Figure 5.2.1 Schematic layout of the jet noise rig.

Table 5.2.1. *Coordinates of the microphone locations (where the angle is measured from the jet direction) in inches and metres in the Lush (1971) experiment.*

R = 120d = 3m				
N	Angle	X[m]	Y[m]	Z[m]
1	$7\frac{1}{2}^0$	2.974	0.392	0
2	15^0	2.898	0.776	0
3	$22\frac{1}{2}^0$	2.772	1.148	0
4	30^0	2.598	1.500	0
5	$37\frac{1}{2}^0$	2.380	1.826	0
6	45^0	2.121	2.121	0
7	$52\frac{1}{2}^0$	1.826	2.380	0
8	60^0	1.500	2.598	0
9	$67\frac{1}{2}^0$	1.148	2.772	0
10	75^0	0.776	2.898	0
11	$82\frac{1}{2}^0$	0.392	2.974	0
12	90^0	0.000	3.000	0
13	$97\frac{1}{2}^0$	-0.392	2.974	0
14	105^0	-0.776	2.898	0

Measurements of a $\frac{1}{3}$ -octave sound pressure level spectra, between frequencies of 40Hz and 20kHz, have been made at all angles to the jet axis between $7\frac{1}{2}^0$ and 105^0 at intervals of $7\frac{1}{2}^0$. Table 5.2.1 summarizes the position of microphones in the Lush (1971) experiment. For each angular position, the velocity was varied in steps from 75 to 300ms^{-1} and the maximum jet velocity corresponded to nozzle choking. For these experiments, the stagnation temperature in the settling chamber was assumed to be equal to the room temperature after several hours of running. In addition, the atmospheric pressure was measured at regular intervals during testing and frequent

checks were made on the microphone calibration using a Bruel & Kjaer pistonphone (type 4220)

Satisfactory measurements of the acoustic field could not be obtained below about $90ms^{-1}$ because the jet noise was merging into the background noise at low frequencies around 100Hz. The background noise in the anechoic chamber was about 50dB overall. At higher jet velocities, the low-frequency noise increases but not as rapidly as the jet noise. It appears that, at these low frequencies, the microphone was still in the near field part of the jet. At the other end of the jet velocity range, the appearance of shock cells tones at about 10kHz, when the nozzle becomes choked, sets an upper speed limit. The microphone response becomes nonlinear above about 10kHz, and measurements above this frequency are in error since no microphone or atmospheric absorption corrections have been applied. However, this is not important since the frequencies of interest for the 25mm jet are below 10kHz. When the microphone is placed at $7\frac{1}{2}$ to the jet axis, a noise cone was fitted because the microphone was in the outer edge region of the jet. Although the signal was dominated by the jet pressure fluctuations, part of the noise spectrum could not be observed.

5.3 2D simulations

In this subsection we perform a detailed 2D simulation of the flow field of the jet with a jet velocity of $195ms^{-1}$. Then we employ a Goldstein acoustic formulation, described in Section 2.5, in order to obtain the special distribution of the noise intensity. This acoustic model requires a 2D axisymmetric flow field simulation data as input information. The choice of the jet velocity is based on the fact that the Mach number of the jet with a velocity of $195ms^{-1}$ is about 0.56, which is close to $M = 0.556$, the Mach number of the hot air jet studied in Chapter 6. This similarity in Mach number makes it possible to compare the acoustic results of the two jets.

5.3.1 Computational grid

A sketch of the 2D axisymmetric grid is illustrated in Figure 5.3.1.1. Here we present a schematic diagram of the jet mean velocity contours in order to illustrate the regions that require a better grid resolution: jet core and jet mixing layer. The jet core is usually about 5 nozzle diameters long and therefore we create this region on

the grid. Here the nozzle diameter is $0.025m$. The grid nodes are compressed near the end of jet potential core and near the nozzle lip where the jet mixing layer is developing. The direction of the node distribution is shown by arrows. In order to diminish the effect of the reflection from the boundaries, we add two coarse mesh damping blocks (2, 3) which surround the finer resolved jet block (1). The jet is fully presented in block (1), so that there is almost no flow in regions (2, 3). As it was mentioned in Chapter 4 the buffer zones are required in order to protect the jet flow solution from the artificially reflected acoustic waves from the boundaries. Here the acoustic waves from outlet boundaries are damped by the buffer zone, but any acoustic waves propagating toward the inlet direction will be reflected back into the computational domain. This is not ideal for certain, but this something we have to accept since there is no way to get rid of the reflection at the inlet. We cannot apply a buffer zone at the inlet since we require a carefully resolved flow field at the inlet. However there might be a reflection of the acoustic waves we can consider it as a minor effect, because the directivity pattern of the jet is of such a shape that almost all noise is propagating toward the downstream and radial directions, leaving a negligible portion of sound going upstream. We will discuss more about non-reflecting boundary in Chapter 7.

The node resolution in the radial direction of block (1): from $0d$ to $0.5d$ – 15 nodes with 0.99 successive ratio (1% increment in size), from $0.5d$ to $5d$ – 65 nodes with 0.98 successive ratio, from $5d$ to $15d$ – 30 nodes with 0.96 successive ratio. The resolution of block (1) in the axial direction: from 0 to $5d$ – 100 nodes equally distributed, from $5d$ to $10d$ – 50 nodes with 0.98 successive ratio, from $10d$ to $50d$ – 55 nodes with 0.96 successive ratio. The resolution of block (2) in the radial direction: from $15d$ to $50d$ - 15 nodes equally distributed; in the axial direction: from $0d$ to $50d$ – 35 nodes equally distributed. The resolution of block (3) in the radial direction: from $0d$ to $0.5d$ – 6 nodes equally distributed, from $0.5d$ to $5d$ – 30 nodes equally distributed, from $5d$ to $15d$ – 15 nodes with 0.94 successive ratio, from $15d$ to $50d$ - 15 nodes equally distributed; in the axial direction: from $50d$ to $100d$ – 35 nodes equally distributed. The total number of nodes of the grid is approximately 24 500.

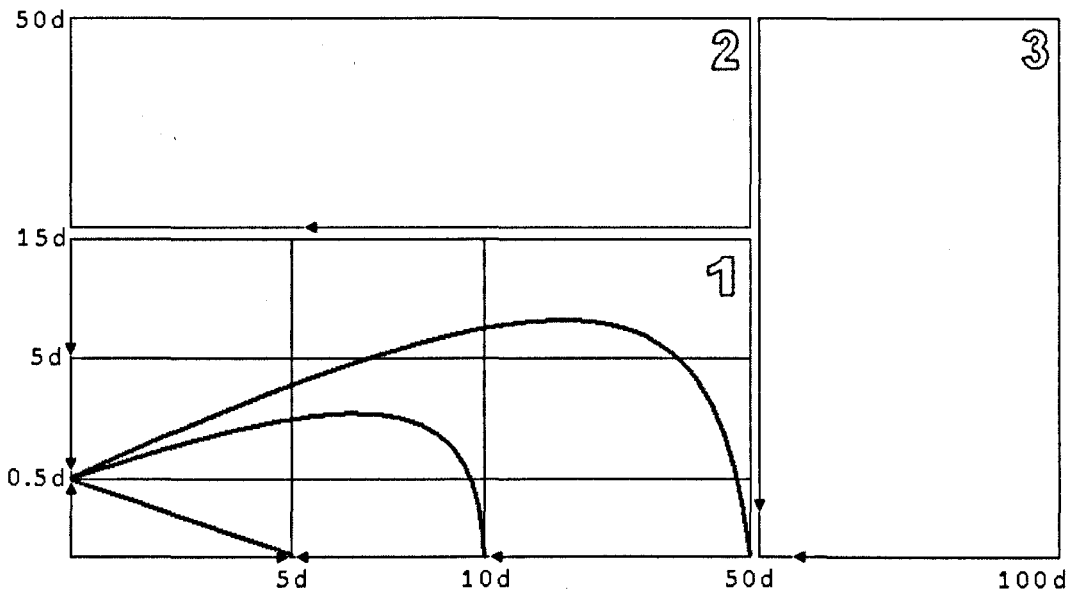


Figure 5.3.1.1 Sketch of the elements of the 2D grid; geometrical dimensions are marked at the key points, the thickening of the mesh size is shown by arrows and the sketch of the jet mean velocity contours by the grey line.

5.3.2 Boundary conditions and simulation strategy

The type of the boundary conditions and the simulation strategy for free jet simulations have been investigated in Chapter 4. Here we employ the same general approach.

Figure 5.3.2.1 illustrates a sketch of the boundary conditions employed. It should be noted that the intermediate surfaces between the blocks of the grid are specified as INTERFACE and then these are connected together in FLUENT. Table 5.3.2.1 summarizes the details of the boundary conditions. Here we employ MASS FLUX type for the flow inlet. The mass flux of the inlet jet flow is $V\rho = 195\text{ms}^{-1} \times 1.225\text{kgm}^{-3} = 238.875\text{kgm}^{-2}\text{s}^{-1}$. In order to stabilize the solution we introduce a small mass flux inlet ($5\text{kgm}^{-2}\text{s}^{-1}$) for the co-flow velocity, but the exact value of the co-flow velocity is unknown from the experimental report. The variation of this value up to approximately 5% ($12\text{kgm}^{-2}\text{s}^{-1}$) of the mean flow does not have any impact in the flow field results at the jet plume.

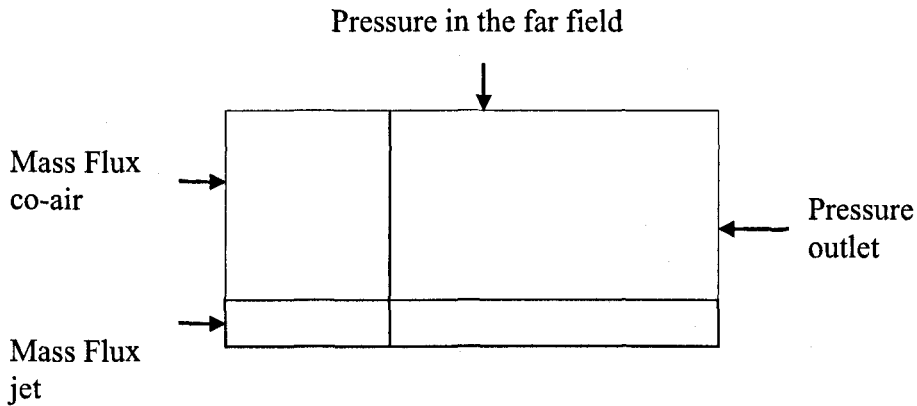


Figure 5.3.2.1. Sketch of the 2D specified boundary conditions.

Table 5.3.2.1: Summary of the boundary conditions employed.

<i>BC type in FLUENT</i>	<i>Details</i>
Mass flux jet inlet	Flat profile: $238.875 \frac{kg}{s \cdot m^2}$, Turbulent intensity 10%, Viscosity ratio 10, or profile from the nozzle simulation, Total temperature 300K.
Mass flux in the co-flow air	$5 \frac{kg}{s \cdot m^2}$, Turbulent intensity 5%, Viscosity ratio 5, Total temperature 300K.
Pressure in the far field	Gauge pressure 0Pa, Mach number 0.001 (axial direction), Turbulent Intensity 5%, Viscosity ratio 5.
Pressure outlet	Gauge Pressure 0Pa, Back flow: Turbulent intensity 5%, Viscosity ratio 5, Total temperature 300K.

Material properties:

Air material details: Density – ideal gas law, Specific heat = $1006.43 \frac{J}{kg \cdot K}$, Thermal conductivity = $0.0242 \frac{W}{m \cdot K}$, Viscosity = $1.7894 \times 10^{-5} \frac{kg}{m \cdot s}$, Molecular weight = $28.966 \frac{kg}{kgmol}$.

Simulation strategy:

Initially, the RANS $k - \epsilon$ RSM turbulent model is used and the simulation strategy is as follows:

- Patch the cylinder region with length $10d$ and radius $0.5d$, where the velocity is fixed to $200ms^{-1}$.
- Activate the FMG: solver/initialization/set-fmg-initialization. Specify 3 multigrid levels and the default values for the rest of the options.
- Apply the FMG. As a result, we obtain a good starting flow field distribution which assists us to reach the convergent solution faster.
- Turbulent model: RANS $k - \epsilon$ standard; Discretization: first-order; Solver: Steady.
- Discretization: first-order \rightarrow second-order; Turbulent model: RANS $k - \epsilon$ standard $\rightarrow k - \epsilon$ RSM.
- Steady solver \rightarrow unsteady solver 1st order implicit $dt = 10^{-6}s$.
- Unsteady solver 1st order \rightarrow 2nd order implicit $dt = 10^{-6}s$, monitor average pressure flux through the $x/d = 10$ plane section of the domain. The number of iterations and the time step should be sufficient to obtain a constant value for the average pressure flux through the plane section. This number decreases as the simulation proceeds from 20 iterations per time step to 5 or 3 iterations per time step.

Note that we have estimated the time step for the unsteady simulation from acoustical resolution requirements. This is because we are interested in the acoustics being resolved for frequencies up to 20 000Hz, which is the upper limit of normal human perception. Therefore the characteristic time for the acoustic signal is $T = \frac{1}{20\ 000} = 5 \times 10^{-5}s$. In order to resolve the acoustic time-scale accurately, we take the time step to be $= 10^{-6}s$.

5.3.3 Grid dependency analysis

Here we study the effect of the grid resolution on the solution of the 2D simulations. The aim is to find the grid resolution for which the simulation results do not change when the grid is refined. We are interested in finding a grid independent solution for the velocity field because the velocity field is used in the calculation of the jet noise in the Goldstein BNS model.

Let us label the grid described in Section 5.2.1 as N_1 . Then we refine this grid by increasing the total number of nodes 0.4 times - N_2 , and making the original grid coarser by reducing the total number of nodes 0.4 times - N_0 . For all three cases we have performed RSM unsteady simulations as described in Section 5.2.2.

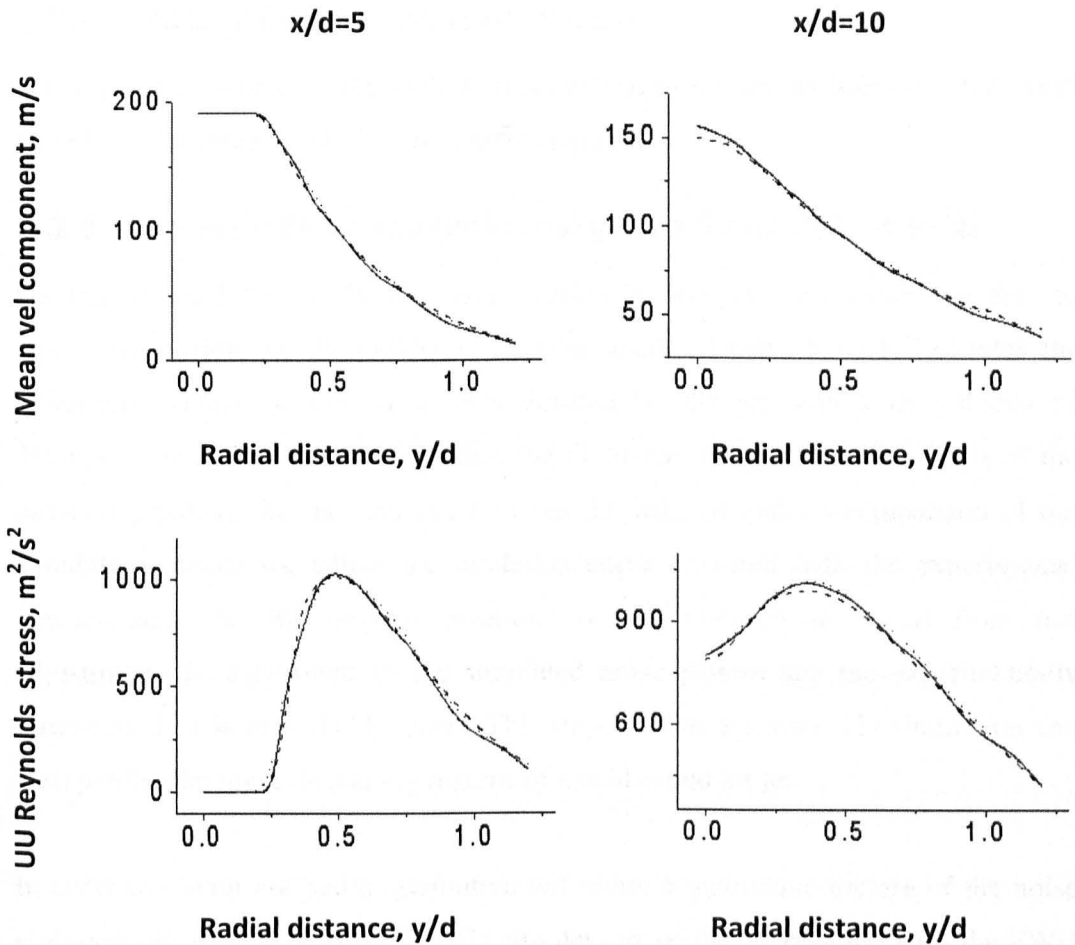


Figure 5.3.3.1 Grid dependency analysis: RSM simulation results for the mean axial and UU Reynolds stress velocity components measured at the two radial sections located at 5 and 10 nozzle diameters downstream, respectively, and for three grid resolutions.

Legend: solid line – simulation results for grid N_1 , dashed line – grid N_0 , dotted line - grid N_2 .

Figure 5.3.3.1 illustrate the simulation results for the mean axial and the UU Reynolds stress velocity components measured at the radial sections of the jet located at 5 nozzle diameters and 10 nozzle diameters downstream. Here we see that the simulation results obtained at the $x/d = 5$ downstream location are almost identical for all grid resolutions. The N_0 grid resolution results (dashed line) at $x/d = 10$ downstream location diverges from N_1 and N_2 (solid and dotted lines) grid

resolutions. This indicates that the N_0 grid resolution is insufficient for grid independent solution. Here we also show that the originally created grid N_1 is fine enough to produce grid independent solutions. Therefore the grid N_1 is used for all the 2D simulations presented in this thesis.

5.3.4 Velocity field simulation results

The input parameters for the Goldstein acoustical model are as follows: axial mean velocity component and turbulent kinetic energy.

5.3.5. Acoustic field analysis using the Goldstein model

Having obtained the steady averaged solution for the jet, we employ this data as input information for the Goldstein acoustic model. Figure 5.3.5.1 illustrates the directivity pattern of the noise level emitted by the jet with a jet velocity of 195ms^{-1} . Here we should recall that the Goldstein model gives the shape of the directivity pattern, but not the exact values. In order to make a comparison of our simulation results we adjust the modelled curve to agree with the experimental measurements at 90° angular positions of the microphone. Apart from this adjustment, the agreement of the simulated noise pattern and the experimentally measured data is remarkably good. This implies that a simple 2D simulation can well predict the noise directivity pattern of a cold round air jet.

In order to obtain not just a qualitative but rather a quantitative picture of the noise emission, we should perform full 3D simulations of the jet coupled with the FWH acoustic model. This is investigated in the following Section.

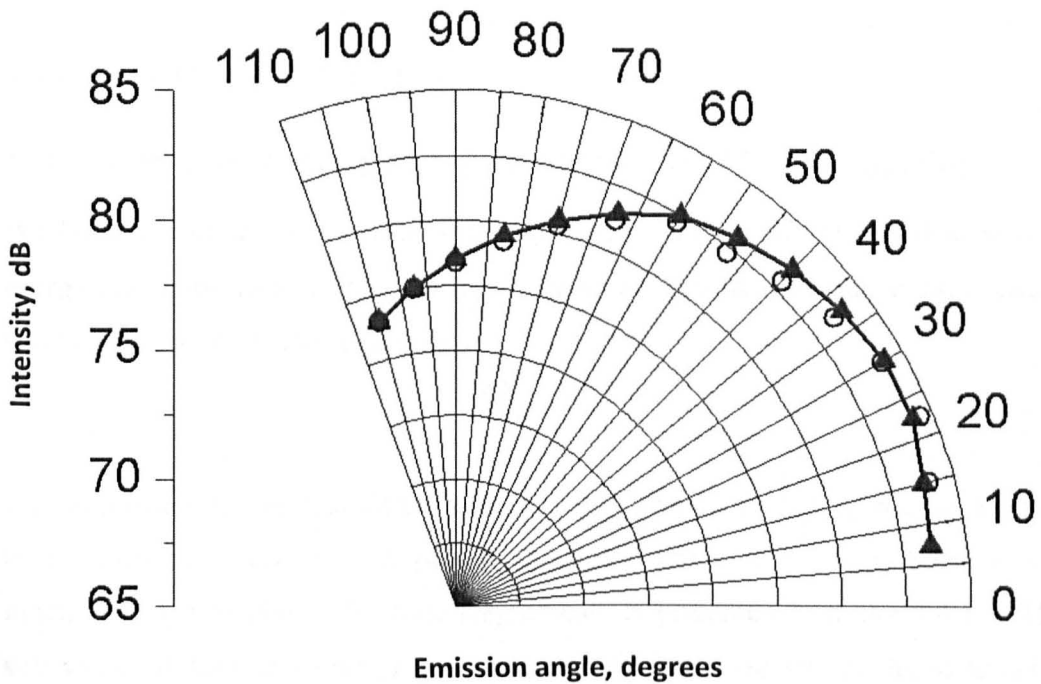


Figure 5.3.5.1 Theoretically predicted directivity compared with the experimentally measured values and the simulation results.

Legend: blue triangle – 2D simulation results and the Goldstein acoustic model, circles – experimental data obtained by Lush (1971).

5.4 3D simulations

The aim of this section is to predict the noise level using the FWH acoustic analogy based on the LES and the unsteady RANS calculations. We build the mesh having the LES computations in mind and then run the unsteady RANS based on the same mesh. The idea is to compare the two approaches in modelling the turbulence. For validation of the acoustic field we employ the data obtained by Lush (1971).

Here we focus on the jet with a bulk velocity of 195m s^{-1} ($M_a = M_j = 0.56$) and with the temperature ratio $TR = 1$, where the ambient temperature is assumed to be 300K . We choose these jet conditions in order to be able to compare the noise simulation results with the results obtained in Chapter 6 for the hot air jet with the same acoustic Mach number, namely $M_a = 0.56$.

From the experimental study we know that the shape of the nozzle was created in such a way to produce a flat velocity profile at the outlet of the nozzle; however the exact shape of the nozzle is unknown. Therefore we simulate the flow starting from

the nozzle edge, ignoring the thickness of the edge, since it is unknown, and enforce a flat inlet condition on the jet inlet boundary.

5.4.1. Pre-processing analysis for the 3D LES simulation

We build the mesh for the LES simulations with respect to the turbulent kinetic energy resolution (KTE). It is worth remembering that the turbulence eddy length scale is defined after Kolmogorov as:

$$l_0 \cong \frac{k^{\frac{3}{2}}}{\epsilon} \quad (5.4.1.1)$$

This expression means that all the eddies having a size less than l_0 will be damped by the turbulence viscosity. A plot of the turbulence kinetic energy spectra as a function of the relative turbulence length scale is presented in figure 5.4.1.1. The key values of turbulent energy and characteristic length-scales are listed in table 5.4.1.1.

Table 5.4.1.1 Key values of the cumulative turbulence kinetic energy spectra against the length-scale of eddies based on the Kolmogorov energy spectrum.

	l/l_0
$k(l) = 0.5k$	1.6
$k(l) = 0.7k$	0.8
$k(l) = 0.8k$	0.42
$k(l) = 0.9k$	0.16

Since the turbulent kinetic energy and turbulent dissipation rate could be obtained from a RANS standard $k - \epsilon$ simulation, we employ a pre-simulation analysis using a simple 2D axisymmetric grid. The sketch of the grid is shown in figure 5.4.1.2, and the well resolved region is $10d \times 5d$ ($250mm \times 125mm$). We stretched the mesh towards the boundaries in order to avoid artificial reflection effects in the RANS simulations. The 2D test mesh consists of 12 500 nodes in total.

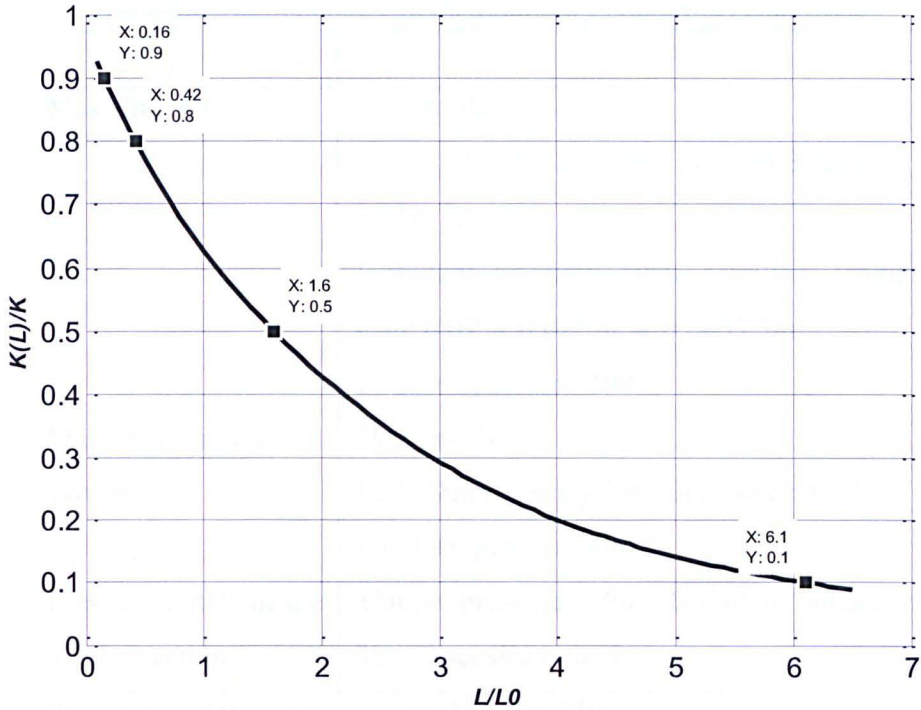


Figure 5.4.1.1 Cumulative turbulence kinetic energy spectra (TKE) against the length-scale of the eddies based on the Kolmogorov energy spectrum.

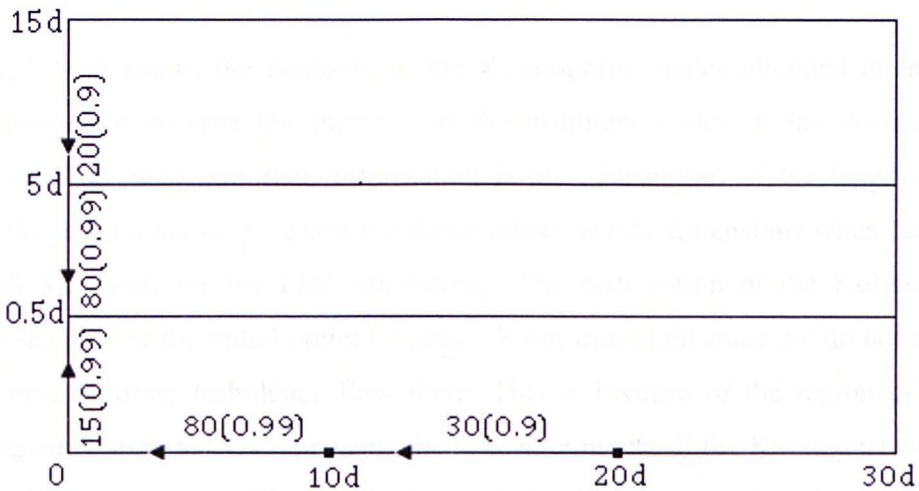


Figure 5.4.1.2 Sketch of the elements of the 2D grid; geometrical dimensions are marked at key points, the number of nodes thickening of the mesh size is shown by arrows and the stretching ratio is defined in round brackets.

A summary of the boundary conditions employed are described in table 5.4.1.2. The choice of the exact type of boundary condition is based on the previous experience of the jet modelling (see Chapters 4). After the RANS standard $k - \epsilon$ simulation has converged, we plot the contours of the Kolmogorov scales of turbulence, as defined by expression (5.4.1.1), using the custom defined function option in FLUENT 12.

Table 5.4.1.2: Summary of the boundary conditions employed.

<i>BC type in FLUENT</i>	<i>Details</i>
Mass flux jet inlet	Flat profile: $195\text{ms}^{-1} \times 1.225\text{kgm}^{-3} = 238.875\text{kg} \cdot \text{m}^{-2}\text{s}^{-1}$, Turbulent intensity 10%, turbulent length scale $0.07 \times 0.025\text{m} = 0.00175\text{m}$, Total temperature 300K.
Mass flux in the co-flow air	$5\text{kg} \cdot \text{m}^{-2}\text{s}^{-1}$, Turbulent intensity 2%, Viscosity ratio 5, Total temperature 300K.
Pressure outlet in the axial direction	Gauge pressure 0Pa, Turbulent intensity 5%, Viscosity ratio 5.
Pressure outlet in the radial direction	Gauge Pressure 0Pa, Back flow: Turbulent intensity 5%, Viscosity ratio 5, Total temperature 300K.

Figure 5.4.1.3 shows the contours of the Kolmogorov scales obtained at the test simulation. We observe the increase of the turbulent scales in the downstream direction. The most important information is the distribution of the length-scales along the jet axis because we will use these values as cell dimensions when building the full 3D mesh for the LES simulations. The distribution of the Kolmogorov length scales near the radial outlet boundary is not important since we do not expect to observe a strong turbulence flow there. This is because of the region of a co-flowing air. Figure 5.4.1.4 represents the refined contours of the Kolmogorov scales in the jet core region. The distribution of the Kolmogorov length defines the resolution of the grid for use in the LES computations.

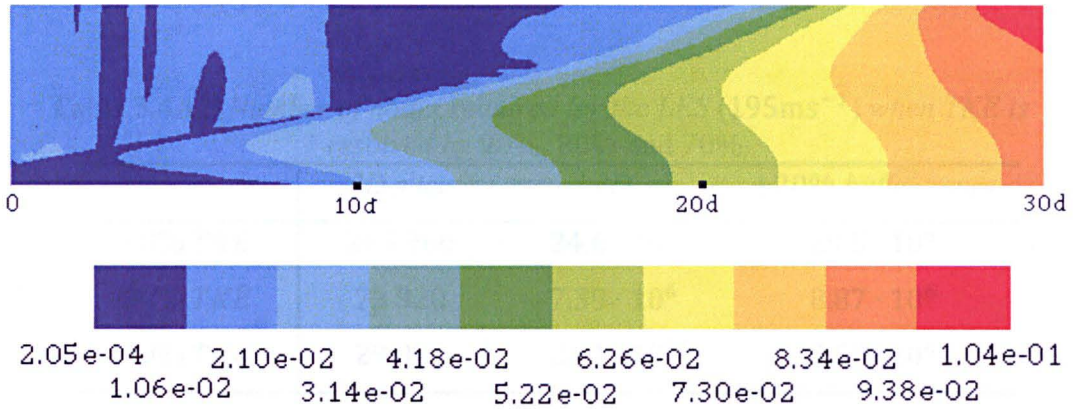


Figure 5.4.1.3 Contours of Kolmogorov length scale (m), obtained in 2D axisymmetrical RANS standard $k - \epsilon$ simulation, bulk velocity is 195ms^{-1} .

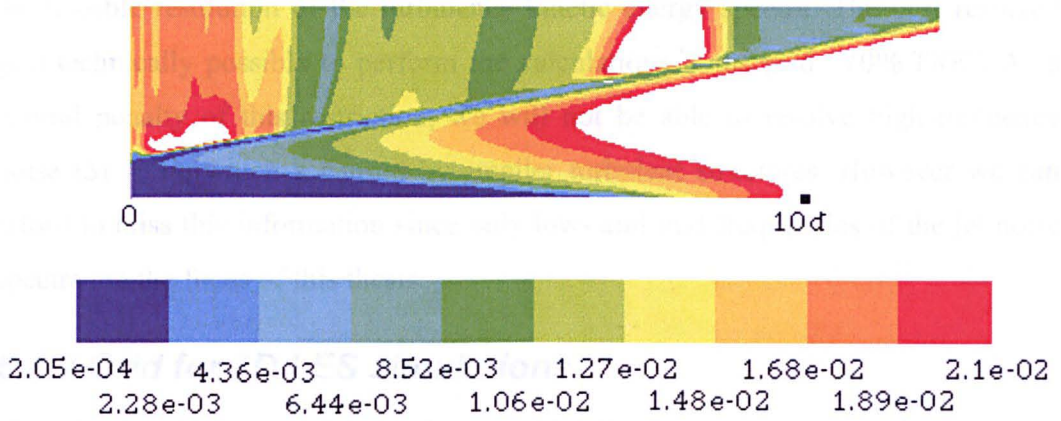


Figure 5.4.1.4 Contours of Kolmogorov length scale (m) in the jet core region obtained in 2D axisymmetrical RANS standard $k - \epsilon$ simulation, bulk velocity is 195ms^{-1} .

The required number of nodes for the 3D LES simulations is resolved by 90%, 80% and 70% TKE and it is estimated using the cumulative turbulence kinetic energy spectra as $0.16l_0$, $0.42l_0$ and $0.8l_0$, respectively, where l_0 is a Kolmogorov turbulence length scale. Based on these values, we have built three 2D grids: "90% TKE", "80% TKE" and "70% TKE". The total number of nodes in the 3D mesh could be estimated as follows: the 2D slice is rotated 100 times around the jet axis plus 20% for the buffer zone. Table 5.4.1.3 provides the details of the grids employed.

Table 5.4.1.3 Number of nodes required for the LES (195ms^{-1}) when TKE is resolved by 90%, 80% and 70%.

	2D slice	3D	+20% buffer zones
90% TKE	245 960	$24.6 \cdot 10^6$	$29.5 \cdot 10^6$
80% TKE	73 920	$7.39 \cdot 10^6$	$8.87 \cdot 10^6$
70% TKE	29 070	$2.91 \cdot 10^6$	$3.50 \cdot 10^6$

Since the computational capacities are restricted, we are not able to run the cases with more than $3 - 4 \times 10^6$ nodes in total. This is the criteria on which we choose the feasible resolution of the turbulence kinetic energy spectra. The best resolved grid technically possible to perform the calculations is the grid "70% TKE". As a natural penalty of this restriction, we will not be able to resolve high-frequency noise ($St \geq 1$), which is caused by smaller turbulent structures. However we can afford to miss this information since only low- and mid-frequencies of the jet noise spectra are the focus of this thesis.

5.4.2 Grid for 3D LES simulations

The full 3D grid for the LES simulations (70% TKE) consists of five joint elements. We employ the joint elements structure in order to create a separate buffer zone, surrounding the finer region of the jet itself.

Figure 5.4.2.1 represents a sketch of the 2D slice of the 3D grid. The finest region of the grid, (1) is created based on 70% TKE. The second element is adjusted to the first element but it has a coarser structure. The third and fourth elements represent the buffer zone where the grid is stretched up to $50d$ in the radial direction. The fifth element is joined from the end of the domain and represents the buffer region up to $100d$ downstream. The 2D slice is rotated around the axis. The total number in the nodes in the 3D cylindrical domain is about $3.25 \cdot 10^6$ nodes. Figure 5.4.2.2 shows front and side views of the 3D grid.

The FWH acoustic analogy requires the definition of the source surface. The straight forward approach is to employ the surfaces that are created as a result of joining the grid elements. For example, the join surface between regions (1) and (2) elements is

an open cylinder with a radius $5d$ and length $30d$ – “FWH-5d”. However this surface is rather long in the axial direction in order to enclose the jet noise sources and it may not be wide enough to enclose all the sources in the radial direction. Therefore the second FWH surface is created, “FWH-10d”: the join surface between regions (2) and (3) elements - an open cylinder with radius $10d$ and length $30d$.

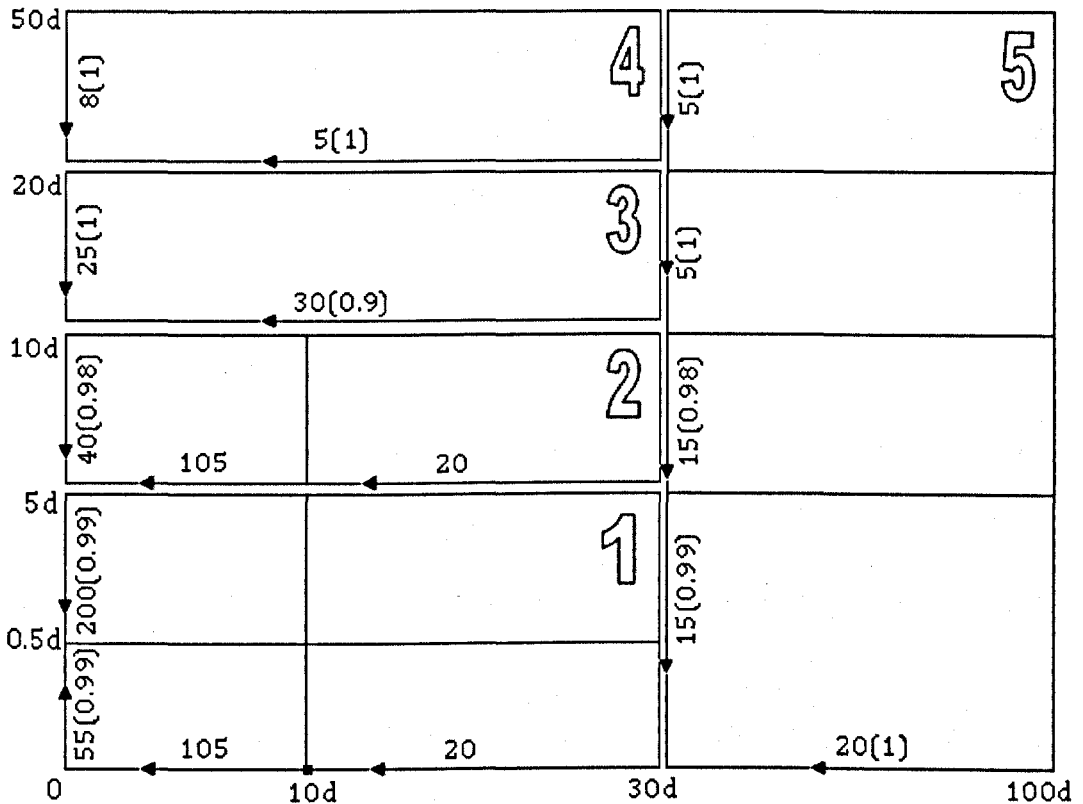


Figure 5.4.2.1 Sketch of the elements of the 2D axisymmetric slice of the 3D grid; geometrical dimensions are marked at the key points, the number of nodes in the thickening of the mesh size is shown by arrows and the stretching ratio is defined in round brackets.

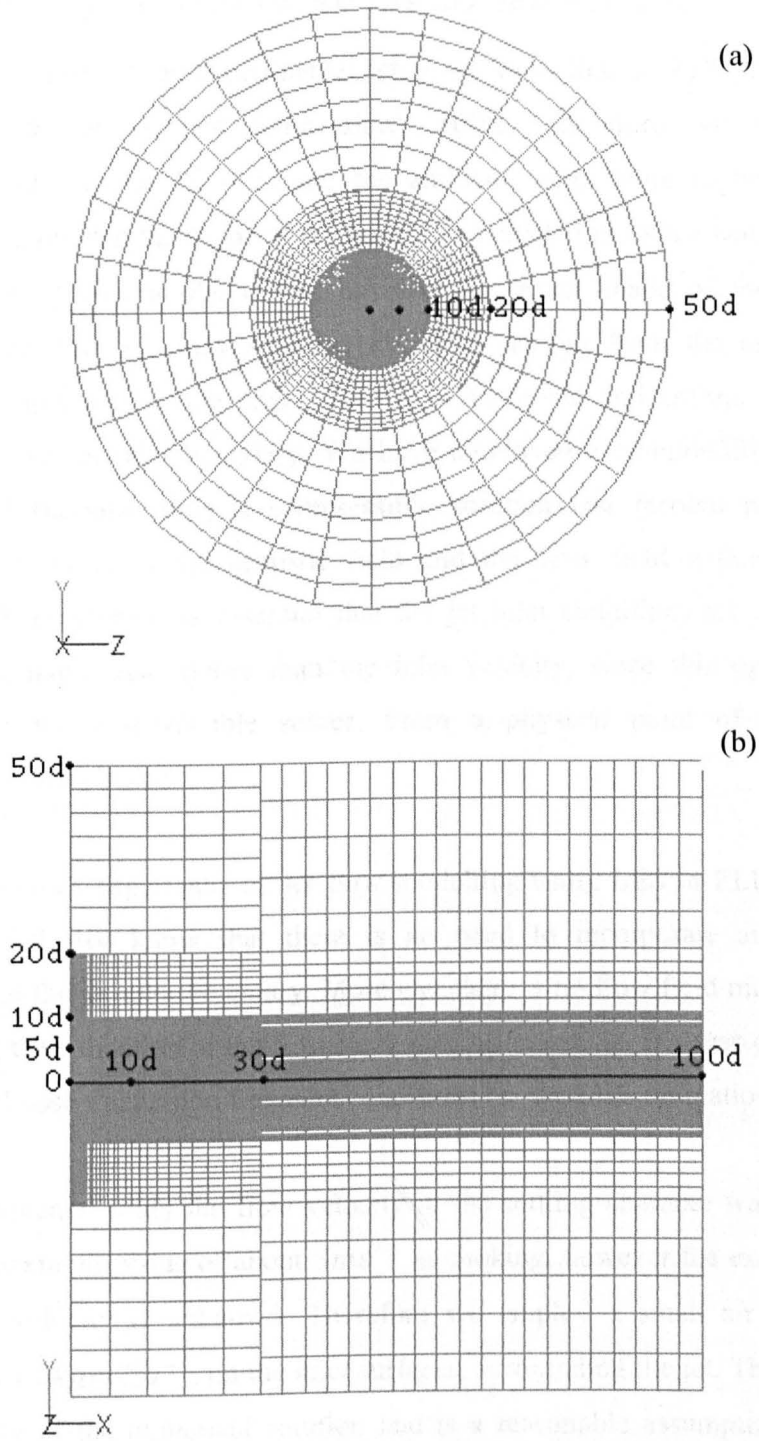


Figure 5.4.2.2 Grid for the LES computations: (a) front view, (b) side view of the 3D grid.

5.4.3 Boundary conditions for the 3D simulations

From the description of the experimental setup, we know that the bulk jet velocity is 195ms^{-1} with an ambient temperature, 300K . Therefore we specify the temperature ratio to be $TR = 1$, and the ambient temperature to be 300K . In addition, we know that the shape of the nozzle was created in such a way to produce a flat velocity profile at the outlet, however the exact shape of the nozzle is unknown. Therefore we may simulate the flow starting from the nozzle edge, ignoring the thickness of the edge, since it is unknown, and enforce a flat inlet condition on the jet inlet boundary. We have employed a compressible solver in FLUENT 12 (because only a compressible solution can resolve properly the complex interactions of the acoustic field and the flow field within the FWH surface), and therefore it is essential that the jet inlet conditions are specified in terms of the mass flux, rather than the inlet velocity, since this option is not available for the compressible solver. From a physical point of view, both formulations are the same.

From our previous experience on jet flow modelling using LES in FLUENT 12.0, see Chapters 4, we know that there is no need to incorporate any artificial fluctuations at the jet inlet boundary. Moreover there is no flow field measurements available for the validation of the flow field simulation results. Because of these two factors, we choose fluctuation free inlet conditions for the LES simulations.

In the experimental study the flow velocity in the settling chamber was very low, rising to a maximum value of about 5ms^{-1} at choking, however the exact value of the co-flow velocity is unknown. Therefore we employ a small air mass flux, approximately $5\text{kgm}^{-2}\text{s}^{-1}$, on the inlet surfaces, surrounding the jet. This approach helps stability of the numerical solution and is a reasonable assumption, since in reality we always observe a small co-flow, caused by natural convection of the air in the laboratory.

The outlet boundaries are specified as pressure-outlet with a fixed pressure equal to the atmospheric pressure level. In general, the fixed pressure at the outlet could reflect the noise back into the domain. In order to avoid these reflection effects in the region of the jet flow, we have introduced very large buffer zones near the

pressure outlet boundaries. The coarse resolution of the buffer zones introduces extra numerical viscosity, and this damps all the reflected waves inside this region.

The material properties of the air are set to the default constants, except the density which is defined to obey the ideal-gas law, i.e. the option for the compressible case.

A summary of the boundary conditions employed is presented in table 5.4.3.1.

Table 5.4.3.1: Summary of the boundary conditions for LES simulations.

<i>BC type in FLUENT</i>	<i>Details</i>
Mass flux jet inlet	Flat profile: $195ms^{-1} \times 1.225kgm^{-3} =$ $238.875kg \cdot m^{-2}s^{-1}$, Total temperature 300K.
Mass flux in the co-flow air	$5kg \cdot m^{-2}s^{-1}$, Total temperature 300K.
Pressure outlet in the axial direction	Gauge pressure 0Pa, Turbulent intensity 5%, Viscosity ratio 5.
Pressure outlet in the radial direction	Gauge pressure 0Pa, Back flow: Turbulent intensity 5%, Viscosity ratio 5, Total temperature 300K.

The numerical strategy adopted for the LES computations is described in Section 3.6.4. Here we briefly describe the main stages of the CFD simulations. Firstly, we start by simulating the steady flow field using the $k - \epsilon$ RANS model. Then, when the solution has converged, we switch to the LES solver with the time-step equal to $dt = 5 \cdot 10^{-6}s$. The choice of the time-step is based on the acoustic wave resolution, namely $dt = 5 \cdot 10^{-6}s$ - is the time-step required for resolving frequencies up to 20 000Hz. The LES should run at least several mean flow residence times, L/U (where L is the characteristic length of the solution domain and U is the characteristic mean flow velocity). The residence time for this simulation is $2.5m/195ms^{-1} \cong 0.013s$. Therefore the minimum required number of time-steps is 15 000, based on 6 residence times. Finally, after 15 000 time-steps we switch on the FHW acoustic model. In principle we can run simulations longer and this will not substantially affect the solution. However it is recommended not to

reduce this number of iterations in order to keep a safe amount of data for accurate averaging. For the FFT analysis of the acoustic signal we employ 4 000 time-steps. This defines the minimum resolved acoustic frequency, $f_{min} = \frac{1}{4000 \times 5 \cdot 10^{-6}} = 50\text{Hz}$.

5.4.4 Acoustic results

We use the FWH acoustic model to simulate the acoustic signal at the receiver positions. It was shown in Chapters 4 that the most appropriate FWH surface is a simple open cylindrical surface centred on the jet axis with a radius of 10 nozzle diameters (250mm). The experimentally measured data was analysed and published in terms of $\frac{1}{3}$ – octave intensity, obtained for fixed Strouhal number values, $St = \frac{fD}{v_j}$: 0.03, 0.1, 0.3 and 1. For this reason we report out simulation results in the $\frac{1}{3}$ – octave range and choose values corresponding to fixed Strouhal numbers expressed in terms of the frequency parameter defined by expression (5.2.1.1). For the jet with a velocity of 195ms^{-1} and nozzle diameter of 0.025m , we may obtain frequencies for each angular position by multiplying the fixed Strouhal number by $(U_j/D)(1 - M_c \cos \theta)^{-1}$ (Lighthill dimensional analysis).

Figure 5.4.4.1 represents the noise simulation results compared with the experimental data, obtained by Lush (1971) for the jet with a velocity of 195ms^{-1} . In general, we may observe that the simulation is able to predict the order of magnitude of the noise level. The simulation results for $St = 0.1$ are in remarkably good agreement with the experimental data for all microphone positions, except very small and very large angles of the microphones, namely we have underpredicted the noise level at 15° by about 9dB and overpredict at 105° by about 8dB.

The discrepancy between experimental and numerical data, 9dB, of the noise level at the 15° microphone position can be referred to uncertainties in the experimental studies, because it is practically very difficult to measure the acoustic noise at such a small angle of acoustic radiation and avoid a “pseudo-noise” contribution, caused by the turbulence of the jet flow. The detecting microphones, which are positioned close to the jet axis, are inevitably affected by the incoming flow from the jet. Therefore the recorded pressure fluctuations incorporate “pseudo-noise” contributions, which in turn artificially increase the noise level.

The numerical over estimation of the acoustic field at 105° for 8dB can be attributed to the configuration of the computational domain employed for this study. We created the computational domain starting from the edge of the nozzle lip, which comfortably resolves the acoustic field distribution from -90° to $+90^\circ$ degrees (because this is the region of major importance for acoustic radiation from the jet), while the noise at the 105° degrees microphone position is estimated without full information of the acoustic sources in the field. We can expect that in reality part of the noise generated downstream in reality is absorbed by the flow upstream from the nozzle (which is especially the case for low frequencies noise components). Therefore the measured noise level is lower than that numerically predicted. Nevertheless we obtained remarkably good results for microphones placed between 30° and 90° angles.

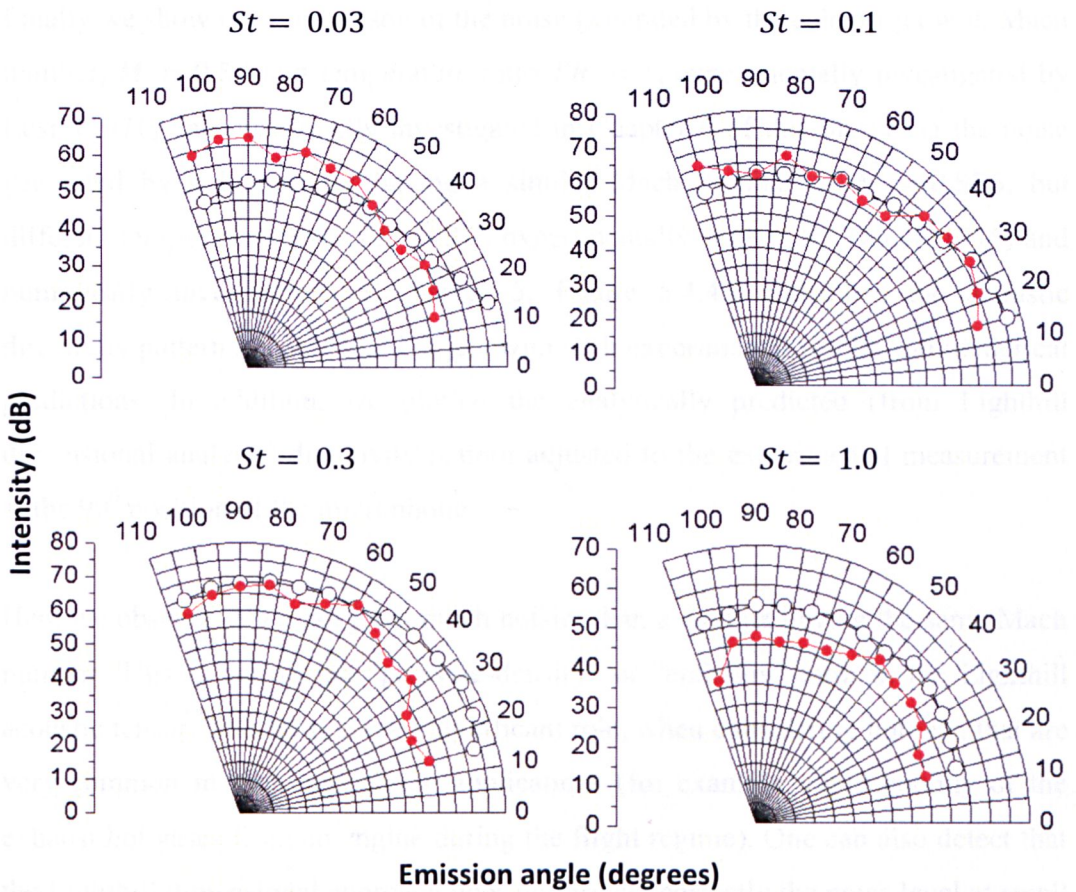


Figure 5.4.4.1 Directivity of the $\frac{1}{3}$ -octave intensity for a jet velocity 195ms^{-1} and for four values of the Strouhal number. Legend: red symbols – simulation results, white symbols – experimental data obtained by Lush (1971).

In figure 5.4.4.1 one may observe that the numerical predictions of the acoustic field in the high frequency range ($St = 1.0$) are underpredicted for at all microphone positions. This is an expected result, and it is caused by the choice of the computational grid discretization, namely 70% *TKE*. In other words, the computational grid employed for this study is able to resolve correctly up to 70% of the energy containing turbulent structures, while in the remaining 30%, then the smallest turbulent vortices are modeled by the subgrid scale model in the LES solver. The smallest turbulent structures are responsible for the high frequency noise generation. Therefore since we did not resolve them accurately enough, and in order to reduce the computationally effort for the LES simulations, the numerically predicted acoustic field is lower at all microphone positions than that measured in the experiment performed by Lush (1971). This is the price to be paid for obtaining less computationally expensive but still accurate simulations.

Finally we show the comparison of the noise generated by the cold air jet with Mach number, $M = 0.56$ and temperature ratio $TR = 1$, experimentally investigated by Lush (1971) and numerically investigated in Chapter 6 of this thesis via the noise generated by a hot air jet having a similar Mach number of $M = 0.556$, but different temperature ratio, $TR = 2.7$, experimentally studied by Tanna (1976) and numerically investigated in Chapter 5. Figure 5.4.4.2 illustrates the acoustic directivity pattern for cold and hot jets with both experimental results and numerical predictions. In addition, we plotted the analytically predicted (from Lighthill dimensional analysis) directivity pattern adjusted to the experimental measurement at the 90° position of the microphone.

Here we observe that a hot jet is much noisier than a cold jet having the same Mach number. This is due to the “pressure-density” or “enthalpy” term in the Lighthill acoustic tensor. This term plays a significant role, when considering hot jets, that are very common in real engineering applications (for example: rapid cooling of the exhaust hot gases from an engine during the flight regime). One can also detect that the Lighthill dimensional approach does not predict correctly the noise level at small angle to the jet axis positions of microphone. We already mentioned the practical difficulties in measurements of the acoustic level at these positions. Therefore the CFD modelling can be considered as the only reliable alternative to the experimental

study and analytical formulation for estimating the noise close to the jet exit directions.

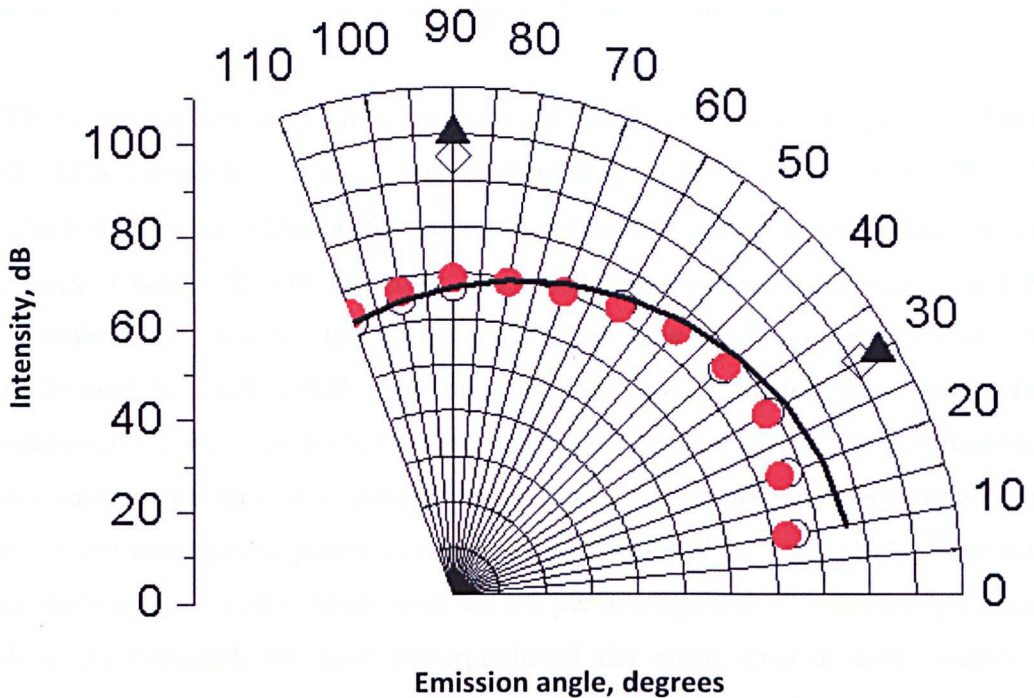


Figure 5.4.4.2 Theoretically predicted directivity compared with the experimentally measured values and the simulation results.

Legend: black triangle – LES simulation result for hot air jet (Chapter 6), diamond– experimental data by Tanna (1976) for hot air jet, circle – experimental data by Lush(1971) for cold air jet, red circle - LES simulation results for cold air jet, black line - theory adjusted to the experimental measurements at 90°.

5.5 Conclusions

A cold air jet has been investigated numerically. For validation of the simulation results we have employed the experimentally measured values for the acoustic field obtained by Lush (1971).

A set of 2D simulations using the RANS(RSM) axisymmetric solver has been performed. Here we have studied the grid dependency of the numerical solutions, while the size of the computation domain and the position of the FWH surface have been adopted from previous studies of cold propane jet (Chapter 4). The semi-empirical Goldstein acoustic analogy was applied to a steady-state 2D RANS solution of the flow field in order to obtain the directivity pattern for the acoustic

field of the jet. The theoretical predictions were adjusted to the experimental measurement at the 90° position of the microphone (model requires adjustment to the experimental values at certain positions). The resulting curves show very good agreement with the experimentally measured data at all microphone positions.

The numerical investigations of the jet in the 3D calculations were performed using the LES approach. The mesh was built in way to be able to resolve 70% *TKE*, which was found sufficient for the low- and mid-frequency ranges of the acoustic energy (Chapter 4). For the noise level predictions we have employed the FWH acoustic model, realised in FLUENT 12.0. The flow field measurements were not performed by Lush (1971) and therefore we have validated the velocity field numerical results with the hot air jet (similar conditions, $M = 0.56$) experimentally measured by Panda et al. (2004). Then the acoustic simulation results were validated for seven microphone positions as originally employed by Lush (1971). The noise predictions are found to be in good, but not perfect, agreement with the experimental data. As expected, we have underpredicted the noise level at high frequencies ($St = 1.0$). This is due to the small turbulent structures of the jet which are not resolved by our mesh. However, in general, the LES-FWH approach demonstrates the ability to capture the spectra shape correctly and give the noise values that are within a 10% error bar. The simulation results are promising since we can employ a rather coarse mesh for obtaining accurate results for the acoustic field.

Chapter 6

Hot Air Jet Simulations

6.1 Introduction

A literature search into the published experimental data has been made in order to find suitable data for a simple configuration of a nozzle shape, low Mach number jet where both the velocity field and the acoustics have been measured in detail. We have found that an experimental work performed by NASA 2004 satisfies, in general, the search conditions. However in Panda et al. (2004) the noise data is presented in more detail than the corresponding velocity field, where only the mass flux, U_{mean} and U_{rms} components have been measured and these at just one radial section which is at a distance $x/d = 3$ from the nozzle of the jet. This radial section is relatively close to the nozzle outlet and therefore is much under the influence of the initial boundary conditions of the experimental setup. In addition, the experimental jet is hot with the temperature ratio, namely the ratio of the plume static temperature to the ambient temperature, $TR = 2.7$, and this could produce a complex effect on the numerical noise simulations.

6.2 Experimental setup

The experiment was performed in the Small Hot Jet Acoustic Rig in the Aeroacoustics Propulsion Laboratory (AAPL) of NASA Glenn Research Centre. AAPL is a 60ft (20m) radius, anechoic, geodesic-dome. The walls of the dome, and approximately half of the floor area, were treated with acoustic wedges made from fibreglass wool in order to render the facility anechoic above about 220Hz. A 60in (1.5m) exhaust fan in the top of the dome provides the air recirculation. Air flows from all the rigs are directed out through a 55ft (16.8m) wide by 35ft (10.7m) high doorway to an open field. The jet facility is capable of producing a heated jet with a temperature ranging from ambient to about 920K in the Mach number range $0 < M < 2$, and therefore it is ideal for studying the effect of heating the jet.

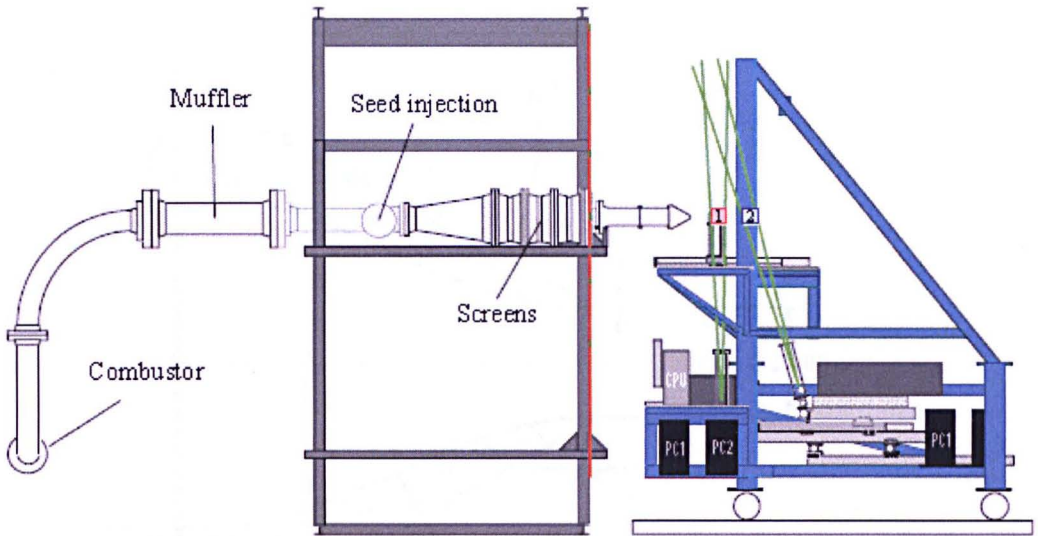


Figure 6.2.1. NASA Dual PIV setup, from Panda et al. (2004).

Two PIV systems were used in this experimental investigation, and they are tied together via a triggering circuit with a variable time delay. Each PIV system consists of a dual headed Nd:YAG laser system, which operates at 532nm and generates a 400 mJ/puls light sheet containing the axis of the jet. Figure 6.2.1 shows the optical layer relative to the jet rig. For more details of the experimental setup, see Bridges and Wernet (2003).

A 2in (50.8mm) diameter convergent nozzle was used for all the measurement condition investigated, see figure 6.2.2, and the operating conditions are shown in table 6.2.1. While the acoustic Mach number is close to unity, the jet Mach number is low, namely 0.6. Therefore the compressibility effects are not strong for the jet under investigation. The jet Reynolds number is about 190 000 and the temperature ratio is about $TR = 2.7$, having a 821K plenum temperature of the jet.

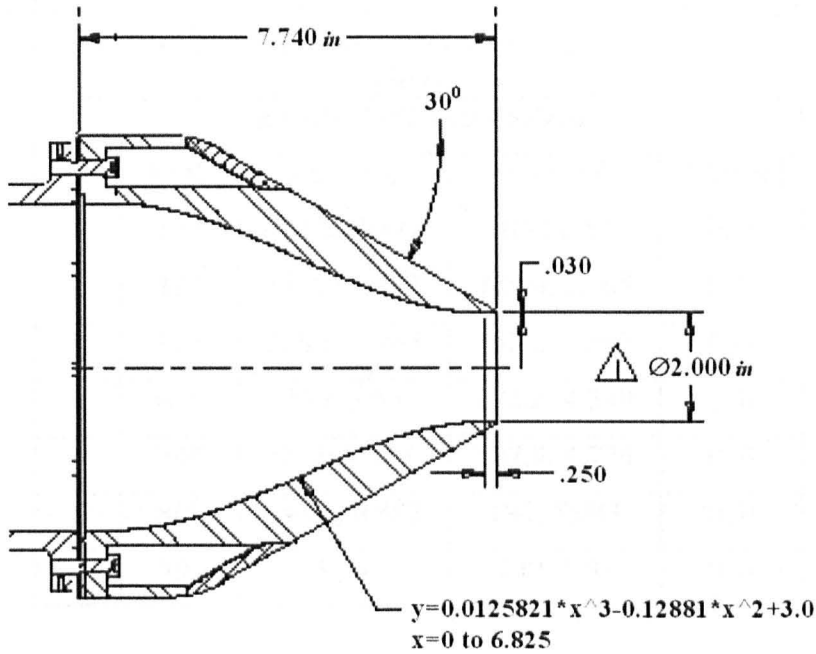


Figure 6.2.2. The NASA Acoustic reference nozzle system, with an ARN2 (2in) nozzle, see Bridges and Wernet (2003).

Table 6.2.1 Operating conditions of the NASA experiment.

$M_a = \frac{U_j}{a_0}$	$TR = \frac{T_j}{T_a}$	$T_{plen}(K)$	$M_j = \frac{U_j}{a_j}$	$U_j \left(\frac{m}{s} \right)$	$\frac{\rho_j}{\rho_a}$	$Re \times 10^6$
0.9	2.7	821	0.557	306	0.37	0.19

The far field sound pressure fluctuations were measured by an array of seven $1/4 \text{ in}$ (6.35 mm) microphones which are situated on an arc of radius $100d$ (5.08 m) and centred at the nozzle exit. The microphones were angularly placed at 10° increments: from 150° to 90° to the direction of the jet exit. Table 6.2.2 summarizes the position of microphones in the NASA experiment. Tanna et al. (1976) measured the acoustic field from the microphones positioned on a 72 diameter arc at angles 150° , 90° and 60° . Table 6.2.3 summarizes the position of microphones in the Tanna et al. (1976) experiment. At NASA, the experiment microphone polar angles were measured from the flight direction, which means that, for example, the angle from the jet axis of 30° corresponds to the angle 150° from the flight direction. The presence of the large traversing unit in the experimental equipment, optical components and other metal surfaces are a concern for significant acoustic reflection. To minimize such reflections, a large part of the metal surfaces were covered with a 50 mm thick polyurethane foam.

Table 6.2.2 Coordinates of the microphone locations (where the angle is measured from the jet direction) in inches and meters in the NASA experiment, Panda et al. (2004).

R = 100d = 200in = 5.08m				
N	Angle	X[in; m]	Y[in; m]	Z[in; m]
1	30 ⁰	173.2; 4.399	100; 2.54	0; 0
2	40 ⁰	153.2; 3.892	128.6; 3.265	0; 0
3	50 ⁰	128.6; 3.265	153.2; 3.892	0; 0
4	60 ⁰	100; 2.54	173.2; 4.399	0; 0
5	70 ⁰	68.4; 1.737	187.9; 4.774	0; 0
6	80 ⁰	34.73; 0.882	197; 5.003	0; 0
7	90 ⁰	0; 0	200; 5.08	0; 0

Table 6.2.3 Coordinates of the microphone locations (where the angle is measured from the jet direction) in inches and meters in the Tanna et al. (1976) experiment.

R = 72d = 144in = 3.658m				
N	Angle	X[in; m]	Y[in; m]	Z[in; m]
1	30 ⁰	124.7; 3.168	72; 1.829	0; 0
2	90 ⁰	0; 0	144; 3.658	0; 0

6.2.1 Experimental data: flow field

The experimental data which is employed in the flow validation presented in Panda et al. (2004) includes the mean and fluctuating velocity components measured at the radial section placed at the fixed axial position of $x/d = 3$. The velocity data were measured using the PIV system described above. Figure 6.2.1.1 represents a plot of the mean axial velocity measurement at the radial section placed at the fixed axial position of $x/d = 3$ obtained by Bridges and Wernet (2003). It is clear from the figure that the mean velocity component goes to zero at a distance of about 2in from the axis of the jet. This implies that there is no significant co-flow around the jet. However Panda et al. (2004) mention that the co-flow has a velocity of up to $20ms^{-1}$, but the experimental data demonstrates that there is none. Therefore it appears to be reasonable to exclude any co-flow around the jet in our numerical simulations, except it may be appropriate to assume that there is a very low co-flow with a speed of about $5ms^{-1}$ in order to improve the numerical stability. The

numerical solution in the jet flow is not sensitive to small co-flow velocities (up to 10 m s^{-1}).

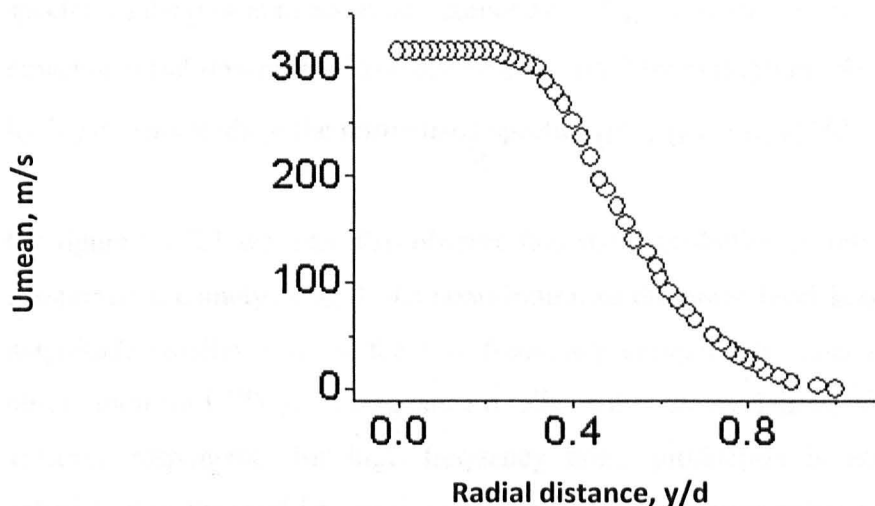


Figure 6.2.1.1 Radial profiles of the mean axial velocity component from a fixed axial position of $x/d = 3$. The axial velocity data were from the PIV measurements of Bridges and Wernet (2003).

6.2.2. Experimental data: acoustic field

For validation, the experimental data on the noise measurements reported by Panda et al. (2004) are not very clear. For example figure 6.2.2.1 illustrates the noise measurement at two positions of the receiver for a jet with various temperatures. For validation purposes we have chosen only one temperature regime $TR = 2.7$, because the Mach number of the flow is low, and therefore we have concentrated only on this set of data.

The noise is represented by normalized pressure fluctuations that are detected at the position of the receiver. The authors intention is to non-dimensionalize the power-spectral-density (PSD) in order to make the results more universal. When one does power-spectrum calculations from a sequence of data then this provides us with the power, i.e. the square of the pressure fluctuations, within a frequency interval Δf . This Δf depends on the time step as well as the number of points used for the Fourier transform. In order to make the spectrum independent of the time step, the authors have divided the power by the frequency resolution, Δf . This provides us

with the power-spectral-density: pressure-fluctuations-squared/Hz. The pressure fluctuations are normalized by the difference between the density of the jet and the density of the ambient flow. Next we need to normalize the '/Hz' part of the power-spectral-density, pressure-fluctuations-squared/Hz. The x-axis for the normalized spectra on the plot is in Strouhal number $St = fd/U_j$; therefore the '/Hz' part in the power-spectral-density is also converted to '/ ΔSt ' by multiplying the spectral values by U_j/d . This leads to the normalized spectra: $\{p'^2/(\rho_j - \rho_a)\}/\Delta St$.

On figure 6.2.2.1 we may also observe that the contribution of the high frequency components, namely $St \geq 0$, the contribution of the noise level is of two orders of magnitude smaller than of the low frequency components. This is an important observation for CFD modelling since it tells us that the modelling of small turbulent vortices responsible for high frequency noise production is not essential for calculation of the total jet noise contribution. In other words we may omit the small (to certain extent) turbulent vortices in the LES turbulence model without lacking accuracy in the noise prediction. However it is important to establish a criterion on what size of vortices can be considered as small.

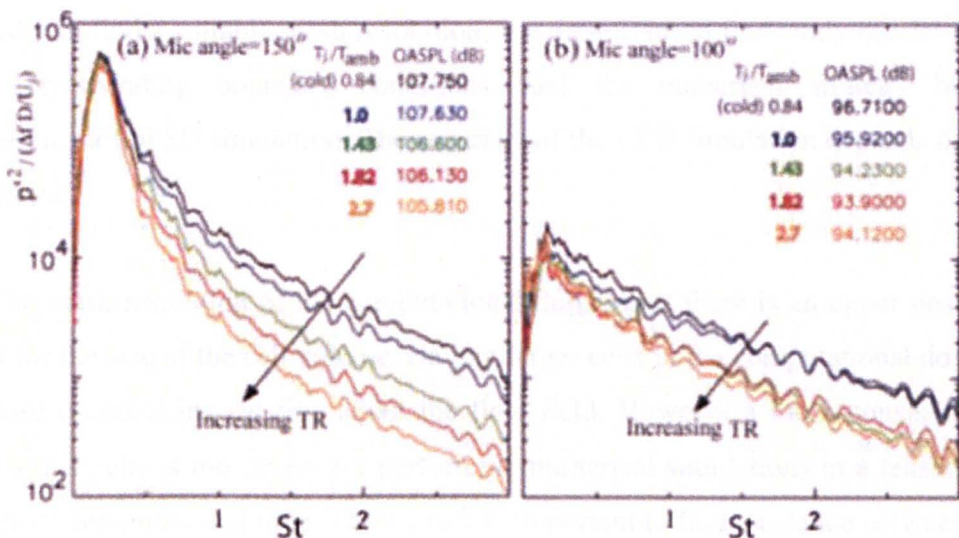


Figure 6.2.2.1 The effect of the heating of the narrowband spectra of the jet, Panda et al. (2004).

For validation purposes we may also employ the noise measurements obtained by Tanna et al. (1976) for a jet operating with the same conditions. Figure 6.2.2.2 illustrate the SPL (Sound Pressure Level) detected at three microphone positions. The SPL format is much clearer for interpretation, than dimensional units used by

Panda et al. (2004). It is interesting that we observe a distinctive pitch at the noise level detected at the 30° to the jet axis microphone position. The jet noise measured at the 90° and 130° microphone positions are more of a broad band nature.

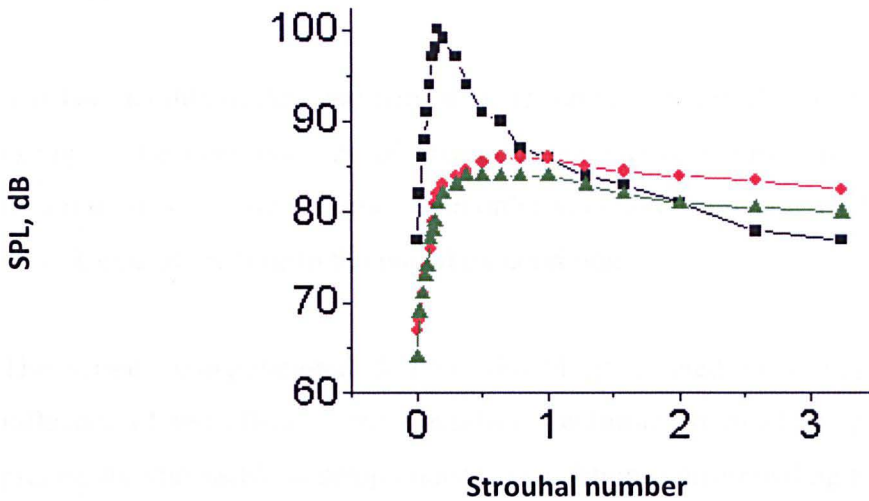


Figure 6.2.2.2 Far field noise spectra measured for different microphone position angles, Tanna et al.(1976). Legend: black symbols – at 30° ; green symbols – at 90° and red symbols – at 130° from the jet axis.

6.3 Simulations

In order to find a suitable mesh resolution, it is important to first study the 2D case, the corresponding boundary conditions, and the numerical strategy before attempting a full 3D simulation. The accuracy of the CFD simulation depends on the following:

(i) The mesh resolution of the computational domain, as there is an upper possible limit for the size of the cell volume. Having larger cells in the computational domain we lose essential information about the flow field. However a mesh consisting of very small cells is too severe for performing numerical simulations in a reasonable length of computational time. Therefore it is important to find a balance between the numerical accuracy and the computational time. Usually the upper limit for the mesh resolution is found by running several sets of sample cases with a gradually increasing mesh resolution.

(ii) The influence of the boundary conditions could be crucial for the accuracy of the numerical simulation. The choice of a particular type of the boundary condition

depends strongly on the geometry of the problem investigated and its physical nature. It is good practice to run sample cases for a simplified mesh (for example the 2D case) with different boundary condition setups in order to choose the best combination.

(iii) The stability of the simulation depends on the numerical strategy employed. For example, the consequences of changing the turbulent viscosity models and the material properties with a time lag in order to obtain a converged solution after each new change of the type in the boundary condition.

The sample computational domain should be created in a way to reduce the influence of the effect of the boundary conditions as much as possible, as it is practically impossible to setup boundary conditions corresponding to what occurs in reality. This is because, for example, there will be always a problem of reflections of the flow back into the domain from the fixed pressure outlet boundary. In general, one makes the computational domain so large that any reflections from the pressure boundary will be damped by the coarse mesh. Hence the numerical viscosity is increased in a region where there is a coarse mesh. Therefore the small flow motion that is caused by reflections from the boundary is damped. In other words, the region of interest with a fine mesh is surrounded by a large damping zone with a coarser mesh. In the inlet zone, the problem of numerical errors could appear if two flows with a relatively large velocity difference are not separated by a nozzle wall. However in this thesis we consider the case when the nozzle lip thickness is ignored.

6.3.1 Grid employed in the simulations

Figure 6.3.1(1), shows a sketch of the first element of the 2D mesh, and this illustrates the configuration of the computational domain employed to accurately resolve the jet flow region. It is an axisymmetric case where the axis is on the bottom of the domain. The region of interest extends to $100in$ (50 nozzle diameters) in the downstream direction (x -direction) and is diverging in the y -direction with an increment of 3%, which has been estimated to be a suitable value during the test simulations. The region covering the potential core is found to be approximately $10in$ in the downstream direction (x -direction) and is resolved by the finest mesh. This mesh has a successive ratio of 0.99 (1% increment from one cell size to

another) in both directions. The region includes most of the mixing layer of the jet. The mesh in the region from 0 to 100in in the x -direction and from 0 to 1in in the y -direction is structured and without any slope gradient. Starting from 10in, the mesh is stretched with an increment of 3% (successive ratio equal to 0.97). The direction of the thickening is marked by the arrows. The number of spacing intervals along the edge is labelled by the numbers with a successive coefficient is in brackets.

The region from 0 to 100in in the x -direction, and from 1in to 5in in the y -direction, is well resolved by the structured mesh with a small slope gradient equal to 3%. The small 3% slope of the cell is acceptable for numerical calculations. The number of spacing intervals along the x -direction repeats corresponding intervals on the axis. The number of spacing intervals along the y -direction is 80, with an increment equal to 1% (successive ratio equal to 0.99) thickening towards the nozzle lip. The number of nodes in the first 2D mesh element is 20 900.

As mentioned above, the region of interest (first element) with a fine mesh should be surrounded by a damping zone with a coarser mesh in order to eliminate the effect of the reflection on the boundaries of the computational domain. The damping zone is composed of several parts in our case. The reason behind this is to find an appropriate position of the boundary in the far field by composing the computational domain of an increasing number of the damping zone elements and extending in this way the far field boundary out from the jet axis.

Figure 6.3.1(2) is a sketch of the second element of the 2D mesh. It illustrates the configuration of the computational domain created to match the first element and place the far field boundary at 15in in the y -direction. The region from 0 to 100in in the x -direction, and from 5in/8in to 15in in the y -direction, is resolved by a structured mesh with a small slope gradient equal to 3%. The number of spacing intervals along the x -direction is halved compared to the corresponding intervals of the first element, namely 90 cells along the x -direction in the second element vs. 190 cells along the x -direction in the first element. In addition, there is no stretching applied to the spacing intervals along the x -direction. Therefore the joint mesh between the first and the second elements is not smooth, which is not ideal but

acceptable by the FLUENT solver, and we do not expect large numerical errors caused by this discrepancy since the flow in the region at the break is expected to be very slow. The number of spacing intervals along the y -direction is 80 with an increment equal to 2% (successive ratio equal to 0.98) thickening towards the axis. There is also a two times jump in the spacing interval in the y -direction from the first element to the second element of the mesh. The number of nodes in the second 2D mesh element is 7 200.

Figure 6.3.1(3) shows a sketch of the third element of the 2D mesh. It illustrates the configuration of the computational domain created to match the second element and place the far field boundary at $30in$ in the y -direction. The rectangular region from 0 to $100in$ in the x -direction, and from $15in$ to $30in$ in the y -direction is resolved by a coarse structured mesh. The number of spacing intervals along the x -direction is half that compared to the corresponding intervals of the second element, namely 45 cells along the x -direction in the third element vs. 90 cells along x -direction in the second element. As for the second element, there is no stretching applied to the spacing intervals in the x -direction. The number of spacing intervals in the y -direction is 15, with an increment equal to 4% (successive ratio equal to 0.96) thickening towards the bottom face. The number of nodes in the third 2D mesh element is 675.

A sketch of the fourth element is shown in figure 6.3.1(4). The configuration of the computational domain is rectangular in order to match the third element and place the far field boundary at a distance of $60in$ in the y -direction. The region from 0 to $100in$ in the x -direction and from $30in$ to $60in$ in the y -direction is resolved by a coarse structured mesh with 15 spacing intervals and an increment equal to 4% (successive ratio equal to 0.96) thickening towards the bottom face. Although the number of the spacing intervals is the same as for the third element but they are stretched along twice the longer edge, which makes the mesh of the fourth element coarser and keeping the structure of the mesh cells the same as for the third element. The number of spacing intervals in the x -direction is half that compared to the third element, namely 25 cells vs. 45 cells third element. No stretching is applied to the spacing intervals in the x -direction. The number of nodes in the fourth 2D mesh element is 375.

The fifth element is plotted in figure 6.3.1(5). The configuration of the computational domain is rectangular in order to match the fourth element and it is placed on the far field boundary at a distance of $90in$ in the y -direction. The region from 0 to $100in$ in the x -direction and from $30in$ to $60in$ in the y -direction is resolved by a very coarse structured mesh with only 8 spacing intervals and with increments of 10% thickening towards the bottom face. The number of spacing intervals in the x -direction is half that compared to the fourth element, namely 12 cells vs. 25 cells for the fourth element. No stretching is applied to the spacing intervals in the x -direction. The number of nodes in the fourth 2D mesh element is 96.

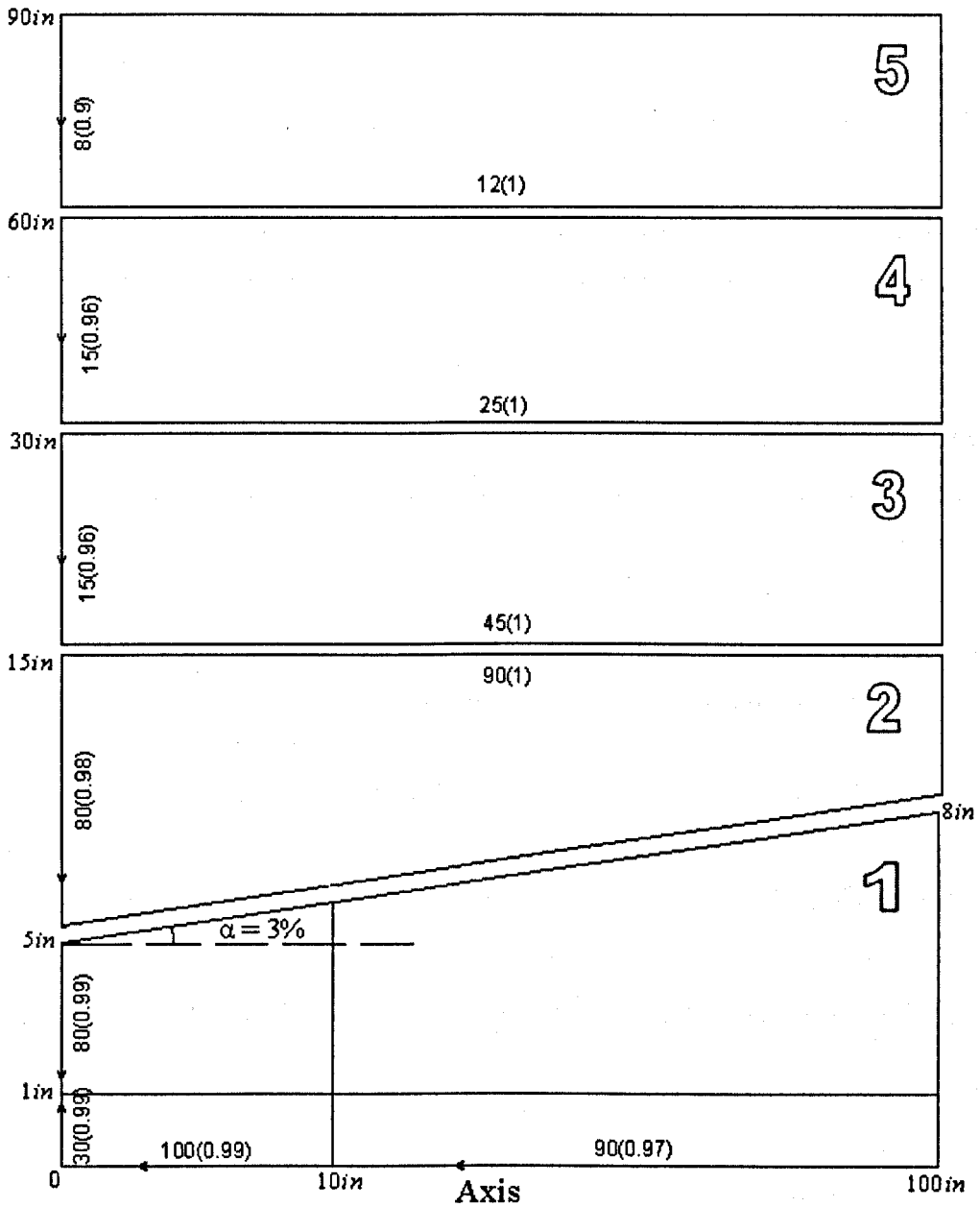


Figure 6.3.1 Sketch of the elements of the 2D grid; geometrical dimensions are marked at the key points, the number of nodes thickening of the mesh size is shown by arrows and the stretching ratio is defined in round brackets.

In order to generate the inlet profile for the jet flow simulations, we have created the outlet part of the nozzle simulating the flow conditions used in the experimental investigation of the jet noise. Figure 6.3.2 shows a sketch of the nozzle in the 2D mesh. It illustrates the configuration of the computational domain created to match the first element inlet boundary. The axisymmetric region, from -7.74in to 0 in the x -direction and from 0 to 3in converging to 1in in the y -direction is resolved by a structured mesh. The number of spacing intervals in the y -direction is equal to the

corresponding number of spacing intervals at the jet inlet of the first element, see Figure 6.3.1, with the same successive ratio, namely 30 cells with a successive ratio of 0.99 thickening towards the nozzle lip. The number of spacing intervals in the x -direction is 50 and with an increment of 1% thickening towards the nozzle lip. The number of nodes in the 2D mesh is 1 500 and in 3D is 129 600. The simulation of the flow inside the nozzle is simulated separately (and in advance) from the jet flow simulation.

In order to extend the 2D mesh to the 3D case, we create a 45° slice of the 3D cylinder (axis of the cylinder is along the flow direction) based on the 2D element where there are 12 equally spaced intervals on the arc. After that the 3D slice is repeated 7 times to complete the full 3D domain and the duplicated surfaces are joined. Table 6.3.1 summarize the size of each element and the total number of nodes for a joined 2D mesh and the final 3D mesh. The resulting most dense mesh slightly exceeds 2.2 million nodes.

It should be noted that the mesh was created in GAMBIT. The dimensions were fixed in inches times 1000 which is done in order to improve the accuracy of the mesh. The rescaling back to the original SI units was done in FLUENT after all the elements were joined together. The joining surfaces of the elements are labelled as “interior” with corresponding names, and then these surfaces are merged to interfaces in FLUENT 12 using the “mesh interfaces” option.

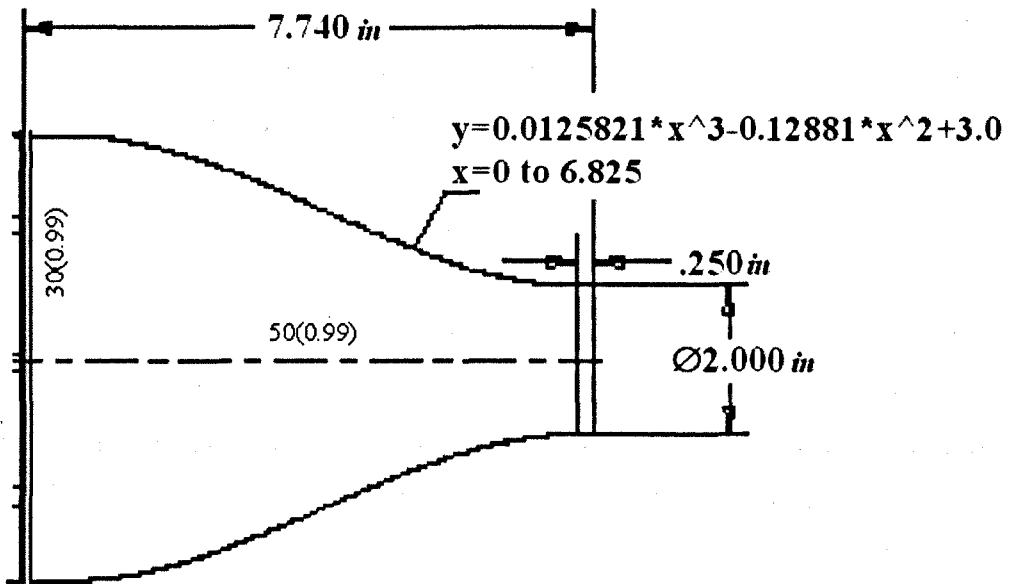


Figure 6.3.2. Sketch of the of the 2D slice of the nozzle; geometrical dimensions are marked at the key points, the number of nodes of the mesh size is shown and stretching ratio is defined in round brackets.

Table 6.3.1 Structural elements of the mesh.

Mesh element	Nodes, 2D	Total, 2D	Nodes, 3D	Total, 3D
First (jet region)	20 900	20 900	1 951 680	1 951 680
Second (BC at 15in)	7 200	28 100	172 800	2 124 480
Third (BC at 30in)	675	28 775	64 800	2 189 280
Fourth (BC at 60in)	375	29 150	36 000	2 225 280
Fifth (BC at 90in)	96	29 246	9 216	2 234 496
Nozzle	1 500	-	129 600	-

For the space resolution, let us estimate the grid resolution with respect to the requirements of the acoustic wave resolution. The acoustic pitch in the NASA experiment is found to be about $St = 0.16$, $f = 1000\text{Hz}$. To capture this pitch we have to resolve waves with a frequency up to 2000Hz . If $f = \frac{c_0}{\lambda}$, then λ , the acoustic wavelength, is about 0.17m . Each wavelength, λ , should be resolved by 20 – 30 grid points, Richards et al. (2004). Therefore the grid resolution must be about 5.7mm for $\frac{\lambda}{30}$ and 8.5mm for $\frac{\lambda}{20}$. It is very important to carefully resolve a region where the mixing process is taking place. This region usually occupies the region from the nozzle lip to about 8 nozzle diameters downstream and about 5 nozzle diameters in the y -direction. In the case presented, the maximum space step in the x -direction is 4mm in the region from 0 to 5 nozzle diameters downstream, and the

maximum space step in the y -direction is 2mm in the region from 0 to 5 nozzle diameters. It is clear that a mixing region is well resolved by this mesh. We have indicated that this mesh is fine enough to accurately resolve acoustic waves with a frequency up to 2000Hz .

6.3.2 Boundary conditions and simulation strategy

We consider three modifications to the jet flow computational domain in order to find the most appropriate position of the grid boundary which does not have a substantial influence on the flow field results as well as on the noise simulation results. In particular, the noise simulation results appear to be more sensitive to the reflection effects from the boundary and therefore we report the noise simulation results for each case as the most important ones. Each case consists of joined grid elements as described in Subsection 6.3.1. The details of all the cases investigated are listed in table 6.3.2.1.

Table 6.3.2.1 *Details of the simulation cases.*

<i>Case</i>	<i>Grid elements</i>	<i>BC position</i>	<i>Total, 2D</i>	<i>Total, 3D</i>
Case 1	1 + 2 + 3	at 30in	28 775	2 189 280
Case 2	1 + 2 + 3 + 4	at 60in	29 150	2 225 280
Case 3	1 + 2 + 3 + 4 + 5	at 90in	29 246	2 234 496

The choice of boundary condition type is still an open question. However a set of test runs assists us to find the best group of boundary conditions for a particular computational domain. Figure 6.3.2.1 illustrates the final version of the BCs employed. In particular, the mass flux was chosen as it is a compressible gas problem, the pressure outlet at the outlet of the domain is the only option for open boundaries and for a compressible gas, the choice of BCs at an opposite side to the axis is negotiable. However it was found that the pressure in the far field BC assists the solution to converge faster and a small flow in the axial direction eliminates the reverse flow on the radial outlet boundary. Note, that the position all the BC details are listed in table 6.3.2.2.

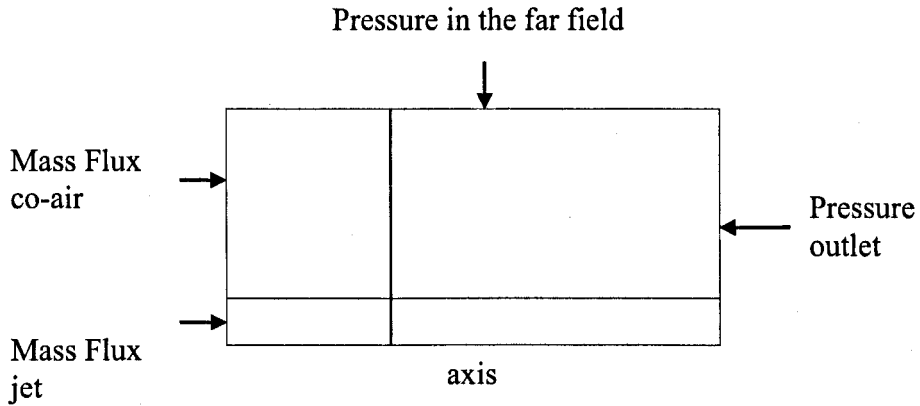


Figure 6.3.2.1. Sketch of the 2D specified boundary conditions.

Table 6.3.2.2: Summary of the boundary conditions employed.

BC type in FLUENT	Details
Mass flux jet inlet	Flat profile: $145 \frac{kg}{s \cdot m^2}$, Turbulent intensity 10% (as defined in the experimental study), Viscosity ratio 10, or profile from the nozzle simulation Total temperature 821K.
Mass flux in the co-flow air	$5 \frac{kg}{s \cdot m^2}$, Turbulent intensity 2% (as defined in the experimental study), Viscosity ratio 5, Total temperature 300K.
Pressure in the far field	Gauge pressure 0Pa, Mach number 0.001 (axial direction), Turbulent Intensity 2%, Viscosity ratio 5.
Pressure outlet	Gauge Pressure 0Pa, Back flow: Turbulent intensity 2%, Viscosity ratio 5, Total temperature 300K.

Material properties:

Air material details: Density – ideal gas law, $C_p = 1006.43 \frac{J}{kg \cdot K}$, Thermal conductivity – kinetic-theory, Viscosity – kinetic theory, Molecular weight = $28.966 \frac{kg}{kgmol}$

The simulation strategy is that initially a RANS $k - \epsilon$ RSM turbulent model is used and this is followed by:

- Patch the cylinder region with length $10in$ and radius $1in$, where the velocity is $300ms^{-1}$, $T = 800K$.
- Activate the FMG: solver/initialization/set-fmg-initialization. Specify 3 multigrid levels and the default values for the rest of the options.
- Apply the FMG. As a result we obtain a good starting flow field distribution which assists us to reach a convergent solution faster.
- Turbulent model: RANS $k - \epsilon$ standard; Discretization: first-order; Solver: steady.
- Discretization: first-order \rightarrow second-order; Turbulent model: RANS $k - \epsilon$ standard $\rightarrow k - \epsilon$ RSM.
- Steady solver \rightarrow unsteady solver 1st order implicit $dt = 5 \cdot 10^{-6}s$.
- Unsteady solver 1st order \rightarrow 2nd order implicit $dt = 5 \cdot 10^{-6}s$, monitor average pressure flux through the $x/d = 10$ plane section of the domain. The number of iterations and the time step should be sufficient to obtain a constant value for the average pressure flux through the plane section. This number decreases as the simulation proceeds from 20 iterations per time step to 5 or 3 iterations per time step.

Note that we have estimated the time step for the unsteady simulation from acoustical resolution requirements and this is because we are interested in the acoustics being resolved for frequencies up to $20\,000Hz$, which is the upper limit of normal human perception. Therefore the characteristic time for the acoustic signal is $T = \frac{1}{20\,000} = 5 \cdot 10^{-5}s$. In order to resolve the acoustic time-scale correctly, we take the time step to be $= 5 \cdot 10^{-6}s$.

6.3.3 Nozzle flow simulations

In order to produce the inlet jet flow profile for the jet flow simulation we have to create a simulation domain for a flow field inside the nozzle, see figure 6.3.2. This is a very simple simulation using the RANS $k - \epsilon$ RSM turbulence model. The purpose is to produce turbulent profiles for k , ϵ , and the mass flux at the outlet of the nozzle.

The boundary conditions for the simulation:

At the nozzle inlet: Mass flux is $15.5 \frac{kg}{s \cdot m^2}$; Turbulent intensity 10%, Hydraulic diameter is $0.01524m$ (6in); Total temperature 821K.

Adiabatic walls with no slip conditions.

At the nozzle outlet: pressure outlet where the gauge pressure is $0Pa$, and Total temperature is 300K.

Air material details:

Density – ideal gas law, $C_p = 1006.43 \frac{J}{kg \cdot K}$, Thermal conductivity – kinetic-theory, Viscosity – kinetic theory, Molecular weight is $28.966 \frac{kg}{kgmol}$.

6.4 2D test simulation results

6.4.1 Jet inlet boundary conditions

The steady solution converges fast with residuals falling below 10^{-14} . Then we save the k , ϵ and the mass flux profile at the nozzle outlet section in order to use in as input information for the jet flow simulations. We have found that the accuracy of the jet flow simulation, especially the U_{rms} velocity component, depends strongly on the turbulent kinetic energy intensity specified at the inlet, which, in its turn, depends on the inlet conditions of the nozzle flow turbulent intensity. For the flow simulation inside the nozzle we employ initial turbulence of 10% based on the hydraulic diameter of $0.01524m$ (6in).

Figure 6.4.1.1 represents the jet flow simulation results for the U_{rms} velocity component plotted at the radial section of the jet placed at an axial distance of $x/d = 3$, where the inlet profiles for k and ϵ are flat (red line) or obtained from the

flow simulation in the nozzle (blue and green lines). The mass flux profile is flat since it was reported by Bridges and Wernet (2003) that the shape of the nozzle was created in such a way to produce the flat velocity profile.

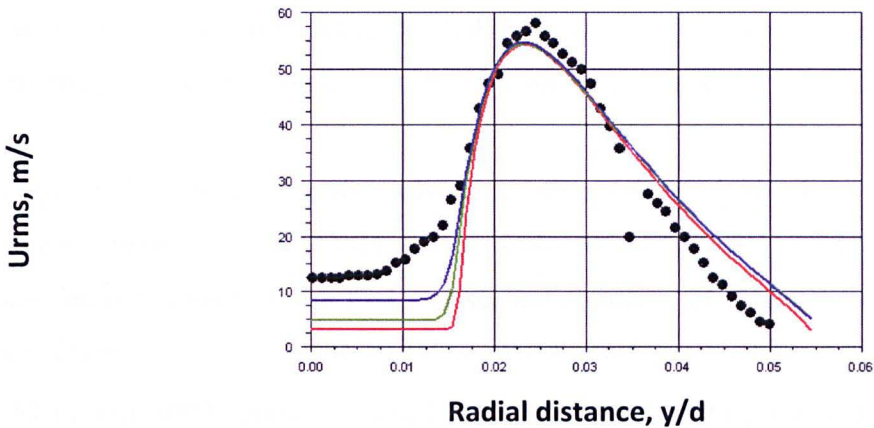


Figure 6.4.1.1 Plots of the U_{rms} velocity profiles at the radial section at an axial distance $x/d = 3$ obtained from the jet flow 2D simulation; the initial and mass flux profile is flat, the turbulence profile is varied.*

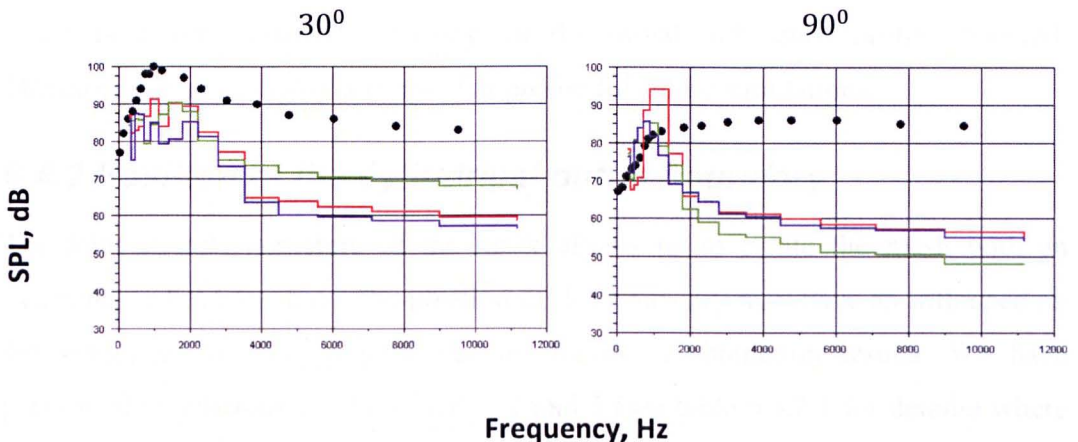


Figure 6.4.1.2 Plots of the noise simulation results for the 2D jet, using FW-H approach, where the initial and mass flux profile is flat, the turbulence profile is varied.*

*Legend: black symbols – experimental data by Bridges and Wernet (2003) [fig. 6.4.1.1], by Tanna (1976) [fig. 6.4.1.2]; red line – flat 10% turbulence intensity, green line – profiles for k and ϵ obtained from the 2D simulations inside the nozzle, where the initial turbulence intensity equal to 10%, blue line - profiles for k and ϵ obtained from 2D simulations inside the nozzle, where the initial turbulence intensity is 20%.

From the simulation results, we observe that the maximum of U_{rms} is captured well for all boundary conditions employed, but the centreline values are underestimated.

The radial profile under consideration is very close to the nozzle exit, and therefore the flow field components are strongly influenced by the initial boundary conditions. We have employed the maximum of 20% for the turbulence intensity at the inlet. This value is already too high for real flow situations. Nevertheless the centreline simulation results are underpredicted. We may not increase the initial turbulence intensity any further because this will become unrealistic.

Figure 6.4.1.2 represents the noise simulation results obtained for the same initial turbulence profiles. The FWH surface is placed at FWH(int1), which corresponds to the surface separating the first and second elements of the computational domain, see Figure 6.3.1. The noise signal is analysed using a Fast Fourier Transformation (FFT) with 4000 points obtained at $dt = 5 \cdot 10^{-6}s$ and presented in the $\frac{1}{3}$ -octave SPL band for receiver positions, employed by Tanna (1976). The 2D simulation results fail to predict correctly the noise level at high frequencies.

There is a very weak dependency on the initial turbulence profile detected. Therefore we may employ a simple flat profile for future simulations.

6.4.2 Position of the cylindrical outlet boundary

The joint element structure of the mesh allows us to create the mesh with an extending radial boundary. The position of this boundary may have an influence on the simulation results, in particular on the noise simulation results. We have performed simulations for the Cases 1, 2 and 3 (see table 6.4.2.1 for details) where the cylinder radius of the computational domain is 30in, 60in and 90in, respectively.

Table 6.4.2.1 *Details of the simulation cases.*

<i>Case</i>	<i>Grid elements</i>	<i>BC position</i>	<i>Total, 2D</i>	<i>Total, 3D</i>
Case 1	1+2+3	at 30in	28 775	2 189 280
Case 2	1+2+3+4	at 60in	29 150	2 225 280
Case 3	1+2+3+4+5	at 90in	29 246	2 234 496

For all three cases investigated, we have calculated the noise level and compared the simulated results with the experimental data. Following the conclusions of Section

6.4.1, we employ a simple flat turbulence profile at the jet inlet. For noise predictions we employ the FWH method, where the FWH surface is placed at the interface between the first element and the second element of the mesh, see figure 6.3.1. The noise signal is analysed using a Fast Fourier Transformation (FFT) with 4000 points obtained at $dt = 5 \cdot 10^{-6}s$ and presented in a $\frac{1}{3}$ -octave SPL band for the receiver positions, employed by Tanna (1976).

Figures 6.4.2.1 present the SPL spectra from the T30 and T90 microphone positions. It is observed that the noise level is highly influenced by the position of the radial outlet boundary. The detected pitch at the frequency of about 4000Hz is the result of the reflection from the radial pressure boundary. Note that the FWH acoustic model was not designed for 2D simulations, and therefore we do not expect an exact agreement with the experimentally measured data, but we expect to capture the right trend.

As the result of the simulations we may conclude that the optimal position of the radial pressure outlet boundary corresponds to Case 3

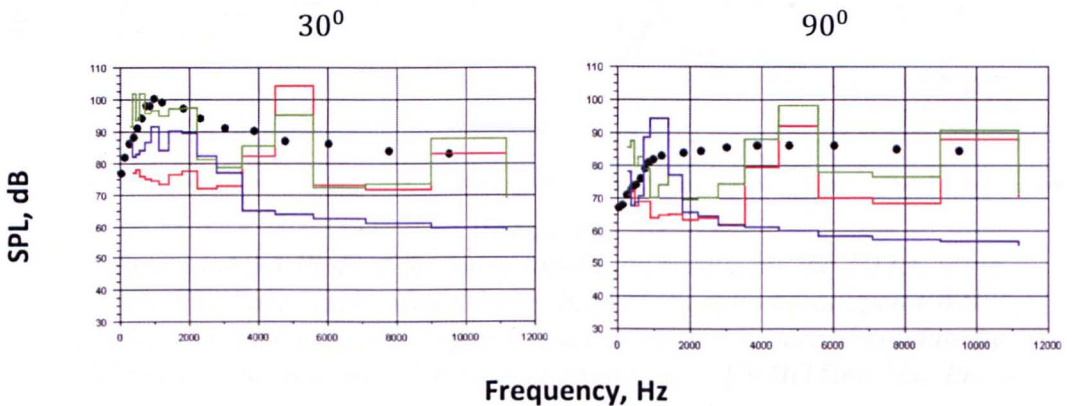


Figure 6.4.2.1 Plots of the noise simulation results for the 2D jet, using the FW-H approach, where the initial jet profile is flat, at the position of the radial pressure outlet varied. Legend: black symbols – experimental data by Tanna (1976); red line – Case 1, green line – Case 2, blue line – Case 3.

6.4.3 FWH source surface

Following the Trucker (2008) recommendations, we employ a simple open cylinder surface as a source surface in the FWH approach for the noise simulations. The only question we need to answer is how far from the jet axis this FWH source surface should be placed. Here we investigate this aspect.

For our research we employ three positions of the FW-H surface, namely: (i) int1, which correspond to the surface separating the first and second elements of the computational domain, (ii) the cylindrical surface is placed at 15in radial distance separating second and the third mesh elements, and (iii) the cylindrical surface is at 30in between the third and the fourth element of the mesh, see the sketch of the computational mesh in Figure 6.3.1.

For the numerical simulations we employ a flat profile on the jet inlet and the computational domain with a radial pressure outlet boundary placed at 90in from the jet axis. The noise signal is analysed using a Fast Fourier Transformation (FFT) with 4000 points obtained at $dt = 5 \cdot 10^{-6}s$ and presented in a $\frac{1}{3}$ -octave SPL band for the receiver positions, as employed by Tanna (1976).

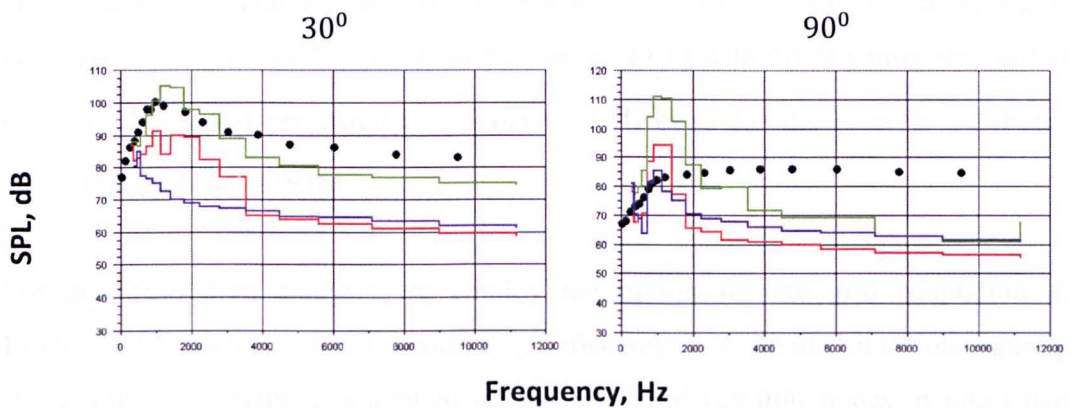


Figure 6.4.3.1 Plots of the noise simulation results for the 2D jet, using the FWH approach, where the position of the cylindrical open FWH source surface is varied. Legend: black symbols – experimental data by Tanna (1976); red line – FWH(int1), green line – FWH(15in), blue line – FWH(30in).

Figures 6.4.3.1 illustrate the 2D simulation results for the noise level obtained using three different FWH surfaces. The FWH surface is open in each of the three cases. The maximum of the simulated SPL is detected for the case with the FWH surface at 15in. The SPL level obtained with the FWH at the conical surface ‘int1’ is slightly lower, and this indicates that the FWH(int1) surface closest to the jet does not enclose all the sources of noise. The SPL level obtained with the cylindrical FWH surface placed at 30in is much lower than the maximum. This is because the

FWH(30in) is placed too far from the jet and incorporates the buffer zone where the acoustic signal is damped.

From this investigation we may conclude that the optimal position of the FWH surface is in the region between FWH(int1) to FWH(15in).

6.4.4 Grid dependency

Finally we performed a grid dependency analysis. In Section 6.3.1 the grid resolution was discussed in detail. However it is worth varying the grid resolution slightly to confirm that we have a grid independent solution. We employed a grid, consisting of five joined elements, where the radial pressure outlet is placed at 90in from the jet axis, as the base case.

For the numerical simulation we employed a flat profile on the jet inlet and the computational domain and the FWH source surface is FWH(15in). The noise signal is analysed using a Fast Fourier Transformation (FFT) with 4000 points obtained at $dt = 5 \cdot 10^{-6}s$ and presented in a $\frac{1}{3}$ -octave SPL band for the receiver positions, employed by Tanna (1976).

For grid resolution analysis we employ the option for the grid adaptation in FLUENT 12, where each cell inside a specified region is divided into four equally sized cells. This method is applied to the basic grid (29 000 nodes in total) two times: firstly for the cylindrical region which is 30in long and 5in radius (76 000 nodes in total), and secondly for the cylindrical region which is 20in long and 4in radius (223 000 nodes in total). Therefore we gradually increase the number of cells in the region where there are the majority of acoustic sources.

Figures 6.4.4.1 represents the noise simulation results compared with the experimental data at two microphone positions, T30 and T90. The results are obtained for grids with a gradually increased number of cells in the source region. We observe that the increased number of cells affect the noise predictions mostly at high frequencies. It is interesting to notice that the second refinement results in a suppressing of the simulated noise level close to the level predicted based on the

unadopted grid. From this analysis we may conclude that the initially created grid could be considered as the one producing a grid independent solution.

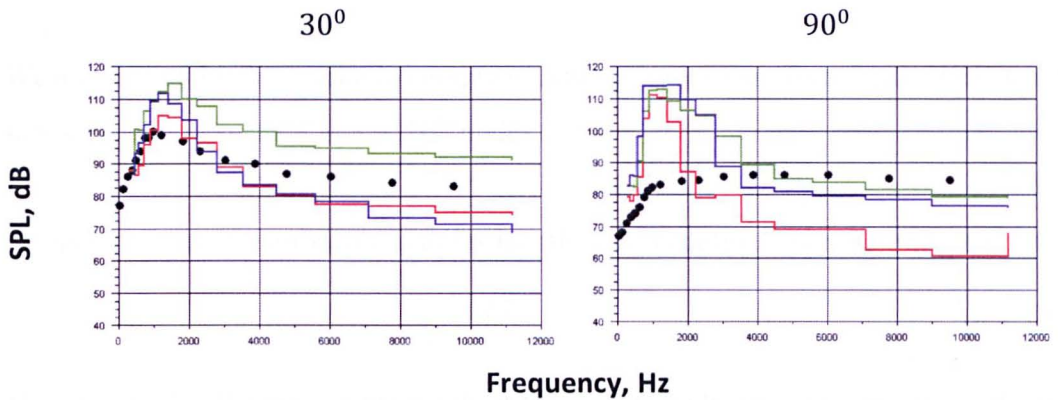


Figure 6.4.4.1 Plots of the noise simulation results for the 2D jet, using the FW-H approach, where the position of the cylindrical open FW-H source surface is varied. Legend: black symbols – experimental data by Tanna (1976); red line – basic grid of 29 000 nodes, green line – once refined grid of 76 000 nodes, blue line – twice refined grid of 223 000 nodes.

6.4.5 2D test results summary

As the result of the set of test 2D simulation runs we have found that (i) the optimal jet inlet profile is flat, (ii) the optimal position of the radial pressure outlet is at 90in from the jet axis, (iii) the position of the FHW cylindrical open source surface is at 15in from the jet axis, and (iv) the grid independent solution is obtained with the grid, consisting of 29 000 nodes in total.

Taking into account the results obtained from the test simulations, we may confidently proceed to the full 3D simulations.

6.5 3D simulation results

6.5.1. Pre-processing analysis for 3D LES simulations

For the LES we perform a pre-processing analysis in order to estimate the discretisation of the mesh. Here we follow the same line of argument as was presented in Chapters 4 and 5. The fineness of the LES mesh depends on the Kolmogorov length scale, which in turn depends on the kinetic energy. However the kinetic energy is practically independent of the mesh resolution, when RANS is

used, then we may build a simple 2D axisymmetrical mesh for the 2D simulations of the jet and then employ the simulation results as estimations of the mesh resolution for the full 3D LES case.

We are limited by the available computational resources therefore the final 3D mesh size should not exceed $2 - 3 \times 10^6$ nodes.

Let us recall that the turbulence eddies length scale is defined after Kolmogorov as:

$$l_0 \cong \frac{k^{\frac{3}{2}}}{\epsilon} \quad (6.5.1.1)$$

This means that the size of the smallest turbulence eddy in the Kolmogorov theory may not be smaller than l_0 , and all eddies having a size less than l_0 will be damped by the turbulence viscosity. We highlight the key values of the spectra in table 6.5.1.1.

From table 6.5.1.1 we may find that if, for example, we are interested in resolving $0.9k$, i.e. 90% of the total turbulence kinetic spectra (TKE), we have to resolve the eddies of size $0.16l_0$, where l_0 is a Kolmogorov scale. Therefore the grid cell dimension is smaller than the size of the smallest Kolmogorov eddy. However, if we decide to resolve 50% of the total turbulence kinetic energy spectra, then the size of the cell should be $1.6l_0$, which is an order of magnitude larger than for the 90% resolution.

Table 6.5.1.1 Key values of the cumulative turbulence kinetic energy spectra against length-scale of the eddies based on the Kolmogorov's energy spectrum.

	l/l_0
$k(l) = 0.1k$	6.1
$k(l) = 0.5k$	1.6
$k(l) = 0.8k$	0.42
$k(l) = 0.9k$	0.16

We employ the same mesh as described in Chapter 4.7.1, but rescaled for current setup, namely $d = 2in = 0.0508m$. We can do this because the turbulent kinetic energy is rather insensitive to the mesh resolution for the 2D RANS standard $k - \epsilon$

simulations. A sketch of the mesh is presented in figure 4.7.1.2, where the total number of nodes is 6045.

We employ the boundary conditions as described in table 6.3.2.2. After the RANS standard $k - \epsilon$ simulation has converged, we plot the contours of the Kolmogorov scales of the turbulence, as defined by expression (6.5.1.1), using the custom defined function option in FLUENT 12. Figure 6.5.1.1 represents the contours of the Kolmogorov scales obtained in the test simulation. We may observe the increase in the turbulent scales in the downstream direction. The most important information for us is the distribution of the length-scales along the jet axis because we use these values as cell dimensions when building the full 3D mesh for the LES simulations. The distribution of the Kolmogorov length scales near the radial outlet boundary is not important since we do not expect to observe a strong turbulent flow there, and this is because this is a region of co-flowing air.

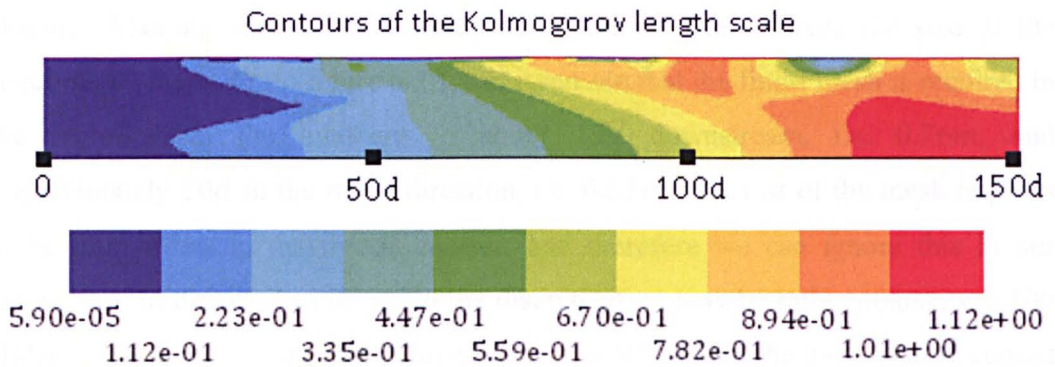


Figure 6.5.1.1 Contours of the Kolmogorov length scale (m), obtained in 2D axisymmetrical RANS standard $k - \epsilon$ simulation.

Table 6.5.1.2 Key values of the turbulence length scale along the jet axis required for the LES when TKE is resolved by 90%, 80% and 50%.

l_0	90% TKE	80% TKE	50% TKE
$5.9 \cdot 10^{-5}$	$9.44 \cdot 10^{-6}$	$2.48 \cdot 10^{-5}$	$9.44 \cdot 10^{-5}$
$1.12 \cdot 10^{-1}$	$1.79 \cdot 10^{-2}$	$4.70 \cdot 10^{-2}$	$1.79 \cdot 10^{-1}$
$2.23 \cdot 10^{-1}$	$3.57 \cdot 10^{-2}$	$9.37 \cdot 10^{-2}$	$3.57 \cdot 10^{-1}$
$3.35 \cdot 10^{-1}$	$5.36 \cdot 10^{-2}$	$1.41 \cdot 10^{-1}$	$5.36 \cdot 10^{-1}$
$4.47 \cdot 10^{-1}$	$7.15 \cdot 10^{-2}$	$1.88 \cdot 10^{-1}$	$7.15 \cdot 10^{-1}$

$5.59 \cdot 10^{-1}$	$8.94 \cdot 10^{-2}$	$2.35 \cdot 10^{-1}$	$8.94 \cdot 10^{-1}$
$6.70 \cdot 10^{-1}$	$1.07 \cdot 10^{-1}$	$2.81 \cdot 10^{-1}$	$1.07 \cdot 10^0$
$7.82 \cdot 10^{-1}$	$1.25 \cdot 10^{-1}$	$3.28 \cdot 10^{-1}$	$1.25 \cdot 10^0$
$8.94 \cdot 10^{-1}$	$1.43 \cdot 10^{-1}$	$3.76 \cdot 10^{-1}$	$1.43 \cdot 10^0$
$1.01 \cdot 10^0$	$1.62 \cdot 10^{-1}$	$4.24 \cdot 10^{-1}$	$1.62 \cdot 10^0$
$1.12 \cdot 10^0$	$1.79 \cdot 10^{-1}$	$4.70 \cdot 10^{-1}$	$1.79 \cdot 10^0$

However it is interesting to plot the contours of the exact Kolmogorov length scales. This is because we are more interested in finding the turbulence scale distribution for the LES simulations when the turbulence kinetic energy spectra is resolved by 90%, 80% and 50%, respectively. Therefore we need to plot values of $0.16l_0$, $0.42l_0$ and $1.6l_0$ respectively, where l_0 is a Kolmogorov turbulence length scale. Clearly the shape of the contours will not change, but the absolute values are scaled. Table 6.5.1.2 presents the absolute values of the Kolmogorov scale contours.

Having obtaining values of the scale resolution we can estimate the size of the required 3D mesh. From figure 6.5.1.1 one can see that the finest mesh is required in the region from the inlet up to about $15d$ downstream, i.e. $0.76m$, and approximately $10d$ in the radial direction, i.e. $0.51m$. The rest of the mesh requires to be four orders in magnitude coarser; and therefore we can ignore this in our estimation. In the rotation direction the discretization may be rather coarse, say 100 slides. Thus we may state that in order to resolve 90% TKE the mesh should consist of more than 4400×10^6 nodes, to resolve 80% TKE - more than 630×10^6 nodes, and to resolve 50% TKE - more than 50×10^6 nodes. This is well beyond our computational abilities limit of $2 - 3 \times 10^6$ nodes. Therefore we have to accept that the TKE will be highly under resolved in our simulations. Instead, we employ the mesh, which is built based on the acoustic resolution criteria, as it was presented in section 6.3.1, and check how well it resolves the TKE.

In order to check how well the mesh from the Section 6.3.1 resolves the Kolmogorov spectra we perform 2D axisymmetric RANS standard $k - \epsilon$ simulations, compute the Kolmogorov scale, as defined by the equation (6.5.1.1), then we compute the TKE resolution corresponding to 90%, 50% and 30% TKE. We can plot the regions where the mesh is fine enough to resolve the TKE with

given accuracy. In order to do so, we divide the cell size, defined in FLUENT as the square root of the 2D cell volume, over the given accuracy TKE scale, for example 90% TKE scale. The region of the mesh where this ratio is less than 1 corresponds to a well resolved 90% TKE. Where the ratio is greater than 1, the mesh is not too coarse to resolve 90% TKE. Figure 6.5.1.2 shows the contours of the cell size over the 90% TKE scale ratio in the limits from 0 to 1. Here we see that the turbulent structures in the jet core region are underresolved by this mesh. It is expected that the mesh is not fine enough to resolve 90% TKE, but the question is to what extent does it actually resolve TKE? In order to answer this question we have to plot contours of the cell size greater than 50% TKE ratio, see figure 6.5.1.3, and the cell size is over the 30% TKE ratio, see figure 6.5.1.4.

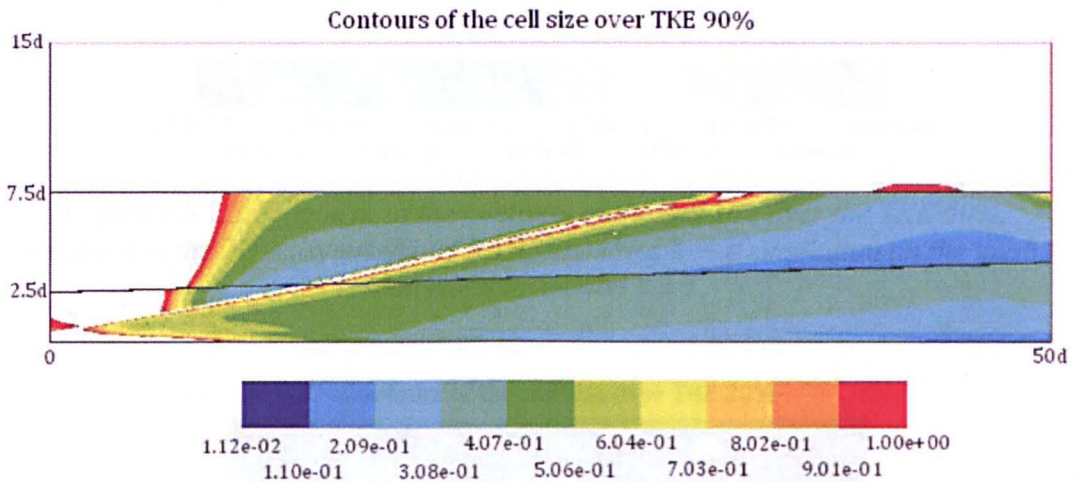


Figure 6.5.1.2 *Contours of the cell size over the TKE 90%, obtained in the 2D axisymmetrical RANS standard $k - \epsilon$ simulation on the mesh as describe in Section 6.3.1*

In figure 6.5.1.3 we observe that the mesh much better resolves the 50% TKE. However there are still some regions in the jet core where the mesh is not able to capture 50% of the turbulent kinetic energy spectra. On figure 6.5.1.4 we present the fragment of the contours near the jet core, where the ratio of the cell size greater than the 30% TKE scale in the range limits from 0 to 1 is plotted. Here we see that the mesh is likely to be able to resolve 30% of the turbulence kinetic energy spectra. This is, of course, not sufficient for very accurate LES simulation, but this is the limitations of the computational power available. The 3D mesh size built on this 2D

slice is within our required limits, namely $2 - 3 \times 10^6$ nodes. For more details on the 3D mesh, see section 6.5.2.

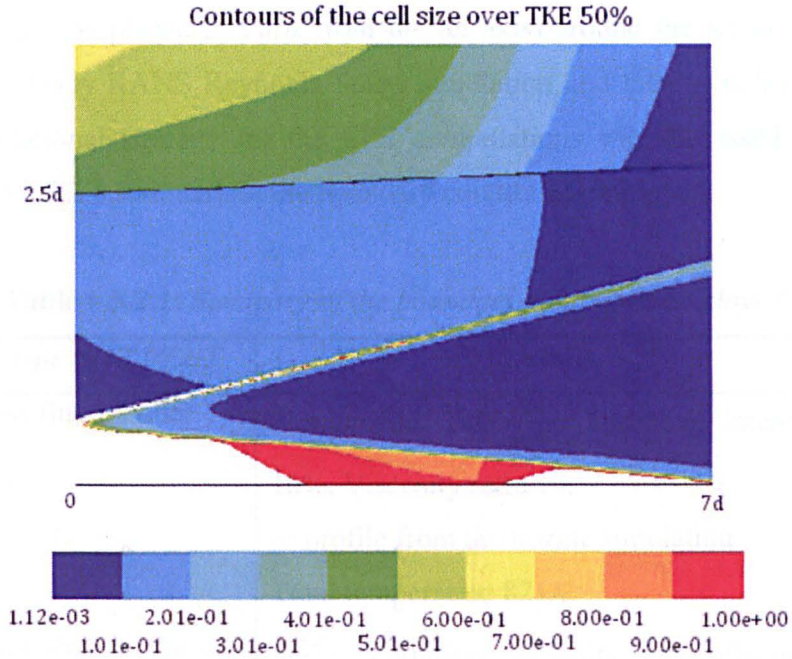


Figure 6.5.1.3 Fragment of the contours of the cell size over the TKE 50%, obtained in the 2D axisymmetrical RANS standard $k - \epsilon$ simulation on the mesh, described in Section 6.3.1

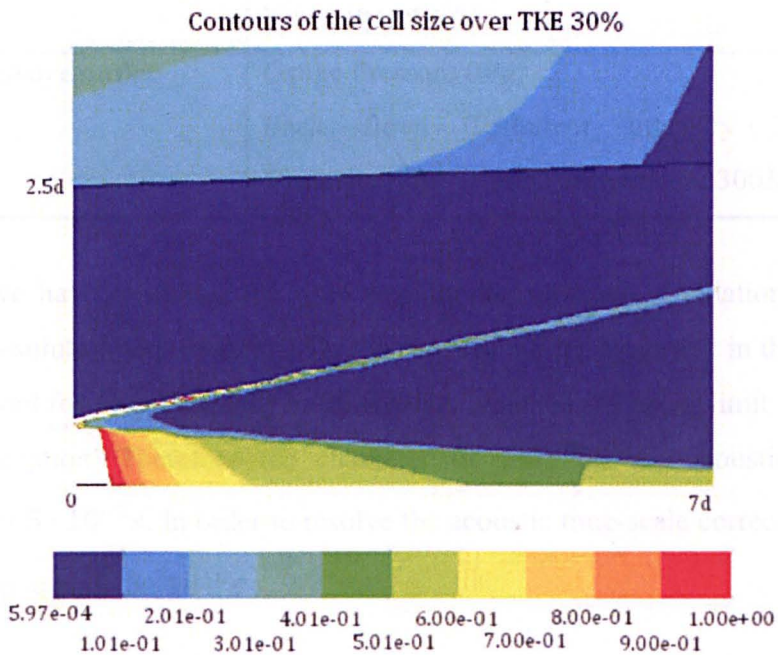


Figure 6.5.1.4 Fragment of the contours of the cell size over the TKE 30%, obtained in the 2D axisymmetrical RANS standard $k - \epsilon$ simulation on the mesh, described in Section 6.3.1

6.5.2 3D mesh and boundary conditions

For the 3D simulations we employ a grid consisting of 2 234 496 nodes. This cylindrical grid is formed by rotating the 2D 29 000 node grid (where the radial outlet boundary is placed at 90in from the jet axis) around the jet axis. We start from the unsteady RANS Reynolds Stress simulation and then switch to the LES. The computational strategy for the LES computations was discussed in Section 3.6.4. Table 6.5.2.1 summarises the boundary conditions employed.

Table 6.5.2.1: Summary of the boundary conditions employed.

<i>BC type in FLUENT</i>	<i>Details</i>
Mass flux jet inlet	Flat profile: $140 \frac{kg}{s \cdot m^2}$, Turbulent intensity 10%, Viscosity ratio 10, or profile from the nozzle simulation Total temperature 821K.
Mass flux in the co-flow air	$5 \frac{kg}{s \cdot m^2}$, Turbulent intensity 2%, Viscosity ratio 5, Total temperature 300K.
Pressure in the far field	Gauge pressure 0Pa, Mach number 0.001 (axial direction), Turbulent intensity 2%, Viscosity ratio 5.
Pressure outlet	Gauge Pressure 0Pa, Back flow: Turbulent intensity 2%, Viscosity ratio 5, Total temperature 300K.

Note that we have estimated the time step for the unsteady simulations from the acoustical resolution requirements. This is because we are interested in the acoustics being resolved for frequencies up to 20 000Hz, which is the upper limit of a normal human perception. Therefore the characteristic time for the acoustic signal is $T = \frac{1}{20\,000} = 5 \cdot 10^{-5} s$. In order to resolve the acoustic time-scale correctly, we take the time step to be $= 5 \cdot 10^{-6} s$.

For the LES computations, we have discovered that the ‘natural’ numerical viscosity of the mesh is enough for the development of the turbulence. The LES computations were run for about 10^4 iterations, where the time-step is $5 \cdot 10^{-6} s$, and

consequently the physical time is $5 \cdot 10^{-2} s$. The mean flow resistance time is estimated to be $t = L/U = 2.54m/306ms^{-1} \cong 8.3 \cdot 10^{-3}$. Therefore the LES simulation runs about 6 resistance times.

We apply the FW-H acoustic model for the noise predictions. The noise signal is analysed using a Fast Fourier Transformation (FFT) with 4000 points obtained at $dt = 5 \cdot 10^{-6} s$ and presented in a $\frac{1}{3}$ -octave SPL band for the receiver positions, employed by Tanna (1976) for two receiver positions: T30 - 30° and T90 - 90° at radius $R = 144in$, see table 6.2.3 for details.

6.5.3 Velocity field

In Chapter 4 we investigated a cold propane jet using LES simulations. We found that no initial fluctuations are needed at the jet inlet boundary to stimulate the turbulence development. Therefore we employ the same approach in this Chapter.

Figure 6.5.3.1 illustrates the LES results: contours of the instantaneous vorticity of the turbulent jet in the middle section. Here we see the length of the potential core of the jet is about five nozzle diameters. This is in qualitative agreement with experimental observations. Therefore we may conclude that the jet is modelled qualitatively correct.

Figure 6.5.3.2 illustrate the combination of the velocity derivatives, q , defined as:

$$q_1 = -\left(\frac{\partial V}{\partial x} \cdot \frac{\partial U}{\partial y} + \frac{\partial W}{\partial x} \cdot \frac{\partial U}{\partial z} + \frac{\partial W}{\partial y} \cdot \frac{\partial V}{\partial z}\right) \quad (6.5.3.1)$$

$$q_2 = -0.5 \left(\left(\frac{\partial U}{\partial x}\right)^2 + \left(\frac{\partial V}{\partial y}\right)^2 + \left(\frac{\partial W}{\partial z}\right)^2 \right) \quad (6.5.3.2)$$

$$q = q_1 + q_2 \quad (6.5.3.3)$$

where U, V, W - velocity components. This combination illustrates well the development of the turbulence in the jet flow.

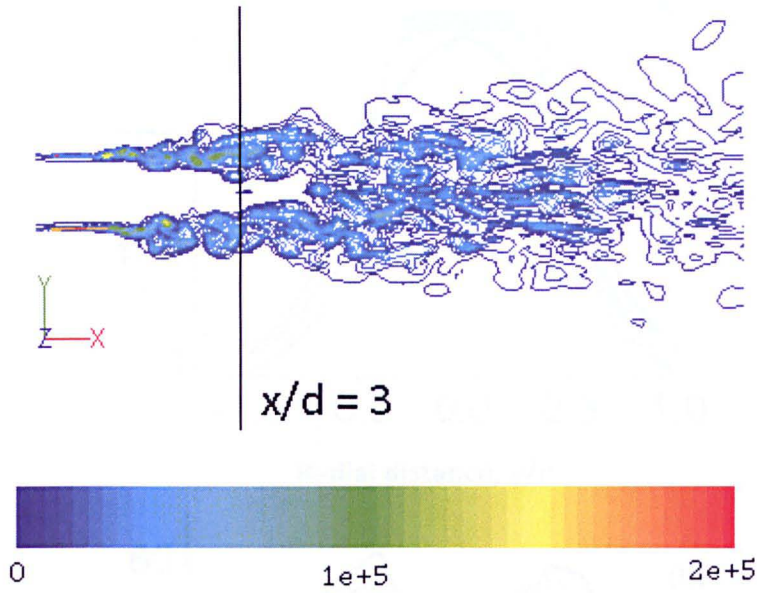


Figure 6.5.3.1 3D LES results: contours of the instantaneous vorticity of the turbulent jet in the middle section.

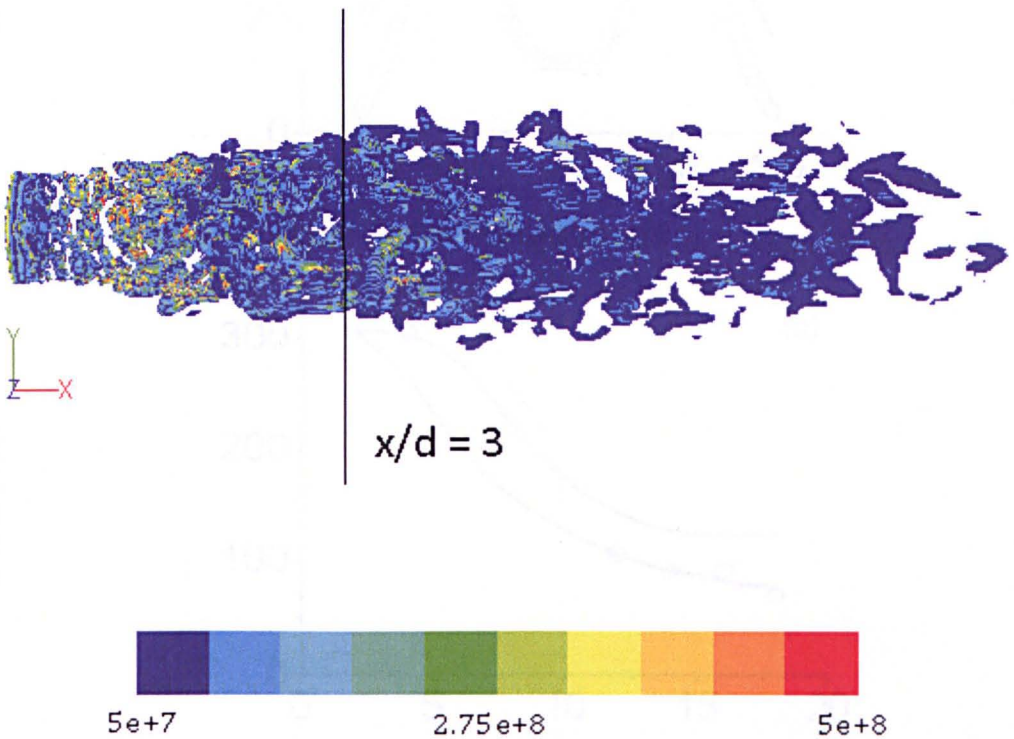


Figure 6.5.3.2 3D LES results: contours of the instantaneous velocity derivatives of the turbulent jet in the middle section.

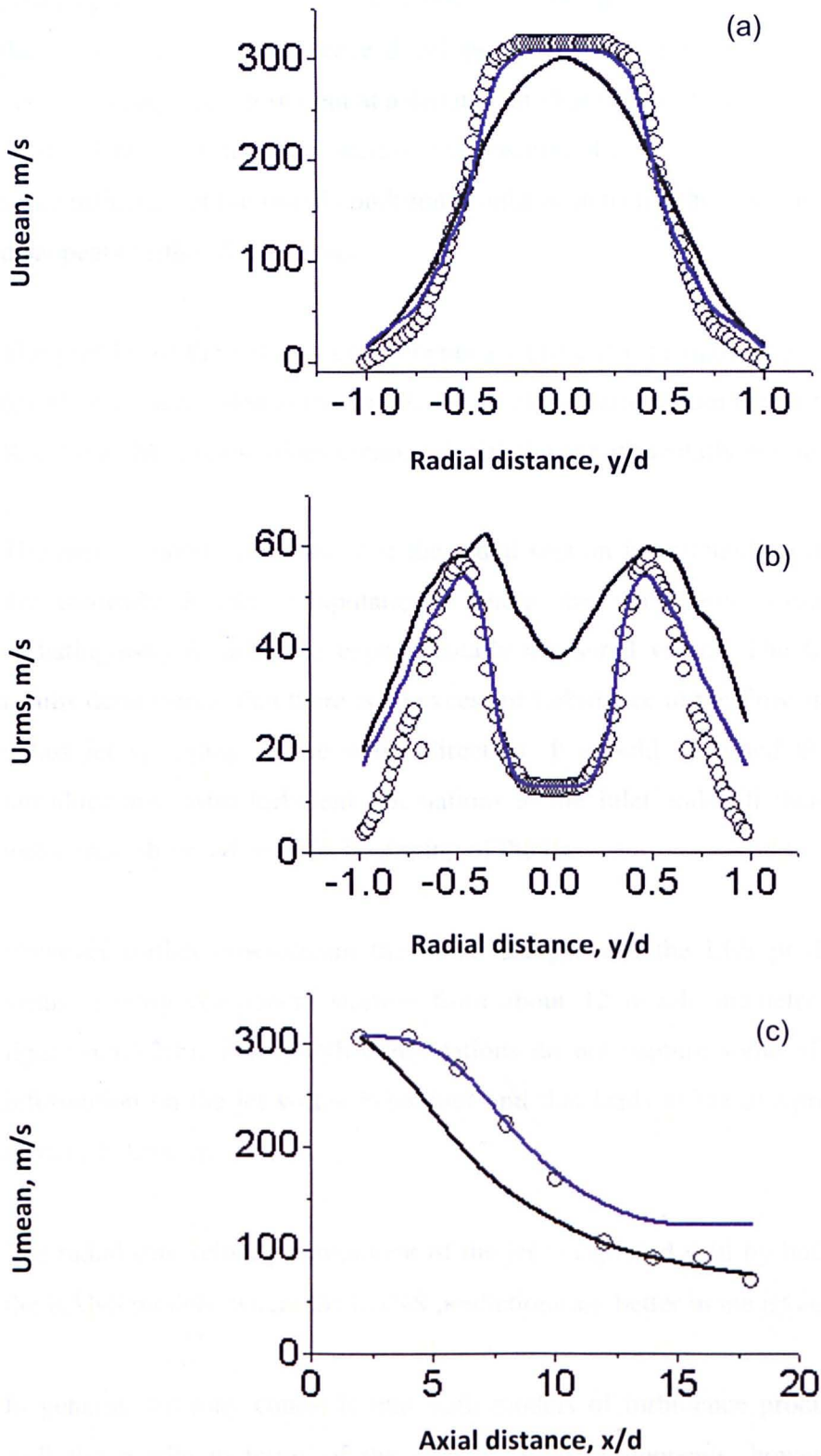


Figure 6.5.3.3 Radial profiles of the mean axial and rms velocity components from a fixed axial position of $x/d = 3$ and centreline mean axial velocity.

Legend: the symbol - experimental data by Bridges and Wernet (2003); the black line - the LES simulation results, blue line - the unsteady RANS (RSM) simulation results, both with a flat profile at jet the inlet.

From figures 6.5.3.1-2 it is clearly observed that there are no initial fluctuations at the jet inlet and the turbulence develops in the mixing layer of the jet. The flow becomes completely turbulent at a distance of about 5 nozzle diameters downstream. At the distance of the radial section (the position of the experimental measurements) some influence of the initial conditions could be detected, however it has practically disappears further downstream.

The profiles of the velocity components are presented in figure 6.5.3.2 (a), (b), and (c). Here we have plotted the simulation results obtained from the LES and unsteady RANS (RSM) computations compared with the experimentally measured values.

The mean velocity component at the radial section is extremely well predicted by the unsteady RANS computations, where the simulation results are almost undistinguishable from the experimentally measured values. The LES simulation results demonstrate that there is an excess of turbulence in the flow and this leads to a fast jet spreading in the radial direction. It should be noted that we did not introduce any extra turbulent fluctuations at the inlet and still there is too much turbulence observed near the beginning of the jet.

However further downstream the trend changes and the LES predicts better the mean velocity component starting from about 12 nozzle diameters downstream, figure 6.5.3.2(c). The RANS computations do not capture some of the important information on the jet vortex behaviour and this leads to the overprediction of the actual jet velocity.

The radial rms velocity component of the jet is captured well by both the LES and the RANS models, where the RANS predictions are better in the jet core region.

In general, we may conclude that both models of turbulence produce reasonably well the results in terms of the velocity field components, however the RANS predictions are in better agreement with the experimental values.

6.5.4 Acoustic field

Figures 6.5.4.1 represent the noise simulation results obtained using the FW-H acoustic analogy based on unsteady RANS (RSM) and LES flow field solutions. The simulation results are presented in a $\frac{1}{3}$ -octave SPL band and for the validation we have employed the experimentally measured values of Tanna (1976) for the two receiver positions: T30 - 30⁰ and T90 - 90⁰ at radius $R = 144in$, see table 6.2.3 for details.

We observe that, in general, both turbulence models capture the shape of the frequency distribution correctly. The LES-based predictions are slightly in excess of the experimentally measured values, and the RANS-based results are lower, especially in the low frequencies range. The largest discrepancy is within a 10% error bar, and this is a good result.

The low frequency range is responsible for large turbulence structures, while the high frequency range represents the noise, generated by the smaller turbulent structures. Therefore, based on the simulation results, we may conclude that the URANS (RSM) model does not resolve sufficiently well the noise effective turbulence vortices to obtain the right quantitative agreement with the experimental measurements. However, we are able to capture the trend representing the noise spectra detected in the different microphone positions. The simulation results are quite promising since we have a chance to improve the noise predictions significantly by simply changing the turbulence model from the unsteady RANS to LES.

In addition, we should mention that the noise predictions obtained based on the LES simulations are closer than the RANS -based predictions to the experimentally measured data - the opposite situation was observed for the flow field predictions as discussed earlier in this Chapter.

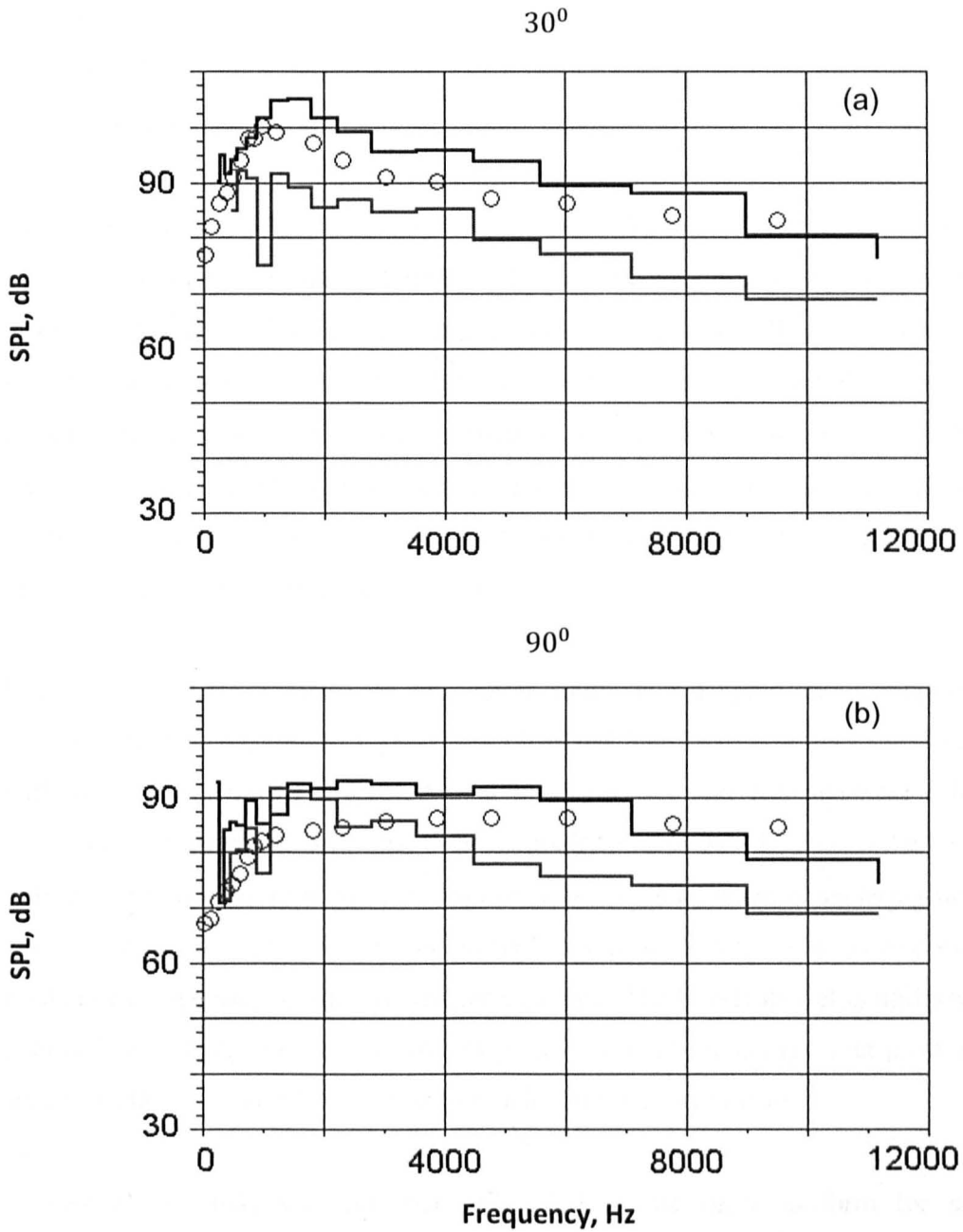


Figure 6.5.4.1 Plots of the noise simulation results, obtained using the FW-H approach, at two angular microphone positions and the radius of 72 nozzle diameters.

Legend: the symbol - experimental data by Tanna (1976); the black line - the LES simulation results, blue line - the unsteady RANS (RSM) simulation results, both with a flat profile at the jet inlet.

In 2007 Khavaran and Kenzakowski numerically predicted the noise from this jet using the NASA code JeNo, where the governing acoustic equations are a set of linearized, inhomogeneous Euler equations. These equations are combined into a single third-order linear wave operator when the base flow is considered as a locally parallel mean flow. The remaining second-order fluctuations are regarded as the equivalent sources of sound and are modelled. The hot jet effect may be introduced primarily through a fluctuating velocity/enthalpy term. Modelling this additional source requires specialized inputs from a 2D RANS-based flow field simulation, usually simple $k - \epsilon$ model. The restriction of the code is that it is capable of predicting noise at 90° degrees to the jet axis only. Khavaran and Kenzakowski modified a physics-based jet noise prediction methodology based on the RANS input to improve the noise prediction for heated jets.

In figure 6.5.4.2 we compare our simulation results with the predictions obtained by Khavaran and Kenzakowski (2007). It is observed that there is a very good match with the experimentally measured data by Khavaran and Kenzakowski (2007). However their approach is limited to noise predictions at 90° degrees to the jet axis only and it is not uniform, since it requires modifications when considering hot jet cases. The predictions from an unmodified model are not as good as any of our predictions, especially in the low frequency range. The FW-H model is uniform for cold or hot jet cases and it is capable of predicting noise at any receiver position in space, but this is achieved by means of much computational effort.

In general, we may conclude that the FW-H approach is uniform for many applications (hot/cold jets), and it is not limited to jet noise problems. FW-H predicts the noise level at any angular position of the microphone, but this approach requires a significant computational effort since it is based on an unsteady LES or RANS solution. On the other hand, the approach employed by Khavaran and Kenzakowski (2007) is relatively fast since it requires simple 2D RANS-based flow field simulations, but it requires modifications for hot jet cases (the model is designed for jet noise problems only) and the predictions are limited to 90° degrees position of the microphone only.

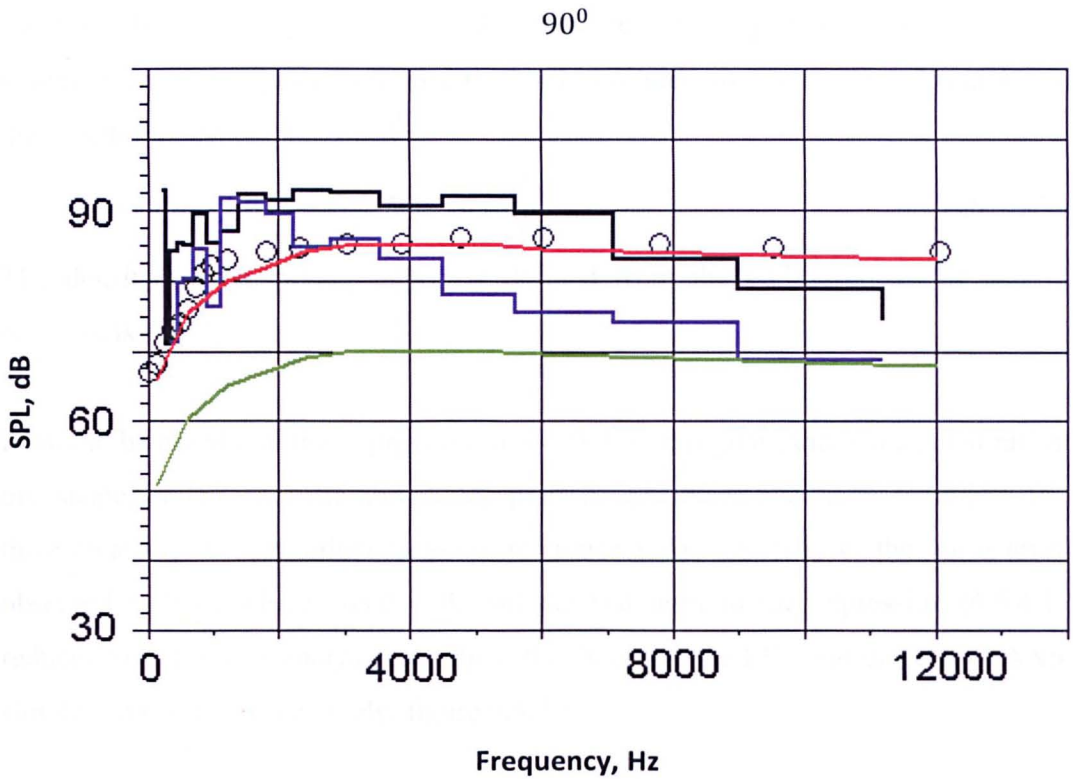


Figure 6.5.4.2 Theoretically predicted directivity compared with experimentally measured values and different simulation results.

Legend: the symbol - experimental data by Tanna (1976); the black line - the LES simulation results, blue line - the unsteady RANS (RSM) simulation results, both with a flat profile at the jet inlet, green line - JeNo simulation results, red line - JeNo modification with enthalpy effects, Khavaran and Kenzakowski (2007).

It is difficult to plot the directivity pattern of the acoustic field because we have information on the noise level at only two microphone positions. However we are interested in comparing our simulation results and the experimentally measured data with the theoretically predicted acoustic directivity. Here we employ the expression for the acoustic intensity in the far field resulting from the Lighthill dimensional analysis:

$$I(\theta, R) \sim \frac{\rho_m^2 U_j^8 D^2}{\rho_0 c_0^5 R^2} \frac{D(\theta)}{(1 - M_c \cos \theta)^5} \quad (6.5.4.1)$$

where ρ_m is the density in the mixing region, U_j the jet velocity, D the nozzle diameter, $\rho_0 = 1.204 \text{ kg m}^{-3}$ and $c_0 = 343 \text{ m s}^{-1}$ the density and speed of sound in the external fluid at a distance R from the jet to the observer and θ the angle between the direction of emission of sound and the downstream jet axis. The

function $D(\theta)$ is the directivity of the unconnected quadrupole distribution. We assume that all the quadrupoles are randomly oriented so that $D(\theta) = 1$ and M_c is the speed of convection defined as:

$$M_c = 0.67 \frac{U_j}{c_0} \quad (6.5.4.2)$$

The density in the mixing region is defined from the CFD simulations and is $\rho_m = 0.8 \text{kgm}^{-3}$.

It should be noted that the expression (6.5.4.1) does not give exact values, but rather the shape of the acoustic directivity pattern. Therefore we have to adjust the theoretically predicted values to some reference values, usually to the noise level observed at 90° , where $\cos \theta = 0$, and the last term in the expression (6.5.4.1) reduces to 1. For this analysis we adjust the theory to the LES and unsteady RANS simulation results, respectively, figure 6.5.4.3.

In general we observe the same trend as in figure 6.5.4.1, where the acoustic field results based on unsteady RANS predictions are slightly below the experimentally measured values and LES-based predictions are very close, but in excess of the experimentally measured values. Also we may observe that, when adjusted at the 90° microphone position, the theory strongly overpredicts the noise level at the 30° microphone position. This is the same trend we observed in Chapter 4, where the cold propane jet was analysed. At the same time the shape of the numerically predicted noise diagram is very similar to the experimentally measured one for both the LES and RANS predictions. This means that the nature of the non-uniform quadrupole orientation is captured well by the CFD simulations, either the LES or the unsteady RANS (RSM). The absolute values have a 5% error bar, which is a very good result for the LES and remarkably good for RANS!

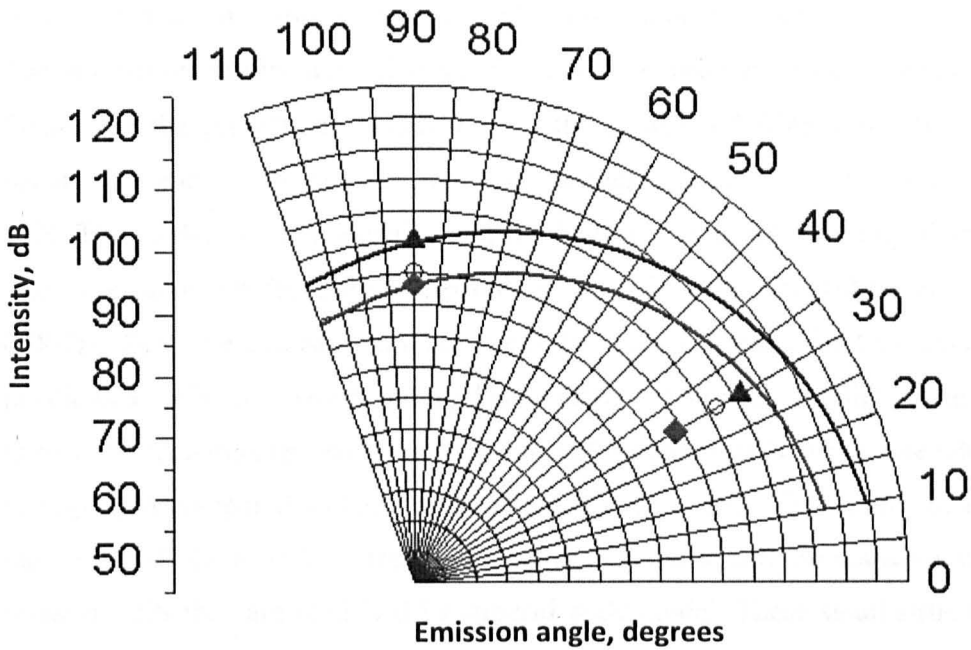


Figure 6.5.4.3 Theoretically predicted directivity compared with the experimentally measured values and the simulation results.

Legend: black triangle – LES simulation results, blue diamond – unsteady RANS (RSM) simulation results, black line - theory adjusted to the LES predictions, blue line - theory adjusted to the unsteady RANS predictions, circles – experimental data by Tanna (1976).

6.6 Conclusions

In this Chapter a hot air jet has been examined numerically. For validation of the simulation results we have employed the experimentally measured values of the velocity field obtained by Bridges and Wernet (2003) and for the noise level measurements that obtained by Tanna (1976).

Initially we employed a set of test 2D axisymmetric RANS (RSM) simulations in order to define: the shape of the jet inlet profile (for that the preliminary inside nozzle simulations were employed), the size of the computational domain, the position of the FWH source surface, and the grid dependency analysis. Then we constructed the 3D full size mesh, taking into account recommendations from the test simulations.

The numerical investigations of the jet in 3D calculations were performed using the LES and the unsteady RANS (RSM) approaches (with the same mesh). For the noise

level predictions we employed the FW-H acoustic model, realised in FLUENT 12.0. The simulation results were first validated for the velocity field components. We found that the predictions obtained from the unsteady RANS simulations are in better agreement with experimental measurements than those obtained from the LES. This is due to high sensitivity of the LES to the initial boundary fluctuations (they are unknown from the experimental investigations of Bridges and Wernet (2003)). Then the acoustic simulation results were validated for two microphone positions as originally employed by Tanna (1976). The noise predictions are found to be in better agreement with the experimental measurements in the case when LES is employed compared to the results obtained with RANS. This is due to the fact, that in RANS the turbulent structures smaller than a grid cell are not resolved at all, while in LES they are modelled by subgrid scale model. These small structures are responsible for high frequency noise production. However, in general, both approaches demonstrate the ability to capture the spectra shape correctly and give the noise values that are within a 5% error bar. The simulation results are quite promising since we have a chance to improve the noise predictions significantly by simply changing the turbulence model from the unsteady RANS to LES.

In addition, we have compared our predictions based on the LES and RANS solutions coupled with the FW-H acoustic model with the predictions of Khavaran and Kenzakowski (2007). They employed an in-house NASA code JeNo, where the governing acoustic equations are a set of linearized, inhomogeneous Euler equations. The modelling requires specialized inputs from a 2D RANS-based flow field simulation, the $k - \epsilon$ model. The restriction of the model is that it is capable of only predicting the noise at 90° degrees to the jet axis, and the modifications for a hot jet are needed. We have found that both the LES-based and unsteady RANS-based predictions, obtained from the FW-H model, are closer to the experimentally measured data than are the predictions obtained from the unmodified JeNo model. This illustrates the capacity of the FW-H approach to predict noise from very different jets without any extra modifications.

Finally, we have analysed the noise simulation results in terms of the directivity pattern. For this analysis we have employed an alternative acoustic model, based on the Lighthill dimensional analysis. The model was calibrated based on the LES and

RANS predictions obtained at the 90° microphone position. We have found that the nature of the non-uniform quadrupole orientation is captured well by the CFD simulations, either the LES or unsteady RANS (RSM). The absolute values varies within a 5% error bar, which is a very good result for LES and remarkably good for RANS!

Chapter 7

Discussion

7.1 General remarks

In this thesis we focus attention on the numerical modelling of the noise generated by a low Mach number turbulent jets. The task is challenging, because computational aeroacoustics (CAA) involves issues that are unique and are, in general, not considered in CFD. In this section we will discuss some these issues. The objective of CAA is not just to develop computational methods but also to use these methods to solve real practical aeroacoustic problems. It is also a goal of CAA to perform direct numerical simulation or similar simulations of aeroacoustic phenomena so as to allow an investigator to determine what the noise generation mechanisms and sound propagation processes are and to obtain a better understanding of the physics of the problem.

The jet-engine noise is well known problem and became an independent research domain in early 1950s. Nowadays, society cannot tolerate additional noise pollution, and traffic growth must be compensated by quieter aircrafts. In fact, potential solutions to reduce jet noise are now often in conflict with the optimization of engine performance. As a consequence, innovative methods must be proposed to reduce the jet noise of existing and new larger subsonic airliners, therefore investigations of the noise generation mechanisms for low Mach number jets is of particular importance.

Over last 20 years advances in computational fluid dynamics have made it possible to improve predictions by replacing flow parameters of semi-empirical models designed in early 1950s, Lighthill (1952), by computed values. Two main classes of methods have been developed in CAA: acoustic analogies or hybrid approaches, which are applied to time-dependant CFD data, and direct methods resolving explicitly compressible unsteady Navier-Stokes equations. The latter methods require tremendous computational resources and are yet unfeasible for practical applications. Therefore the hybrid approach is adopted in this study. This approach

has been successfully employed by Bastin et al. (1997), Collonius et al. (1997), Bogey et al. (2002), Bogey et al. (2003).

7.2 Numerical scheme

Usually higher order numerical schemes (fourth-, fifth- and six-order) are utilized for computational investigations in aeroacoustic, Schulze et al. (2009). High order finite-difference schemes are useful for problems where accurate resolution of the smallest turbulent structures is required. The major shortcoming of these types of schemes is that they are usually unstable (Carpenter et al. (1993)) and, in general, cannot be applied for unstructured meshes (Ollivier-Gooch and Van Altena (2002)) - widely applied meshes for real-life complex geometry problems.

When the order of a finite-difference approximation is higher than the order of the governing partial differential equations, the boundary and initial conditions provided by the physical problem no longer define a unique numerical solution. As a result, any high-order scheme is capable of supporting spurious numerical waves. Usually these parasite numerical waves have short wavelengths that are not resolved by spatial finite-difference operator. Tam et al. (1993) examined the behaviour and characteristics of the short wave components from the wavenumber point of view. Spurious waves can be generated by solution discontinuities, solid surfaces, computational domain boundaries, grid interfaces and other computational irregularities. They contaminate the numerical solution, degrade its quality and sometimes even lead to numerical instability. To improve the quality of the numerical solution, it is imperative to remove parasite numerical waves in a way that has a negligible effect on the useful band of waves present in physical solution.

Tam et al. (1993) proposed to add explicit artificial selective damping to the numerical scheme. The artificial damping terms are designed to damp out short spurious waves leaving the long waves effectively untouched. The idea was later developed by Zingg et al. (1996) and Kennedy and Carpenter (1994). Another approach is to impose a selective damping Lockard et al. (1995), Zhuang and Chen (2002). All of these methods require additional tuning of the damping parameters for every particular calculation. Therefore we decided to focus our attention on the

stable second-order numerical scheme solvers and achieve high accuracy of the numerical results by refined mesh resolution.

Acoustic waves usually have small amplitudes. They are very small compared to the mean flow. Oftentimes, the sound intensity is five to six orders smaller. In order to compute sound waves accurately, a numerical scheme must have extremely low numerical noise, Tam (1995, 1998). Numerical noise in FLUENT is well dumped by high numerical viscosity, so that it is another argument in favour of using this commercial code for this study.

A relatively new method – the Discontinuous Galerkin (DG) – has been recently applied for aeroacoustic problems, Bartoli et al. (2010). This method presents very low numerical dissipation and dispersion errors. The method has major advantages compared to more classical methods such as finite difference or finite element method. Due to its flexibility, some local refined meshes are performed to handle some complex geometries and the approximation order can be adopted locally. The DG method appears to be a promising tool for aeroacoustic applications. However the it is yet on the development phase which made it impossible to employ at the time of this study has been initiated. However we strongly believe that the approach will be successfully utilised for numerical simulations of the noise radiation.

7.3 Reflection on the boundaries

The reflection on the boundaries is an important problem in computational acoustics. The ordinary boundary conditions such as fixed pressure at the outlet or velocity (mass flow) at the inlet are “seen” by the acoustic waves, generated inside the computational domain, as “walls”, because by fixing pressure\velocity at the boundary we kill the fluctuating component of the acoustic wave thus forcing the wave to reflect backwards from the boundary. Why it is so undesirable?

A large amount of experimental evidence suggests that acoustic waves are strongly coupled to many mechanisms encountered in turbulent flows. The free shear layers (such as jet) are especially sensitive to acoustic waves, see Bechert and Stahl (1988). This interaction may lead to large flow instabilities as, for example, the case of the edgetone experiment, Ho and Nosseir (1981), Tang and Rockwell (1983). Therefore

it is important to avoid artificial reflection of the acoustic waves in numerical simulations. How can we do that?

Poinsot and Lele (1992) proposed the Navier-Stokes characteristics boundary condition (NSCBC), where it is possible to fix the mean pressure value, allowing the fluctuating component to exist, thus allowing the acoustic wave to leave the computation domain through the boundaries. They achieved it by linearizing the Navie-Stokes equations in near the boundary and extracting the perpendicular component of the pressure wave. This type of boundary conditions is implemented in FLUENT 12.0 named NRBC.

Polifke et al. (2006) developed the NSCBC by calculating the plane wave pressure component before it reaches the boundary and extracting it from the solution on the boundary. This not only improves the accuracy of the reflection from the boundaries, but also allows for exciting the system externally through the boundaries, so that only externally imposed wave enters the domain, not the reflected one.

All these methods appear to be very attractive, but they have a limitation – it is applicable to plane waves. In case of the jet exhausting to infinite medium we deal with mainly spherical waves in the far field. Therefore NRSBC are not effective for our case. What other mechanisms to avoid reflection can we use?

Instead of “killing” the plain component we employ a different strategy – we damp reflected waves by numerical viscosity, using a coarse mesh near the outlet boundaries (buffer zones). One may argue that this works only for outlet boundaries, and we can't use the buffer zone at the inlet. It is true, that the inlet must be well resoled at the very beginning of the computational domain, because in this region the important information about the flow field and potential hydrodynamic instabilities is contained. However, on the other hand, the directivity pattern of the jet acoustic field has a shape of petal, stretched along the jet axis, so that major part of noise is emitted in the outlet direction, see acoustic field results in Chapters 4, 5 and 6, so that we may ignore the acoustic emission in the inlet direction and therefore reflection from the inlet.

Finally we would like to remark, that we won't be able to make the same assumption if part of the nozzle pipe is presented inside the computational domain, because the acoustic field in pipes always form two waves propagating in opposite directions, so that one of them is definitely travelling towards inlet, and therefore is reflected by the fixed pressure boundary.

7.4 RANS vs LES

It is well known that RANS models are less computationally expensive for numerical simulations than LES. This is due to the fact, that many RANS solvers are capable to handle 2D instead of full 3D formulation, and in many cases it is possible to reduce the symmetrical case to just one fraction of the mesh. In addition RANS does not require very fine mesh resolution, especially if there are no walls involved in the computational domain, like in case of a free jet. To the contrary LES demands a full 3D (at least a symmetrical fraction) with the mesh resolution capable to resolve the smallest turbulent structures, so that the higher the Reynolds number of the flow the finer mesh is required by LES. This makes LES computationally costly for simulation of the flows in real regimes, i.e. high Reynolds numbers, large geometrical scales.

However LES provides very full information about the flow (mean and dynamic values), this information is limited to the scale of the resolution of the turbulent structures, so that we know a lot about turbulent scales up to certain manually imposed limit, i.e. mesh resolution, and have almost no information (except provided by sub-grid models) for smaller scales, even the mean values are not known. In other words LES provides us with full information on limited scales, while RANS, on the contrary, provides with limited information (mean values) for all turbulent scales. This conceptual difference between RANS and LES plays an important role in some applications. In this research we tried to answer the question: what is more important for jet noise predictions – mean values for all scales, or dynamic behaviour of large vortices?

Current state of the art in aeroacoustics: there is a clear distinction between acoustic models formulated on the mean flow values obtained from 2D RANS, Bechara et al.

(1995), Bailly et al. (1996, 1997) and Khavaran (1999) and models based on dynamic properties of the flow, Morris and Farrasat (2002). The latter is usually based on LES (Bogey et al. (2003)) or DNS (Freund (2003)) simulations. As to author's knowledge no attempts has been performed to employ unsteady RASN solution for coupling with FWH. This is a challenge of this research.

7.5 FWH surface

In the original Ffowcs-Williams and Hawkings (1969) formulation sound at a far field location can be computed from flow information on an arbitrarily-shaped surface, known as FWH surface, and the volume-distributed sources outside of that surface. However due to the difficulties associated with using volume-distributed sources, the FWH surface is often chosen such that it encloses flow-generating sound sources. As a result, the volume term can be assumed small enough that its effect can be neglected, as it is realized in FLUENT code.

The shape and position of the FWH surface for jet noise predictions is a subject of many studies. Here we mention the latest results. The nature of FWH analogy requires that the FWH surface encloses all acoustic sources generated by the flow. The surface in general should be fully closed. Practically, however, the surface used is open at the inflow, but this has no consequence on the calculated sound, Mendez et al. (2009) The outflow disc is usually employed for the closing of the FWH surface. There is a problem however: the closure of FWH surface can cause the spurious noise, Shur et al. (2005). Shur et al. (2005) and Freund et al (1996) discussed whether the FWH surface should be closed or open at the outlet. Authors shown that better far field predictions might be gained by tuning the closing discs. However it is not the interest of this research, hence open surfaces are used. Recently Xia et al. (2009) successfully adopted the open FHW surface approach for noise predictions of the chevron jet flows using LES and Fosso Pouangue et al. (2010) for noise prediction of low-Mach number high Reynolds number jet.

The location of the FWH surface is still an open question which must be defined and tuned for every particular application. The very rough estimation tells that the FWH surface must be "far enough" in order to enclose all acoustic sources generated by flow, but "near enough" not to miss acoustics in propagation damping, caused by

numerical effects. Mendez et al. (2009) studied the question and concluded that “no clear criterion has been determined to define the optimal location of the FWH surface. To make noise results less sensitive to the FWH surface location, the grid has to be designed with care, to ensure the proper propagation of acoustic waves from the location where they are generated to the surface”. During this study we came to the same conclusion.

7.6 Experimental data for validation

FLUENT code has not been tested for jet noise modelling when this research was originated. Therefore it was decided to simplify the investigated case as much as possible. We concentrated on low Mach number jets, below 0.6. Only single round jets with simple nozzle configurations are considered here. Since for validation of CAA approach we need both flow field and acoustic field measurements, it was a challenging task to find an appropriate experimental data, satisfying our criteria. In fact there is not complete detailed experimental measurement of the jet with both detailed flow field characteristics (velocity field measured in different locations, pressure field, temperature field) and acoustic field in the far distance from the jet. The main reason behind this difficulty is that flow field measurements and acoustic measurements require rather different laboratory conditions, and, as the result, it is very challenging to measure all parameters simultaneously. In addition, as for author’s knowledge, there is no experiment specially designed for the purpose of CAA validation. Eventually we went to the combination of three experimental data in order to validate the hybrid approach in CAA.

First data are based on the cold propane jet, originally investigated by Schefer (1988) from the SANDIA National Laboratory. The choice of this particular jet was because of its very detailed information for the flow field, i.e. the velocity components and mass fractions, as provided by Schefer (1988). However no acoustic field measurements were performed in the experimental study. This data set is used to demonstrate that the CFD simulation of the flow field, which implies acoustic sources, is correct.

The second data set we chosen to be the jet noise performed by Lush (1971), where very detailed information of the far field acoustics of the cold low Mach number jet

is presented. However no experimental data on the flow field was provided. As the flow field characteristics of this jet are similar to the first one, by Schefer (1988), one can expect that using the same CFD procedure, verified on cold SANDIA jet, we obtain correct flow field. And once the acoustic field is verified, using one of the hybrid models we employ in this study: FWH or Goldstein's jet model, then the CAA approach is valid.

And finally we refer to the hot air jet experiment studied by Bridges and Wernet (2003) and Tanna (1976). The data includes both the flow field components, however not so detailed as for the cold propane jet studied by Schefer (1988), and acoustic field measurements, but just at three microphone positions – this is not sufficient for an accurate validation of the acoustic field directivity pattern. In this case we are able to verify both CFD simulation of the flow field as well as acoustic field.

7.7 On the numerical results

As it is mentioned in the introduction of this Chapter we adopted a hybrid approach for a jet noise modelling. The hybrid approach implies that the acoustic sources and sound propagation are modelled independently. Acoustic sources modelling require the simulation of the flow field. The very detailed experimental results on the flow field are required for the validation of the first step. Ideally validation of the pressure field in the jet plume is needed, but, unfortunately, this information is unavailable from the experimental data sets. Therefore we can rely only on velocity field and/or temperature and mass fraction matching.

For the validation of our CAA approach we model first the cold propane jet, studied experimentally by Schefer (1988) from the SANDIA National Laboratory. The simulation has been performed using axisymmetric RANS model of turbulence and then for full 3D configuration with unsteady RANS and LES models. We validated the simulation CFD results with experimental measurements of the velocity field (mean and rms values) and mass fractions of the propane, measured at 4 radial sections of the jet. The simulations results are, in general, in good agreement with experimental measurements. For axisymmetric simulation we checked different velocity inlet profiles and found the Prandtl inlet profile as an input gives the best

matching with experimental measurements. The simulation of the full 3D case appeared to be more challenging as we realised that it is almost impossible to obtain perfect fit with experimental data for all sections of the jet. This unexpected discrepancy inspired us to reanalyse the experimental measurement on consistency manner. And we realised that some of the measurements, namely at the section closed to the jet lip, are not fully consistent with the rest of the scope of the experimental measurement. Therefore we decided to omit this data set from the validation procedure. After this has been done, the matching between CFD and experimental measurements are in very good agreement. LES model captures really well the rms velocity field at every section of the jet, while unsteady RANS smooth down the rms profile in the downstream sections of the jet. However in general one may conclude that the CFD model of the jet works really well. This simulation helped us to establish the procedure of the CFD modelling of this type of jets (initial and boundary conditions, mesh resolution etc.)

Using the validated flow field of the jet, we applied the acoustic models in order to calculate the noise generated by the jet. We used three models: analytical estimator from Lighthill theory (require only mean velocity and fluid parameters), Goldstein's model (require the meal flow field information from RANS simulation), and Ffowcs Williams – Hawking (FWH) approach (require pressure fluctuations on the special surface obtained from unsteady CFD). The Goldstein's model in the existing in FLUENT formulation provides only the qualitative information of the acoustics of the jet. In order to estimate if we are on the right way in our predictions, we performed additional simulation with varied co-flow velocity. It is well known from the experimental studies how the total jet noise should change when the co-flow is varied. Using Goldstein's model we obtained the same qualitative trend.

Application of the FWH approach gave as rather unexpected results, namely the noise level obtained using the unsteady RANS solution is about 15dB higher than the noise levels obtained using LES. This is rather surprising result, because we know that the flow field obtained in both simulations is very similar. However one must remember that we validate the flow field based on it's velocity and mass fraction values, while FWH approach require the pressure field distribution. The pressure field is more sensitive to any small changes, therefore even when the

discrepancy in the velocity field is negligible the pressure field may significantly vary. However since there is no information from the experimental measurements about the true noise level of the jet, we cannot definitely state which one of the results is correct.

The second set of the experimental on the other hand provides very detailed information on the acoustic field of the jet, Lush (1971). We adopt the procedure for CFD simulation developed for cold propane jet. The flow field is calculated using FWH model and Lighthill's dimensional approach. The LES computation are performed on the grid capable to resolve up to 70% of the kinetic turbulent energy. This is not the finest grid, so we expect that the small vortex structures are not resolved properly, therefore the high frequency noise is not well predicted (underestimated). This is exactly what we observe for a high Strouhal numbers (high frequency noise). However the important point is that the total noise is predicted rather well, therefore one can conclude that the high frequency component is not important for this type of jet and rather coarse grid resolution can give a reasonable idea about true noise radiation from the jet. Having a coarser mesh saves a lot of computational time and effort - something which is very important for industrial applications.

Finally we focused on the hot jet, where both flow field details and acoustics are available from the experiment. Though both measurements are not as detailed as we considered for previous jets. The Reynolds number of the jet is relatively high. Therefore we went for unsteady RANS simulations, which does not require very fine mesh resolution as does LES. The simulation of the flow field is in a very good agreement with experimental data for both unsteady RANS and LES (employed on the same mesh). This is not surprising, because for validation we have only one set of data, measured on the radial section near the nozzle lip. It is much more difficult, as we know from the first jet simulations, to design CFD setup where the jet simulated is in a good agreement with experimental values in several sections downstream. Nevertheless it is interesting to note that unsteady RANS captures the low field of the jet near the nozzle lip better than the LES for this setup (of course the LES here is just 50%KTE..) However as soon as it comes to acoustics, we observe that the FWH model coupled with LES produces the results which are in

some better agreement with the experimental measurements, while FWH coupled with unsteady RANS underpredict the noise level at the positions of the measurements.

One should also notice that the latter jet is a hot jet. Many existing models in aeroacoustics require some modifications of the model when dealing with the hot jet cases. For example as it is done by Khavaran and Kenzakowski (2007) in in-house NASA code JeNo. Application of the FWH model doesn't require any specific modification when for thermal jets – this is a very strong advantage for using FWH in industrial applications.

In the latter jet case we have also demonstrated that the simple switch from unsteady RANS to LES gives much better predictions of the noise radiation. This change doesn't make the problem more computationally difficult, since solution of RANS Reynolds Stress equations require approximately the same effort (even more..) than LES with subgrid modelling. The advantage of using LES instead of RANS is that the LES implies some modelling of the subgrid vortices – the information omitted in unsteady RANS simulations. The contribution of this subgrid vortices to the noise generation is essential in this case.

Finally we would like to conclude that by committing this study we demonstrated the ability of the commercial code FLUENT to deal with jet noise problems – something that, as to authors knowledge, has not been done before. It is absolutely possible to employ FLUENT standard models for jet noise radiation estimations. However for really detailed scientific insight into noise generation mechanism we would suggest to use some high-order numerical solvers, which are unfortunately much more unstable and very often not designed for tackling complicated geometries, but which are powerful tool for precise scientific study of the physical processes.

Chapter 8

Conclusions and Future Work

8.1 Conclusions

The conclusion Chapter is divided as follows: in the first subsection we summarize the conclusions of each Chapter, aiming to remind the reader of the content of this thesis, and in the second subsection we give final general conclusions of the research performed in this thesis.

8.1.1 Summary of conclusions

In the first Chapter an introduction to the problem and the motivation for the research performed in the thesis has been described. The second Chapter provides a literature review of the state of art in the development of the acoustic models employed in this thesis. In addition we have emphasised the shortcomings of the current implementation of the acoustic analogy (the Goldstein model) in the commercial CFD code FLUENT and suggested a way for improvement. The third Chapter focuses on a literature review of the turbulence models employed in the CFD simulations. We have stressed our attention particularly on the RANS Reynolds Stress model and the Large Eddy Simulation (LES) approach, which are extensively employed in this study.

Chapter 4 accumulates the results obtained for the numerical study of the cold propane jet, originally investigated by Schefer (1988) from the SANDIA National Laboratory. The choice of this particular jet was because of its very detailed information for the flow field, i.e. the velocity components and mass fractions, as provided by Schefer (1988). However no acoustic field measurements were performed in the experimental study. A critical analysis of the experimental data has been performed and it has been demonstrated that the data is not consistent in at least one monitoring surface. The numerical investigation of the jet was performed in 2D using the RANS model and in 3D using the unsteady RANS and LES models. An optimal mesh configuration for the problem has been established and the optimal boundary conditions have been found. The flow field results have been validated

with the experimentally measured data, where we observed good agreement. For the acoustic field calculations we employed the Goldstein approach coupled with 2D axisymmetric simulations. The computational results have been compared with the experimentally measured data for a cold air jet under similar conditions, Lush (1971). It was shown that the cold propane jet generated a noise +2dB higher than a similar air jet, i.e. having the same Mach number and temperature ratio. This result is expected from the Goldstein theory and is due to the higher density of propane, compared to air. The density difference between the jet and the surrounding air generates additional shear stresses which in turn are responsible for the extra noise production. Moreover we have performed a parametric analysis of the acoustic power varying co-flow air velocity and found a behaviour which is in qualitative agreement with the experimental observations performed by, for example, Papamoschou (2007). Finally we have employed the FWH acoustic modelling coupled with unsteady RANS and LES simulations for the flow field. We have demonstrated that the FWH-LES results could be closer to real noise expectations (if the noise would be measured experimentally), estimated with the assistance of Lighthill dimensional analysis. However the FWH-RANS also provides good predictions for the noise level.

We continued the numerical investigation of the jet noise in Chapter , where we have concentrated our investigation on acoustical field validation. For this purpose we have employed the results of the experimental study of the jet noise performed by Lush (1971). No experimental data on the flow field was provided. The numerical simulations have been performed in both 2D and 3D configurations and the numerical mesh construction has been improved over that discussed in Chapter 5. The shape and position of the FWH surface has been adopted from previous studies, reported in Chapters 4. The acoustic field predictions, obtained from the 2D CFD simulations coupled with the Goldstein acoustic model, have been validated with the experimentally measured data. The nature of the Goldstein analogy requires an initial adjustment of the analytical curve to the experimentally measured data at a certain point, typically to the noise level at the 90° position of the microphone. After this adjustment, we found that the acoustic directivity pattern is in very good agreement with the experimental data at all microphone positions. The 3D LES simulations were performed with the aim of resolving the turbulent energy spectra

up to 70%. This restriction is due to the limited computational resources and a focus on the low- and mid- frequency of aerodynamic noise (high-frequencies noise is effectively damped by the atmosphere). The FWH-LES approach has been employed and good agreement with the experimental data has been achieved, with the expected underestimation (due to “just” 70% turbulent energy resolution) of the noise level at high Strouhal number (high-frequency range). The approach has proved to be effective for the noise predictions in the low- and mid-frequencies and requires reasonable computational effort (about one week on a fast 8-processor PC)

In the sixth the hot air jet was experimentally studied by Bridges and Wernet (2003) and Tanna (1976). The data includes both the flow field components, however not so detailed as for the cold propane jet studied by Schefer (1988), and acoustic field measurements, but just at three microphone positions – this is not sufficient for an accurate validation of the acoustic field directivity pattern. For the numerical investigation, an inlet velocity profile had to be determined during the pre-simulations of the flow inside the nozzle. The shape and position of the FWH surface (a surface, incorporating equivalent acoustic sources of the jet) has been improved compared to the setup applied in Chapter 4. This time we aimed to examine how much the acoustic field could be improved by changing the turbulence model but maintaining the same numerical mesh. It was found that the velocity field simulation results are in better agreement with the experimental data for the case of the unsteady RANS (Reynolds Stress) model, than for the LES. This can be explained by the fact that LES is more sensitive to the initial conditions than is RANS. It is interesting to report that the acoustic field numerical predictions, obtained from the FWH, in contrast to the flow field results, are in better agreement with the experimental data in the case of the FWH-LES coupling, than for the FWH-RANS. This can be explained by the sub-grid modelling of the turbulent vortices in the LES approach, which is responsible for the high frequency noise production. However, in general we still may conclude that the accuracy of the FWH-RANS approach is good, within a 5% error bar, and, more important, to the best of the author’s knowledge, this combination has never been previously studied. Finally we have compared our numerical predictions with the modelling results obtained by Khavaran and Kenzakowski (2007) for the same jet conditions. They have employed a linearized Euler equation model coupled with the $k - \epsilon$ flow field solution for the

jet. The major shortcomings of their approach are as follows: the model has to be modified for cold and hot jet conditions and the model provides information about acoustic energy only at 90° degree positions of the microphone. In contrast, our FWH-CFD approach is not sensitive to the physical conditions of the jet flow and provides information about the acoustic field at any position in space (outside the FWH surface). Finally we have analysed the directivity pattern of the acoustic field and compared the computational results with the Lighthill dimensional analysis. We have demonstrated that the qualitative nature of the directivity pattern is captured well by the FWH-CFD approach. While a closer quantitative agreement with analytical predictions was observed for the FWH-LES type of modelling.

8.1.2 General conclusions

The numerical study performed in this thesis illustrates the capacity of the commercial CFD solver to predict the noise level in turbulent jets. The overall concluding remarks on the thesis are as follows:

- The finite-volume, second-order numerical scheme solver (commercial code FLUENT) can be employed with confidence for jet noise simulations. To the best of the author's knowledge, the second-order solver in FLUENT has not been employed before for studying jet noise problems.
- We have demonstrated that the unsteady RANS (Reynolds-stress) turbulent model can be used for the simulation of acoustic sources in the jet. To the best of the author's knowledge, no attempt at using the unsteady RANS for the calculation of the acoustic sources have been previously performed.
- We have shown that the LES simulations of the flow field of the jet improves the accuracy of the acoustic field predictions over the unsteady RANS results, even when performed on the same mesh as that built for the unsteady RANS calculations. This is due to the subgrid scale modelling employed in the LES solver, which allows for reasonable modelling of the acoustic sources.
- The semi-empirical models developed especially for jet noise predictions, such as the Goldsten model and the dimensional Lighthill approach, accurately predict the directivity pattern of the jet noise level. However both approaches require an initial adjustment to the reference point (usually with

the experimentally measured data at the 90° microphone position). The CFD-FWH approach could be used as an initial reference point for certain jet flow regimes and the noise level for other regimes could be estimated from the Goldstein analogy.

- Accurate validation of the CFD-FWH approach for jet noise modelling requires the validation of the acoustic field of the jet as well as the flow field. The experimental measurements of both aspects are usually not available from one experimental study due to technical difficulties in measuring both the flow (velocity) and acoustic (noise) fields. We have demonstrated that it is possible to combine the experimental data of the flow field obtained from one experimental study with the acoustic field data obtained from another experimental study, but for jets with similar conditions (Mach number, temperature ratio, configuration, etc.)

8.2 Future work

1) The capacity of FLUENT to predict the jet noise has been demonstrated for rather simple round jets. A more complicated chevron-shaped nozzle may be simulated with the aim to numerically predict the noise reduction caused by the chevron structure of the nozzle compared to a simple round jet configuration. According to recent studies, Tide and Srinivasan (2009), the chevron configuration of the nozzle suppresses the jet noise by approximately 4.5dB. Thus it would be very interesting to investigate if the same results could be achieved using the CFD simulations. The detailed experimental study performed by Brown and Bridges (2006), from the NASA Glenn Research Center, can be utilized for the validation of the numerical results.

2) Another important problem in aeroacoustics is the “bound wall noise problem” formulated for jets near the wall (such as the exhaust jet of a plane during take off), Miles (1975). The noise generated by the turbulent sources in the jet is reflected by the ground and forms a feedback and this has an impact on the turbulent flow of the jet itself. This nonlinear phenomena can be numerically simulated. The noise level can be calculated directly from accurate CFD simulations, which resolves both the turbulent acoustic sources and acoustic propagation effects, as well as the feedback formed by the reflection from the ground. Alternatively, the acoustic analogy may

be employed. However it is a challenging problem, involving an alternative Green function formulation for the solution of the wave equation in the Lighthill analogy. The direct simulation of the acoustic wave propagation involves modification of the turbulence model, such as the LES, which does not operate properly in the vicinity of solid boundaries, Wang and Moin (2002). An alternative formulation, DES, could be of use, or another more appropriate turbulence model that is suitable for aero-acoustic problems formulation should be established.

3) Equally important is the interaction between the jet flow and the frame of the airplane, Mengle et al. (2006). This can be investigated numerically. The FWH approach implemented in FLUENT allows for the simulation of the acoustic waves propagation and the interaction with solid surfaces (dipole noise). For numerical simulations, one has to take into account the solid surfaces of the airplane and introduce them into the computational domain of the problem. The CFD simulations will require a modification in the formulation of the LES model in order to take into account the formation of the boundary layers at the solid surfaces.

4) The existing formulation of the FWH acoustic analogy does not stress the attention on the enthalpy (so called pressure-density) term in the Lighthill tensor, Lilley (1996). This term can play a significant role when taking into account the gases exhausted from real engines. A more careful analysis of the impact of this term on the acoustic predictions is required. An important application where this term could be important is in the rapid cooling of hot exhaust gases from the airplane engine at high altitude.

5) The major problem in the validation of any “analogy like” numerical model for noise predictions is the lack of detailed experimental studies. In general, the experimental work is focused either on detailed measurements of the flow field or on detailed measurements of the acoustic field. However the nature of the computational aeroacoustics requires validation of both these aspects. Therefore a complete experimental study of the turbulent jet, including PIV measurements of the velocity field at several locations, as well as acoustic measurements detecting the directivity of the acoustic field at several points and several radial distances from the acoustic sources is required. This study should include subsonic jets at different

Mach numbers and temperature ratios. Also alterations in the nozzle shape would be an important contribution to the study.

6) The core of the semi-empirical acoustic models for jet noise (Ribner (1964), Goldstein (1973)) is a fourth-order correlation tensor of the turbulent jet:

$$R_{ijkl} = \overline{u_i u_j u'_k u'_l}$$

It is a common approach to decompose this tensor into lower order (second-order) correlations such as the following:

$$\overline{u_i u_j u'_k u'_l} = \overline{u_i u_j} \cdot \overline{u'_k u'_l} + \overline{u_i u'_l} \cdot \overline{u_j u'_k} + \overline{u_i u'_k} \cdot \overline{u_j u'_l}$$

To the best of the author's knowledge, the validity of this decomposition has never been proved experimentally. Therefore there is a strong request for direct measurements of the fourth-order correlation tensor in complex turbulent flows. These types of measurements are difficult to perform in practice (due to the high accuracy required in the measurements and the long sample series for an adequate averaging of the signal), however it is possible to perform this experimental investigation. It is very important to show experimentally that the decomposition of the fourth-order correlation tensor into the second-order correlation tensors does not introduce any artificial effects or loses in any of the important physical effects.

References

M.Azarpyvand and R.Self, "Noise prediction of a short-cowl jet using energy transfer rate time-scale", *14th AIAA/CEAS Aeroacoustics Conference (29th AIAA Aeroacoustics Conference) AIAA-2008-2937*, (2008).

M.Azarpyvand and R.Self, "Improved jet noise modelling using a new time-scale", *Journal of the Acoustical Society of America*, 126 (3), 1015-1025, (2009).

G.K.Batchelor, "The theory of axisymmetric turbulence", *Philosophical Transactions of the Royal Society*. London, Ser. A 186, 480-502, (1946).

C.Baily, P.Lafon, and S.Candel, "Prediction of supersonic jet noise from a statistical acoustic model and a compressible turbulence closure", *Journal of Sound and Vibration*, 194(2), 219-242, (1996).

C.Baily, P.Lafon, and S.Candel, "Subsonic and supersonic jet noise predictions from statistical source models", *Journal of the Acoustical Society of America*, 35(11), 1688-1696, (1997).

C.Bailly, C.Bogey and S.Candel, "Modelling of sound generation by turbulent reacting flows", *Journal of Aeroacoustics*, 9 (4-5), 461-490, (2010).

N.Bartoli, P.-A.Mazet, V.Mouysset, and F.Rogier, "Highly accurate schemes for wave propagation systems: Application in Aeroacoustics", *AIP Conference Proceedings*, 1281, 313, (2010).

F.Bastin, P.Lafon, and S.Candel, "Computation of jet mixing noise due to coherent structures: the plane jet case", *Journal of Fluid Mechanics*, 335, 261-304, (1997).

W.Bechara, P.Lafon, C.Bailly, and S.Candel, "Application of k-e model to the prediction of noise for simple and coaxial free jets", *Journal of the Acoustical Society of America*, 97(6), 3518-3531, (1995).

D.W.Bechert and B.Stahl, "Excitation of instability waves in free shear layers Part 2. Experiments", *Journal of Fluid Mechanics*, 186, 63-84, (1988)

J.Bridges and M.Wernet, "Measurements of the aeroacoustic sound source in hot jets", *NASA/TM-2004-212508, AIAA-2003-3130*, (2004).

C.A.Brown and J.Bridges, "Acoustic efficiency of azimuthal modes in jet noise using chevron nozzles", *AIAA-2006-2654, NASA/TM-2006-214364*, (2006)

C.Bogey, C.Baily, and D.Juve, "Computation of flow noise using source terms in linearized Euler's equations", *Journal of the Acoustical Society of America*, 40 (2), 235-243, (2002).

C.Bogey, C.Baily, and D.Juve, "Noise investigation of a high subsonic, moderate Reynolds number jet using a compressible LES", *Theoretical Computational Fluid Dynamics*, 16 (4), 273-297, (2003).

C.Bogey and C.Bailly, "Influence of nozzle-exit boundary-layer conditions of the flow and acoustic field of initially laminar jets", *Journal of Fluid Mechanics*, 663, 507-538, (2010).

D.J.Borodny and S.K.Lele, "LES of turbulent jets and progress towards a subgrid scale noise model", *In Proceedings of LES for Acoustics, Gottingen, Germany, 7-8 Oct*, (2002).

M.Carpenter, D.Gottlieb and S.Abarbanel, "The stability of numerical boundary treatments for compact high-order finite-difference schemes", *Journal of Computational Physics*, 108(2), 272-295, (1993).

D.Choundhury, "Introduction to the renormalization group methods and turbulence modeling", *Fluent Inc. Technical Memorandum*, TM-107, (1993).

Citation Classic, *ET&AS*, 22(38), Sept.23, (1991).

T.Colonius, S.K. Lele, and P.Moin, "Sound generation in a mixing layer", *Journal of Fluid Mechanics*, 330, 375-409, (1997).

D.G.Crighton and J.E.Ffowes Williams, "Sound generation by turbulent two-phase flow", *Journal of Fluid Mechanics*, 36, 585-603, (1969).

N.Curle, "The influence of solid boundaries upon aerodynamic sound", *Proceedings of the Royal Society. London Ser. A* 2314, 505-514 (1955).

B.J.Daly and F.H.Harlow, "Transport equations in turbulence", *Physics of Fluids*, 13, 2634-26-49, (1970).

R.W.Dibble, W.Kollmann and R.W.Schefer, "Conserved scalar fluxes measured in turbulent nonpremixed flame by combined laser Doppler velocimetry and laser Raman scattering", *Combustion Flame*, 55, 307-321, (1984).

R.W.Dibble, W.Kollmann and R.W.Schefer, "Scalar dissipation in turbulent reacting flows measurements and numerical model predictions", *Twentieth Symposium (International) on Combustion*, the Combustion Institute, Pittsburgh, USA, (1985).

R.W.Dibble, V.Hartmann, R.W.Schefer and W.Kollmann, "Conditional sampling of velocity and scalars in turbulent flames using simultaneous LDV-Raman scattering", *Experiments in Fluids*, 5, 103-113, (1987).

A.T.Fedorchenko, "On some fundamental flaws in present aeroacoustic theory", *Journal of Sound and Vibration*, 232(4), 719-782, (2000).

J.E.Ffowcs-Williams, "The noise from turbulence convected at high speed", *Philosophical Transactions of the Royal Society. London Ser. A* 225, 469-503, (1963).

J.E.Ffowcs-Williams and D.L.Hawkings, "Sound generation by turbulence and surfaces in arbitrary motion", *Philosophical Transactions of the Royal Society London Ser. A* 1151, 264-321, (1969).

J.E.Ffowcs-Williams, "Aeroacoustics", *Journal of Sound and Vibration*, 190(3), 387-398, (1995).

J.B.Freund, "Noise sources in a low-Reynolds-number turbulent jet at Mach 0.9", *Journal of Fluid Mechanics*, 438, 277-305, (2001).

J.B.Freund, "Noise-source turbulence statistics and the noise from Mach 0.9 jet", *Physics of Fluids*, 15(6), 1788-1799, (2003).

J.B.Freud, S.K.Lele, and P.Moin, "Calculation of the radiated sound field using an open Kirchhoff surface", *AIAA Journal*, 34(5), 909-916, (1996).

M.Germano, U.Piomelli, P.Moin, and W.H.Cabot, "Dynamic subgrid-scale eddy viscosity model", In *Summer Workshop, Centre for Turbulence Research*, Stanford, CA, 249-258, (1996).

M.M.Gibson and B.E.Launder, "Ground Effects on Pressure Fluctuations in the Atmospheric Boundary Layer", *Journal of Fluid Mechanics*, 86, 491-511, (1978).

M.E.Goldstein and B.Rosenbaum, "Effect of anisotropic turbulence on aerodynamic noise", *Journal of Acoustical Society*. 54, 630-645, (1973).

F.C.Gouldin, R.W.Schefer, S.C.Johnson and W.Kollmann, "Nonreacting turbulent mixing flows", *Progress in Energy and Combustion Science*, 12, 257-303, (1986).

M.Hirschberg, "Basics of Aeroacoustics and Thermoacoustics", VKI Lecture Series 2007-09 ISBN-13978-2-930389-79-6, 14-34, (2007).

C.M.Ho and N.S.Nosseir, "Dynamics of an impinging jet. Part I. The feedback phenomenon", *Journal of Fluid Mechanics*, 105, 119-142, (1981).

M.Ihme, H.Pitsch and D.Bodony, "Radiation of noise in turbulent non-premixed flames", *Proceedings of the Combustion Institute*, 32, 1545-1553, (2009).

S.A.Karabasov, M.Z.Afsar, W.A.McMullan, C.D.Pokora, G.J.Page and J.J.McGuirk, "Jet noise:Acoustic analogy informed by Large Eddy Simulation", *AIAA Journal*, 48 (7), 1312-1325, (2010).

C.A.Kennedy and M.H.Carpenter, "Several new numerical methods for compressible shear-layer simulations", *Journal of Applied Numerical Mathematics*, 14, 397-433, (1994).

A.Fhavarani, "Role of anisotropy in turbulent mixing layer", *AIAA Journal*, 37(7), 832-841, (1999).

A.Khavarani and D.C.Kenzakowski, "Progress towards improving jet noise predictions in hot jets", *13th AIAA/CEAS Aeroacoustics Conference AIAA-2007-0012*, (2007).

S.-E.Kim, D.Choudhury and B.Patel, "Computations of complex turbulent flows using the commercial code FLUENT", *In Proceedings of the ICASE/LaRC/AFOSR Symposium on Modelling Complex Turbulent Flows*, Hampton, Virginia, (1997).

S.-E.Kim, "Large eddy simulation using unstructured meshes and dynamic subgrid-scale turbulence models", *Technical Report AIAA-2004-2548, American Institute of Aeronautics and Astronautics, 34th Fluid Dynamics Conference*, (2004).

I.Kroo, lecture notes "AA 241 Aircraft Design: Synthesis and Analysis", available on the web: <http://adg.stanford.edu/aa241>, *Stanford*, (2005).

B.E.Launder and D.B.Spalding, "Lectures in mathematical models of turbulence", *Academic Press*, London, UK, (1972).

B.E.Launder and D.B.Spalding, "The numerical computation of turbulent flows", *Computer Methods in Applied Mechanics and Engineering*, 3:269-289, (1974).

B.E.Launder, G.J.Reece, and W.Rodi, "Progress in the development of Reynolds-stress turbulence closure", *Journal of Fluid Mechanics*, 68(3), 537-566, (1975).

M.J.Lighthill, "On sound generated aerodynamically –Part I. General theory", *Proceedings of the Royal Society. London Ser. A* 211, 564-587, (1952).

M.J.Lighthill, "On sound generated aerodynamically –Part II. Turbulence as a source of sound", *Proceedings of the Royal Society. London Ser. A* 222, 1-32, (1954).

G.M.Lilley, "On the noise from jets", *AGARD Thechnical Report*, No. CP-131, (1974).

D.K.Lilley, "A proposed modification of the Germano subgrid-scale closure model", *Physics of Fluids*, 4, 633-635, (1992).

G.M.Lilley, "The radiated noise from isotropic turbulence with application to the theory of jet noise", *J. Sound Vib.*, 190(3), 463-476, (1996).

D.P.Lockard, K.S.Brentner, and H.L.Atkins, "High-accuracy algorithms for computational aeroacoustics", *AIAA Journal*, 33(2), 246-251, (1995).

P.A.Lush, "Measurements of subsonic jet noise and comparison with theory", *J.Fluid Mech.*, 46(3), 477-500, (1971).

F.Mathey, D.Cokljat, J.P. Bertoglio, and E.Sergent, "Specification of LES inlet boundary condition using vortex method", *4th International Symposium on Turbulence, Heat and Mass Transfer*, Antalya, Turkey, (2003).

V.G.Mengle, L.Brusniak, R.Elkoby, and R.H.Thomas, "Reducing propulsion airframe aeroacoustic interactions with uniquely tailored chevrons: 3 jet-flap interaction ", *In Proc. 12th Aeroacoustic Conference (27th AIAA Aeroacoustic Conference), 8-10 May, Cambridge, Massachusetts, AIAA-2006-2435*, (2006).

J.H.Miles, "Analysis of ground reflection of jet noise obtained with various microphone arrays over an asphalt surface", *J.Acoust.Soc.*, 57(S1), 32-37, (1975)

P.J.Morris and F.Farassat, "Acoustic analogy and alternative theories for jet noise predictions", *J.Acoust.Soc.*, 40(4), 671-680, (2002).

J.Nikuradse, "Laws of flows in rough pipes", *NASA Technical Memorandum 1292* (1937)

C.Ollivier-Gooch and M. Van Altena, "A high-order-accurate unstructured mesh finit-volume scheme for the advection-diffusion equation", *Journal of Computational Physics*, 181(2), (2002).

J.Panda, R.G.Seasholtz, K.A.Elam, A.F.Mielke and D.G.Eck, "Effect of heating on turbulent density fluctuations and noise generation from high speed jets", NASA/TM-2004-213126, AIAA-2004-3016, (2004).

D.Papamoschou, "Small-aperture phased array study of noise from coaxial jets", *Proceedings of the 45th AIAA Conference*, Reno, Nevada, USA, (2007).

B.L.Pierson, "Optimal aircraft landing-approach trajectories: A comparison of two dynamic models", *Annual Review in Automatic Programming*, 13(2), 139-145, (1985).

T.Poinsot and S.K.Lele, "Boundary conditions for direct simulation of compressible viscous flows", *Journal of Computational Physics*, 101, 104-129, (1992).

W.Polifke, C.Wall and P.Moin, "Partially reflecting and non-reflecting boundary conditions for simulation of compressible viscous flow", *Journal of Computational Physics*, 213, 437-449, (2006).

W.C.Reynolds, "Fundamentals of turbulence for turbulence modelling and simulation", *Lecture Notes for Von Karman Institute Report No. 755*, (1987).

H.S.Ribner, "The generation of sound by turbulent jets", in *Advances in Applied Mechanics*, Academic, New York, (1964a).

H.S.Ribner, "Quadrupole correlations governing the pattern of jet noise", *J. Fluid Mech.* 38(1), 1-24, (1964b).

S.Sarkar and L.Balakrishnan, "Application of a Reynolds-stress turbulence model to the compressible shear layer", *ICASE Report 90-18, NASA CR 182002*, (1990).

R.W.Schefer, "Data base for a turbulent, nonpremixed, nonreacting propane jet flow", Sandia National Laboratories web page <http://www.sandia.gov/TNF/DataArch/ProJet.html>, (1988)

R.W.Schefer, S.C.Johnson, R.W.Dibble, F.C.Gouldin and W.Kollmann, "Nonreacting turbulent mixing flows: a literature survey and data base", *Sandia Report SAND86-8217*, Sandia National Laboratories, Livermore, CA, USA, (1985).

R.W.Schefer and R.W.Dibble, "Rayleigh scattering measurements of mixture fraction in a turbulent nonreacting propane jet", AIAA-86-0278, AIAA 24th Aerospace Sciences Meeting, Reno, USA, January 6-9, (1986).

R.W.Schefer and R.W.Dibble, "Mixture fraction field in a turbulent non-reacting propane jet", *AIAA Journal*, 39, 64-72, (2001).

R.W.Schefer, V.Hartmann and R.W.Dibble, "Conditional sampling of velocity in a turbulent nonpremixed propane jet", *Sandia Report SAND87-8610*, Sandia National Laboratories, Livermore, CA, USA, (1987).

J.Schulze, J.Sesterhenn, P.Schmid, C.Bogey, N.de Cacqueray, J.Berland and C.Bailly, "Numerical simulation of supersonic jet noise", *Notes on Numerical Fluid Mechanics and Multidisciplinary Design*, 104/2009, 29-46, DOI: 10.1007/978-3-540-89956-3_2, (2009).

E.Sergent, "Vers une methodologie de couplage entre la Simulation des Grandes Echelles et les modeles statistiques", *PhD thesis*, L'Ecole Centrale de Lyon, Lyon, France, (2002).

T.-H.Shih, W.W.Liou, A.Shabbir, Z.Yang and J.Zhu, "A new k - ϵ eddy-viscosity model for high Reynolds number turbulent flows – model development and validation", *Computers Fluids*, 24(3), 227-238, (1995).

M.L.Shur, P.R.Spalart, and M.Kh.Strelets, "Noise prediction for increasingly complex jets. Part ii: Applications", *International Journal of Acoustics*, 4(34), 247-266, (2005).

M.L.Shur, P.R.Spalart, M.Kh.Strelets, and A.K.Travin, "Towards the prediction of noise from jet engines", *International Journal of Heat and Fluid Flow*, 24(4), 551-561, (2003).

J.Smagorinsky, "General Circulation Experiments with the Primitive Equations. I. The Basic Experiment", *Monthly Weather Review*, 91:99-164, (1963).

Y.P.Tang and D.Rockwell, "Instantaneous pressure fields at a corner associated with vortex impingement", *Journal of Fluid Mechanics*, 126, 187-204, (1983).

H.K.Tanna, "An experimental study of jet noise. Part 1: Turbulent mixing noise", *Journal of Sound and Vibration*, 50(2), 405-428, (1970).

H.K.Tanna, P.D.Dean and R.H.Burrin, "Turbulent mixing noise data, the generation and radiation of supersonic jet noise", *U.S. Air Force Aero Propulsion Laboratory Technical Report AFAPL-TR-76-65*, 3, (1976).

C.K.W.Tam, J.C.Webb, and Z.Dong, "A study of the short wave components in computational acoustics", *Journal of Computational Acoustics*, 1, 1-30, (1993).

C.K.W.Tam "Computational aeroacoustics: Issues and methods", *AIAA Journal*, 33, 1788-1796, (1995).

C.K.W.Tam "Advances in numerical boundary conditions for computational aeroacoustics", *Journal of Computational Aeroacoustics*, 6, 377-402, (1998).

C.K.W.Tam "Dimensional analysis of jet noise data", *AIAA-2938*, (2005).

P.S.Tide and K.Srinivasan, "Novel chevron nozzle concepts for jet noise reduction", *In Proceedings of the Institution of Mechanical Engineers, Part G: Journal of Aerospace Engineering*, 223(1/2009), 51-67, (2009).

O.G.Tietjens, "Applied hydro- and aeromechanics: based on lectures of L.Prandtl", New York, London: McGraw-Hill, (1934).

P.Tipler, "Physics for scientists and engineers", Third Edition, by Worth Publishers, (1991).

P.G.Tucker, "The LES model's role in jet noise", *Progress in Aerospace Sciences*, 44, 427-436, (2008).

A.Uzun, A.S.Lyrintizis, and G.A.Blaisdell, "Coupling of integral acoustics methods with LES for jet noise prediction", *International Journal of Aeroacoustics*, 3(4), 297-346, (2005).

M.Wang and P.Moin, "Dynamic wall modelling for large-eddy simulation of complex turbulent flows", *Journal Physics of Fluids*, 14(7), 2043-2051, (2002).

R.Westley and J.H.Woolley, "An investigation of the near noise fields of a choked axisymmetric air jet", *Technical report N69-10531, NTIS NRC-10352 LR-506*, (1968).

H.Xia, P.G.Tucker, and S.Eastwood, "Large-eddy simulations of chevron jet flows with noise predictions", *International Journal of Heat and Fluid Flow*, 30(6), 1067-1079, (2009).

C.Yu, W.R.Wolf, R.Bhaskaran, and S.K.Lele, "Study of noise generated by a tandem cylinder configuration using LES and fast acoustic analogy formulations", *AIAA Workshop in Aeroacoustics*, Stockholm, Sweden, (2010).

D.W.Zingg, H.Lomax, and H.M.Jungens, "High-accuracy finite-difference schemes for linear wave propagation", *SIAM Journal of Scientific Computations*, 17(2), 328-346, (1996).

M.Zhuang and R.F.Chen, "Application of high-order optimized upwind schemes for computational aeroacoustics", *AIAA Journal*, 40(3), 443-449, (2002).